ACCELERATOR MASS SPECTROMETRY

FOR RADIOCARBON DATING

Advances in Theory and Practice

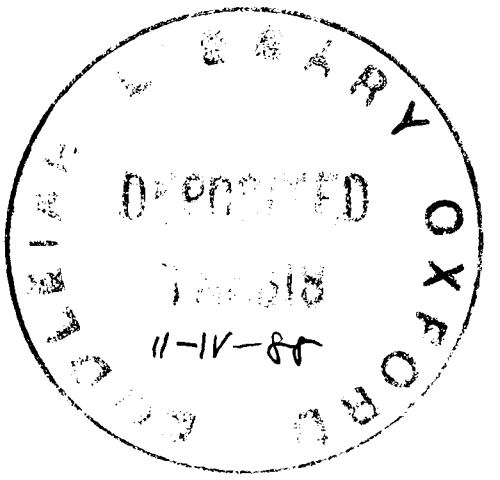

Christopher Ramsey Bronk

Merton College

A thesis submitted for the degree of Doctor of Philosophy

at Oxford University, Trinity Term 1987

ACCELERATOR MASS SPECTROMETRY FOR RADIOCARBON DATING

Advances in Theory and Practice

A thesis submitted for the degree of Doctor of Philosophy
at Oxford University, Trinity Term 1987

Christopher Ramsey Bronk
Merton College

ABSTRACT

Accelerator mass spectrometry (AMS) has been used routinely for radiocarbon measurements for several years. During this period it has become evident neither the accuracy nor the range of the technique were as great as had originally been hoped. This thesis describes both theoretical work to understand the reasons for this and practical solutions to overcome some of the problems.

The production and transport of the ions used in the measurements are found to be the most crucial stages in the process. The theories behind ion production by sputtering are discussed and applied to the specific case of carbon sputtered by caesium. Experimental evidence is also examined in relation to the theories. The phenomena of space charge and lens aberrations are discussed along with the interaction between ion beams and gas molecules in the vacuum. Computer programs for calculating phase space transformations are then described; these are designed to help investigations of the effects of space charge and aberrations on AMS measurements. Calculations using these programs are discussed in relation both to measured ion beam profiles in phase space and to the current dependent transmission of ions through the Oxford radiocarbon accelerator. Improvements have been made to this accelerator and these are discussed in the context of the calculations.

There are many reasons for wishing to produce C^- ions directly from carbon dioxide. The most suitable type of source for achieving this is the Middleton High Intensity Sputter Source. Experiments to evaluate the performance of such a source are described and detailed design criteria established.

An ion source designed and built specifically for radiocarbon measurements using carbon dioxide is described. Experiments to evaluate its performance and investigate the underlying physical processes are discussed. The source is found to have a high efficiency enabling small samples (<100 μg of carbon) to be measured. The cross contamination is measured to be low (<0.1%) and the background currents are small; the implications of these results are discussed.

Quelli che s'inamora di pratica saza scietia so como 'l nocchiere che etra navilio sanza timione e bussola, che mai a certezza dove si vada

[Leonardo da Vinci]

(Those who fall in love with practice without science are like a sailor who enters a ship without a helm or a compass and who never can be certain whither he is going)

ACKNOWLEDGEMENTS

First and foremost I would like to thank Robert Hedges for his help and support throughout the progress of this research, and for innumerable discussions and ideas. My gratitude is also due to Prof. E.T. Hall for his interest and help, especially with the construction of the new ion source. I owe much to Colin Perry for his help with the electronics and computing involved and for invaluable discussions on other topics as well.

This research would not have been possible but for the close cooperation of the Oxford Nuclear Physics Department. In particular, I would like to thank Dr. G. Doucas for the loan of the High Intensity Sputter Source and for a number of interesting discussions. I wish to thank Mr. W. Linford for his help with the design of the sample changing mechanism for the new ion source and Dr. I.C. McArthur for his patience and guidance in the use of the Nuclear Structure VAX computer. Thanks are also due to the members of the Nuclear Physics Workshop for their help and cooperation.

I am indebted to Prof. R. Middleton, both for his pioneering work in this field, and for his encouragement with the development of the gas ion source. I am also grateful to Prof. A.E. Litherland for interesting discussions on various topics.

I would like to thank Martin Humm and John Foreman for their help in the laboratory and Dave Seeley for carrying out many of the difficult machining jobs required in the course of this research. I am also grateful to Lucy de Trafford for her help with measurements made on the ion source test bench and with the preliminary drawings for the new ion source. I thank Stephen Roberts for his assistance in sorting out the electronics for the computer control of the new ion source.

I am grateful to my parents for their helpful suggestions during the writing of this thesis.

The final word of thanks must go to the S.E.R.C. for supporting this research and to the Royal Society for funding the development of the new ion source through the Paul fund.

C.R. Bronk,

August 1987

CONTENTS

Note on cross references:

The format for cross references is:

part"/"*chapter*":"*section*"."*subsection*

where the more general labels are only used when necessary. Thus subsection 4 of section 3 of chapter 2 in part I is referred to as I/2:3.4 from part II, as 2:3.4 from chapter I/1 and just as 3.4 from within chapter I/2. In a similar fashion figures, tables and equations are referred to as:

part"/"*chapter*":"*figure number*

part"/"*chapter*":"*section*"."*subsection*"."*table number*

part"/"chapter":"section"."subsection"."equation number

Note on units:

In general S.I. units have been used throughout this thesis. However pressures are given in atmospheres. It should be noted, therefore, that:

$$1 \text{ atmos.} = 1.013 \times 10^5 \text{ N m}^{-2}$$

CONTENTS

LIST OF FIGURES

PART I ION OPTICS and Related Physical Phenomena

Chapter 2: Sputtering

Chapter 3: Brightness Profiles

FIGURES

FIGURES

FIGURES

FIGURES

FIGURES

LIST OF TABLES

PART II ION SOURCES and Associated Techniques

TABLES

PREFACE

In 1959 C.P. Snow talked of the great gulf that existed between 'the Two Cultures' and, of research which spanned this bridge, he said [1]:

> *'In the history of mental activity, that has been where some of the breakthroughs came. The chances are there now. But they are there, as it were in a vacuum, because the two cultures can't talk to each other.'*

And yet in the decade preceding this, one such breakthrough had taken place, for it was in 1949 that W.F. Libby put forward the idea of radiocarbon dating [2]. The great antiquity of man had been appreciated since the early part of the nineteenth century (see for example the writings of Sir John Lubbock [3]). However, the advent of radiocarbon dating allowed the passage of archaeological time to be measured directly and to be measured in absolute terms. The importance of this to archaeology has been enormous: in the words of G. Daniel [4]:

> *'It is no exaggeration to say that the discovery of radiocarbon dating is the most important development in archaeology since the discovery of the antiquity of man and the acceptance of three technological ages.'*

These words were written in 1967, the same year in which H.E. Suess produced the first calibration of radiocarbon dates [5,6]. The effect of this on prehistory was almost as profound as the initial discovery and over the next decade our understanding of the relationships between the prehistoric cultures of Europe and the civilisations of the Aegean and the Near East had to be completely revised.

It would be wrong to suggest that the history of radiocarbon, or indeed of archaeological science as a whole, has been without its inglorious moments. In a sense the gulf of which C.P. Snow talked has

taken its toll: archaeologists have at different times been both too trusting and too dismissive of the scientific evidence and scientists have paid to little attention to the archaeological dimension of the problems which they are trying to solve. Increasingly, however, there is a realisation that the uncovering of the past cannot be neatly divided into the disciplines of science and archaeology, and that many of the problems must be tackled by those familiar with both fields.

All of the major advances in archaeological understanding which I have alluded to above have come about through the application of conventional radiocarbon dating. Over the past four decades there have been substantial improvements in this technique (for an overall discussion of the techniques and principles see ref. [7] and references therein), but then in 1977 the new method of radiocarbon dating by accelerator mass spectrometry was discovered [8,9]. The principles of the method are described elsewhere [10,11,12], but essentially the aim is to count the ^{14}C atoms in a sample directly instead of counting only those that decay. The main advantage of this is that there is a reduction in the sample size that is needed to measure the age to a particular accuracy. This, in turn, means that for a sample of given size one can, in principle, make a more precise radiocarbon measurement; this precision should also allow the age of samples of greater antiquity to be determined. In practice, there are difficulties both with the age range and with the accuracy, and a discussion of these and ways to overcome them will form the basis of this thesis.

Before describing the scientific research that has been undertaken, it is important to look at the archaeological context of this work.

1. Accuracy and Age Range

The accuracy of radiocarbon dates is clearly of paramount importance. If the technique is to be of value in solving problems in the historical period, accuracies of less than a hundred years are often necessary and, given the vagaries of the calibration curve, this is frequently not possible. For periods such as the Post Roman Dark Age, for example, identical radiocarbon measurements might be made on material from several centuries [13]. In other periods conventional radiocarbon measurements can achieve this aim and accelerator mass spectrometry can already or will soon be able to do the same. In going back from the historic to the prehistoric periods the need for absolute accuracy might be expected to diminish. However, in the study of relative chronologies and in looking at the development of sites or whole 'cultures', the greater the temporal resolution, the more can be seen.

The age range over which radiocarbon dating is useful is virtually all of the upper paleolithic right up to recent centuries. However, at present the techniques of accelerator mass spectrometry cannot reliably be used beyond about 50,000 years, and this puts the emergence of *homo sapiens sapiens* just out of reach. Although a few conventional laboratories can date back further than this, the sample sizes required are almost prohibitively large (25 g or greater) especially given that the preservation of organic material of such an age is almost always very poor.

2. The Importance of Large Numbers of Samples

The ability of accelerator mass spectrometry to use only small amounts of material has a large impact on the number of potential samples available for dating. Already the ability to look at many different samples on a

site in order to get a clearer understanding of the chronological structure is providing new insights into the problems of archaeological interpretation (see, for example, the series of measurements from Abri Pataud [14]). In many ways this would seem to be one of the most important contributions which radiocarbon dating has to make. Furthermore, the investigation of time spans need not only be applied to archaeological sites: art historical work of this kind is also possible and is much more valuable than simple authenticity tests. Examples of this are work done on Islamic doors at the Ashmolean Museum [15] and on the bindings of the Domesday books [16].

It is clear that the detailed examination of chronological structure requires the examination of many different samples, preferably of different types. Except in a minority of sites, the amount of surviving organic material is very sparse, and so it is important that one should be able to measure the age of samples even if they are very small so that one can make maximum use of the available material. This approach can have its difficulties because of the mobility of small samples within archaeological layers [17] and because of the contamination to which they are prone. The first of these problems can only really be tackled by choosing samples of primary, rather than associative importance or by measuring a large number of samples so that a distribution can be built up. The second can be tackled by greater chemical selectivity.

Finally it is worth bearing in mind that many of the above benefits can only be realised if there are the resources to measure large numbers of samples.

3. Sample Selection

Fortunately the activities of man are very often closely associated with organic materials; it is this which makes radiocarbon such a valuable tool. The most obvious example is his skeletal remains, and human bones are certainly a very rich source of material for dating. However, human occupation is sometimes continuous over long periods and human remains are frequently difficult to associate with the activities under examination. In some ways, therefore, it is more important to date the buildings, tools, food and other objects which make up the material culture. Except in the case of large scale structures, this usually requires one to make use of small samples.

Although an exhaustive list of the types of archaeological samples suitable for radiocarbon dating would be out of place here, it is useful to introduce some real examples into this discussion:

3.1. Human Remains

These are most important when the date at which human occupation of any kind is of interest, for example in the case of early man in America. Much work on this particular area has now been done (see for example [18]) and has helped to clear up some of the controversy. Radiocarbon dating will certainly play a vital role as more evidence comes to light. The surviving organic fractions of such bones are frequently small and so the required chemical selectivity (see below) necessitates the use of small samples.

3.2. Building materials

Some of the most impressive parts of the archaeological record are the building structures which survive. These can, however, almost always be

dated using fairly large samples and so, until the accuracy of AMS dating exceeds that of conventional techniques, the main interest in applying the accelerator method to these materials is for 'known age' measurements [16].

3.3. Tools

Many of the existing chronologies are based on tool and weapon types and these make up a substantial portion of the surviving material culture. By their nature tools and weapons are often small or contain little organic material.

Examples of this kind of sample are the bone and antler points from Northampton and Sproughton [19]. Finds of this kind are fairly rare and, because of their small size, their association with other material can be uncertain. Direct radiocarbon dating of the tools themselves is clearly desirable, and this is really only possible if small samples of material can be used.

Another type of sample which is fairly rare but which might help to tie down the typological chronologies of the Bronze Age is that of bronze tools which retain a little organic material, such as the socketed and pegged Bronze Age spearhead found at Jackscar Cave [18].

3.4. Clothes

Finds of clothes from the prehistoric periods are very rare. Cloth from an archaeological site is also fairly vulnerable to contamination and must therefore undergo extensive chemical pretreatment before radiocarbon measurements are made. For both of these reasons it is important that small samples can be dealt with satisfactorily. This is also often true for cloth from the historical periods which may be valuable for other reasons. This is the case for the 'Turin Shroud'.

3.5. Food

The three classic periods of the Stone Age are defined by the methods of food production. When one is studying changes in these methods, it is clearly ideal if one can base the chronology of the study on the food itself rather than on associated material. One of the finest examples of this is the dating of individual seeds which can be recognized as being cultivated species such as the *hordeum spontaneum/distichon* grains from Netiv Hagdud [16]. The scope for this kind of work and similar studies on floral remains is enormous if sample size can be sufficiently low and if the number of samples is high enough to give reasonable geographical and temporal distributions.

Bones discarded on archaeological sites provide one of the most important types of material for the correlation of radiocarbon age with stratification. There is often a continuous distribution of these throughout an occupation site, and faunal bones are not as subject as human bones to special treatment such as burial. Depending on the state of preservation and the species concerned, small sample techniques are very often necessary after the required chemical treatment.

3.6. Faunal Remains

In addition to the value of animal bones in the dating of associated material, they provide the archaeologist with useful information on the animals in the environment and under domestication at the time of occupation. It is, therefore, clearly valuable to be able to discover the age of bones from particular species directly so that the domestication of animals can be traced or, in earlier periods, the presence and exploitation of wild species be studied.

The bones of interesting species are often rare and so one may be forced to date bones in a state of preservation which is far from ideal.

3.7. Charred Material

Fire is an important pointer to human activity. Fortunately charred remains also tend to survive well. It is for this reason that a large proportion of radiocarbon measurements have been made on charcoal or other burnt materials. Small samples of charcoal, however, tend to move about within the soil after deposition (see for example the dates for Hengisbury Head [18]), and it would clearly be unwise to base too much on small quantities of material of this kind.

Charred bones provide material which is possibly less mobile and yet still often requires small sample techniques.

Charred seeds can sometimes survive in conditions where ordinary seeds would not and can be a valuable source of material although obviously again mobility is a problem unless the stratigraphy is really undisturbed (see for example the dates for Wadi Hammeh [16]).

Sometimes small amounts of charred material can be found physically attached to artifacts and this can allow vessels to be dated by association with their charred contents (for example the sherd from Montechito [15]).

3.8. Carbon from Industry

Crude pottery often contains small amounts of organic material as a temper and this could in principle be used to make direct measurements on the age of pottery where thermoluminescence dating may not be applicable or not sufficiently accurate. At present more work needs to be done on the extraction methods for this to be a routine technique.

Metal-smelting involves the use of charcoal, remains of which can be found in the slags associated with metalworking sites. Such charcoal has been dated [15], although perhaps a more important contribution which AMS can make in this field is the direct dating of carbon dispersed in metals

and slags. Work on the carbon found in iron has shown that this is possible [20] but clearly more research needs to be done.

3.9. Tree Rings

Tree rings play a vital role in the process of radiocarbon dating. The calibration curves derived from long sequences of rings have been built up using conventional radiocarbon techniques and are now extremely accurate [13]. It seems unlikely that there will be a pressing need to repeat this work using AMS. Tree rings do however provide a valuable source of 'known age' material.

There is also an exciting new possibility which arises from the ability to measure the radiocarbon content of small samples: by making such measurements on a sequence of rings one should be able to match the fluctuations to those of the calibration curve. This would enable one to discover the age of the wood to an accuracy of a few years and furthermore, might allow one to build up dendrochronological sequences for new areas and periods. The accuracy required for work of this kind is very high.

4. Chemical Selectivity

As already stated, there are sometimes difficulties with radiocarbon measurements made on small samples because of their vulnerability to contamination by chemicals containing different proportions of ^{14}C. The only way to circumvent this problem, in many cases, is to be more chemically selective than would be necessary for measurements on larger samples. The approach is obviously highly dependent on the type of sample under consideration. This is not the place for a detailed discussion of sample treatment but it is useful to look at some examples in order to see how the subject impinges on the physical measurements that are to be made.

4.1. Charcoal

In making measurements on charcoal one is attempting to find the radiocarbon age of the elemental carbon present in the sample. Because the great majority of the material is carbon there is usually little difference between the size of the archaeological sample and the sample that is to be measured, although some cleaning is necessary.

4.2. Wood, Linen et cetera

The remains of plant material all contain cellulose which is fairly stable and does not readily exchange its carbon with the environment. It is therefore desirable when dealing with such material to select only the cellulose for dating.

The proportion of the material remaining after such pretreatment varies according to the state of preservation of the artifact but typical values are 10 to 30%.

4.3. Bone

Measurement of the radiocarbon age of bones is fraught with difficulties. The most important of these is that the carbonate in the bone is subject to exchange of carbon dioxide with the environment. In order to get around this the amino acid fraction can be extracted [21]. Doing this removes a very large portion of the sample since even in a well preserved bone less than 25% of the mass is in the form of amino acids.

If the proportion of amino acids is below about 1% as it can be in poorly preserved bones there seem to be further problems with contamination [22]. It is likely that extracting only proline and more especially hydroxyproline (an amino acid which is very specific to bone) might improve the situation. However, for a bone with only 1% of its mass in the form of

amino acids the total amount of these two specific acids would not be more than 0.2% of the initial mass of the bone. This clearly puts very severe limits on the size of the sample that is to be measured.

Conclusion

Although radiocarbon dating has been in use for nearly forty years, it is clear that the recent developments in it by accelerator mass spectrometry open up the way for many new and interesting areas of investigation. It is difficult to appreciate the scale of the increase in the numbers of potential radiocarbon samples. The most important effect of this is that, whereas in the past the type of sample was almost always dictated by the constraints of large sample size, it is now possible to make the choice on the basis of archaeological criteria. It also means that samples of many different types can be measured enabling the chronological structure of an archaeological site to be established independently of the stratigraphic evidence. The fact that only small quantities of carbon are necessary is also a great benefit when it comes to the chemical pretreatment of sample, as most of the best techniques involve the extraction of only a small chemical fraction of the archaeological sample for isotopic measurement.

There are, however, still considerable problems: firstly, there is little point in creating many new applications for the method if there is no way of fulfilling the inevitable increase in demand; secondly, the technique is still not accurate enough to be useful in many situations; thirdly, a large number of samples, after suitable treatment, are too small to be measured; and finally, the contamination levels are too high to enable the method to be used for material much older than 40,000 years. The aim of anyone working in this field must therefore be to tackle these

four problems; if they could be overcome, the benefits to archaeology would be enormous.

References

[1] C.P. Snow, The Two Cultures (C.U.P., New York, 1959) p. 17.

[2] W.F. Libby, E.C. Anderson and J.R. Arnold, Science 109 (1949) 227.

[3] Sir John Lubbock, Prehistoric Times, (1865) 1.

[4] G. Daniel, The Origins and Growth of Archaeology, (Penguin, Harmondsworth, Middlesex, 1967) p. 280.

[5] H.E. Suess, Radioactive Dating and Methods of Low Level Counting, International Atomic Energy Authority, Vienna (1967) 24.

[6] H.E. Suess, Radiocarbon 28 part 2A (1986) 259.

[7] W.G. Mook and H.T. Waterbolk, Radiocarbon Dating, Handbooks for Archaeologists No. 3 (European Science Foundation, Strasbourg, 1985).

[8] D.E. Nelson, R.G. Korteling and W.R. Stott, Science 198 (1977) 507.

[9] C.L. Bennett, R.P. Beukens, M.R. Clover, H.E. Gove, R.B. Leibert, A.E. Litherland, K.H. Purser and W.E. Sondheim, Science 198 (1977) 508.

[10] R.E.M. Hedges, Nucl. Instr. and Meth. 220 (1984) 211.

[11] A.E. Litherland, Nucl. Instr. and Meth. B5 (1984) 100.

[12] R.J. Batten, C.R. Bronk, R. Gillespie, J.A.J. Gowlett, R.E.M. Hedges and C. Perry, Radiocarbon 28 (1986) 177.

[13] M. Stuiver and B. Becker, Radiocarbon 28 part 2B (1986) 863.

[14] P.A. Mellars and H.H. Bricker, Archaeological results from accelerator dating (ed. J.A.J. Gowlett and R.E.M. Hedges), Oxford University Committee for Archaeology Monogr. 11 (1986) 73.

[15] R. Gillespie, J.A.J. Gowlett, E.T.Hall and R.E.M. Hedges, Archaeometry 26 (1984) 15.

[16] J.A.J. Gowlett, R.E.M. Hedges, I.A. Law and C. Perry, Archaeometry 28 (1986) 206.

[17] W.G. Mook, Nucl. Instr. and Meth. B5 (1984) 297.

[18] R. Gillespie, J.A.J. Gowlett, E.T. Hall, R.E.M. Hedges and C. Perry, Archaeometry 27 (1985) 237.

[19] J.A.J. Gowlett, E.T. Hall, R.E.M. Hedges and C. Perry, Archaeometry 28 (1986) 116.

[20] R. Creswell, private communication.

[21] R. Gillespie, R.E.M. Hedges, and M.J. Humm, Radiocarbon 28 (1986) 451.

[22] R.E.M. Hedges, Phil. Trans. R. Soc. A (1987) (in press).

PREFACE

INTRODUCTION

The methods of radiocarbon dating by accelerator mass spectrometry (AMS) are now fairly well established (see, for example [1],[2] and [3] for a detailed discussion of the technique). However, as indicated in the preface a number of difficulties remain. The first of these is one that will probably always remain: it is not possible to carry out the number of measurements that are needed. The second is that the age range of the technique is still well short of the 80,000 years that was at first envisaged. Finally the accuracy of the measurements is not yet as high as for conventional radiocarbon measurements (with large samples) which puts limitations on the usefulness of the technique. It is the purpose of this thesis to investigate the physical phenomena underlying these problems and to try to find solutions to them where this is possible.

The requirements of the users of radiocarbon dating outlined in the previous chapter can be translated into requirements for the actual measurement technique which is to be applied. Broadly speaking, there are four such requirements:

a. an increased number of measurements
b. a reduction in the levels of contamination
c. improved counting statistics on small samples
d. higher accuracy

It is instructive at this stage to take an overall view of the strategy underlying this research and the ways in which it is hoped these objectives will be attained.

1. Increasing the Number of Measurements

As has already been indicated, although this seems on the face of it to be a change which, albeit desirable, makes no fundamental difference, in fact the number of age measurements that can be made does have a very great impact on the quality of work that can be done. There are four mechanisms by which this number is restricted; each has a direct bearing on the measurement technique which is to be applied:

a. The selection of samples for dating is frequently a problem, both for the archaeologist, who must find enough samples on the archaeological site, and for the chemist who might want to select particular fractions of the sample for measurement. In both cases the ability to date samples of very small size is of paramount importance.

b. The inevitable limitations on the time of chemists involved in the treatment of samples make it desirable that the material required for measurement is as easy to produce as possible. The first stage in the preparation at which all of the samples have the same form is when they are burnt to form CO_2. Ideally, therefore, the chemical preparation should end at this point.

c. Ultimately the ability of an accelerator unit to produce large numbers of measurements depends on the rate at which the accelerator can sift samples for ^{14}C. In other words, the carbon current must be sufficiently high for accurate measurements to be made in as short a time as possible.

d. Finally the number of samples that can be dated can clearly not be divorced from financial considerations. There is little point in developing techniques which, although technically viable, are too expensive for the archaeological community. This requirement for low cost must be met by minimising both the measurement time on the actual accelerator system (which makes high currents necessary) and the chemical preparation time (hence the desirability of using CO_2 directly; see section b above).

2. Reductions in Contamination

The limited age range of radiocarbon dating by AMS is not determined by counting statistics, as it usually is in conventional radiocarbon dating, but by the levels of contamination found in the small samples that are used.

Contamination is essentially the inclusion of carbon which was not originally present in the living organism in the ionic carbon beam on which the measurement is made. There can be three sources of contamination:

a. Almost all samples have some form of contamination when they are dug from an archaeological site (for example, recent root penetration) or taken from a museum (such samples might have been subjected to conservation techniques). This contamination can, in varying degrees, be removed by physically and chemically selecting particular portions. Inevitably, however, this leads to a reduction in sample size, and so often the ability to date very small samples is a prerequisite of being able to achieve the desired level of selectivity.

b. The second source of contamination comes from the chemical procedures

adopted for treating samples and used for preparing graphite targets. This is another reason for making direct measurements on CO_2. (See, for example, ref. [4]. for a discussion of this type of contamination.) The improvement of the chemical procedures employed in the production of CO_2 are an important area for further research.

c. Finally, there will be some contamination introduced when the sample is ionised because of residual hydrocarbons in the vacuum system and possibly because of cross contamination. This can be minimised by the use of UHV techniques, but it is also desirable to have a source for which it is possible to continuously monitor this form of contamination.

3. Improvements in Counting Statistics

The accuracy of measurements is fundamentally limited by the statistical uncertainty. This is a particular problem for old samples. Two deductions can be made concerning the operation of the ion source that is to be used:

a. Given the limited time available for measurements (see 1c), the current produced by the ion source must be large.

b. Because a sample is usually of strictly limited size, it is desirable to ensure that the proportion of ^{14}C nuclei present in the original sample that are actually counted is as high as possible. This implies a high source efficiency.

4. Higher Accuracy

Accuracy is essentially dependent on the extent to which the proportion of the different isotopes which are measured corresponds to the ratio in the environment of the original sample. Fractionation of a reproducible kind is not important if everything is done with respect to standards and this is the normal practice. It is, therefore, variable fractionation which is of concern here. There are five major contributions to this:

a. The incorporation of the atmospheric CO_2 into living organisms is a process subject to variable fractionation (dependent on diet, for example, in animals). The degree to which this has taken place can be estimated from the $^{13}C/^{12}C$ ratio.

b. The chemical treatment of the sample is also another possible cause of fractionation. The chance of this is eliminated if all of the chemical reactions used go to completion, and this should always be the aim. Failing this, however, the fractionation must be corrected using the $^{13}C/^{12}C$ ratio.

c. The production of graphite is a process which certainly introduces some fractionation and this is particularly troublesome as the degree of fractionation is frequently not homogeneous throughout the graphite. This is a very good reason for trying to eliminate the graphite production stage from the process.

d. The ionisation of the sample is usually achieved by sputtering. In this process the ion formation probability is at least somewhat

dependent on the velocity with which the carbon atoms are ejected and on the work function of the surface. It can therefore vary with ion source conditions and with changes in the geometry of the sputtered target. Again the degree to which this has taken place can be estimated from the $^{13}C/^{12}C$ ratio.

e. Because of various ion optic effects, the acceptance of the accelerator seems to be dependent on the current [5]. This makes variable fractionation difficult to monitor and, furthermore, makes it impossible to measure the 13C/12C ratio for the correction of any of the effects described above. It is therefore desirable that the source operates at a constant current, and it is essential that a good understanding of the ion optics leading to this effect is reached; otherwise, the accuracy of the technique will be seriously limited.

Summary

In order to make further progress in the techniques of radiocarbon dating it is clearly necessary to come to a better understanding of the physics involved in the production and transport of the ion beams.

In addition, there are various criteria for the design of a new source for radiocarbon dating. These are:

a. the direct production of C^- currents from CO_2

b. the production of high currents

c. the use of small samples

d. high efficiency (implied by b and c)

e. measurable and low background current

f. low cross contamination

The purpose of this thesis is to reach the higher level of understanding of the ion optics which is needed and to describe the development of an ion source to meet the criteria outlined above.

References

[1] N.R. White, D. Phil. Thesis, Oxford University (1981).

[2] A.E. Litherland, Nucl. Instr. and Meth. B5 (1984) 100.

[3] R.E.M. Hedges, Nucl. Instr. and Meth. 220 (1984) 211.

[4] G.A. Klouda, L.A. Currie, D.J. Donahue, A.J.T. Jull and E.H. Zabel, Nucl. Instr. and Meth. B5 (1984) 265.

[5] R. Gillespie, R.E.M. Hedges and C. Perry, Nucl. Instr. and Meth. B5 (1984) 167.

INTRODUCTION

PART I

ION OPTICS

and

Related Physical Phenomena

Introduction

The subject of ion optics is of prime importance to all measurements made by accelerator mass spectrometry. This field is almost unique in requiring one to give a detailed account of all of the material put into the ion source. If a sputter source is being used, there are essentially just four processes which must be described to explain in detail the conversion of the target material into the ion beam which is to be measured:

a. the production of the primary ion beam

b. the sputtering process

c. the extraction of the secondary ion beam

d. the transport of the secondary ion beam

Each of these will be considered in turn. The subject of ion detection and current measurement will not be dealt with.

1. The Production of the Primary Ion Beam

A sputter ion source requires a beam of ions (usually caesium for AMS) to sputter the target. The extent to which this beam is well focussed is an important factor in determining the quality of the secondary ion beam and so the ion optics relating to this is something which has received much attention. The relevant sections of an ion source are frequently cylindrically symmetric and so the particle trajectories can, in principle, be calculated fairly easily by finding solutions to Laplace's equation for the Electrostatic field. By a process of iteration space charge effects

can even be included in such calculations. In practice the only way in which such calculations can be carried out is to find the potential at a grid of points and use this for the calculations. (For examples of the use of this method, see [1,2].)

It transpires, however, that obtaining a primary beam which can be well focussed does not really pose any problems. Typical spot sizes for the incident beam are a fraction of a millimetre. As pointed out elsewhere [3], further reduction of this increases the thermal load on the sputter target and therefore reduces the sputter efficiency at the focus point. The net result of this is that one cannot expect to increase the secondary beam quality greatly by altering the primary beam optics. Most attempts to do this are based around essentially hemispherical geometries (for example [4]). Such an approach is valuable if the 'halo' that surrounds the focus point in a source such as that described in [5] is believed to have some adverse effects.

The subject of primary beam optics will not be considered further here.

2. The Sputtering Process

The relationship between the primary beam optics and those of the secondary beam are determined by the sputtering process. There are three aspects of this process which are of particular interest:

a. the total yield of different isotopes
b. the angular distribution of ejected ions
c. the energy distribution of ejected ions

The total ion yield for different isotopes is clearly of crucial

importance for AMS measurements. Fortunately in normal circumstances the sputtering process will be in a steady state (this is demonstrated by [6]). It follows that the proportions of the different isotopes sputtered will be the same as those in the target material. The isotopic yields are then dependent only on the probability of the ejected atoms being in the relevant state of ionisation.

The collision cascade theory [7,8] gives a detailed model for the actual sputtering process. One must then apply some quantum mechanical theory [6,9] to find the relative ionic abundances. These theories are not particularly well understood at present but a strong dependence on surface conditions is indicated.

As well as affecting the overall fractionation, the ionisation probability will also affect the angular distribution of ions with different masses. This is very important as it means that any subsequent limitation of the beam with apertures will cause fractionation (and this fractionation will vary with the surface conditions of the target).

For a complete description of the optical properties of an ion beam it is necessary to understand the energy distribution of the ions in the beam. collision cascade theory together with quantum mechanical models for the ionisation [6,9] are capable of giving predictions for the energy distribution as a function of the angular distribution. Measurements of the energy distribution are fairly difficult to make but have been made on carbon ions sputtered by caesium [10,11].

If the optical properties of the initial beam are known then the distribution in phase space of the secondary beam is fully determined by the sputtering process. This can be calculated with the aid of collision cascade theory [7] together with quantum mechanical treatments of the ionisation probability [6,9]. Calculations of this type have been undertaken by others (see for example [1]).

3. The Extraction of the Secondary Ion Beam

Once the secondary ion beam has been formed it will be subject to the electrostatic fields within the ion source. As stated in section 1, these are normally calculated over a grid of points, assuming cylindrical symmetry. Much work has been done elsewhere on this topic (see for example [1,2,3]). Fractionation is unlikely in this process as the extraction is purely electrostatic unless the ion beams for the different isotopes are different because of sputtering effects.

4. The Transport of the Secondary Ion Beam

Ion beam transport is usually performed in AMS systems by the application of electrostatic and magnetostatic fields in conjunction with apertures for limiting the extent of the ion beam. Electrostatic fields are normally used for all of the beam steering and focussing operations which are common to the isotopes for which the abundances are to be determined; this is because all isotopes with the same energy will respond in an identical manner. Interactions between the ions in the beam (space charge effects) are also electrostatic and so until the ion beams are magnetically separated there is no mechanism for fractionation except for the effect of sputtering (see above and chapter 2) and interactions of the ion beam with the residual gas (see chapter 6). Ideally, therefore, all of the ion beam limitation should be carried out at this stage if this is possible. In practice, aberrations (including space charge effects) and the energy spread of the ion beam, make this difficult. Once magnetic separation of the ion beams has taken place ion beams for different isotopes will not behave in the same way because of their unequal currents.

Hence it is essential to understand any physical mechanisms which are dependent on the current.

In practice, because of fractionation in the sputtering process, and because of space charge effects, the ion beams for different isotopes do not have identical forms. Furthermore, because the fractionation due to sputtering is likely to change with time and from target to target, and because space charge effects will obviously vary with current, the differences between the ion beams will not be constant. For this reason, any apertures which limit the beam are liable to result in variable fractionation and so it is essential that the transmission through an accelerator mass spectrometry system is as high as possible.

Another important stage in the ion beam transport is the ion stripping which takes place at the terminal of a tandem accelerator. The process is fairly well understood and it is certainly a source of fractionation (see refs. [12,13,14]). This need not be too serious as long as the fractionation is constant because all isotopic ratio measurements are normally carried out relative to standards. If this process were to depend in any way on the ion current, however, it would clearly have important consequences.

First order calculations of ion optics are fairly easy to carry out (using, for example, [15]) but it is clear that aberrations and space charge are important if very high transmissions through an accelerator system are required, as they are in AMS.

Measurements on the Oxford radiocarbon accelerator show that there the main limitation to transmission is at the terminal of the accelerator, and that current dependent fractionation does occur (see refs. [16,17]). This indicates that the injection system and low energy accelerator tube are the most critical elements in the system.

Summary

Ion optics and the related physical phenomena are clearly crucial in accurate accelerator mass spectrometry. Many different processes and variables are involved and so it is not feasible to model the performance of an AMS system exactly. What are most important are those elements which might introduce variable fractionation.

The production of the ions by sputtering is the first important stage, both because it is a source of variable fractionation and because it has an influence on all that follows. Space charge is also of paramount importance as are any other current dependent processes. Aberrations are not crucial in themselves but, because they make it harder to obtain high ion beam transmissions through the AMS system, they exacerbate the other effects which can give rise to variable fractionation and for this reason they are of interest.

In the following chapters all of these effects and the ways in which they affect AMS measurements will be discussed. Because of the complexity of the problem the calculations done here on aberrations and space charge are not intended to be very precise (so, for example, only generic lens types rather than specific designs are considered). The emphasis is, instead, on finding ways to model the performance of an extended ion optical system.

References

[1] J.H. Billen, Nucl. Instr. and Meth. 220 (1984) 225.

[2] H. Matthes, W. Pfestorf and L. Steinert, Nucl. Instr. and Meth. 220 (1984) 112.

[3] R. Balzer, G. Bonani, M. Nessi, Ch. Stoller, M. Suter and W. Wölfli, Nucl. Instr. and Meth. B5 (1984) 204.

[4] N.R. White, Nucl. Instr. and Meth. 206 (1983) 15.

[5] R. Middleton, Nucl. Instr. and Meth. 220 (1984) 105.

[6] N. Shimizu and S.R.Hart, J. Appl. Phys. 53(3) (1982) 1303.

[7] P. Sigmund, Phys. Rev. 184 (1969) 383.

[8] W.H. Gries and F.G. Rudenauer, Int. J. Mass Spectrom. Ion Phys. 18 (1978) 111.

[9] J.K. Nørskov and B.I. Lundqvist, Phys. Rev. B 19 (1979) 5661.

[10] G. Doucas, Int. J. Mass Spectrom. Ion Phys. 25 (1977) 71.

[11] G. Doucas, J. Phys. D 17 (1984) 429.

[12] K.B. Winterbon, Nucl. Instr. and Meth. 144 (1987) 311.

[13] H.D. Betz, Rev. Mod. Phys. 44 (1972) 465.

[14] H.J. Hofmann, G. Bonani, E. Morenzoni, M. Nessi, M. Suter and W. Wölfli, Nucl. Instr. and Meth. B5 (1984) 254.

[15] T.J.L. Greenway, Computer Program OPTRYK, Nuclear Structure Lab., Oxford University.

[16] R. Gillespie, R.E.M. Hedges and C. Perry , Nucl. Instr. and Meth. B5 (1984) 167.

[17] R.E.M. Hedges, Phil. Trans. R. Soc. A (1987) (in press).

Chapter 1

The Theory of Ion Optics

Introduction

Before discussing the calculations that have been undertaken on ion optics associated with AMS it is necessary to look at the theory of beam optics in some detail, as this is a field about which there is frequently much confusion.

The fundamental aspects of beam transport theory will be investigated and then the techniques which are normally used in calculations are described.

1. The Six Dimensional Phase Space

When dealing with ion optics one is essentially dealing with the motion of particles in space. Any pseudo-pointlike particle has six independent degrees of freedom: these can be written:

(1.0.1) $$q_x , q_y , q_z , p_x , p_y , p_z$$

where the q terms are the normalised Cartesian co-ordinates and the p terms the corresponding momenta.

This is a canonical set of co-ordinates which means that they obey Hamilton's equations:

$$q_i' = (\partial H/\partial p_i), \quad p_i' = -(\partial H/\partial q_i)$$

(here and elsewhere the notation a' is used to denote the partial differential of a with respect to time)

At this stage, it is worth introducing the symplectic notation for Hamilton's equations as this is important in understanding the symmetries arising in the phase space.

1.1. The Symplectic Condition

The canonical co-ordinates of a system with 2n degrees of freedom can be written as a column matrix $\underline{e}$ with the 2n elements q_i, p_i. Hamilton's equations then become [1]:

$$\underline{e}' = \underline{J}\,(\partial H/\partial \underline{e}) \tag{1.1.1}$$

where $\underline{J}$ is the matrix defined by:

$$\begin{pmatrix} \underline{0} & \underline{1} \\ -\underline{1} & \underline{0} \end{pmatrix} \qquad \begin{matrix} (\underline{0} = \text{nxn null matrix}) \\ (\underline{1} = \text{nxn unit matrix}) \end{matrix}$$

The purpose of this exercise is to study transformations of the coordinates. At this point the first assumption is introduced into the derivation: that the interactions of the particle can be fully described by a Hamiltonian which does not vary during the transformation. This is the condition which must be met for a transformation to be canonical. The system can be described at the final stage by the equation:

$$\underline{f}' = \underline{J}\,(\partial H/\partial \underline{f}) \tag{1.1.2}$$

The transformation from one state to the other can in general be described by the matrix equation:

(1.1.3) $$\underline{f}' = \underline{M}\ \underline{e}'$$

where the elements of the matrix are defined by : $M_{ij} = (\partial f_i/\partial e_j)$.

This can clearly be written as:

(1.1.4) $$\underline{f}' = \underline{M}\ \underline{J}\ (\partial H/\partial \underline{e})$$

However we can write $(\partial H/\partial \underline{e})$ in terms of $(\partial H/\partial \underline{f})$ because of the identity:

$$(\partial H/\partial e_i) = (\partial H/\partial f_j)(\partial f_j/\partial e_i)$$

which in matrix notation is written:

$$(\partial H/\partial \underline{e}) = \underline{M}^T\ (\partial H/\partial \underline{f})$$

Equation (1.1.4) can be rewritten:

(1.1.5) $$\underline{f}' = \underline{M}\ \underline{J}\ \underline{M}^T\ (\partial H/\partial \underline{f})$$

From (1.1.2) it then follows that

$$\underline{M}\ \underline{J}\ \underline{M}^T = \underline{J}$$

or as it is usually written:

(1.1.6) $$\underline{M}^T\ \underline{J}\ \underline{M} = \underline{J}$$

This is the so called symplectic condition and holds for all canonical transformations.

1.2. The Coordinates

In order to describe an ion optical system classically we would need to specify the six independent parameters for all of the particles in the beam. Clearly for most situations this is impossible and anyway, given the quantum mechanical uncertainty associated with these parameters for any one particle, it is not even desirable. Instead some way is needed of describing the way in which the particles which make up the beam are distributed within a space made up of these co-ordinates.

In the case of beam optics, however, the co-ordinates described above (1.0.1) are not very satisfactory since for each particle they are a function of time. In order to investigate what is essentially a steady state the most obvious way to describe the system is to define some time, t_0, at which each particle is deemed to have entered the system and then write down a probability distribution:

(1.2.1) $$f(q_x, q_y, q_z, p_x, p_y, p_z, t-t_0)$$

which is the probability density of finding a particle with those co-ordinates at that time $t-t_0$.

It is, however, at this point necessary to look in a less abstract way at what is to be described and the measurements which are to be made.

Usually, it is of interest to consider groups of particles whose velocity is predominantly in one direction; this, for simplicity, is assumed to be the z direction. Furthermore measurements are normally made on the beam at points which are a defined distance along the beam line rather than after a defined time of flight. It follows that the probability distribution described above is normally going to be considered with respect to q_z.

Many optical elements do not alter the total energy of any one

particle and it is thus convenient to use the canonical co-ordinate set:

$$(1.2.2) \qquad (q_x\ ,q_y\ ,t\text{-}t_0\ ,p_x\ ,p_y\ ,E)$$

In the cases investigated here the particles all have similar energies and times of flight, $(t\text{-}t_0)$, and so the probability distribution can be written as:

$$(1.2.3) \qquad f(q_x\ ,q_y\ ,\Delta t\ ,p_x\ ,p_y\ ,\Delta E)$$

The transformations which occur for individual 'rays' with these co-ordinates are well described [2]. All ray tracing procedures work on transformation of the six dimensional space or some subset of them (see for example [3]).

1.3. Application of the Symplectic Condition

If we generalise the co-ordinates to r_i we get the relationship:

$$(1.3.1) \qquad \begin{aligned} r_{i1} &= f(r_{j0}\ ) \\ &= f(r_{10}\ ,r_{20}\ ,r_{30}\ ,r_{40}\ ,r_{50}\ ,r_{60}\ ) \end{aligned}$$

where the second index is 0 for the initial phase space coordinates and 1 for the transformed set.

By expanding in a Taylor series we get:

(1.3.2)

$$r_{i1} = r_{j0}\left(\left(\frac{\partial r_{i1}}{\partial r_{j0}}\right) + r_{k0}\left(\left(\frac{\partial^2 r_{i1}}{\partial r_{j0}\ \partial r_{k0}}\right) + r_{10}\left(\left(\frac{\partial^3 r_{i1}}{\partial r_{j0}\ \partial r_{k0}\ \partial r_{10}}\right) + ..\right)\right)\right)$$

where the Einstein summation convention is assumed. This convention is used everywhere in this thesis unless otherwise stated. (Note that the co-ordinates which we are partially differentiating with respect to are taken to be zero.)

This formula is applicable for all canonical transformations. Each successive term corresponds to a higher order of the transformation and so, in conventional optical notation, the first term corresponds to the paraxial approximation, the third term the spherical and associated aberrations, et cetera. Furthermore the co-ordinates are canonical and so we can describe the transformation of co-ordinates using the symplectic notation developed above.

In this case we write the transformation as:

(1.3.3) $$\underline{r}_1 = \underline{M}\ \underline{r}_0$$

and the elements of the matrix are $M_{ij} = (\partial r_{i1}/\partial r_{j0})$ (note that this is not necessarily taken at $r_{j0} = 0$) which in turn can be expressed as (from (1.3.2)):

(1.3.4)

$$M_{ij} = \left(\left(\frac{\partial r_{i1}}{\partial r_{j0}}\right) + r_{k0}\left(\left(\frac{\partial^2 r_{i1}}{\partial r_{j0}\,\partial r_{k0}}\right) + r_{l0}\left(\left(\frac{\partial^3 r_{i1}}{\partial r_{j0}\,\partial r_{k0}\,\partial r_{l0}}\right) + ..\right)\right)\right)$$

where the co-ordinates which we are partially differentiating with respect to are taken to be zero.

This equation, together with the symplectic condition (1.1.6) form the basis for all constraints on phase space transformations (see [2] for a detailed treatment of the higher order relations between the elements of transfer matrices).

2. Liouville's Theorem

2.1. The Conservation of Phase Space Volume

One very simple constraint on the transformations of the phase space that can take place arises immediately from the symplectic condition (1.1.6). Taking the modulus of the equation:

$$|\underline{M}|^2 \, |\underline{J}| = |\underline{J}| \tag{2.1.1}$$

it can be seen that the modulus of the matrix $\underline{M}$ must be ± 1. This means that the size of a volume in the phase space will remain unchanged under any canonical transformation. This result is known as Liouville's theorem and is fundamental to the study of ion optics.

2.2. The Limitations of Liouville's Theorem

The arguments outlined above rely on there being a Hamiltonian that fully describes the system. This is not the case if there are interactive forces between the particles whose motion is being described. Therefore, the theory does not, in principle, hold if space charge effects are important.

This limitation is, however, not important in the case of ion optics because the number of particles that we are dealing with is very large in all cases where space charge is important. The electric fields that the particles experience are therefore, on average, the same for any two particles traversing the same path at different times. Hence there is a Hamiltonian which describes the environment in which the particles must travel even though one can only find out what it is once the beam profile has been fully determined.

Another way of looking at this problem is to imagine that one can label a small proportion of the ions in the beam. This poses no fundamental problems because we are dealing with classical mechanics and so the indistinguishability of the particles is unimportant. The space charge effects between these particles is then insignificant and the Hamiltonian that describes their environment is determined by the charge density of the unlabelled ions.

One can therefore see that, although it is not possible to write down a Hamiltonian from which one can deduce the motion of the particles, there exists a Hamiltonian which determines their motion to a very good approximation and therefore Liouville's theorem will hold.

The other assumption inherent in Liouville's theorem is that which was introduced to arrive at (1.1.2). This was the assumption that the Hamiltonian is a constant during the transformation which is likely to be the case in non-pulsed beams.

3. Restricted Descriptions of the Phase Space

In many cases the full six dimensional description of the phase space is too complicated to be dealt with. Instead one works with only a subset of the dimensions or a value derived from such a subset.

3.1. The Five-Dimensional Description

This is a description sometimes used in beam optics calculations. The five dimensions are usually given as:

(3.1.1) $$q_x, q_y, a_x, a_y, b_z$$

where $a_x = p_x/p_a$, $b_z = \Delta p_z/p_a$, $\Delta p_z = p_z - p_a$ and p_a is the average momentum

of the particles in the direction of the optical axis.

3.2. The Four-Dimensional Description

Frequently the third dimension is independent of the others and so one can restrict one's description to the four dimensions:

(3.2.1) $$q_x, q_y, p_x, p_y$$

If the third dimension and its conjugate momentum are truly independent Liouville's theorem will hold in this limited space. It is based on this assumption that the concepts of emittance and acceptance have arisen.

Emittance is simply the four dimensional volume which is filled by an ion beam or part of an ion beam. Because of convenience of measurement the coordinates most frequently used are:

(3.2.2) $$q_x, q_y, a_x, a_y$$

These are clearly not canonical coordinates. However, assuming non-relativistic behaviour, the area in this space multiplied by the energy of the beam is a constant. Thus, the units used for the normalised emittance are usually π^2 mm^2 mrad^2 MeV.

Acceptance is a concept which arises out of the effect of an aperture or series of apertures on the phase space. Any aperture limits the phase space in the q_x and q_y dimensions. An optical device will usually contain many effective apertures. A phase space can then be defined at the entrance to the element which is such that all particles contained within it will pass through the device, and all particles outside it will not. The volume of this hypothetical region of phase space is called the

acceptance of the optical element. It is equal to the maximum possible emittance of a beam which will all pass through and the units used are the same as those for emittance.

3.3. The Three-Dimensional Description

As a further simplification it is sometimes possible to separate the x and y coordinates and treat them independently. This gives rise to the two sets of coordinates:

(3.3.1) q_x, a_x, b_z

(3.3.2) q_y, a_y, b_z

For any transformations of the phase space for which the x and y dimensions are truly independent this description can be used. To describe an ion beam in terms of distributions within these spaces poses severe restrictions on the form of the beam. This will be discussed more fully in section 3.5.

3.4. The Two-Dimensional Description

The simplest description of all is that which assumes the independence of all three sets of coordinates and momenta. If this is the case, then one can apply Liouville's theorem to each set in turn. The notation most often used is similar to (3.2.2). The coordinates are:

(3.4.1) q_x, a_x

(3.4.2) q_y, a_y

and the normalised units are π mm mrad $MeV^{1/2}$.

Once again the concepts of emittance and acceptance can be used

although, as for the three-dimensional description this puts limitations on the form of the ionic beam which can be described.

3.5 Descriptions of Particle Beams

It is now necessary to look at the simplifications which can be made to the description of a beam of particles (1.2.3).

One approach is to integrate over the unused coordinates. This gives one a distribution of the form:

$$g(r_i) = \int_{r_j=-\infty}^{+\infty} f(r_i, r_j)\, dr_j \tag{3.5.1}$$

where the notation implies multiple integration over the unused coordinates r_j. This can be further integrated over the remaining coordinates to give the total particle flux. This function is conventionally called the brightness of the beam.

Another possibility is to consider the function of brightness only in the coordinates of interest while defining limits in the others. The variations are numerous, but one frequently used description for the two dimensional case is:

$$g(q_x, p_x) = \int_{q_y=-\Delta q_y}^{+\Delta q_y} \int_{q_z=-\infty}^{+\infty} \int_{p_y=-\Delta p_y}^{+\Delta p_y} \int_{p_z=-\infty}^{+\infty} f(q_x, q_y, q_z, p_x, p_y, p_z)\, dq_y dq_z dp_y dp_z \tag{3.5.2}$$

and the corresponding expression for $g(q_y, p_y)$. Often the functions are given in the form $g(q_x, a_x)$ where a_x is as defined for equation (3.1.1). This expression clearly lacks elegance and, in addition, is capable of fully describing only a very restricted set of beams. Its value lies in the ease with which it can be measured and in the fact that no averaging is taking place over dimensions in the four dimensional phase space, and so

descriptions of this type are useful for studying non linear transformations. This description of the brightness profile in phase space is sometimes referred to as the section-emittance. (See ref. [4] for a detailed discussion.)

Because the two-dimensional phase space is frequently used in calculations and measurements it is worth considering the amount of information that is lost when the two descriptions (3.5.1) and (3.5.2) are used.

The equation (3.5.1) essentially represents a projection of the six dimensional phase space onto the dimensions to be used. The function obtained can be integrated to give the total intensity. Also, assuming the transformations themselves do not mix the dimensions under consideration with those integrated over, Liouville's theorem indicates that:

$$g_1(r_{i1}) = g_0(r_{i0}) \tag{3.5.3}$$

where g_0 and g_1 are the initial and final brightness functions and where r_{i0} and r_{i1} are the initial and final phase space coordinates.

The equation (3.5.2) on the other hand has neither of these properties. The constancy of the brightness function under transformation (3.5.3) is only valid for (3.5.2) in the special case for which the functional form of the brightness is separable between the x and y coordinates. Given the approximate radial symmetry of most ion beams, the only likely function of this form is:

$$g(q_x,q_y,a_x,a_y) = \exp(Ar_x^2+Br_y^2+Cs_x^2+Ds_y^2) \tag{3.5.4}$$

where r_x and s_x correspond to any linear transformation of q_x and a_x and likewise for the y dimension. (This corresponds to a Gaussian ellipsoid in

each dimension.) This is fortunately often approximately true for the ion beam emerging from an ion source and, if this is the case, it continues to be valid until there is mixing of the three dimensions which will usually take place if there are any non linear transformations.

There is also another situation in which the description (3.5.2) is useful; this is when the brightness can be described as a function of r only and one can ignore skew rays. In this case the brightness function can be written as:

$$f(q_r,q_\theta,p_r,p_\theta) = \delta(p_\theta).h(q_r,p_r) \tag{3.5.5}$$

This function will obey Liouville's theorem assuming the z coordinates of the transformations are independent. Assuming Δq_y is small, the equation (3.5.2) can then be written as:

$$\begin{aligned} g(q_x,p_x) &= \int_{q_\theta=-\Delta q_y/r}^{+\Delta q_y/r}\int_{p_\theta=-\infty}^{+\infty} f(q_r,q_\theta,p_r,p_\theta)\ q_r\ dq_\theta\ q_r\ dp_\theta \\ &= \int_{q_\theta=-\Delta q_y/r}^{+\Delta q_y/r} h(q_r,p_r)\ q_r^2\ dq_\theta \\ &= 2\ \Delta q_y\ q_r\ h(q_r,p_r) \end{aligned} \tag{3.5.6}$$

where the integrations over z have been assumed. As $q_r = q_x$ and $p_r = p_x$ one can see in this case that $g(q_x,p_x)/q_x$ will transform correctly, and one can write:

$$g_1(q_{x1},p_{x1})/q_{x1} = g_0(q_{x0},p_{x0})/q_{x0} \tag{3.5.7}$$

This can be very useful in calculations, although in practice ion beams rarely fulfil these requirements.

4. First Order Matrix Theory

It is clear from equation (1.3.4) that the matrix elements for any transformation of the phase space are, in general, a function of $\underline{r}_0$, the initial phase. This makes any simple calculation impossible, and so one frequently considers just the first order constant part of the matrix element. This is an approximation which is good for particles with trajectories close to the axis of motion.

4.1. 'Ray Tracing'

One application of this technique is so called 'ray tracing' which is essentially just the calculation of the transformation of individual points in phase space. For this, the equation to be used is simply that given in (1.3.3):

$$\underline{r}_1 = \underline{M}\,\underline{r}_0 \tag{4.1.1}$$

The calculations can be done in any of the restricted coordinate sets described in section 3 given the same provisos. However, the calculations are most often done in five or six dimensions [3].

4.2. Beam Envelopes

In the first order approximation it is frequently convenient to assume that an envelope which contains the beam or some function of it is in the form of an ellipsoid in phase space. The value of this assumption lies in the fact that first order transformations always leave the ellipsoid as an ellipsoid. This is not a valuable approach if one is considering higher order terms in the transformation.

One can describe an ellipsoid in n dimensions by n vectors which have the directions and magnitudes of the n axes. These can be written in the form of an nxn matrix $\underline{A}$. The transformation of the ellipse is then described by the equation:

(4.1.2) $$\underline{A}_1 = \underline{M}\ \underline{A}_0$$

Even if the initial beam is not actually of this shape it is sometimes worth considering the transformation of the smallest possible ellipsoid which encloses some proportion of the beam. This is because the acceptance of many ion optical elements is approximately ellipsoidal in shape.

Summary

With the assumption that the motion of particles in an ion beam can be described by Hamilton's equations it can be shown that one can transform the phase space from one place in the beam to another. Restrictions on this transformation arise because of the symplectic condition. Liouville's theorem is one such restriction.

The ion beam can be described as a brightness distribution within the phase space. Because of Liouville's theorem such a distribution transforms in the same way as the space itself.

Restricted descriptions of the phase space are possible if the transformations to be investigated do not couple those coordinates that are to be kept with those that are not. However, if brightness distributions are to transform correctly, further restrictions are put on the form of the ion beam itself.

If only a first order description is required, then the phase space occupied by the beam can be approximated to an ellipsoid or a series of

ellipsoids containing particular proportions of the beam.

References

[1] H. Goldstein, Classical Mechanics (Addison-Wesley, Reading Massachusetts, 1980) p. 392.

[2] H. Wollnik and M. Berz, Nucl. Instr. and Meth. A238 (1985) 127.

[3] T.J.L. Greenway, Computer Program OPTRYK, Nuclear Structure Lab., Oxford University.

[4] C. Lejeune and J. Aubert, Adv. Electron. Electron Phys., Suppl. 13A (1980) 159 (see page 223).

Chapter 2

Sputtering

Introduction

It is clearly very important to understand the process of sputtering in relation to the production of ion beams for AMS. There is now an increasing body of research material on this subject both in the form of theoretical models and of measurements. A stage has been reached at which it is possible to explain many of the observed effects.

There are essentially two different processes which must be understood: firstly there is the ballistic motion of the atoms which are being sputtered which determines the velocity distributions of the ejected species, and secondly there is the process of ion formation which determines the proportions found in different charge states.

Particular attention will be given to the implications for sputtering from solid graphite and adsorbed carbon dioxide.

1. Collision Dynamics

There are two major contemporary theories to explain the ejection of atoms and ions after the impact of sputtering ions. These are the collision cascade theory and the thermal spike theory. Both theories have their strengths in explaining what is happening under different conditions.

We are interested in the velocity distribution of the ejected ions and in the angular dependence of their ejection flux. In addition, it would be useful to know the angular dependence of the velocity distribution. All of these properties are important in defining the brightness profile of the

beam produced by an ion source. In general it is the form of the function $d^2N/dEd\Omega$ that we wish to discover (where d^2N is the number of ions in the energy range dE ejected into the solid angle $d\Omega$).

1.1. Collision Cascade Theory

When an energetic ion impinges on a solid surface it suffers collisions with the atoms in the solid. The atoms recoil from these and further collisions result. Collision cascade theory treats these chains of events and allows predictions to be made about the species that are finally ejected from the surface [1].

In addition to this theory there are two main types of computer simulation which are based on this type of process: these are the molecular dynamic (MD) and binary collision approximation (BCA) simulations. MD calculations are made by considering the target-target atom interactions simultaneously with the projectile-target interactions; the precise evolution of individual cascades can thereby be studied in detail but unfortunately only with very substantial use of computer time. Most sputtering simulations are, therefore based on the BCA model which assumes that only one interaction is taking place at any one time and makes use of the Monte Carlo technique. For a discussion of these computer simulations, see ref. [2].

The energy distributions of the ejected atoms, from the basic collision cascade theory can be shown to be [1]:

$$N(E) = C\, E/(E+E_b)^{n+1} \qquad (1.1.1)$$

where C is a constant, E_b is the 'binding energy' which is usually assumed to be close to the energy of sublimation. This distribution is based on the assumption that the cascades are isotropic and that the surface

potential is planar. In addition to this, it is found that n is approximately equal to 2 as long as the interaction energies in the solid are low. This is a reasonable assumption for many solids and the E^{-2} dependence at high energies is a common feature of the energy distributions of sputtered material [3].

The angular dependence of the distribution function depends on the form which one assumes for the binding energy. There are two current models for this and these are the isotropic binding energy and the planar binding energy. Both of these models predict a cosine distribution. Computer simulations, however, predict that the distributions will differ from this, and that for high energies they will generally be more outwardly peaked than the cosine function. Experimental results always seem to give a distribution of the form:

$$Y(\theta) = C \cos^{s}\theta \qquad (1.1.2)$$

where s increases from 1 with increasing energy and with increasing target to projectile mass ratio [4].

The discussion so far has, of course, assumed that the distribution is separable in energy and angle. In practice this is not the case but, in order to get any predictions of the cross terms, it is necessary to use computer simulations. These are also able to calculate the effect of different angles of incidence for the bombarding ions.

The dependence of the energy distribution and the yield on the angle of incidence is, to a large extent, governed by the angular distributions of the primary recoils at different angles of incidence. It is found that there are many more primary recoils in the forward direction for oblique bombarding angles. The average energy for the forward scattered atoms is also found to be greater as a result [5]. However, for normal incidence

both the primary recoil yield and the mean energy of ejected ions is found to be more or less independent of ejection angle.

1.2. Thermal Spike Theory

This theory is based on the principle that when an ion strikes the surface of solid the effective temperature of that surface will be locally raised, thereby enabling some of the material to be evaporated.

The energy distribution resulting from this kind of mechanism is essentially just a Maxwell-Boltzmann distribution [2]:

$$N(E) = C\ E \exp(-(E + E_b)/kT_s) \tag{1.2.1}$$

where T_s is the characteristic temperature of the thermal spike which is greater than the ambient temperature.

The angular distribution would again be expected to be a cosine distribution.

1.3. Preferential Sputtering and Isotope Effects

In some applications of secondary ion mass spectrometry the isotopic dependence of the yields of different isotopes is important. This preferential sputtering of particular elements or isotopes from the target is dependent on three main processes: kinetic effects, radiation induced segregation and radiation enhanced diffusion. The collision cascade will result in certain fractions of the target being removed faster than others which leaves behind an altered layer. Radiation induced segregation in the region of ionic damage results in atoms with lower surface energies moving to the surface, and the dislocations caused by the bombardment allow more rapid diffusion to take place in the surface region [6]. These surface effects take place over about ten atomic layers.

Once a steady state has been reached, the material ejected from the surface must be identical in composition to the bulk material and so no fractionation can take place by this mechanism. Typical erosion rates for targets used in AMS are several hundred atomic layers a second, and so steady state is effectively reached instantaneously.

There is some evidence that the angular distribution of the sputtered atoms depends on the distributions of the isotopes in the surface region from which the sputtered particles come. It is expected that if one component is enriched at the surface, then that component should show enrichment at high angles [7]. In sputtering from elemental targets it is

average mass M	isotope mass M_j	$(M/M_j)^{2m}$	max. fractionation relative to ^{12}C
12 (graphite)	12	1.000	-
12	13	0.991	0.9 %
12	14	0.983	1.7 %
48 (titanium)	12	1.165	-
48	13	1.155	0.9 %
48	14	1.145	1.7 %

Table 1.3.1
The maximum fractionation expected in any one direction as a result of the collision cascade

found that, at low fluence, there is an overall enrichment of the light isotope indicating that the surface layer is enriched in the heavier isotope and so the angular distribution for the lighter isotope should be more forward peaked. This is experimentally found to be the case (see ref. [7] for a discussion of these results). The magnitude of the variations in the isotopic ratios with angle at high fluence will be approximately the same as the overall fractionation at low fluence and this is found to be well described by $(M/M_j)^{2m}$, where m is predicted to be 0.055 assuming a Born-Meyer interaction between the atoms in the target, M is the mean mass

of the target atoms and M_j is the mass of the sputtered species. Table 1.3.1 shows the relevant values for carbon and gives an upper limit to the fractionation that one might expect in the atoms sputtered in any one direction (remembering that at high flux there will be no overall fractionation).

It is wrong to try to apply this theory to the sputtering of adsorbed species as it is based on the assumption that the sputtering is taking place from a random medium. It seems likely [8] that if the sputtered species come entirely from the surface layer there should be no angular dependence of the isotopic fractionation.

Simple ballistic considerations indicate that the energy distributions should be almost identical [9]: consider an atom A incident on another atom B with a zero impact parameter; the energy of B after the collision will be:

$$E_B = E_A \, (4 \, m_A \, m_B)/(m_A + m_B)^2 \qquad (1.3.1)$$

which gives, for example $E_B = 0.994 \, E_A$ for a ^{14}C atom struck by a ^{12}C atom. If collisions at different angles are to be considered then the functional form of the interaction must be known. However, it is clear from equation (1.3.1) that the energy distributions of different isotopes will differ by only a fraction of a percent as long as the predominant target material is one of the isotopes. Table 1.3.2 shows the how the above equation affects sputtered carbon atoms from a predominantly ^{12}C target and one made from ^{48}Ti.

target mass m_A	carbon isotope m_B	E_B/E_A	$E_B/E_{(12C)}$
12	12	1.000	1.000
12	13	0.998	0.998
12	14	0.994	0.994
48	12	0.640	1.000
48	13	0.671	1.048
48	14	0.699	1.093

Table 1.3.2
Relative energies of the carbon isotopes sputtered from graphite and titanium targets

1.4. Sputtering of Adsorbed Species

There has been a great deal of experimental work on the sputtering of molecules adsorbed onto single crystals [10]. The angular dependence of the emission is found to depend strongly on the adsorption site and to be strongly correlated with the directions in the crystal structure. However if the surface is multicrystalline these effects would be expected to disappear. As mentioned in section 1.3, atoms sputtered from the top layer of a surface are not expected to exhibit an isotopically dependent angular distribution. Adsorbed species are really on the surface rather than being in the top layer, but the distinction is probably unimportant for a surface which is severely damaged by sputtering.

If a surface is covered by adsorbates and subsequently sputtered, the concentration of those adsorbates does not fall as a simple exponential [11]. This indicates that sputtering is not the only mechanism by which they are removed; some of the adsorbates suffer recoil implantation, coming to the surface again as the target is sputtered away. The importance of recoil implantation is different for different substrate/adsorbate systems and can be gauged by the functional form of the loss of adsorbate material from the surface.

1.5. Measurements for Carbon

There are, unfortunately, no good data on the angular distributions to be expected for sputtering from carbon by caesium ions which is the arrangement found in most ion sources used for radiocarbon AMS. It is desirable to have measurements for the specific energies and projectile species because of the dependence of m in equation (1.1.2) on these parameters.

Information on the energy distributions of sputtered carbon atoms is available [12,13]. This indicates that, up to about 1000 K, the energy distribution is well described by the equation (1.1.1) with n = 2. At very high temperatures (about 2000 K) a Maxwell-Boltzmann distribution is found with a characteristic temperature about 30% above ambient. However, the production of clusters is not in line with the thermal spike theory and suggests instead a thermal desorption due to the disturbance of the surface structure.

2. The Formation of Negative Ions

There is really only one comprehensive theory for the production of ions in the sputtering process; this is based on an electron tunnelling mechanism. The fact that this is the only good theory does not, of course, mean that it is necessarily complete and some of the evidence for and against it will be discussed here.

2.1. The Electron Tunnelling Mechanism

It is normally the case that the ground state of a sputtered atom is neutral (since ionisation energies are usually larger than work functions which are in turn larger than typical electron affinities). The production of ions by sputtering must therefore rely on its non-adiabatic removal from

the surface, unless the temperature or effective temperature is sufficiently high for the charged states to be populated.

The process can be best understood with reference to figure 1. (This is based on calculations made in ref. [14] for a typical transition metal.) Here the electron affinity minus the Fermi level energy is plotted as a function of the distance of the sputtered atom from the surface; this curve essentially shows the energy that is required to form a negative ion. Because the charged state can decay extremely rapidly while the atom is still in its substrate (this is particularly true if the substrate is a metal), its energy band is very wide. There is, therefore, an appreciable probability that the atom is in this state.

As the atom leaves the surface, the width of the charged state's energy level falls off since it becomes increasingly difficult for the electron to tunnel from the atom to the surface, or vice versa. The result of this is twofold: the equilibrium occupation of the level falls, and the probability of the ion surviving in its present charge state (this is P(z) in figure 1) rises. The position at which further tunnelling becomes unlikely is given by the sharply peaked function $\Delta P(z)$ (see figure 1) which is a function of velocity: the peak of $\Delta P(z)$ moves closer to the surface as the velocity increases. Thus, if the species is removed very slowly (adiabatic limit), it will be in the neutral state and if it is removed very fast (sudden limit) the populations of the charged states will just be those which existed in the substrate itself. If the velocity is in the intermediate region then the theory gives the probability of forming an ion [14]:

$$P^- = (2/\pi)\exp((-c_1\pi(\varphi - \varepsilon_A)-c_2\pi)/\hbar\gamma v\cos\theta) \tag{2.1.1}$$

$$P^+ = (2/\pi)\exp((-c_1\pi(\varepsilon_I - \varphi)-c_2\pi)/\hbar\gamma v\cos\theta) \tag{2.1.2}$$

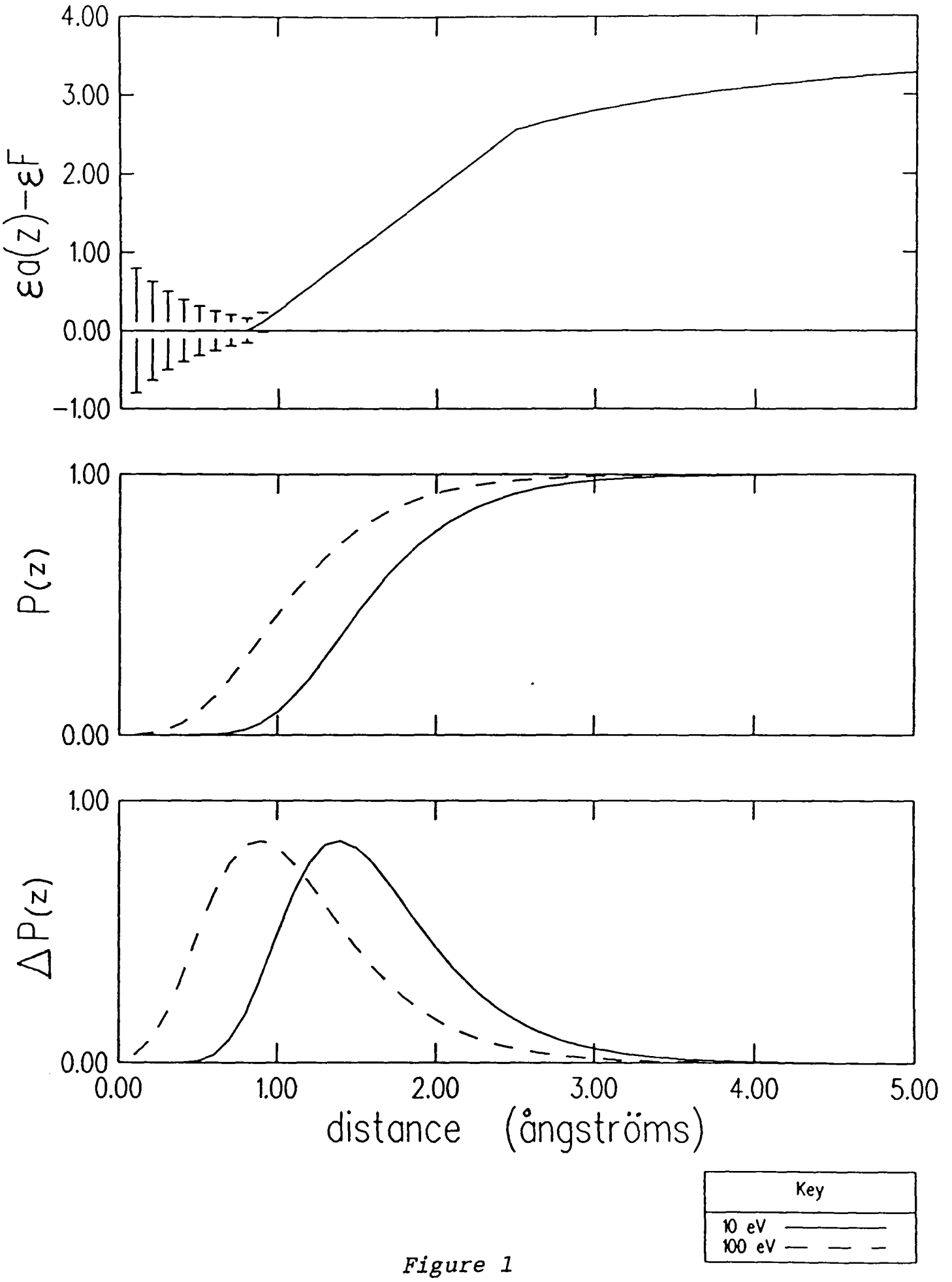

Figure 1

The difference between the electron affinity and the Fermi level, $(\varepsilon_a(z)-\varepsilon_F)$, in eV with error bars showing the single electron width; the probability of ion survival, P(z), and its differential, ΔP(z), in $Å^{-1}$ for a typical transition metal sputtered from an elemental target at 10 eV and 100 eV (based on calculations in ref. [14])

where ϵ_A, ϵ_I and φ are the electron affinity, ionisation energy and the work function of the surface respectively; v is the velocity of the neutral atom and θ the angle from the normal of the surface; c_1 and c_2 are constants and γ is the reciprocal of the characteristic distance in the fall off of the charged state energy bandwidth.

The equations (2.1.1) and (2.1.2) are arrived at by application of first-order time dependent perturbation theory and will only be valid in the limit $\hbar\gamma v << (c_1\pi(\varphi - A) + c_2\pi)$ in the case of (2.1.1) and a comparable limit for (2.1.2). The straightforward implication of this is that it is not reasonable to assume the validity of this expression in situations where the ion production probability is high.

The problems with applying equations (2.1.1) and (2.1.2) come in trying to evaluate the constants c_1, c_2 and γ. c_1 is determined by the position at which the tunnelling probability effectively disappears (this is related to the function $\Delta P(z)$; see figure 1) and c_2 is given by:

$$c_2 = c_1 V_i + (1 + c_1)(\epsilon_a{}^0 - \epsilon_F) \qquad (2.1.3)$$

where V_i is the image potential at the position which determines c_1 and $(\epsilon_a{}^0 - \epsilon_F)$ is the difference between the electron affinity level at the surface and the Fermi level. The latter will almost certainly be affected by the caesium coverage and by the presence of other adsorbates and only in the case of metal ions sputtered by Ar^+ has the assumption that it can be put equal to zero been tested [15].

In the derivation of the above equations, assumptions are made about the variation in the electron affinity level of the sputtered atom with distance from the surface, $\epsilon_a(z)$. The function is taken to be linear close to the surface. It has been shown that, for example, in the case of chemisorbed species, that a more realistic form of $\epsilon_a(z)$ based on an

exponential function gives results in better agreement with experimental data [16].

Another important consideration when studying slow ions (with energies close to the binding energy) is the fact that the ions are not travelling at a constant velocity as they leave the surface. The effect of this is that the ion production probability reaches a minimum at energies close to the heat of ionic desorption [16]. There is also evidence that there is additional dependence on the angle at which the sputtered species leave when this is taken into account.

2.2. The Bond Breaking Model

An extension to the electron tunnelling model has been suggested [17] to cover the sputtering of ions from covalent structures where it is necessary to break bonds. Whereas when sputtering from metals the electron can tunnel to or from the conduction band, when ions from covalent structures are concerned the tunnelling must take place between specific energy levels. This process has a strong angular dependence, and there is a similar relationship to velocity as that found in the normal tunnelling model:

$$P^+ = G \exp(-v_0/v) \tag{2.2.1}$$

There is an analogous expression for negative ion production. Here v is the velocity of the neutral atom from the original site of the atom and both G and v_0 will depend on the direction of v relative to the bonding structure. It should be noted that, in this case, as for the tunnelling model the velocity in the equation is that for the neutral atom and therefore in the event of ion formation taking place it will not correspond to the final velocity of the negative ion.

2.3. The Effects of Caesium Coverage

One of the consequences of equation (2.1.1) is that it should be possible to increase the negative ion yield by reducing the work function. This can be done, for example, by the adsorption of small quantities of Caesium on the surface, and the correlation between the production of negative ions and the reduction in the work surface has been demonstrated [18]. The minimum in the work function occurs when the caesium coverage is a fraction of an atomic layer. This has been demonstrated for silicon for which 1/4 to 1/2 of a monolayer produces the smallest work function [19] which is slightly below that of pure caesium. At higher coverages the variation in the negative ion yield arises not only from a change in the work function, but also from changes in c_2 (equation (2.1.3)).

2.4. Total Ion Yields and Isotopic Fractionation

Let us assume that the energy distribution for the sputtering of neutral atoms can be described by the equations (1.1.1) and (1.1.2). The yields for negative ions, assuming the tunnelling model, may then be written as:

(2.4.1)
$$Y^- = C \frac{2\ E/\pi}{(E + E_b)^{n+1}} \exp\left(\frac{-(c_1\pi(\varphi - \varepsilon_A) + c_2\pi)m^{1/2}}{\hbar\gamma(2E)^{1/2}\cos\theta}\right) \cos^s\theta$$

It is possible to deduce some interesting results from this equation without making any assumptions about the values of those constants which are uncertain. Let us write the equation in a different form to remove some of the complexity and to make it compatible with the bond breaking model and applicable to both positive and negative ions; writing the energy as a multiple of E_b with $A = E/E_b$, we get:

$$(2.4.2) \qquad Y = C'(A/(A+1)^3)\ (2/\pi)\ \exp(-c(m/A)^{1/2} f_1(\theta))\ f_2(\theta)$$

where n has been assumed to be equal to 3, which is valid for a broad range of sputtering processes, and where $f_1(\theta)$ and $f_2(\theta)$ are functions of angle relevant to the tunnelling or bond breaking models. The constant c depends on the relevant surface conditions. The maximum of this function occurs at A_{max} where:

$$(2.4.3) \qquad c = \frac{4A_{max} - 2}{A_{max} + 1} \left(\frac{A_{max}}{m}\right)^{1/2} \frac{1}{f_1(\theta)}$$

From this we can deduce the probability of ion formation, P, in terms of the parameter A_{max}. This gives:

$$(2.4.4) \qquad P = \left(\frac{2}{\pi}\right) \exp\left(-\frac{4A_{max} - 2}{A_{max} + 1} \left(\frac{A_{max}}{A}\right)^{1/2}\right)$$

and one can also calculate the mass fractionation $F = (\partial P/\partial m)/P$ from equation (2.4.2) and write the solution in terms of A_{max}:

$$(2.4.5) \qquad F = -\frac{2A_{max} - 1}{A_{max} + 1} \left(\frac{A_{max}}{A}\right)^{1/2} \frac{1}{m}$$

These equations are consistent with both the linearly interpolated form of $\varepsilon_a(z)$ and the exponential form. It is possible to approximate the effect of the ions' variable velocity near the surface by taking P(A) = P(1) for A < 1. In fact the probability seems to actually rise slightly at energies of A < 1, although this is not understood from a theoretical standpoint [16].

probability of ion formation

The total P_{tot} can then be found using numerical integration to find the average of P weighted with the neutral sputter yield $(A/(A + 1)^3)$. Figure 2 shows how P_{tot} varies with A_{max}.

The overall isotopic fractionation F_{tot} can also be calculated by weighting F with the ion yield. Figure 3 shows the relationship between F_{tot} and P_{tot} and figure 4 the variation of F_{tot} with A_{max}.

The importance of these relationships is that they are between measurable quantities. It should therefore be possible to test the validity of the models by measurements of the peak energy in the spectrum of the ions, the ion to neutral ratio and the fractionation.

The final effect that will be considered here is the effect of having a target with a different mass from the atom which is to be sputtered. From equation (1.3.1) it can be seen that the energy distributions of the sputtered particles are dependent on the ratios of the masses. To obtain the total fractionation it is essential to take this into account:

$$\frac{dP}{dm} = \left(\frac{\partial P}{\partial m}\right)_E + \left(\frac{\partial P}{\partial E}\right)_m \frac{dE}{dm} \tag{2.4.6}$$

Assuming that the energy distributions are only slightly perturbed the fractionation is then given by:

(2.4.7)

$$F = -\frac{2A_{max} - 1}{A_{max} + 1}\left(\frac{A_{max}}{A}\right)^{1/2}\frac{1}{m} + \frac{2A_{max} - 1}{A_{max} + 1}\left(\frac{A_{max}}{A^3}\right)^{1/2} 4Am_T \frac{m_T - m}{(m_T + m)^3}$$

$$= \frac{2A_{max} - 1}{A_{max} + 1}\left(\frac{A_{max}}{A}\right)^{1/2}\left(-\frac{1}{m} + \frac{4m_T(m_T - m)}{(m_T + m)^3}\right)$$

where m_T is the mass of the predominant species in the target. The effect of this if the target mass is greater than the mass of the sputtered atoms,

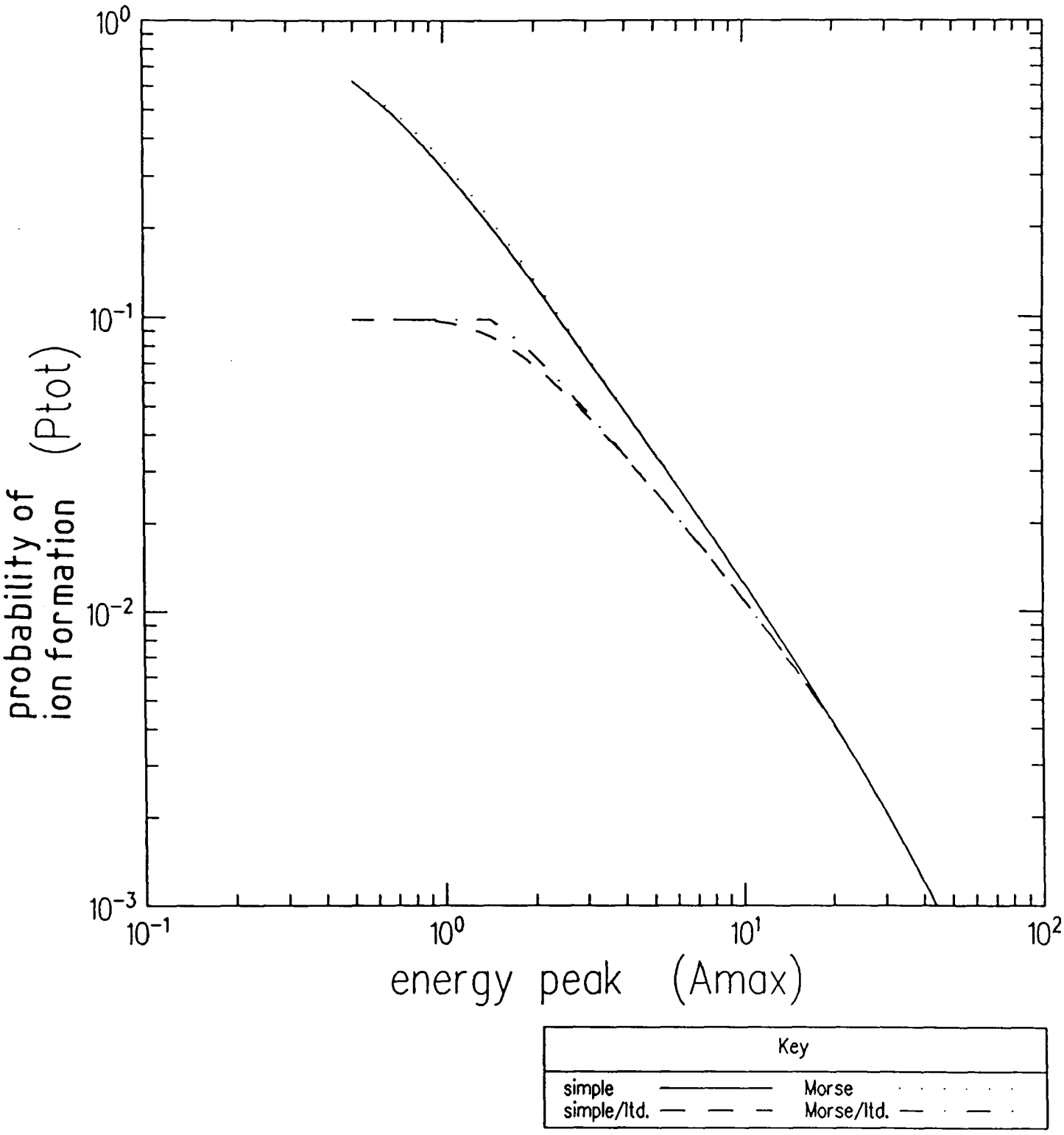

Figure 2

The variation of the overall probability of ion formation, P_{tot}, with the position of the energy peak A_{max} (A_{max} is a multiple of the binding energy, E_b); the curves are calculated either assuming a 'simple' model in which the atoms leave at constant velocity or assuming a 'Morse' potential. The curves marked 'ltd.' assume a limiting high velocity ionisation probability, P_∞, of 10 %

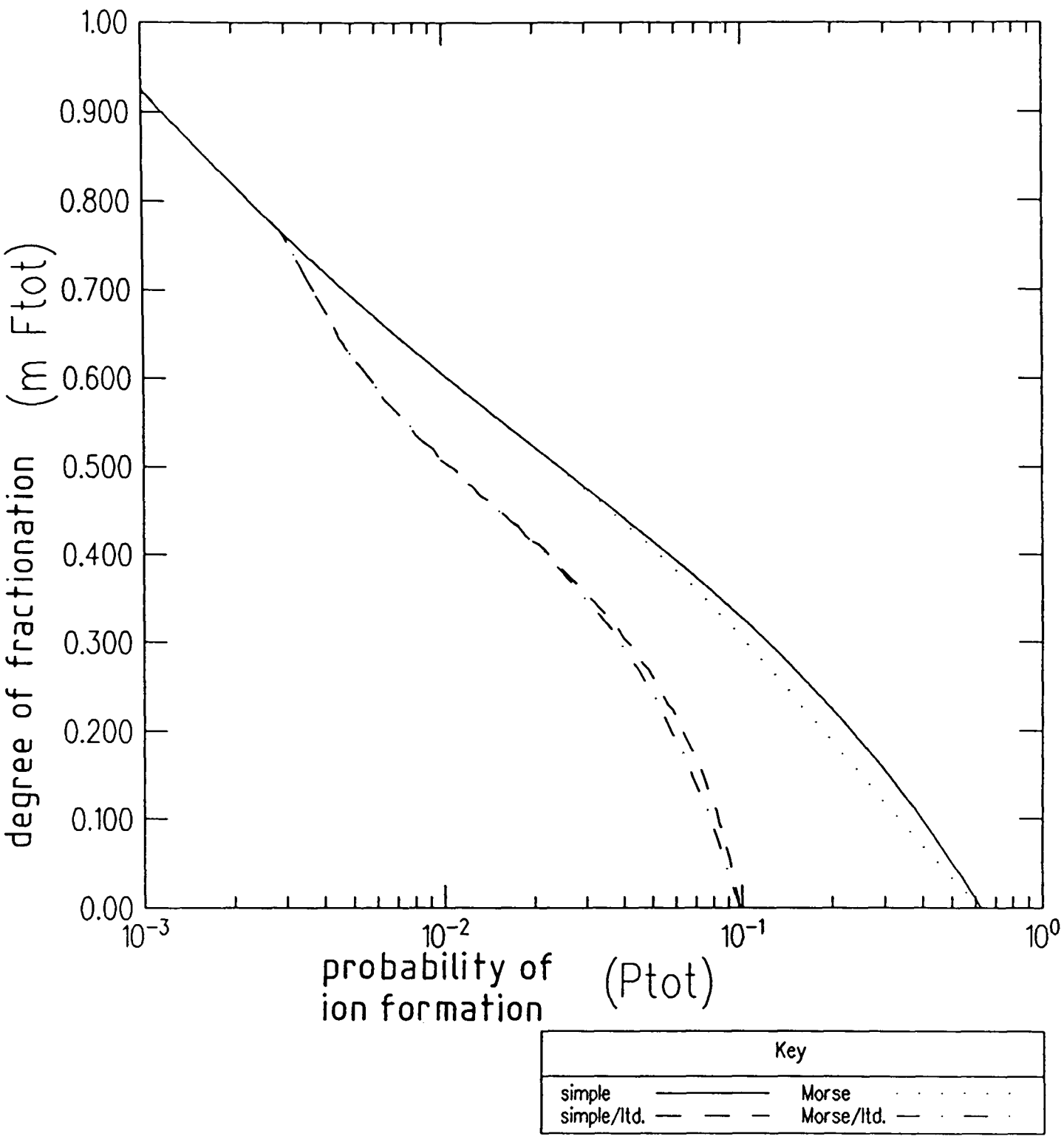

Figure 3

The variation of the overall fractionation, m F_{tot} with P_{tot} (m F_{tot} is the power of the fractionation with mass)

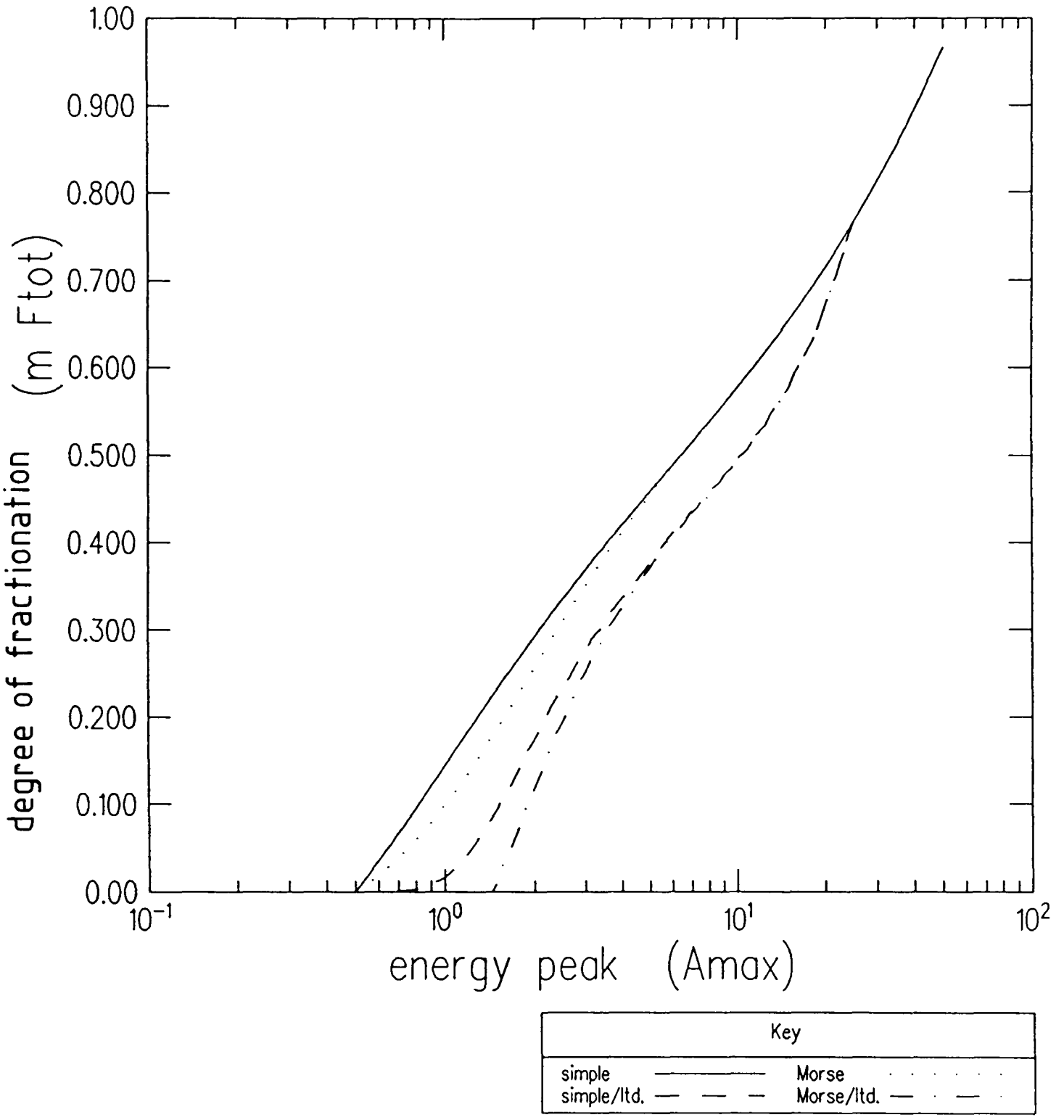

Figure 4

The variation of overall fractionation, m F_{tot}, with the position of the energy peak, A_{max}

is to reduce the fractionation slightly for a given ion production probability. For example, for carbon ions sputtered from titanium, the fractionation will be about 38% lower than it would be from carbon, given the same ion production probability.

2.5. The Validity of the Model

Before discussing the experimental evidence relating to the validity of the electron tunnelling model it is worth considering some of the restrictions which are imposed by the derivation itself. It should be remembered that in the sudden limit the probability of ion formation is simply equal to the initial occupation of the charged state; this probability will be referred to as P_∞. On decreasing the velocity the probability must monotonically decrease and so it is effectively limited by P_∞. In figures 2, 3 and 4 the curves are shown for $P_\infty = 0.1$ as an example. As was stated in section 2.1, the first order time dependent perturbation theory is not sufficient if the ion yield is high. To look at this in another way, the ion formation probability given in equation (2.1.1) and (2.1.2) rises to $(2/\pi)$ at high enough energies and in reality the probability will only rise to P_∞ so that there will be no velocity dependence at high energies. It should be noted that this limitation will always result in the fractionation being smaller than that found from the theory given above.

The searches for experimental evidence for the tunnelling model have centred on investigations of the velocity dependence of ion production [8,15]. The fact that some sputter systems do not exhibit such a dependency has given rise to speculation about other mechanisms such as direct ion production in the collision cascade [20], and it is worth considering the most developed of these theories which assumes a local electron plasma temperature T_S and takes tunnelling into account [21]. The

principles on which this theory are based are essentially fairly simple. As in the simple tunnelling model charged states are considered to have some population as sputtered atoms leave the surface, and these populations are determined by the temperature T_s; the final ionisation probability can be correlated with the difference in energy of the charged and neutral states at some critical distance which is itself velocity dependent but which is normally of the same order as the atomic separation. If the energy associated with the formation of the ion at a distance z from the surface is $E_i(z)$, then the probability of ion formation at very high velocities is $\exp(-E_i(0)/kT_s)$ and at very low velocities is $\exp(-E_i(\infty)/kT_s)$. (In the case of negative ions, for example, this is $\exp((\epsilon_A-\varphi)/kT_s)$.) The effective temperature of the electrons is selected to be of the order of 1000 - 3000 K as this gives results which are approximately in accord with experiment. There is, however, a fundamental difficulty with this as a theory. If one considers the velocities of the electrons found in the Fermi electron gas of the target (typically of the order of 10^6 ms^{-1}), it is clear that the thermal spike associated with the collision will dissipate with a time constant of about 10^{-16} s which is much shorter than the time for a sputtered atom to leave the surface. (For example a 10 eV ^{12}C atom will only travel 1.3×10^{-12} m in this time.) There is therefore little justification for considering this theory to be realistic for anything except the determination of P_∞, the ionisation probability of a fast sputtered species. In this particular case it is clear that the rapidly changing potentials that exist during the collision will have some bearing on the population of the ionised states.

There has been some good evidence for the validity of the tunnelling model in the case of adsorbed oxygen, for which the velocity dependence of the ionisation probability has been investigated in some detail [8]. There are also clear indications that the dependence on work function can be very

sharp [22]; these results agree very well with the tunnelling model but could not be explained satisfactorily if the electron temperature were assumed to be very high.

The first exponents of the tunnelling model suggested that the enrichment factor for light/heavy ions would depend on (m_H/m_L) [23]. This has since been demonstrated for a variety of elements [24]. However it is clear that the variation will, in general, be of the form $(m_L/m_H)^{mF_{tot}}$, and it can be seen from figure 3 that mF_{tot} can take a whole range of values. The elements investigated by Shimizu and Hart [24] all had very low ion yields (for example Cr has an ion fraction of about 4×10^{-3} [15]), and this is the reason for the approximate (m_H/m_L) form of the variation.

One clear prediction of the model is that the fractionation should fall off as $E^{-1/2}$ and it should be possible to study this experimentally. The limitations discussed above suggest that it might fall off faster than this at high energies. This has been investigated [24] but the results do not tally well with the theory. However, these experiments are difficult to perform and were, on the admission of the authors, not very systematic so that perhaps one should not deduce too much from them.

2.6. Theoretical Considerations for Carbon

It is important at this stage to relate the ion formation theories described above to the case of carbon, and in particular to that of carbon sputtered from a caesiated surface (the arrangement found in ion sources used for AMS radiocarbon determination). The electron tunnelling mechanism is essentially controlled by the form of the function $\epsilon_a(z)-\epsilon_F$ which is the energy difference between an electron on the sputter target surface and one on the sputtered atom as a function of the distance of the atom from the surface. It is also somewhat affected by $\Delta(z)$ which is the single electron width. It can be shown that $\Delta(z)$ does not actually vary monotonically with

z but reaches a maximum for some small value of z (about 0.3×10^{-10} m) [16]. There is, at present, no way in which this can be calculated for the case in which we are interested and so here the method of ref. [14] will be followed but with $\Delta(0)$ taken to be 2 eV (rather than 1) which will probably give an overestimate of the effect of tunnelling. Δ is then given by:

$$\Delta(z) = \Delta(0)\, e^{-\gamma z} \tag{2.6.1}$$

From this one can calculate the probability P(z) that an atom at position z has reached its final state of ionisation and a function $\Delta P(z)$. (This is just $\partial P(z)/\partial z$) which is the probability distribution for the position of the last interaction with the surface.) If constant velocity is assumed, P(z) is given by [14]:

$$P(z) = \exp\left(-\frac{2\,\Delta(z)}{\hbar\gamma v}\right) \tag{2.6.2}$$

Typical values of γ are 2.3×10^{10} m^{-1} [14] and this parameter will be fairly insensitive to the surface conditions.

It is difficult to estimate the precise form of $\varepsilon_a(z)-\varepsilon_F$, particularly for carbon dioxide adsorbed onto titanium. However the behaviour of this function far from the surface is simply given by the classical image charge energy:

$$\varepsilon_a(z)-e_F = -\frac{e^2}{(4\pi\varepsilon_0)\ 4\ z} + \varphi - \mathcal{E}_A \tag{2.6.3}$$

For an optimally caesiated surface φ will be approximately equal to or slightly less than 2.14 eV which is the work function of caesium itself and, as $\mathcal{E}_A$ is 1.12 eV for carbon, it transpires that $\varepsilon_a(z)-\varepsilon_F$ drops below

zero at values of z less than about 3.5×10^{-10} m. For pure graphite we know that $\epsilon_a(0)-\epsilon_F$ would be zero and so for an optimally caesiated surface one might assume that it would be lower than this by the amount that the work function had been lowered (estimated to be about 2.86 eV as the work function of graphite is 5 eV), but this will be dependent on the degree of caesiation of the surface and on the presence of other impurities. As a first approximation, a linear interpolation can be used for $\epsilon_a(z)-\epsilon_F$ for low values of z.

Figure 5 shows the values for $\epsilon_a(z)-\epsilon_F$, P(z) and $\Delta P(z)$ calculated here for carbon ions leaving the surface with energies of 10 eV and 100 eV. It should be noted, following the discussion above, that the curve for $\epsilon_a(z)-\epsilon_F$ is fairly certain for $z > 2 \times 10^{-10}$ m but rather conjectural for lower values of z. It should also be noted that z (as used in other references [14,16]) is the distance from the image plane which is 1.5 to 2.0×10^{-10} m outside the first atomic layer. The situation here is clearly very different from that discussed in refs. [14,16] where the value of $\epsilon_a(z)-\epsilon_F$ is greater than zero at least for most of the region in which electron tunnelling takes place. One would expect from this that all of the ions would reach their final ionisation state while negative ion formation was energetically favourable. This would lead to high yields and negligible velocity dependence. If the work function were raised by 1 eV there would be an appreciable proportion of ions having their last interaction with the surface at a point where negative ion formation was energetically unfavourable (about 10%). Velocity dependence and work function dependence of the ion formation would then begin and this would be most marked at low energies. At high energies the ion formation probability will be largely determined by the shape of $\Delta(z)$ and it is not clear that P^- will be greater for atoms that are removed faster, although the dependence on φ will clearly be very strong.

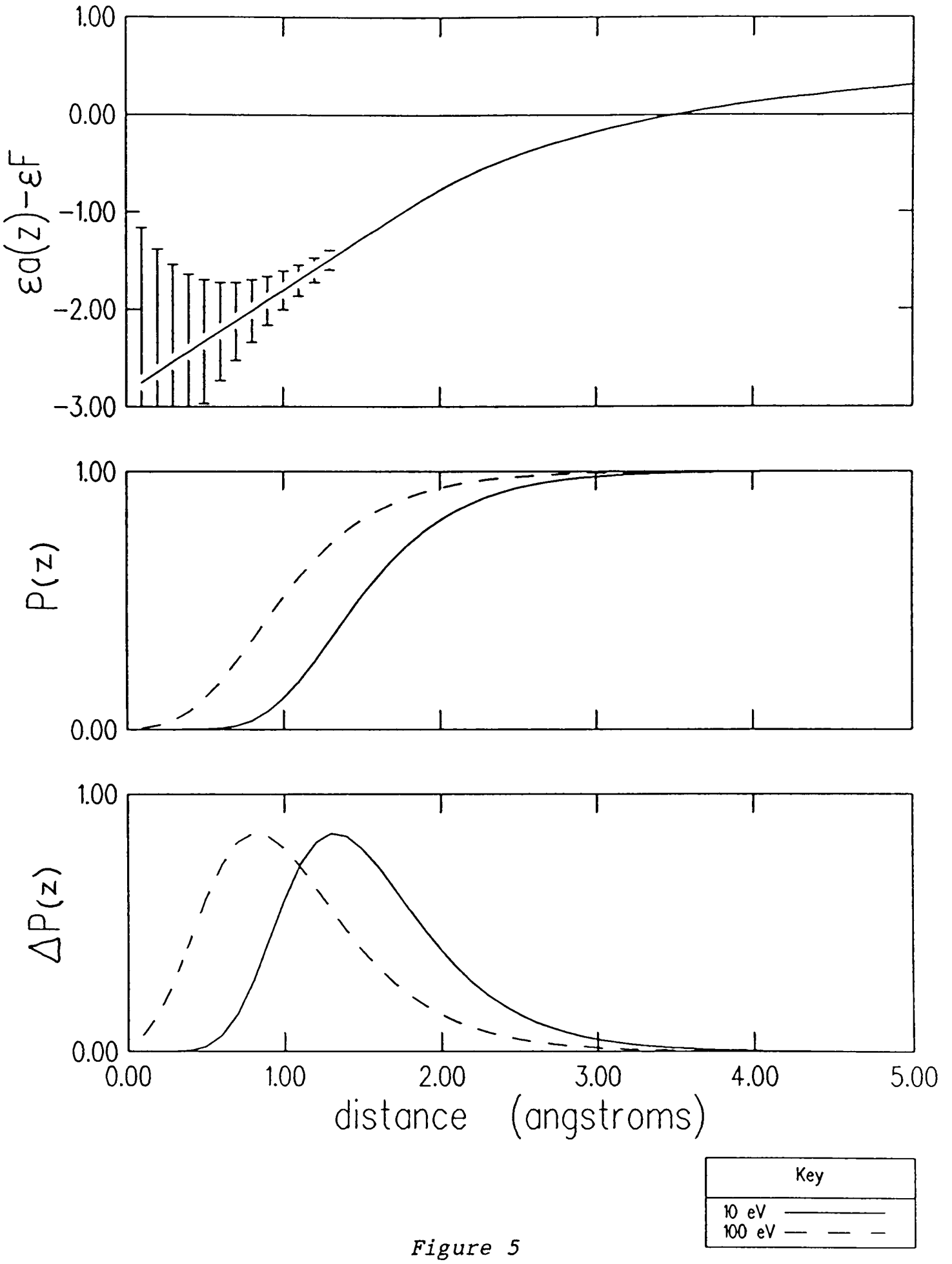

Figure 5

The difference between the electron affinity and the Fermi level, $(\epsilon_a(z)-\epsilon_F)$, in eV with error bars showing the single electron width; the probability of ion survival, P(z), and its differential, ΔP(z), in $\mathring{A}^{-1}$ for carbon sputtered from a caesiated surface at 10 eV and 100 eV as calculated in this chapter

We expect therefore that, unlike the systems considered in the literature, the caesiated carbon system will not rely on the very nonadiabatic removal of an atom from the surface for a negative ion to be formed. This is because $\epsilon_a(z)-\epsilon_F$ is negative in the region in which electron tunnelling is most prevalent. The corollary of this is that we expect the velocity dependence of P^- to be weaker than suggested by the discussion in section 2.4., and that the variation in P^- with the work function would be small until the work function was about 1 eV below optimum.

A further complication is that the value P^- discussed above is the probability that a single carbon atom sputtered from the surface forms a negative ion. The measured values usually relate to the probability of any sputtered carbon atom becoming a negative ion. In the case of the sputtering of adsorbed carbon dioxide, these values are likely to be similar (although the neutral CO flux is unknown and may be fairly high and carbon implanted in the titanium may form TiC and TiC^-; the probability for the latter is small [25]), but for sputtering from graphite about 67% of the elemental carbon found in negative ions is in the form of clusters (see table I/8:1.3.1). In addition to this, some of these clusters break up as they leave the surface. Because clusters are at the most only singly charged this will probably tend to further reduce the measured value of P^-. It should be noted that the break up of clusters may itself be a mechanism susceptible to isotopic fractionation.

The case of adsorbed carbon dioxide on titanium is simpler in that clusters are much less important, but the value of $\epsilon_a(z)-\epsilon_F$ is very difficult to estimate close to the surface. It is also necessary to consider the population of carbon dioxide molecules on the surface since it is clear that the presence of these will tend to raise the work function. The considerations discussed above suggest that there will be high yields

of C^- ions for low gas flows, and that the ion production probability will be fairly insensitive to changes in the work function until it has risen by about 1 eV. Thereafter, the yield will drop in a fashion that is strongly dependent on the form of $\epsilon_a(z)-\epsilon_F$ and $\Delta(z)$ close to the surface. The effect of the carbon-oxygen bond which initially exists is difficult to assess but one would expect it to have some effect on the angular dependence of the ion formation probability.

2.7. Experimental Evidence Relevant to Carbon Ion Formation

The first piece of experimental evidence that casts some light on the ion formation process is the probability for ion formation which, in the case of carbon, is very high but difficult to determine exactly for the reasons discussed above. The measurements presented in chapter II/4 of this thesis indicate that P^- is probably close to 1 for carbon atoms sputtered from the adsorbed gas phase but probably substantially lower for atoms implanted in the titanium target. For graphite the C/Cs^+ ratio is believed to be about 2 [20] while the C^-/Cs^+ ratio is roughly 0.3 [9]. This puts a lower limit on P^- of circa 0.45. There is also some evidence for the formation of C^- by the break up of clusters [26] which indicates that the true P^- will be somewhat higher than this.

It is also informative to see how the ion yield varies with the work function. The evidence for adsorbed carbon dioxide is that the variation is small until the work function has changed by a substantial amount and thereafter the dependence becomes very strong (see chapter II/4 for a more detailed discussion of these results). For graphite the variation seems to be more uniform [27].

Direct measurements have also been made on the energy spectrum of the sputtered C^-, C_2^- and C_4^- ions [27,28]. From these measurements a number of things can be deduced. The measurements made on the ions emerging from

an ion source [28] show an energy distribution for the C^- ions with a high energy tail that falls off as $E^{-2.29}$ which, given that an ion source acts as a low energy pass filter, fits the E^{-2} expected for the neutral atoms very well, suggesting that the velocity dependence of the ion formation is not very great at high energies. In addition to this, the peak in the energy distribution is found to be very approximately half of the binding energy of carbon, again in line with the expected neutral distribution. (These measurements are actually prone to offset errors because of the uncertainty in the work function of the source target and of the detector so there might be some doubt about this.) Perhaps most interesting are the measurements of the variation in the energy distribution with target temperature [27]. These show that there is an optimum target temperature of about 480 K which presumably corresponds to the optimum caesium coverage discussed above (see section 2.3). Variations in the work function of about 1.5 eV are deduced and these are found to alter the ion yield by a factor of somewhere between 4 and 7. The shift in the peak in the energy distribution is calculated to be 2.5 eV (in the notation of ref. [27] the shift in the energy peak ΔE_p is equal to $\Delta E_m - \Delta\varphi$; this is the shift in the maximum of the energy distribution minus the shift in the work function). These calculations are based on the tunnelling theory outlined in ref. [14].

The measurements that are most obviously consistent with the theory outlined in section 2.6 are those for sputtering from adsorbed carbon dioxide which show high yields and insensitivity to the work function for small changes from the optimum. The reason for the ion yield being lower for the carbon implanted in the titanium is not obvious, and may just be a result of cluster formation lowering the measured value for P^- or it may be a consequence of sputtering from beneath the surface (see below).

The ion yield from carbon is also very high but the results discussed above (from ref. [27]) indicate that it is sensitive to even small changes in the work function. This may be due to the inhomogeneity of the work function. Another possibility is that ions formed from within the material of a target do not behave in the same way as those sputtered from the surface; this would explain both the lower ion yields from graphite and the anomalously low ion yield from the implanted carbon discussed above. Clearly in such cases the surface is very severely disrupted, and a theory based on a plane surface which is in equilibrium might be expected to break down.

Further evidence for carbon not obeying the simple tunnelling theory of ref. [14] is the variation in yield with the shift in the peak of the energy distribution (see above and ref. [27]). As shown in section 2.4., the simple tunnelling theory predicts a direct correlation between yield and A_{max} but the change in the yield observed (by about 4 to 7) is larger than that expected from the change in A_{max} (or E_p in the terms of ref. [27]); this can be seen by reference to figure 2. This is exactly what one would predict from the discussion of the previous section (section 2.6) where reasons for expecting a less pronounced velocity dependence were put forward.

3. The Implications for Ion Optics

The primary ion beam is defined by the electrostatic fields within the ion source. The way in which this then relates to the secondary ion beam is determined by the sputtering process. Clearly if the brightness profile of the secondary beam is to be kept constant the form of the primary beam must be kept as constant as possible. This can be done by keeping the geometry simple and by reducing the number of variable parameters (see

chapter II/2). However, even if the primary beam is kept constant, the cratering of the target and variations in the work function of the target will produce variable ion beams. This is clearly very important since different targets are liable to have different properties (especially if they are made of catalytically deposited or pyrolytic graphite) and such differences should obviously be kept to a minimum. The mechanisms for such effects have been described above and they will now be discussed in relation to ion optics.

3.1. The Effects of the Collision Cascade

The collision cascade defines the distribution $d^2N/dEd\Omega$ for the sputtered atoms. The angular distribution is approximately of cosine form but small variations are expected for different isotopes. The energy distribution is also expected to vary slightly for different isotopes, especially if the target material is not the same as that of the sputtered species. The effect of these characteristics of the collision cascade process will be to introduce small differences between the brightness profiles in phase space for different isotopes. Slight variations in these differences will occur if target cratering takes place, and this could result in variable fractionation if only a proportion of the ion beam were used. It should, however be stressed that these effects are small (probably producing fractionation of only a fraction of a percent) and the variations will be very much smaller. It is unlikely that such effects will impair the accuracy of AMS measurements.

The use of electrostatic energy analysis will clearly introduce some fractionation because of the different energy profiles for different isotopes but these profiles will be very constant (even if cratering takes place) and so the resulting fractionation should be stable.

3.2. The Effects of Ion Formation

For the ion formation process to have any effect on the brightness profile of the secondary ion beam it must be velocity dependent. The theory put forward in section 2.6. and supported by the measurements of chapter II/4 indicate that this is probably not the case for C^- ions sputtered from carbon dioxide adsorbed onto titanium, but there is clearly a small velocity effect for graphite [27] although this is smaller than one would expect from the simple tunnelling theory of ref. [14]. In many applications of secondary mass spectrometry, however, the ion yields are low and there is a strong velocity dependence for the ion formation.

The velocity dependence is most marked at low energies and so energy analysis will tend to exacerbate the effect. Unlike the collision cascade mechanism the ion formation process can itself cause overall fractionation. This is particularly worrying as it is dependent on the work function of the surface and is therefore sensitive to variations in target and ion source conditions. The effects of this can be quite large (see, for example, ref. [6]).

In addition to the overall fractionation that can take place, the selection that takes place in ion formation will alter the distributions of ions in phase space and will do so differently for different isotopes. If the acceptance of the analysis system is limited, as it must be, this will lead to further fractionation which again can vary if the target geometry is altered by cratering.

3.3. Clusters

It has been demonstrated that the break up of clusters can have an effect on the emittance of a beam [26]. This is because ions that are formed in this way generally have a less well defined energy than those produced at the target surface. It is also possible that, in cases where a

significant proportion of the beam is formed in this way, there could be isotopic fractionation because of the different vibrational/rotational states of the clusters. In particular, these states will be very different for $^{12}C^{12}C^-$ which is a homonuclear diatomic molecular ion, and therefore subject to overall symmetry restrictions (the overall vibrational/rotational wave function for the nuclei must be symmetric).

Such effects are likely to be of minor importance for the sputtering of adsorbed carbon dioxide but will certainly be significant in determining the emittance of ion beams produced from graphite [27] although there is no experimental evidence bearing on fractionation from this process. The increase in emittance from this process will be very sensitive to the electric field strength at the surface and is therefore likely to change when target cratering takes place.

3.4. Summary of Fractionating Effects

It is useful at this stage to summarise all of ways in which sputtering can produce fractionation in the ion beam.

There are essentially three types of fractionation which can arise as a result of the sputtering process. These are: angular fractionation (in which the angular distributions for different isotopes are not the same), energy fractionation (in which the energy distributions are different) and global fractionation (for which the overall isotopic ratio in the ion beam different from that in the target). The two mechanisms responsible for the fractionation are the collision cascade and the formation of the ions (possibly also the break up of clusters).

Because isotopic measurements are almost always carried out in relation to standards, it is really only variations in the fractionation that are very important. Such variations can be caused by cratering, by changes in the work function of the target surface and by alterations in

the primary ion beam distribution.

Variations in global fractionation are obviously important. However, changes in the angular and energy fractionation can be just as detrimental to isotopic ratio measurements; this is because, if the phase space of the ion beam is limited, these types of fractionation become global.

Table 3.4.1 summarises the types of fractionation which are believed to be important.

type of fractionation	mechanism for fractionation	mechanism for variation
angular	collision cascade	cratering
		primary ion beam
	ion formation	cratering
		primary ion beam
		work function
energy	collision cascade	none
	ion formation	work function
global	ion formation	work function

Table 3.4.1
Summary of fractionating effects in the sputtering process

Summary

The physical processes involved both in the sputtering of neutral atoms and in the formation of ions have been discussed. The electron tunnelling model for ion formation has been looked at in detail and the expected correlations between various measurable parameters have been calculated.

On the basis of the calculations presented here and with reference to

the limitations of the tunnelling model, it is argued that the fractionation for species with high ion yields is expected to be low. Calculations based on the caesiated carbon system suggest that the velocity dependence of ion production should be small. The theory put forward here is in good agreement with measurements made on carbon dioxide adsorbed onto titanium (see chapter II/4).

Consideration of the ion optical implications of the sputtering process indicate that where there is fractionation from the sputtering itself there is likely to be yet more as a result of differences in the ions' distributions in phase space. The fractionation due to ion formation is also strongly dependent on target conditions, and is therefore susceptible to variations which will affect the accuracy of AMS measurements.

Although it may be possible to avoid appreciable global fractionation with a CO_2 ion source, the angular and energy fractionation from the collision cascade will remain. The effects of this can be minimised by ensuring high transmission of the ion beam through the rest of the AMS system. In the following chapters, therefore, a strong emphasis will be placed on the requirements for high transmission.

References

[1] M.W. Thompsom, Philos. Mag. 18 (1968) 377.

[2] H.H. Andersen, Nucl. Instr. and Meth. B18 (1987) 321.

[3] M.W. Thompson, Nucl. Instr. and Meth. B18 (1987) 411.

[4] H.H. Andersen, B. Stenum, T. Sørensen and H.J. Whitlow, Nucl. Instr. and Meth. B6 (1985) 459.

[5] J. Dembowski, H. Oechsner and Y. Yamamura, Nucl. Instr. and Meth. B18 (1987) 464.

[6] R. Shimizu, Nucl. Instr. and Meth. B18 (1987) 486.

[7] P. Sigmund, Nucl. Instr. and Meth. B18 (1987) 375.

[8] M.L. Yu, Phys. Rev. Lett. 47 (1981) 1325.

[9] N.R. White, D. Phil. Thesis, Oxford University (1981).

[10] D.J. Garrison and N. Winograd, Science 216 (1982) 805.

[11] K. Morita, H. Morii and Y. Horino, Nucl. Instr. and Meth. B18 (1987) 407.

[12] E. Vietzke, K. Flaskamp, M. Hennes and V. Philipps, Nucl. Instr. and Meth. B2 (1984) 617.

[13] V. Philipps, K. Flaskamp and E. Vietzke, J. Nucl. Mater. 111 & 112 (1982) 781.

[14] J.K. Nørskov and B.I. Lundqvist, Phys. Rev B19 (1979) 5661.

[15] M.J. Vasile, Phys. Rev. B29 (1984) 3785.

[16] N.D. Lang, Phys. Rev. B27 (1983) 2019.

[17] M.L. Yu, Nucl. Instr. and Meth. B18 (1987) 542.

[18] M.L. Yu, Phys. Rev. Lett. 40 (1978) 574.

[19] R.E. Weber and W.T. Peria, Surf. Sci. 14 (1969) 13.

[20] Ch. Lukner, Nucl. Instr. and Meth. 167 (1979) 249.

[21] Z. Sroubek, Phys. Rev. B25 (1982) 6046.

[22] M.L. Yu and N.D. Lang, Phys. Rev. Lett. 50 (1983) 127.

[23] J.M. Schroeer, T.N. Rhodin and R.C. Bradley, Surf. Sci. 34 (1973) 571.

[24] N. Shimizu and S.R. Hart, J. Appl. Phys 53(3) (1982) 1303.

[25] R. Middleton, Nucl. Instr. and Meth. B5 (1984) 193.

[26] J.L. Yntema and P.J. Billquist, Rev. Sci. Instr. 57(5) (1986) 748.

[27] G. Doucas, J. Phys. D17 (1984) 429.

[28] G. Doucas, Int. J. Mass Spectr. Ion Phys. 25 (1977) 71.

Chapter 3

Brightness Profiles

Whence and what art thou, execrable shape? [Milton: Paradise Lost]

Introduction

At this stage it is worth looking at a few examples of measurements made on the brightness profiles of ion beams to see what effects turn out to be most important in the transport of ion beams. In the next chapter the discussion of the theoretical aspects of these effects will be resumed.

1. Sample Profiles from a High Intensity Sputter Source

Figures 1, 2 and 3 all show measurements of the brightness profiles of ion beams from the High Intensity Sputter Source which is discussed in chapters II/2 and II/3. The ion source test bench used for the measurements and the methods employed are discussed at length in chapter II/1; suffice it to say here that the measurements are of the type described by equation (1:3.5.2). The energy of the ion beam was 25.84 keV. In this chapter we shall only be concerned with qualitative analysis of the measurements. The contours shown are such that each successive contour encloses 10% less of the ion beam; thus the outer contour encloses 90%, the next 80%, et cetera (see section 7:3.1.).

The brightness profile of a beam emerging from an ion source is normally assumed to be roughly ellipsoidal in shape with an approximately Gaussian functional form. The first thing to be noticed is that the distributions are not dissimilar to the gaussian one shown in figure 4, but

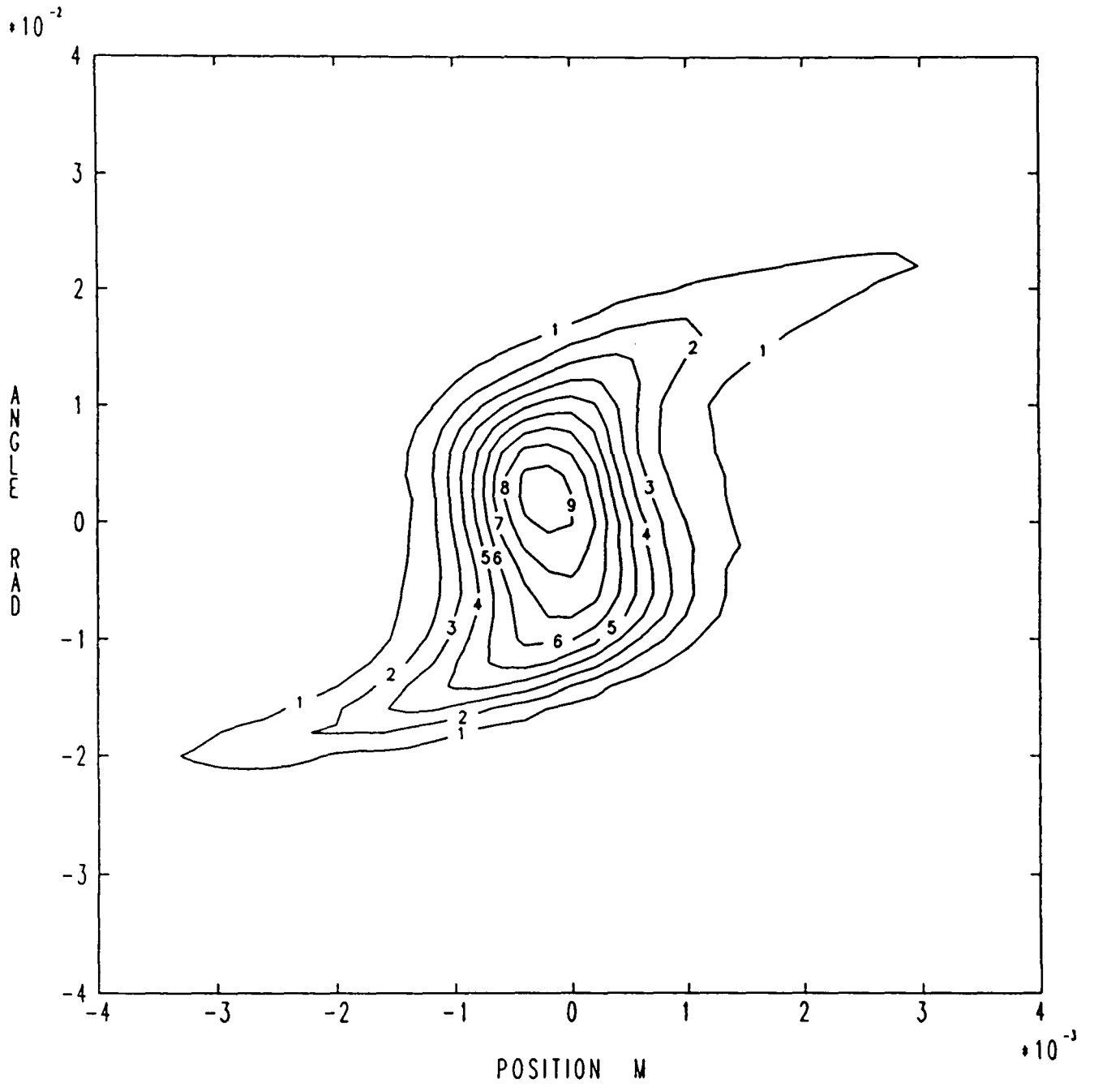

Figure 1

Brightness profile measured at 2 μA using the ion source test bench and a HISS

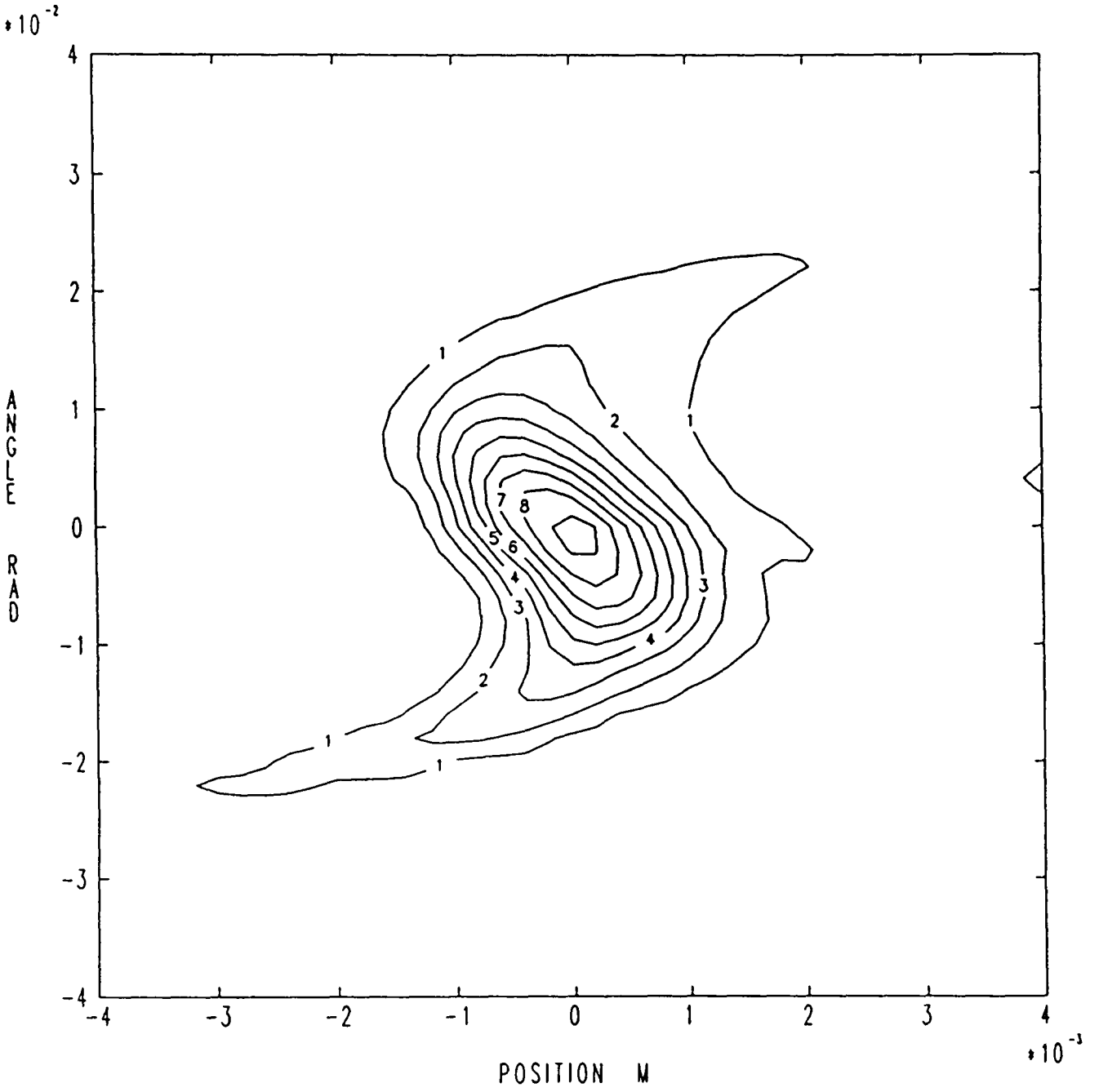

Figure 2

Brightness profile measured at 24 μA

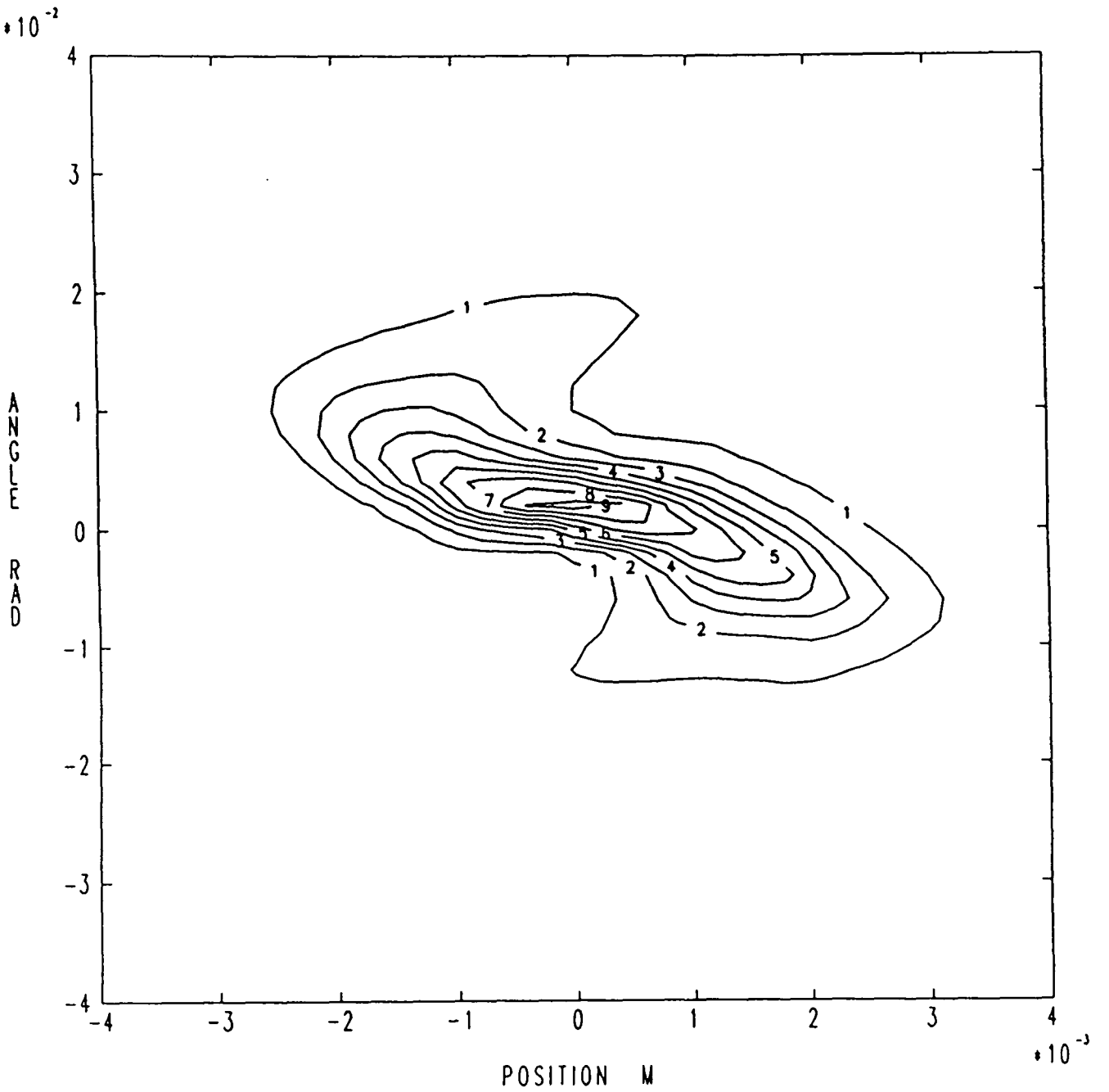

Figure 3
Brightness profile
measured at 114 μA

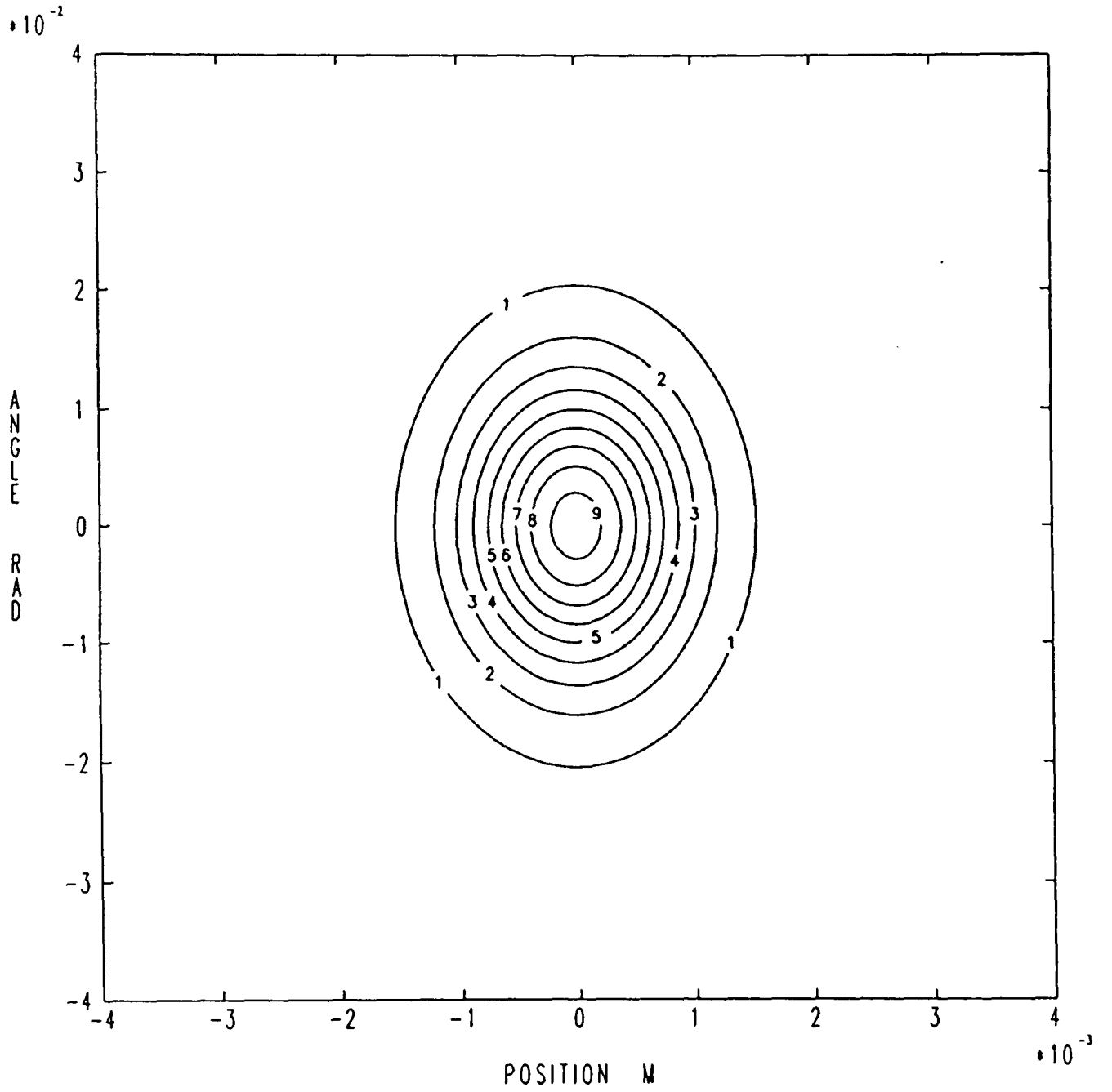

Figure 4

Calculated Gaussian brightness profile (for comparison)

the shape of the envelope within which the distributions sit are far from ellipsoidal.

2. Lens Aberrations

The measurements are made at a waist produced by the focussing effect of a gridded lens as described in chapter II/1. It was found that the shapes of the brightness profiles did not behave as one would expect from first order calculations when the strength of the lens was altered. First order theory, by definition, allows only linear transformations. Hence, the only alterations in the shape of the brightness profiles that would be allowed by first order theory are a combination of rotations and shears. In practice, the shape of the envelope was seen to be distorted in a distinctly non-linear fashion. Furthermore, the shape of the profile's envelope was found to be independent of the extract geometry of the ion source. It became clear, therefore, that its 'S-bend' form might well arise from the gridded lens itself.

Calculations were undertaken on the gridded lens as outlined in the next chapter, and these confirmed that the aberrations of the lens could account for the observed envelope shape of profiles such as figure 1.

There might, of course be other sources of aberration, in particular the pole pieces of the analysing magnet. However, one would expect this to be astigmatic and, although brightness profiles were taken in both the vertical and horizontal planes, there was no evidence for astigmatic aberrations.

3. Space Charge Effects

There still remains the problem of identifying the reason for the difference between the three profiles of figures 1, 2 and 3. These are just a sample of many profiles taken with different beam currents but with all other conditions kept the same (extract voltage, lens voltage, sputter voltage et cetera). Assuming for the moment, therefore, that the beams emerging from the source in the three different cases were more or less identical except for their intensity, the difference between the three profiles measured must arise from the differences in the transport of the beams with different currents. The most obvious mechanism for such a difference is the space charge effect.

The currents measured when each of the three measurements were taken were 2, 24 and 114 μA respectively. Theoretical calculations of the effect of space charge on the transport of beams, assuming these currents, were done (see chapter 5) and indicate that the differences in the shapes of the profiles can be explained by these effects.

Summary

Brightness profiles measured at different currents have been qualitatively analysed. Their functional form can be explained in terms of an ellipsoidal and roughly Gaussian distribution in phase space at the ion source which is then altered in the subsequent transformations before measurement.

The form of low current beam profiles can be explained by the aberrating effects of the gridded lens used in the measurements. There may be other aberrating elements, but they are believed to be of subsidiary importance.

The differences that arise at higher currents can be explained in terms of the space charge effect.

Chapter 4

Aberrations

Introduction

The term aberrations can be used to cover any of the reasons for which transformations of the phase space are non linear. In this chapter all such effects will be considered except for space charge, which will be dealt with separately in the next chapter. The different possible causes of aberration will be discussed, and then the aberrations due to three generic lens types will be considered. These are the idealised gridded, tube and aperture lenses and can each be treated analytically. Clearly the aberrations from any optical element can be calculated using available computer programs (such as [1]). The intention here is to see how the aberrations of individual elements affect the overall performance of an AMS system, and so it is not necessary to study the details of design for each optical element. For this reason, there are advantages in restricting the discussion to generic lens types which are of general interest as they will have broadly similar aberrating characteristics despite small variations in design.

1. Aberrating Elements

Virtually any optical element in an ion beam transport system is capable of producing aberrations of some description. However, the aim of this thesis is to investigate these effects in relation to AMS and so this prescribes those elements which need to be considered. Furthermore, because the high energy beam fits the paraxial model much more closely, the

transmission in this region is found to be much more 'flat topped', and so it is really necessary to consider only those elements which occur in the injection system and accelerator. The radiocarbon accelerator facility at Oxford which is well described elsewhere [2] will be taken as a typical example of an AMS system.

1.1. The Optical Elements

After the ion source itself the optical elements (not including drift lengths) are:

1. gridded lens
2. gap lens
3. injection magnet
4. gap lens
5. gridded lens
6. accelerator tube
7. stripper
8. accelerator tube

followed by the high energy beam line. The possible aberrations arising from each of the different types of element will be considered.

1.2. Gridded Lenses

Gridded lenses are often described as being low aberration lenses. This is true in as much as they have much lower aberration coefficients than, for example, Einzel lenses. (See ref. [3] for a discussion of the advantages of gridded lenses.) Unfortunately in many situations they do produce appreciable spherical and higher order aberrations. This is because they are frequently used in places where the beam size is large in

comparison to the dimension of the optical elements. The lenses are cylindrically symmetric, and so the transformation matrix (see equation I.1/1.3.4) will only have odd terms in the elements relating the x and y coordinates; these elements will also be symmetric.

1.3. Gap Lenses

In principle, a gap lens will produce fairly bad aberrations of the same order of magnitude as an Einzel lens. However, in this particular application the gap lenses are very weak [4] and are near waists, where the beam size is small. The aberrations due to these will be neglected.

1.4. The Injection Magnet

The injection magnet in use at the Oxford facility is a 90 degree, double focussing magnet with a horizontal bend plane. The aberrations in the horizontal plane will, therefore be largely determined by the effective edge of the magnet, and those in the vertical plane by the form of the fringing fields. A detailed calculation of the high order aberrations in such a magnet would be very complex, and is beyond the scope of this thesis.

Fortunately, in brightness profile measurements made on the injection system itself, there was no evidence for aberrations occurring between the two waists which are situated just before and just after the injection magnet. Furthermore, neither on the test bench nor in the injection system was there any significant difference in the brightness profiles measured in the horizontal and vertical planes, whereas one would expect the aberrations of a magnet to be highly astigmatic. Both of these facts support the view that the injection magnet does not contribute significantly to the aberration of the beam.

1.5. The Accelerator

The uniform electric field which performs the acceleration does not introduce any aberrations in the phase space transport (except in the z dimension). The ends of the tubes, however act as lenses, with properties similar to those of Einzel or gap lenses. The aberrations that arise from these might, therefore, be very significant and the theory applied to them is treated fully in section 3.

2. Aberrations due to Gridded Lenses

In this section we shall consider in detail what happens to particles as they pass through a gridded lens. There are many other treatments of the effects of the grid itself [5] and as this is insignificant with the small grid sizes usually used, it will ignored here.

2.1. The Idealised Gridded Lens

An idealised gridded lens may be defined as consisting of an infinite cylinder at ground potential, of radius Q which is intersected at right angles by the plane z = 0 (local coordinates) which is at some potential W (figure 1a). This description has the advantage that one can derive an exact equation for the electrostatic fields in such a lens.

The fact that the optical properties are close to those of a real gridded lens may be induced from the agreement between the results of calculations on such an idealised lens and brightness plots measured on the ion source test bench (see section 4).

It was decided, therefore, that the increase in complexity of the calculations that would arise from trying to calculate the fields due to the precise physical geometry of specific gridded lenses was not warranted.

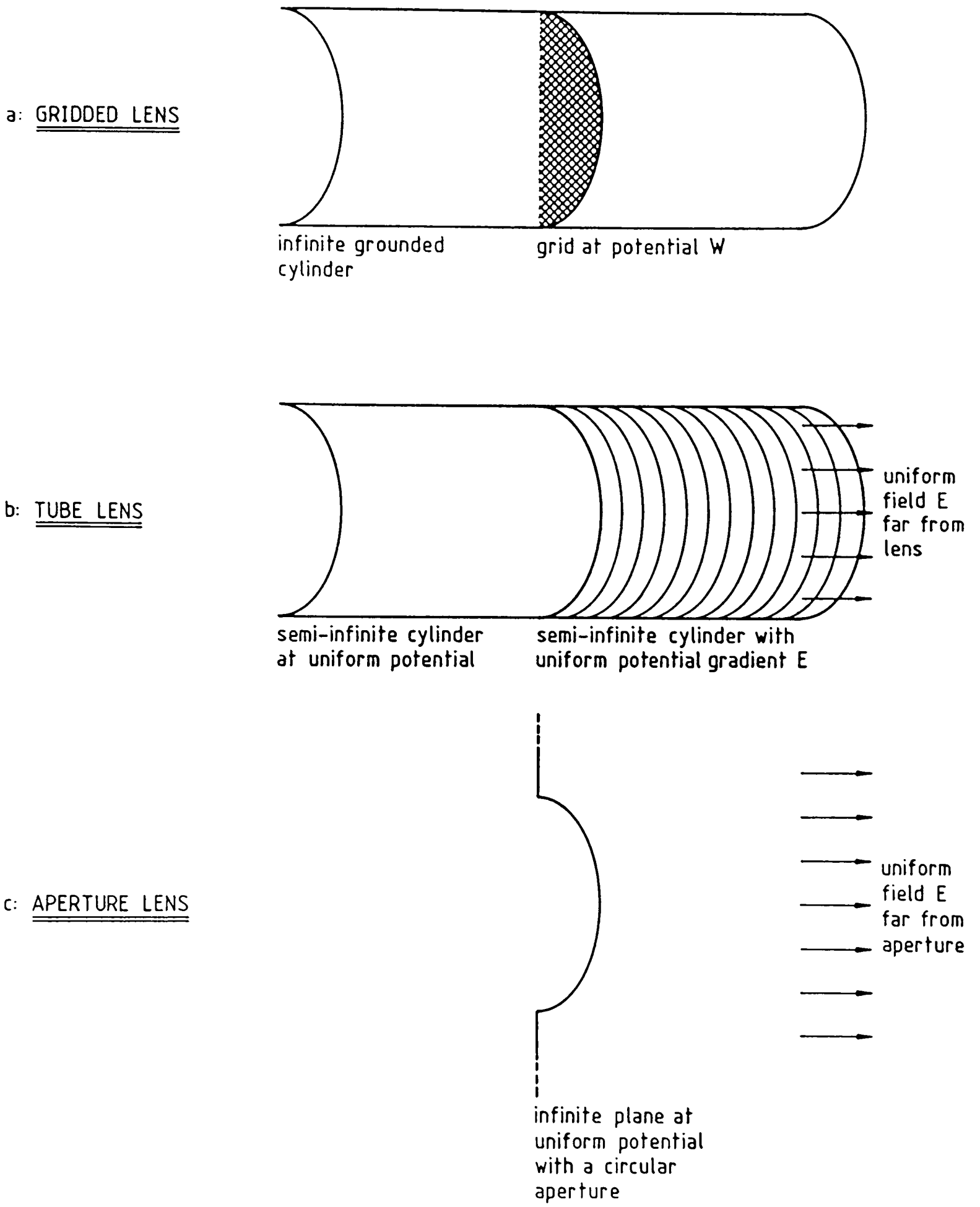

Figure 1

Sectional views of the three generic lens types considered here

2.2. The Electrostatic Field

In a charge free region the potential satisfies Laplace's equation, which in cylindrical coordinates can be written as [6]:

$$\nabla^2 V = \frac{1}{r}\frac{d}{dr}\left(r\frac{\partial V}{\partial r}\right) + \frac{1}{r^2}\frac{\partial^2 V}{\partial \theta^2} + \frac{\partial^2 V}{\partial z^2} = 0 \qquad (2.2.1)$$

The field will have no dependence on θ and so we can assume a solution of the form:

$$V = R(r)\,Z(z) \qquad (2.2.2)$$

This gives us:

$$\frac{1}{R}\frac{1}{r}\frac{d}{dr}\left(r\frac{dR}{dr}\right) + \frac{1}{Z}\frac{d^2 Z}{dz^2} = 0 \qquad (2.2.3)$$

Since each term is a function of only one independent variable, each must independently be constant. Thus we get the two equations:

$$\frac{r}{R}\frac{d}{dr}\left(r\frac{dR}{dr}\right) + k^2 r^2 = 0 \qquad (2.2.4)$$

$$\frac{1}{Z}\frac{d^2 Z}{dz^2} = k^2 \qquad (2.2.5)$$

The radial equation is just a form of the Bessel equation and has well behaved solutions:

$$R(r) = J_0(kr) \qquad (2.2.6)$$

The axial equation has solutions of the form:

$$Z(z) = e^{kz} \quad \text{or} \quad e^{-kz} \tag{2.2.7}$$

As we expect the potential to tend to 0 as z tends to infinity, the first will apply in the region $z < 0$ and the second in the region $z > 0$.

The radial function is identically zero at $r = Q$. Therefore the only values of k which will appear in the solution are $k = k_i/Q$ where k_i are the zeros of the Bessel function J_0. This means that the potential at $z = 0$ can be described by:

$$\sum_{m=1}^{\infty} c_i \, J_0(k_i r/Q) = W \tag{2.2.8}$$

The Bessel functions $J_0(k_i r)$ are orthogonal on integration from 0 to 1 with respect to the weight function r. Thus we can write [6]:

$$\frac{c_i}{Q^2} \int_0^Q r \, [J_0(k_i r/Q]^2 \, dr = \frac{1}{Q^2} \int_0^Q W \, r \, J_0(k_i r/Q) \, dr \tag{2.2.9}$$

$$\frac{c_i}{2} J_1^2(k_i) = \frac{W}{k_i} J_1(k_i) \tag{2.2.10}$$

$$c_i = \frac{2 \, W}{k_i \, J_1(k_i)} \tag{2.2.11}$$

Hence the potential anywhere in the gridded lens can be written, using the coefficients from (2.2.11) :

$$V = \sum_{i=0}^{\infty} c_i J_0(k_i r/Q) \exp(-k_i z/Q) \qquad z > 0 \tag{2.2.12}$$

$$V = \sum_{i=0}^{\infty} c_i J_0(k_i r/Q) \exp(k_i z/Q) \qquad z < 0 \tag{2.2.13}$$

This gives one an exact value for the electric potential, and thus the electrostatic field in the gridded lens. In practice, of course, we can compute only a limited number of elements in the series but the series can be made to converge fairly fast except at the intersection between the z = 0 plane and the grounded cylinder.

2.3. The Motion of Charged Particles

The motion of charged particles in an electric field can be described in three dimensions by the equation:

$$m\,\underline{r}'' = Ze\,\nabla V \tag{2.3.1}$$

where m denotes the particle mass and Ze its charge.

Equations (2.2.12), (2.2.13) and (2.3.1) define the motion of particles in an ideal gridded lens absolutely. It is, however, difficult to make use of this if one wishes to do calculations on the whole phase space. At this stage, therefore, we will introduce the assumption that the beam is radially symmetric and that skewed rays are unimportant. This enables us to make use of the results outlined in equation (I.1/3.5.7) and in the preceding passage while allowing us to reduce the description of the beam to the r and z dimensions and their conjugate momenta:

$$p_r' = Ze(\partial V/\partial q_r) \qquad p_z' = Ze(\partial V/\partial q_z) \tag{2.3.2}$$

These are the equations that will be used in the following calculations.

2.4. Fitting the Results to a Function

Unfortunately 'ray tracing' calculations of the accuracy required in the study of phase space transport are fairly lengthy. If one needs to use the properties of a lens in a large number of calculations, therefore, it is desirable to fit the behaviour of the lens to some function which can be readily calculated.

To do this, one calculates the transformation for a representative selection of points in the initial phase space and then fits the transformation to some polynomial. It was decided that only effects up to fifth order would be considered as it becomes very difficult to get meaningful fits for polynomials which have a very large number of terms.

In order to arrive at a description which was easy to apply, the particle trajectories were extrapolated to the plane of the grid and the initial coordinates taken to be the q_r and p_r at this plane. Their motion was then calculated over the region of the lens and the final trajectories extrapolated back to the plane of the grid.

Having done this, one finds that the dependence of the final coordinates can be approximated to a separable function f(q)g(p). It is therefore appropriate to have a polynomial that has elements with high powers in both p and q. Taking into account the cylindrical symmetry of the lens, the following 18 element polynomial is capable of describing the system to fifth order and was found to give a very good simulation of the traced rays:

$$(2.4.1)\quad q_1 = c_1 q + c_2 p + c_3 q^3 + c_4 q^2p + c_5 qp^2 + c_6 p^3 + c_7 q^5 + c_8 q^4p + c_9 q^3p^2 + c_{10}q^2p^3 + c_{11}qp^4 + c_{12}p^5 + c_{13}q^5p^2 + c_{14}q^4p^3 + c_{15}q^3p^4 + c_{16}q^2p^5 + c_{17}q^5p^4 + c_{18}q^4p^5$$

with a corresponding equation for p_1. The p's and q's on the right hand side are the initial coordinates in phase space, and the terms c_i are the coefficients of the polynomial.

The computer programs used for these calculations will be described in chapter I/7.

3. Aberrations in the Accelerator

It is clearly difficult to make any measurements of the brightness profile of a beam within the accelerator. However, a change made in the diameter of the gridded lens which was believed to be contributing most to the aberration of the Oxford injection system, made surprisingly little difference to the overall transmission through the accelerator or to the sensitivity of the transmission to the beam control parameters (the so called 'flat-top-ness' of the transmission). For this reason one was led to consider the possibility that the accelerator itself was producing a considerable increase in the effective emittance of the beam.

3.1. Lenses in the Accelerator

In the main part of an accelerator tube, the field is more or less uniform. (In fact the field is spiralled slightly to disperse secondary electrons; the effect of this will be ignored here; see [7].) A uniform field transforms the phase space in a well behaved fashion and introduces

no aberrations (except in the direction of acceleration). Unless the ends of the tubes are covered with a gauze, however, the fringing fields obtained act as lenses, and these are bound to introduce higher order terms into the phase space transformation. In some accelerators, a section of the tube is kept at a constant potential. Either end of such a drift length also acts as a lens. Such lenses are sometimes called 'tube lenses', 'aperture lenses' or 'entrance' and 'exit' lenses.

In practice, an accelerator tube is not a cylinder which is uniformly graded in voltage, but is instead made up from a series of apertures with potential differences maintained between them. If the spacing of these apertures is very close compared to their diameter then the lenses produced are tube lenses; otherwise they behave much more like aperture lenses.

3.2. The Idealised Tube Lens

In order to make simple calculations of the effect of tube lenses, an idealised tube lens is defined. The boundary conditions applying in such a lens are shown in figure 1b. It is assumed that on one side of the lens there is a semi-infinite tube at constant potential, and on the other a tube on whose walls a uniform potential gradient is maintained. For the purposes of this chapter it will be assumed that the tube at constant potential lies in the region $z < 0$.

3.3. The Electrostatic Field for a Tube Lens

Much of the theory for tube lenses is similar to that covered in section 2. We can write the fields as:

(3.3.1)
$$V = V_1(r,-z) \qquad z < 0$$
$$V = E \times z + V_2(r,z) \qquad z > 0$$

where E is the potential gradient in the accelerator tube. If the tube diameter is Q, the boundary conditions are:

(3.3.2) $$V_1(Q,-z) = 0 \qquad V_2(Q,z) = 0$$
$$V_1(r,0) = V_2(r,0)$$

and from $\nabla^2 V = 0$,

(3.3.3) $$\left(\frac{\partial V_1}{\partial z}\right)_{z=0} = \left(\frac{\partial V_2}{\partial z}\right)_{z=0} + E$$

From (3.3.2) it follows that $V_1(r,-z) = V_2(r,z)$ which we shall define to be $V_0(r,z)$. From (3.3.3) we find:

(3.3.4) $$(\partial V_0/\partial z) = E/2$$

By analogy with the gridded lens (equations 2.2.12 and 2.2.13) the solution will be of the form:

(3.3.5) $$V_0(r,z) = \sum_{i=0}^{\infty} c_i \, J_0(k_i r/Q) \, \exp(-k_i z/Q)$$

where the coefficients can be shown to be:

(3.3.6) $$c_i = \frac{E}{k_i^2 \, J_1(k_i)}$$

by the arguments given in (2.2.9 to 2.2.11) with the condition (3.3.4). Hence the potential anywhere in the region of the lens is defined, using the coefficients (3.3.6), by:

$$V = Ez + \sum_{i=0}^{\infty} c_i \, J_0(k_i r/Q) \, \exp(-k_i z/Q) \qquad z > 0 \tag{3.3.7}$$

$$V = \sum_{i=0}^{\infty} c_i \, J_0(k_i r/Q) \, \exp(k_i z/Q) \qquad z < 0 \tag{3.3.8}$$

3.4. Idealised Aperture Lenses

An aperture lens is formed if there is a hole in a conducting surface which bounds a region of uniform electric field. The ideal configuration is shown in figure 1c. In practice, in an accelerator tube there will be other conducting surfaces nearby, and these will tend to increase the aberrations produced by the lens. For a given aperture the tube lens imparts the greatest transverse forces and the aperture lens the least. The aperture lens, however, gives a fairly good description of many systems and is used as the model for first order calculations (see for example [8]).

3.5. The Electrostatic Field for an Aperture Lens

This boundary condition problem is treated in detail elsewhere [9]. The added potential in the region of the aperture is:

$$V_1 = - Q^2 \int_0^{\infty} j_1(kQ) \, \exp(-k|z|) \, J_0(kr) \, dk \tag{3.5.1}$$

where J_0 is the zeroth order Bessel function and j_1 is given by:

$$j_1(kQ) = \frac{1}{\pi Q^2} \left(\frac{\sin(kQ)}{k^2} - \frac{Q\cos(kQ)}{k} \right) \tag{3.5.2}$$

The overall potential is then given by:

(3.5.3) $V = Ez + V_1 \qquad z > 0$

(3.5.4) $V = V_1 \qquad z < 0$

3.6. Calculating Particle Trajectories

The equations governing the motion of charged particles are given in section 2.3. Once again, the 'ray tracing' calculations are quite long and so the transformation of a representative selection of points in phase space is calculated through the lens region. The resulting points in phase space are then extrapolated back to the plane of the lens (assuming a uniform electric field). The transformation is then fitted to a function of the form described in (2.4.1). This function can be used to describe the motion of particles entering and leaving accelerating sections of the tube, and the transformations within those regions can be described by the simple, non-relativistic equations:

(3.6.1) $q_{r1} = q_{r0} + p_{r0}t/m$

(3.6.2) $q_{z1} = q_{z0} + p_{z0}t/m + EQt^2/2m$

(3.6.3) $p_{r1} = p_{r0}$

(3.6.4) $p_{z1} = p_{z0} + EQt$

In general, the length over which the acceleration takes place is defined ($L = q_{z1} - q_{z0}$) and so one calculates the time from equation (3.6.2).

Computer programs working on these principles are described in chapter I/7

3.7. Current Dependent Aberrations

In addition to the aberrations which are caused by the lenses at the

ends of the acceleration tubes there is a possibility that the accelerating sections of the tubes might result in current dependent aberrations. Secondary electrons travelling between elements of a tube will not draw a current from the terminal but they will distort the accelerating gradient. This will alter the optical properties of the accelerator tubes and result in current dependent transmission. This is a good reason for ensuring that the tubes are well conditioned and that only a very small proportion of the primary beam strikes the walls of the accelerator tubes which can be achieved by phase space limitation before the accelerator.

4. Calculations on the Ion Source Test Bench

The impetus for doing these calculations had come from a desire to explain the brightness profile plots made on the ISTB and described in the previous chapter. It was therefore on that system that these methods of calculation were tested.

Clearly the calculations of transformations taking place in the accelerator cannot be tested in this way. However, the methods used for the different types of lens are sufficiently similar that the validity of the one is a strong argument for the validity of the other.

4.1. Methods used for Displaying the Transformations

In order that comparisons of the calculated trajectories can be made with the brightness distributions which have been measured, the output of the ion source is modelled by a Gaussian distribution in phase space. The parameters of this Gaussian function are chosen to give a good fit to the measured profiles. The calculated profile should then correspond exactly to that measured. (See chapter 7 for an explanation of exactly how this is done.)

4.2. The Results of the Calculations

Figure 2 shows the transformed phase space calculated at the measurement plane on the ISTB. Comparison with numerous brightness profiles measured on the test bench (see, for example figure 3:1) show that this calculation models the production of the 'tails' that are seen at high divergence on all such measurements as well as is possible within the limits of experimental accuracy and consistency.

This result, along with the lack of any appreciable astigmatism, means that the phase space transformations taking place at low current on the test bench can be well described by assuming that the gridded lens is responsible for almost all of the aberration. Furthermore, the mathematical modelling of the lens properties outlined above gives results in good agreement with experiment.

Summary

The low current aberrations of the ion source test bench and, as far as one can tell, of the injection system of the accelerator facility at Oxford, are dominated by the effect of the gridded lenses.

A mathematical technique for modelling the transformation of phase space through gridded lenses is outlined and found to give results in accord with brightness profiles measured on the ion source test bench.

A similar technique for modelling the effects of aberrations in the accelerator is also outlined. There is no straightforward way of testing the validity of these calculations experimentally. In addition to this, a possible mechanism for current dependent loss of transmission is discussed briefly.

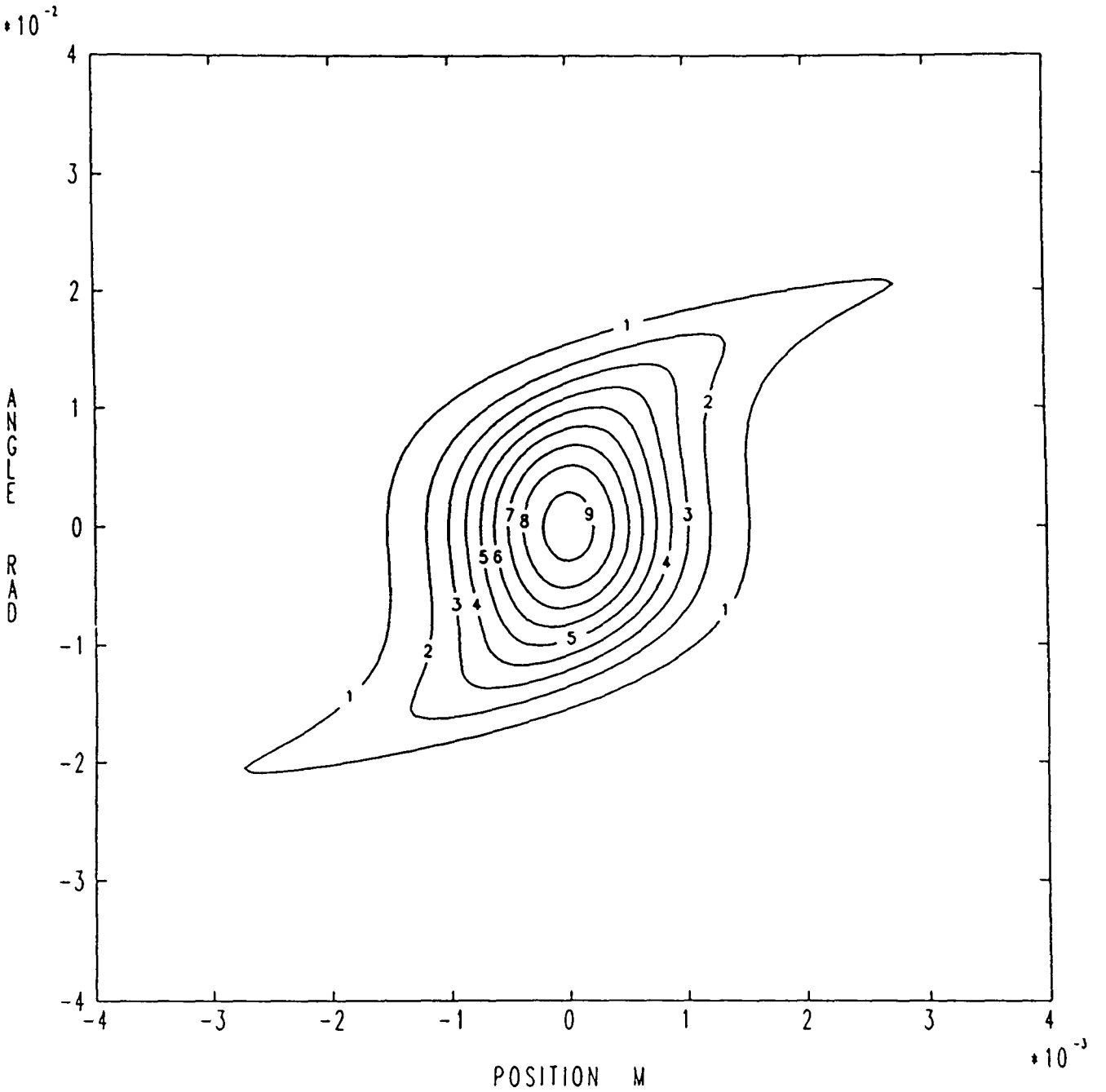

Figure 2

Low Current Phase Space Transformation
calculated for the the ISTB
cf. figure 3:1

References

[1] D. Dirmikis, Computer Program for Numerical Analysis of Electron Flow Systems, University of Sheffield, (1975).

[2] N.R. White, J.O. Wand, R.E.M. Hedges and E.T. Hall, Symposium on Accelerator Mass Spectrometry, Argonne (1981) 472.

[3] P. Grivet, Electron Optics (Pergamon Press, Oxford, 1965) p. 179.

[4] N.R. White, D. Phil. Thesis., Oxford (1981) 181.

[5] P. Dahl, Introduction to Electron and Ion Optics (Academic Press, New York, 1973) p. 57.

[6] M.L. Boas, Mathematical Methods in the Physical Sciences (Wiley, New York, 1966) p. 644.

[7] H.R.McK. Hyder and G. Doucas, Proc. Int. Conf. on Technology of Electrostatic Accelerators, Daresbury, (1973) 352.

[8] T.J.L. Greenway, Computer Program OPTRYK, Nuclear Structure Lab., Oxford University.

[9] J.D. Jackson, Classical Electrodynamics (Wiley, New York, 1975) p. 121.

Chapter 5

Space Charge Effects

Introduction

One problem which has beset the radiocarbon accelerator facility at Oxford, amongst others, has been the current dependence of the $^{13}C/^{12}C$ ratio. A number of possible causes of this have been investigated, such as the possibility of the terminal voltage being affected, but no good explanation for the effect has come to light.

Conventional wisdom led one to believe that, with currents of about 20 μA and energies of about 23 keV, space charge effects would be insignificant. The measurements on the ion source test bench described in chapter 2, however, indicated that this was far from the case. For this reason a method was sought to calculate the expected effect of space charge on the transformation of the phase space. The subject of space charge optics is dealt with elsewhere (see [1] and in particular [2] for a detailed treatment), but it is usually discussed in relation to very intense beams where the effects are large. Here we find subtle changes in the form of the phase space profile and consequently the methods that must be employed are rather different.

1. The Regions of Importance

It is worth, at this stage, considering the regions in which the space charge effect is likely to be most important.

The charge density per unit length along a beam of charged particles will simply be proportional to the current. The electric fields present

near the edge of the beam will be approximately proportional to one over the radius. It follows, therefore, that the net effect of space charge on the particles in the beam will be very roughly proportional to:

$$\int \frac{I(q_z)}{R(q_z)}\, dq_z \qquad (1.0.1)$$

where $R(q_z)$ is some measure of the radius of the beam and $I(q_z)$ the current flowing in it.

From this equation it is clear that we can by no means ignore the effect in the regions between waists. Because of the isotopic ratios, space charge effects on the ^{13}C and ^{14}C beams on their own are going to be negligible in comparison to those experienced where there is a ^{12}C beam.

The effect is purely electrostatic and so, assuming that the initial brightness profiles are the same for different isotopes (see chapter 2), all of them will be affected in the same way until the beam is mass analysed.

Hence it is clear that this effect is capable of explaining a $^{13}C/^{12}C$ ratio dependence on ^{12}C current, but not variations in the $^{14}C/^{13}C$ ratio. This is precisely the pattern that is seen at the Oxford accelerator where the $^{14}C/^{13}C$ ratio is used for dating because of its relative stability.

2. Comprehensive Theory

Detailed calculations of the effect of space charge on phase space transformations will now be outlined. A brief discussion of the comparison of these calculations with measurements made will be given in the following section.

2.1. Assumptions about the Form of the Beam

The electric fields arising from a beam which has an arbitrary shape in phase space would involve very lengthy numerical integrations over the charge distribution for every point at which one needed to know the field. Given that we wish to investigate the transformation of the whole phase space, this is simply not feasible.

We will make the assumption that the beam is symmetric in the x and y co-ordinates and that the form of the brightness profile in phase space is separable in these two dimensions. This will allow the properties outlined at the end of section (1:3.4) to be used.

In addition to this, we shall assume that the divergence of the beam is very much less than 1 radian; this implies that the electric fields arising from the charge density of the beam will be purely radial.

2.2. The Electric Field

To evaluate the electric field we make use of Gauss's theorem, which can be written as:

$$\oint_S \underline{E}.\underline{ds} = \frac{1}{\varepsilon_0} \int_V f(\underline{r})\ dv \qquad (2.2.1)$$

where $f(\underline{r})$ is the charge density per unit volume.

Consider, then, a Gaussian cylinder of length Δz and radius R which is centred on the axis of the ion beam. Using the equation (1:3.5.2) and assuming that Δz is small, the number of particles with $x < R$ at any one time will be proportional to:

$$\int_{q_x=0}^{R} \int_{p_x=-\infty}^{\infty} g(q_x, p_x)\ dq_x\ dp_x \qquad (2.2.2)$$

The total ion population within a radius R will be approximately proportional to:

$$(2.2.3) \qquad \left(\int_{q_x=0}^{R} \int_{p_x=-\infty}^{+\infty} g(q_x,p_x)\, dq_x\, dp_x \right)^2$$

where $g(q_x,p_x)$ is as defined in equation (1:3.5.2).

The total charge in the beam length Δz can be calculated directly from the beam current and the mean particle velocity. It will be:

$$(2.2.4) \qquad (I/v)\Delta z$$

where I is the beam current and v the velocity in the z direction.

Thus, if we define the constant G as the result of (2.2.2) with $R = \infty$ then the charge contained within the Gaussian cylinder under consideration will be:

$$(2.2.5) \qquad \frac{I\ \Delta z}{v} \left(\int_{q_x=0}^{R} \int_{p_x=-\infty}^{+\infty} \frac{g(q_x,p_x)}{G}\, dq_x\, dp_x \right)^2$$

and, therefore, if we assume that there is no component of the electric field through the ends of the cylinder, from (2.2.1) we find that the radial component of the electric field is:

$$(2.2.5) \qquad E_r(R) = \frac{I\ \Delta z}{2\pi R\ \varepsilon_0\ v} \left(\int_{q_x=0}^{R} \int_{p_x=-\infty}^{+\infty} \frac{g(q_x,p_x)}{G}\, dq_x\, dp_x \right)^2$$

2.3. The Motion of Charged Particles

From equation (2.2.5), using the equation of motion of a charged particle in an electric field on the y = 0 plane, we get:

(2.2.6) $$p_x' = Q\ E_r(q_x)$$

One can calculate the transformation of the phase space by a process of iteration.

It should be pointed out that precisely the same equations also apply to the y plane, using instead $g(q_y,p_y)$.

A computer program working on these principles will be described in chapter 7.

3. Calculations on the Ion Source Test Bench

In chapter 2 measurements on the ISTB at different currents were discussed briefly. These showed the effect of the beam transport variation due to current on measured brightness profiles.

Calculations of the phase space transport in the ion source test bench have been carried out using the above theory. The initial two dimensional brightness profile of the beam must be assumed, and this is chosen to be an upright ellipsoidal gaussian distribution with dimensions chosen to be consistent with the measurements made (see chapter 3).

It is found that these calculations give a very considerable over-estimate for the size of the effect, and the transformations measured can be adequately modelled by assuming that the space charge forces are about ten times smaller. The reasons behind this will be discussed in the next chapter. The functional form of the effect is, however, very well reproduced by the calculations. The results of these are shown in figures 1, 2 and 3 for currents of 0μA, 24μA and 114μA respectively (they are displayed in the same way as those of the previous chapter and include the effects of aberration in the gridded lens). Comparison of these figures

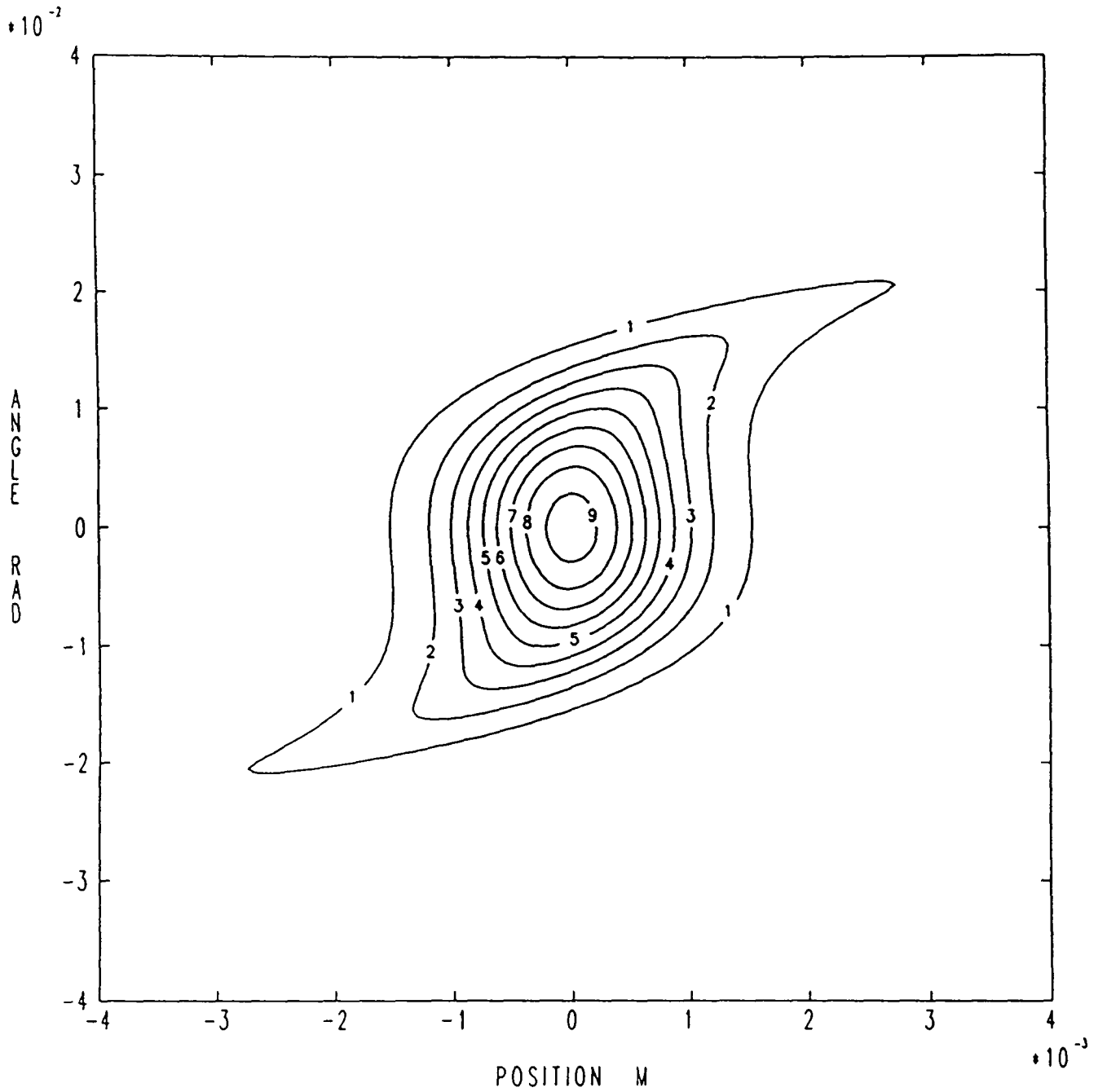

Figure 1

Phase space transformation calculated for the ISTB assuming a 0 μA C^- *current: cf. figure 3:1*

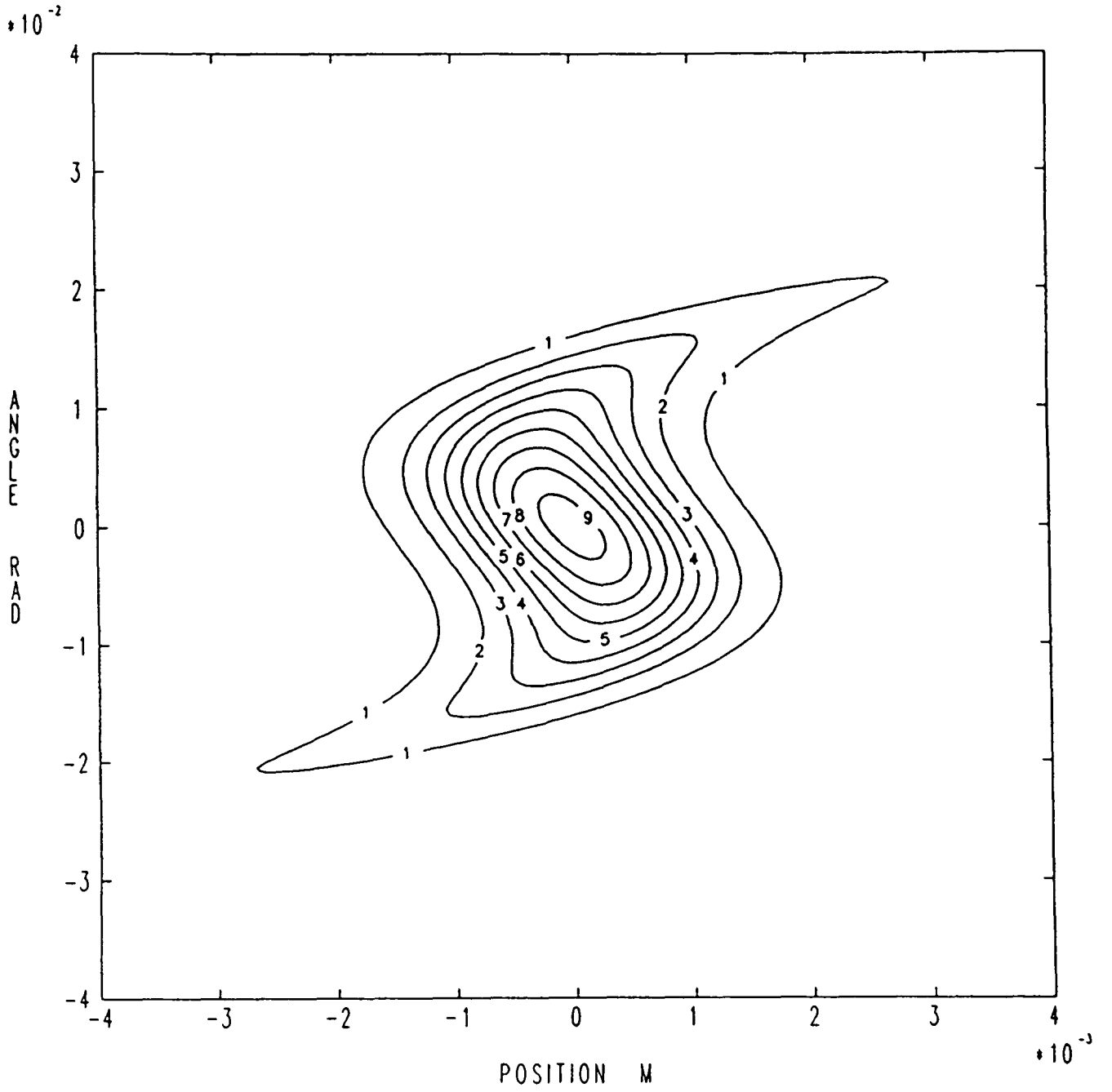

Figure 2

Phase space transformation calculated for the ISTB assuming a 24 μA C^- current: cf. figure 3:2

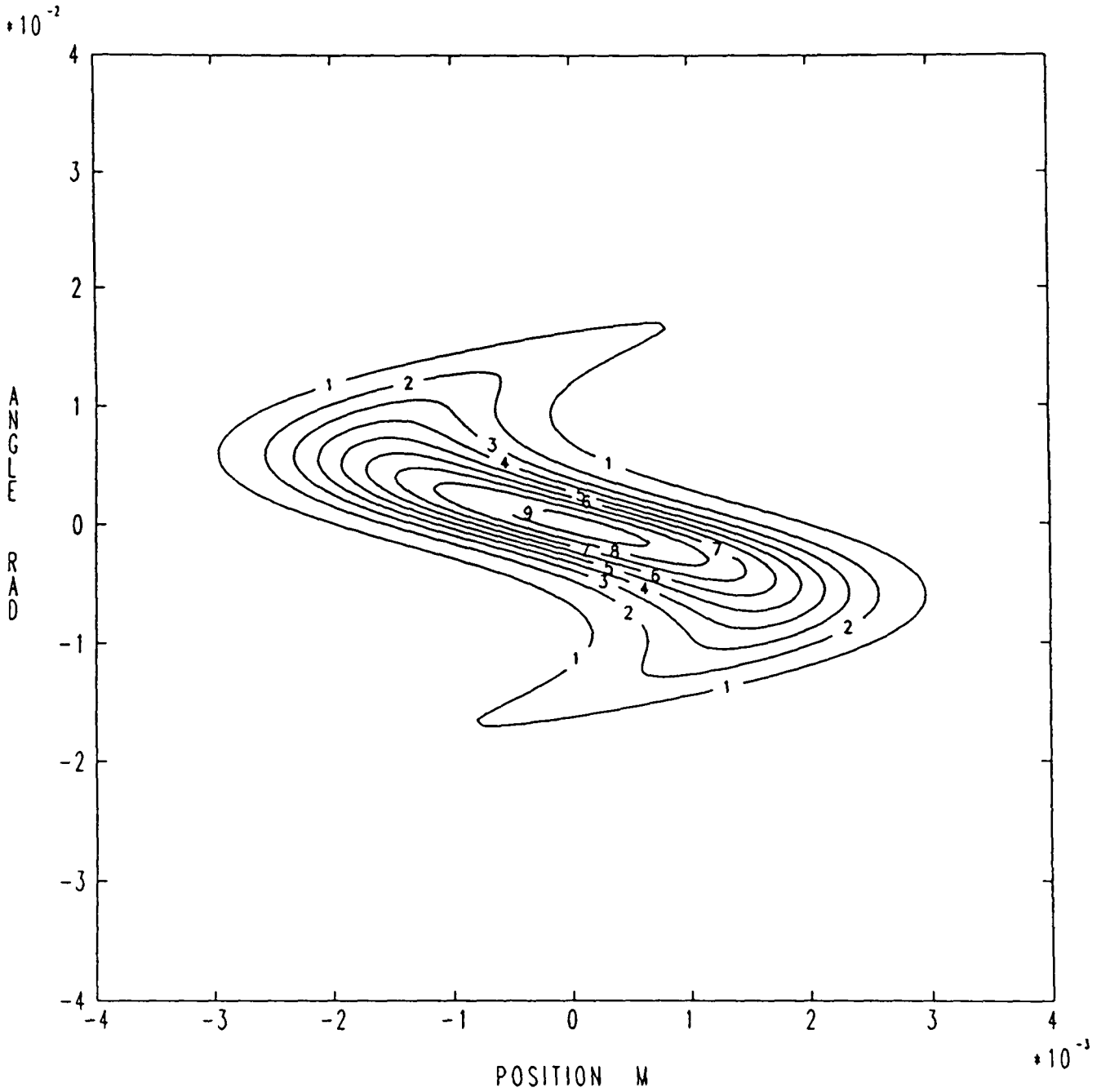

Figure 3

Phase space transformation calculated for the ISTB assuming a 114 μA C^- *current: cf. figure 3:3*

with figures 3:1,3:2 and 3:3 give a representative impression of how well the calculations match the measurements.

For more details of these and other calculations see chapter 8.

Summary

A method for calculating the phase space transformations resulting from the space charge effect is developed. This is seen to model the transformations seen on the ion source test bench satisfactorily, but to give a considerable over-estimate of the size of the effect.

References

[1] A. Septier (ed.), Adv. Electron. Electron Phys., Suppl 13 part C (1980).

[2] J.D. Lawson, Adv. Electron. Electron Phys., Suppl 13 part C (1980) 1.

Chapter 6

Residual Gas

Introduction

As was discovered in the last chapter, the space charge effect is substantially smaller than that predicted by a simple theory. This demonstrates that ion optics cannot be fully understood without considering the effects of the residual gas in the vacuum through which the ion beam under consideration is travelling. In this chapter, therefore, all such effects will be considered. In particular, space charge neutralisation will be investigated in some detail.

1. The Vacuum

The quality of the vacuum found in ion beam transport systems used for AMS varies quite widely. However the density of particles in the vacuum is almost always substantially higher than the density of particles in the ion beam itself. The density of particles in a vacuum can be written as:

(1.0.1) $$N = N_A \, P \, / \, V_m$$

where P is the relative pressure, N_A is Avogadro's number and V_m is the molar volume of an ideal gas at STP. For reference the values used here are:

$$N_A = 6.02 \times 10^{23} \qquad V_m = 2.24 \times 10^{-2} \ m^3 \ mol^{-1}$$

Typical pressures are 10^{-8} to 10^{-10} atmos..

2. Interactions with the Beam

When a ion trajectory comes close to a residual gas molecule there are essentially three possible outcomes of the interaction:

1. The incident particle is scattered
2. The incident ion changes its charge
3. The gas molecule is ionised

In considering these effects it is necessary first to look at the ion velocities with which one is dealing. The ion beam energies in an AMS injection system are typically of the order of 20 keV. At such energies the ion velocity is lower (by about one order of magnitude) than that of the electrons in the residual gas molecules. The effect of this is that the cross section for interaction with the neutral molecules in the gas will, in general, be less than πR^2 where R is the largest distance at which there is overlap between the electron wave functions of the ion and gas molecule. In other words, one can write:

$$\sigma < \pi(\langle r_I \rangle + \langle r_M \rangle)^2 \qquad (2.0.1)$$

where $\langle r_I \rangle$ and $\langle r_M \rangle$ are the expected outer electron wave function radii for the ion and molecule respectively. Thus, as $\langle r_I \rangle + \langle r_M \rangle$ is typically less than or approximately equal to 2×10^{-10} m, we can assume that within an order of magnitude:

$$\sigma < 4\pi \times 10^{-20}\ m^2 \qquad (2.0.2)$$

and the maximum probability for any of the above interactions taking place per unit length will be of the order of:

(2.0.3) $$P\ N_A\ \sigma\ /\ V_m$$

For the values given above, with a pressure of 10^{-9} atmospheres this gives $3.4 \times 10^{-3}\ m^{-1}$.

In much of the subsequent discussion it is necessary to assume specific conditions so that quantitative calculations can be undertaken. As a typical example the conditions prevailing at the Oxford radiocarbon accelerator will be used. Table 2.0.1 summarises these conditions.

isotopes for separation	^{12}C, ^{13}C & ^{14}C
injected beam	C^-
injected beam energy	20 keV
$^{12}C^-$ beam currents	10 - 20 μA
stripper gas	O_2
charge state measured	C^{3+}
typical vacuum quality	10^{-10} - 10^{-9} atmos.

Table 2.0.1
Typical conditions in a radiocarbon AMS system

2.1 Scattering

For scattering to take place, there must be an appreciable force on the ions concerned which is perpendicular to their direction of motion. At low energies the limit is imposed by the extent of the electronic wave functions. These screen the charge of the nuclei in the neutral gas molecules so that the only forces are those from induced dipoles. Such forces will not be large enough to produce significant scattering at the energies being considered and so the total cross section for this will be

given approximately by (2.0.1).

At higher energies it is possible to do more precise calculations. Under the adiabatic regime [1] one can apply the first Born approximation [2]. This deals with the scattering of charged particles from a potential and is based on a quantum mechanical treatment of the problem. For this approximation to be good, one must meet a complicated set of criteria which can, however, be summed up by the condition that the time spent in the 'range' of the potential should be smaller than the characteristic time for the changes wrought by the potential on the wave function of the incident particle. For the scattering of ions from the potentials due to residual gas molecules and atoms, this condition is met fairly well for small angle scattering at ion energies in the MeV range but is not really met at the energies found in the injection systems of AMS systems.

If the scattering takes place from a reduced potential $U(\underline{r})$ (where the reduced potential is $U(\underline{r}) = (2m/\hbar^2)V(\underline{r})$), then the scattering amplitude is given by:

$$f = -\frac{1}{4\pi}\int \exp(-\underline{\Delta}.\underline{r})U(\underline{r})d\underline{r} \qquad (2.1.1)$$

where $\underline{\Delta} = \underline{k}_i - \underline{k}_f$ and $\underline{k}_i$ and $\underline{k}_f$ are the initial and final wave-vectors respectively. The differential cross section given by the first Born approximation is:

$$\left(\frac{d\sigma}{d\Omega}\right) = |f|^2 \qquad (2.1.2)$$

A suitable potential for analytical calculations of the scattering of ions from residual gas atoms is the 'screened Coulomb' or Yukawa potential (this has the coulomb potential of the nuclei at small radii and falls off

in the way one might expect because of the electron wave functions):

(2.1.3) $$U(r) = U_0 \exp(-r/a)/r$$

and $U_0 = (2\mu/\hbar^2)(q_A q_B/(4\pi\epsilon_0))$ with q_A and q_B being the charges on the incident and target nuclei and (a) being of the order of the dimensions of the atom. The non relativistic differential cross section for scattering at an angle θ in the laboratory co-ordinate frame is:

(2.1.4)

$$\left(\frac{d\sigma}{d\Omega}\right) = \frac{(1 + m_A/m_B + 2(m_A/m_B)^2\cos\theta)^{3/2}}{|1 + (m_A/m_B)\cos\theta|} \left(\frac{q_A q_B}{4\pi\epsilon_0}\right)^2 \frac{1}{(\hbar^2/(2\mu a^2) + 4E\sin^2(\theta/2))^2}$$

where E is the energy in the centre of mass frame ($\mu v_A^2/2$) and μ is the reduced mass ($m_A m_B/(m_A+m_B)$), giving $E = (E_{lab} m_B/(m_A+m_B))$. This compares with the differential for Rutherford scattering which is [3]:

(2.1.5)

$$\left(\frac{d\sigma}{d\Omega}\right) = \frac{(1 + m_A/m_B + 2(m_A/m_B)^2\cos\theta)^{3/2}}{|1 + (m_A/m_B)\cos\theta|} \left(\frac{q_A q_B}{4\pi\epsilon_0}\right)^2 \frac{1}{16E^2\sin^4(\theta/2)}$$

This equation will be valid over all non-relativistic velocities and becomes very similar to equation (2.1.4) at high angles. This is because the electronic screening is only relevant for low angle collisions. At low energies one can therefore use equation (2.1.5) for high angle scattering and assume a limit on the cross section for low angle scattering from equation (2.0.2).

From these equations it is possible to deduce interesting isotopic effects. Considering, for example, the cross sections for the scattering of carbon nuclei off ^{16}O, nuclei it is found that at a given E_{lab} the cross

section for ^{14}C nuclei is nearly 40% higher than that for ^{12}C nuclei. This demonstrates very clearly that any scattering of the ion beams could result in serious fractionation.

It is sometimes useful to consider the energy transfer which takes place from an ion beam to the nuclei of the residual gas. To calculate this one can use the Rutherford scattering cross section. The momentum transfer from a small angle collision will be $(2m_A E_{lab})^{1/2}\sin\theta$ and the energy transfer $(m_A/m_B)E_{lab}\sin^2\theta$. Assuming that most of the collisions will be small angle ones, one can then calculate the rate of energy transfer to each residual gas nucleus:

(2.1.6)

$$R = \frac{I}{e\pi r^2}\,\frac{(1 + m_A/m_B + 2(m_A/m_B)^2)^{3/2}}{|1 + (m_A/m_B)|}\left(\frac{q_A q_B}{4\pi\epsilon_0}\right)^2 \frac{(m_A+m_B)^2 m_A}{m_B{}^3\, E_{lab}} \ln\left(\frac{\pi}{\theta_{min}}\right)$$

where I is the beam current, r is the beam radius and θ_{min} is defined by the requirement that the cross section is limited by equation (2.0.2) (i.e. scattering with an impact parameter greater than the classical radius of the residual gas atoms is ignored).

2.2. Charge Changing Reactions

These reactions are important in considering the transport of ion beams because ions subject to such processes are lost from the beam (except in the stripper canal of a tandem accelerator where electron detachment is intentional).

The theory of electron detachment from negative ions [4] is based on the Frank-Condon principle. The potential energy for the negative ion and an atom or molecule in the residual gas can be expressed as $U_i(R)$ where R is their separation; a similar function $U_d(R)$ describes the neutral atom in

the vicinity of the gas species. Below some critical radius R_{cr}, $U_i(R)$ rises above $U_d(R)$ and the negative ion suffers electron detachment. The cross section for this process is given simply by:

$$\sigma_{det} = \pi R_{cr}^2 (1 - U(R_{cr})/E) \qquad (2.2.1)$$

where E is the energy of the incident ion. The cross section will also drop off at high energies as the time spent with $R < R_{cr}$ drops below the characteristic time for the detachment reaction.

The value of R_{cr} itself is difficult to predict with any degree of certainty, although calculations made for H^- ions travelling through O_2, N_2 and H_2 agree well with experiments [5].

At high energies the ions with which we are dealing are multiply charged. The cross section for electron detachment from such ions is well modelled by the theory of electronic evaporation. If the positive ions are in their equilibrium charge state then the cross sections for further electron loss will be small. (For a discussion of charge state distribution theory, see [6].)

The low energy cross sections are well described by the formula of Firsov [7] which is semi-empirical and based on a semi-classical statistical description of the detachment process. If the energy for this reaction is E_i, then the cross section for the reaction is given by:

$$Q_i = Q_i^0\{(v/v_0)^{1/5}-1\}^2 \qquad (2.2.2)$$

where:

$$v_0 = 2.9 (Z_a + Z_b)^{-5/3} a_0 E_i / \hbar$$

$$Q_i^0 = 39 (Z_a + Z_b)^{-2/3} \pi a_0^2$$

Z_a, Z_b : atomic numbers of the species

a_0 : Bohr radius

In addition to this, the states of ionisation can be changed by charge transfer reactions. The semi-empirical theory which describes this process was developed by Firsov and by Rapp and Francis [8,9].

The transfer cross sections for symmetrical charge exchange given by this theory are:

(2.2.3) $$Q_{tr} = \pi p_0^2/2 + \pi^3 p_0/16$$

where

p_0 : $p_0^3 \exp(-2 p_0) = \pi v^2 \hbar^2/8A^2$

v : relative velocity

A = e^2/a_0^2

= $(E_i/E_H)^{1/2}/a_0$

E_i : ionisation energy or electron affinity

E_H : ionisation energy of hydrogen

In practice, in a ion beam one is frequently not concerned with symmetric charge transfer. At high energies the cross sections for symmetric and asymmetric charge transfer converge. Rapp and Francis discuss the general theory of asymmetric charge transfer.

If very precise cross sections are required then it is essential that all three processes are considered together; however in this discussion only rough cross sections are required and so the interaction of these processes will not be considered in any calculations done here.

2.3. Ionisation of the Gas Molecules

In general, the ionisation of gas molecules is a very difficult theoretical problem. However, there is some relevant experimental data for the production of ions in various gases over a range (0 to 50 keV) of incident ion energies [10,11,12]. This data is based on hydrogen and helium ions, and shows that the total cross sections for the production of positive ions from CO_2, O_2, N_2 and other small molecules are all fairly constant at around 10^{-19} m^2. Without particular measurements on, for example, C^- ions, it is hard to say more than that one expects the corresponding cross sections to be slightly larger, but of the same order of magnitude.

At higher energies, when the velocity of the ions exceeds that of the electrons in the residual gas molecules, the energy loss per unit length is given by the semi empirical equation of Bethe (see [13]):

$$(2.3.1) \qquad -\frac{dE}{dz} = \frac{P\ N_A\ Z}{V_m} \frac{z^2\ e^4}{(4\pi\varepsilon_0)^2 m_e v^2} \left(\ln\left(\frac{2m_e v^2}{I(1-\beta^2)}\right) - \beta^2 \right)$$

where:

z	:	charge of the ion
v	:	velocity of the ion
β	=	v/c
I	=	$9.1\ Z\ (1 + 1.9\ Z^{-2/3})$ eV
Z	:	atomic number of the residual gas

This energy loss is due almost entirely to the interaction with electrons; the energy loss due to interactions with nuclei is smaller by a factor of approximately $Zm_e/(2m_u)$ which is of the order of 10^{-3}.

3. The Practical Effects of Gases in the Vacuum

There are essentially five different practical effects which need to be considered in relation to gases when discussing AMS:

1. the attenuation of the ion beam
2. the deterioration of the beam quality
3. the stripping of the ions at the terminal of the accelerator
4. the loss of energy of particles in gas filled detectors
5. the production of secondary ions by the beam

Each of these effects will be considered in turn.

3.1. Beam Attenuation

It is clearly important that as much of the beam as possible is transmitted through the ion optical system. However, beam attenuation can take place through large angle scattering, electron detachment and charge transfer.

At low energies the cross section for large angle scattering can be shown to be very substantially less than the cross section given by the Rutherford scattering formula because of the effect of the electron clouds in screening the two nuclei. With a beam energy of 20 keV this gives the cross section for scattering at angles greater than 10 mrad from oxygen nuclei as 1.5×10^{-20} m^2.

Charge transfer from negative ions is very dependent on the particular molecular species found in the residual gas. As has already been stated, the principal constituent of the residual gas is water vapour and, as H_2O^- does not exist, this mechanism is not important over most of the beam line. However, in some tandem accelerators, oxygen is used as a stripper gas and

is, consequently, the most abundant gas in the accelerator tubes. Cross sections for charge transfer to oxygen molecules are of the order of 10^{-20} m^2.

Electron detachment will normally be the dominant effect and for molecules such as H_2O and O_2 the cross sections at low to intermediate energies will be about 1×10^{-19} m^2.

The total cross section for these three effects will therefore be approximately 1×10^{-19} m^2. The implications of this are very important: in the main part of the injection beam line where pressures are typically 10^{-9} atmos., the attenuation rate is only about 0.003 m^{-1}; however, if a terminal pump is not used to recirculate the gas used for stripping, the pressure in the low energy accelerator tube can be fairly high resulting in very significant losses from the beam. As an example of this, the Oxford radiocarbon facility has been operated for a long time with tube pressures of around 10^{-8} to 10^{-7} atmos. which gives an attenuation rate of about 3 to 30% per metre. The total attenuation before the stripper has been measured to be about 20%, which is in line with this as the tube length is about two metres. Because the cross sections for all of these processes are velocity dependent these interactions with the residual gas are a source of isotopic fractionation.

After the stripper canal, the positive ion can be removed from the effective beam by charge exchange, ionisation or large angle scattering. However the cross sections for these reactions will all be much smaller at the higher energies, and thus the beam attenuation will not be significant in comparison to the beam loss at low energies. At energies above 100 keV the cross sections for charge exchange drop off as v^{-12}, and at still higher energies as v^{-11} [14].

3.2. Reduction in Beam Quality

Scattering is responsible for a reduction in the quality of the beam. As stated in the chapter on ion optical theory, Liouville's theorem does not cover interactions which affect the beam particles individually rather than by way of a macroscopic field. The effect of scattering is to increase the volume of phase space associated with the beam which clearly has important implications for the transmission of the beam through the rest of the system. One aspect of this is that the 'halo' surrounding the beam is increased in intensity, making the resolution of isotopes and isobars more difficult.

The low angle scattering cross sections at low energies are fairly difficult to estimate. It is, however, reasonable to assume that the cross section for collisions in which the scattering angle is greater than a few milliradians (and consequently likely to alter the position of the particle in the phase space appreciably) will be of the order of $\pi \times 10^{-20}$ m^2 (see equation (2.0.2)). At pressures of around 10^{-9} atmos. this gives an interaction rate of 0.001 m^{-1} and without a stripper pump in the terminal of the accelerator it gives a rate of 0.03 m^{-1} at the entrance to the accelerator. Over the entire injection system the proportion of the beam being affected in this way will be only a couple of per cent, which is hardly significant. Multiple low angle scattering will probably be most important and the effect of this will be dominated by events which take place in the stripper canal. Here the thickness of the stripper gas should be of the order of 2×10^{19} m^{-2} [15] which corresponds to a pressure of about 0.75×10^{-6} atmos. of oxygen for a stripper one metre long. It is necessary to treat this process statistically and so a Monte Carlo calculation has been carried out for the particular case of interest. More general calculations have been carried out by others using the Thomas-Fermi and Lenz-Jensen potentials and employing wholly analytical methods [16].

The value of a Monte Carlo calculation is that it enables one to look at the expected effect on the brightness distribution in phase space. The conditions assumed for this calculation are:

stripper length	=	1 m	
stripper gas pressure	=	0.75×10^{-6} atmos.	
stripper gas	:	$^{16}O_2$	
scattered species	:	^{12}C	
scattering potential	:	U(r)	[see equation (2.1.3)]
a	=	1.5×10^{-10} m	
beam energy	=	1.8 MeV	

The program for this calculation splits the stripper into 1 mm lengths (and assumes that there are no multiple collisions within such a region). The initial trajectory for ions entering the stripper is axial (ie. $q_x = q_y = p_x = p_y = 0$), and so the initial beam emittance is assumed to be zero. Random interactions with the calculated probability distributions are assumed, thereby allowing the distribution of final trajectories to be deduced. The distribution shown in figure 1 represents slightly more than 250,000 trajectories for ^{12}C ions. The contours mark 10% increments in the proportion of the beam enclosed, and the implications of this for emittance growth can be seen in figure 2 which shows the emittance enclosing percentages of the final beam for the three carbon isotopes normally measured. Given that the initial emittance was zero, this gives some indication of the emittance growth; the increase in emittance is about 50% of that measured for ion beams produced by the ion sources discussed in part II of this thesis, and is therefore very significant. The effect will be substantially higher for the heavier isotopes, and is therefore a source of possible fractionation.

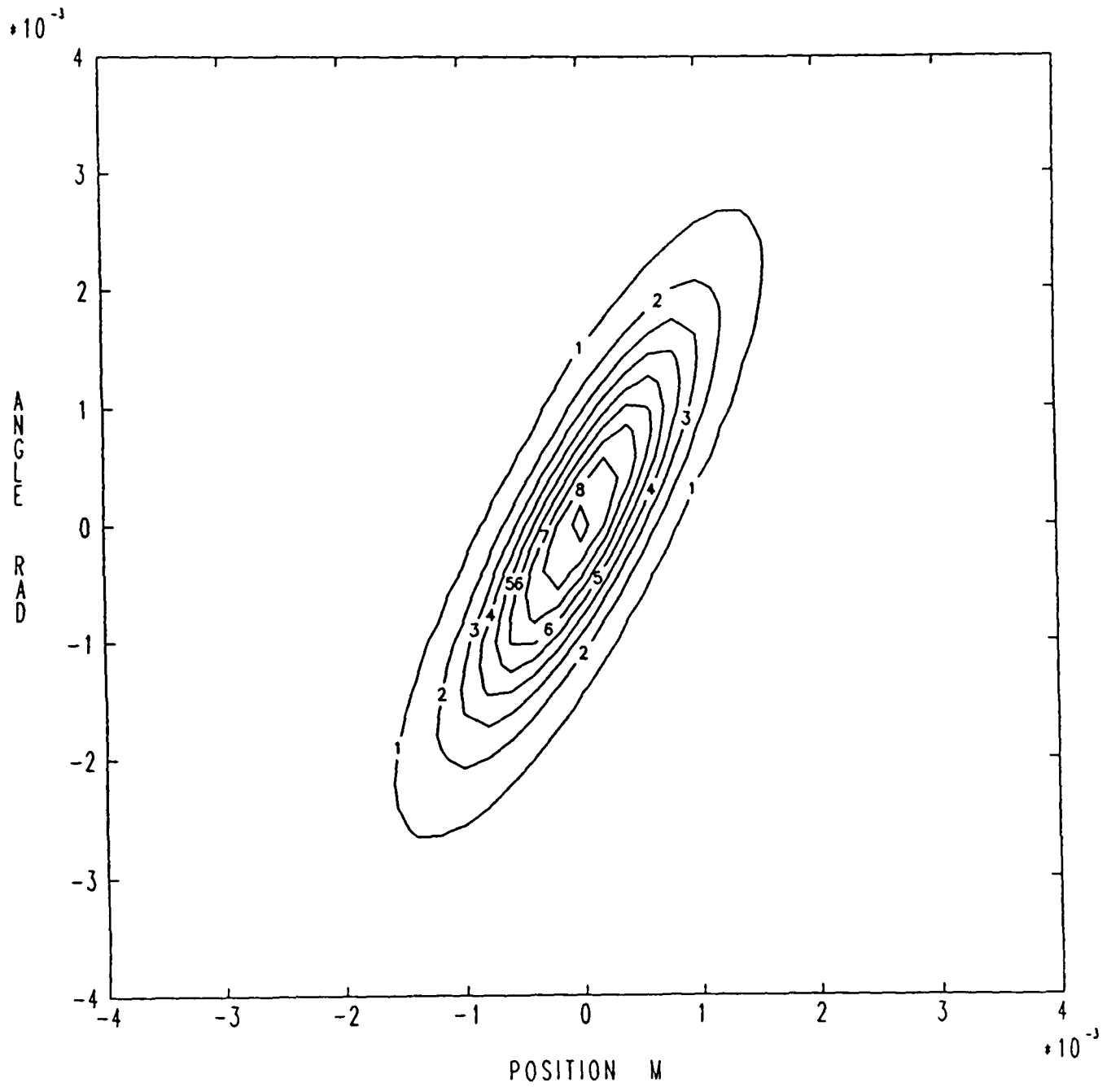

Figure 1

Emittance profile of a zero-emittance ^{12}C beam after scattering in a gas stripper

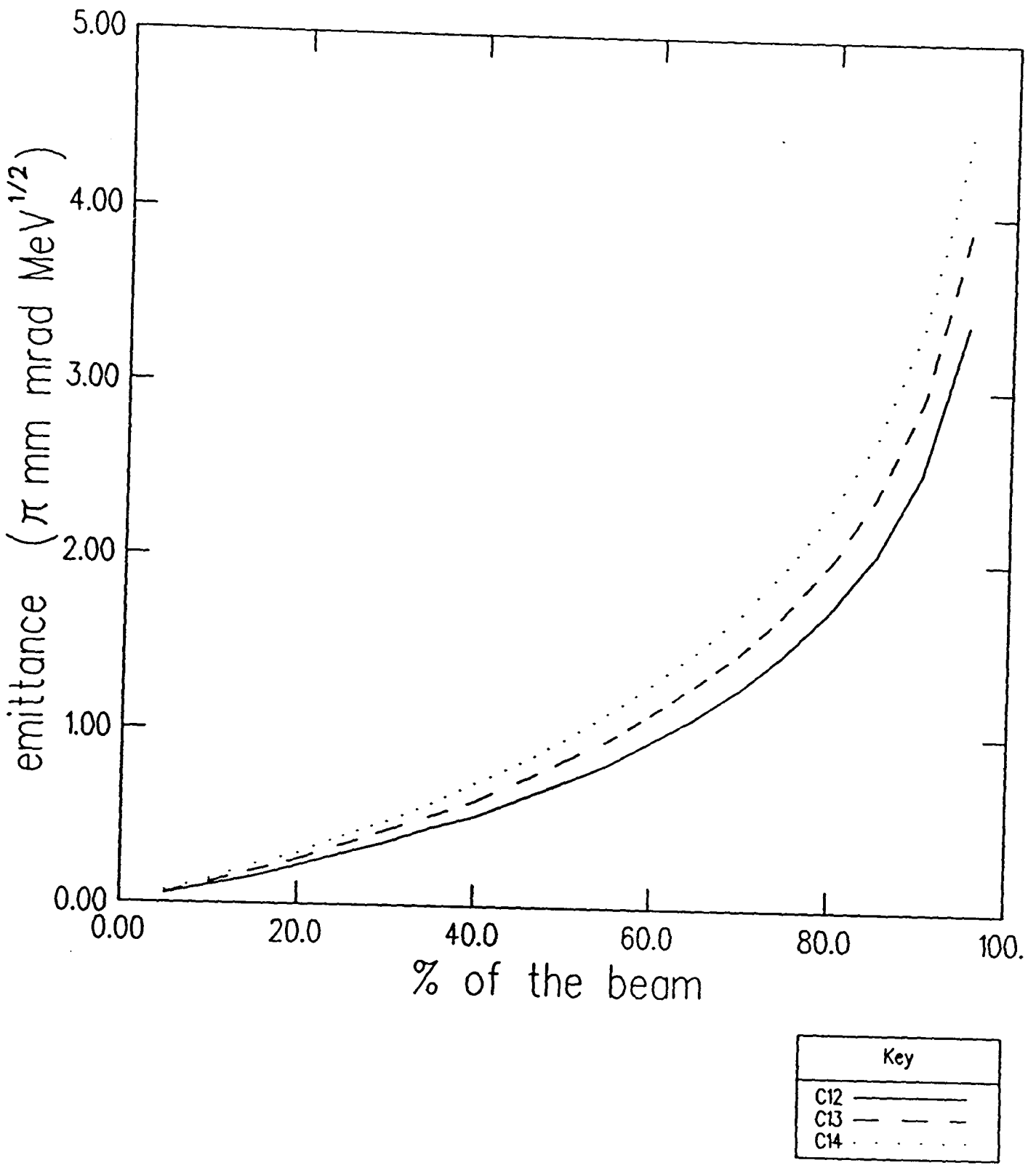

Figure 2

Emittance growth caused by scattering in a gas stripper for ^{12}C, ^{13}C, and ^{14}C

In addition to scattering, energy straggling will also reduce the quality of the beam (see ref. [16]).

There is another region of an AMS system in which scattering from the residual gases can be very important. This is in the high energy section of the beam line where the final separation of ions is taking place. Scattering here contributes significantly to the 'tails' of the beams that are being separated out, and can contribute significantly to the background measurements of, for example, radiocarbon. At the Oxford radiocarbon facility a reduction in the number of ^{13}C ions entering the detector was effected by adding an extra turbo-molecular pump close to the analyser magnet. Scattering was responsible for the fact that ^{13}C ions (from the break up of $^{13}CH^-$) which should have been removed from the path of the ^{14}C beam continued to travel in that direction.

To understand the mechanism for this effect we can use the differential cross section from equation (2.1.5). The angular acceptance of the detection system is roughly 10^{-5} rad^2, and the angular separation of the ^{13}C and ^{14}C beams in the Oxford analyser magnet is of the order of 0.01 rad. From equation (2.1.5) this gives us a cross section of 6×10^{-28} m^2. With a pressure of 10^{-9} atmos. the probability of such an interaction taking place within the magnet is about 8×10^{-10}. Given beam currents of about a nannoamp, there will be several particles directed towards the detector every second. Because of further velocity filtering, clearly not all of these will enter the detector, but as the scattered ions are not well collimated the Wien filter will not be very effective. Ideally this problem would be entirely solved by using a detector which could discriminate between the ions.

Scattering can also be put to positive use in the high energy section of AMS systems by the use of gas filled magnet detectors [17].

3.3. The Stripping Process

Obviously one of the most important regions of interaction between the beam and gas molecules is the stripping which takes place at the terminal of a tandem accelerator (assuming a foil stripper is not being used).

The subject is dealt with in detail elsewhere [6,18] and fortunately there are very good measurements for carbon ions passing through an oxygen stripper [15] which is the arrangement found in many radiocarbon accelerators.

When operating at voltages below the optimum for the particular charge state that is being used there is considerable fractionation in this process. This effect can, however, be corrected for by the use of standards. More important, therefore, is the observation that if one is operating at a stripper pressure which is below that which ensures an equilibrium charge state distribution, the fractionation will alter with small changes in the gas thickness and the transmission will alter very rapidly with gas thickness.

One effect not discussed elsewhere is the effect of the high energy beam on the stripper gas. Using equation (1.3.7) and assuming a $^{12}C^-$ current of 20 μA with a radius at the stripper of 2 mm, the parameter θ_{min} works out at about 2×10^{-4} rad and the rate of energy transfer to the gas nuclei is 2.53×10^{-19} Js^{-1}. Assuming that the stripper gas molecules have thermal velocities of about 300 ms^{-1}, their lifetime within the stripper will only be about 0.003 s and so within this period the average energy gained by a residual gas molecule from ionic collisions will be about 8×10^{-22} J which corresponds to an effective temperature rise of 60 K (although obviously there will not be a thermal velocity distribution). The mean free path of oxygen molecules at 1.5×10^{-6} atmos. is about 0.1 m and so the scattered molecules should come into equilibrium with the surrounding gas fairly rapidly (within their lifetime in the stripper).

Because the gas stripper thickness is controlled by maintaining a constant flow of gas, the effective temperature rise of 60 K which takes place if a 20 μA current is injected will result in a drop of about 10% in the stripper thickness. If the stripper gas pressure is below the optimum, this will greatly reduce the $^{12}C^{3+}$ yield relative to the $^{13}C^{3+}$ and $^{14}C^{3+}$ yields, and thereby introduce a current dependent fractionation relative to the high current isotope.

3.5. Gas Detectors

The subject of ionic interactions with gases also impinges on the methods used for detection. There is no new material presented here on this topic but it is mentioned for completeness (For a general discussion of the topic see [19].)

The most common sort of gas detector used in AMS is the gas filled 'ΔE, E' detector [20]. The rate of loss of energy experienced by an ion passing through a gas is dependent on the ion's velocity and charge. This is shown by the form of the equation (2.3.1). In the 'ΔE, E' detector the number of ions formed per unit length is determined just after the ion has entered the detector (sometimes this is done for several parts of the trajectory), and then the total number of ions formed in the detector is measured. The number of ions formed per unit length gives the energy loss per unit length, and therefore the velocity, while the total number of ions formed yields a measure of the total energy of the ion, and together they give the charge.

Another type of detector which hitherto has not been used in this field but which looks promising for the separation of high atomic number isobars [21] is the gas filled magnet detector [17]. This makes use of both multiple scattering and multiple charge changing reactions to give trajectories specific to different isobars.

3.6. Gas Ionisation and Space Charge Neutralisation

The ionisation of the residual gas is important because of the influence that it has on the space charge effect discussed in the previous chapter. This effect will be considered only for the low energy beam where the space charge is most important.

As discussed in section 2.3., the cross sections for the production of positive ions from the residual gas molecules will be of the order of 10^{-19} m^2. With gas pressures of 10^{-9} atmos. this gives an ion production rate per unit length of:

(3.6.1)
$$R = (I\ P\ N_A\ \sigma)/(q\ e\ V_m)$$
$$= 1.68 \times 10^{16}\ I\ m^{-1}s^{-1}$$

where I is the beam current and q is the ionic charge.

The principle of space charge neutralisation is essentially very simple: the potential well, formed by the (in this case negative) ions of the beam, traps ions formed in the residual gas, thereby decreasing the depth of the potential well and effectively neutralising the space charge forces. For neutralisation to take place there must be as many ions formed in the residual gas per unit length as there are in the beam. Consider, for example, a $^{12}C^-$ beam of current I and energy 20 keV; the number of ions per unit length is $1.1 \times 10^{13}\ I\ m^{-1}$. The time for this number of ions to build up in the residual gas is 6.6×10^{-4} s. In general this time constant will be:

(3.6.2)
$$\tau = (q\ V_m)/(v\ P\ N_A\ \sigma)$$

where v is the ion velocity.

There are four effects to be considered which interfere with the space charge neutralisation. Firstly, if the high intensity beam is pulsed with a time constant of the order of τ or less, then the distribution of ions produced from the residual gas will not have time to build up. Secondly, as the ions will have a thermal velocity distribution, the potential well will not be fully populated by them. Thirdly, the voltage gradients associated with the space charge of the ion beam are not very large and therefore if there is an external electric field, the ions produced in collisions will be removed. Finally, although if the neutralisation is almost complete the wave functions of the residual gas ions overlap almost exactly with the charge density of the beam, this will not be the case if, for the reasons given above, the neutralisation is incomplete.

In order to get some idea of the depth of the potential well that we are dealing with, consider a uniform ion beam of radius (a) enclosed in a grounded cylinder of radius a_0. The potential at radius r (assuming cylindrical symmetry) will be:

$$V(r) = \frac{I}{2\pi\varepsilon_0 v} \ln\left(\frac{a_0}{r}\right) \qquad r > a \tag{3.6.3}$$

$$V(r) = \frac{I}{4\pi\varepsilon_0 v} \left(\frac{a^2-r^2}{a^2} + 2\ln\left(\frac{a_0}{a}\right)\right) \qquad r < a \tag{3.6.4}$$

which gives a maximum depth at the axis of:

$$V_{max} = \frac{I}{4\pi e_0 v} \left(1 + 2\ln\left(\frac{a_0}{a}\right)\right) \tag{3.6.5}$$

Let us then consider the four effects which interfere with the neutralisation:

a. Frequently in AMS it is not desirable to inject the high current isotope into the accelerator continuously, both because of the loading on the terminal voltage, and because of the difficulties in subsequently separating the rare isotope from the more abundant ones. It is, therefore, often the practice to pass the abundant isotopes through the accelerator in short pulses in order to establish a ratio. Because it takes a time τ (see equation (3.6.2)) for the neutralising ion density to build up, the space charge effect will remain important unless the pulse length is much longer than τ, even if all of the requirements for neutralisation are met.

b. The ions formed from the residual gas will have thermal velocities of the order of $(2kT/m_{ion})^{1/2}$ and, as ions are contained in a region with dimensions of about (a), it is possible to give a characteristic frequency for the motion of the ions within the potential well formed by the ion beam. This is $(2kT/m_{ion}a^2)^{1/2}$ where m_{ion} is the mass of a molecular ion. Furthermore, we know that the mean lifetime of a residual gas ion in the neutralising plasma is τ, and so, assuming a Boltzmann distribution for the ionic velocities, the mean potential energy of the ions must be approximately:

$$V = - kT \ln((\tau/a)(2kT/m_{ion})^{1/2}) \qquad (3.6.6)$$

Considering, for example H_2O^+ ions formed in residual gas of pressure 10^{-9} atmos. at a temperature of 293 K with a beam radius of 4 mm, the mean potential energy of the ions in the neutralising plasma will be approximately 0.17 eV. This implies that there is a residual space charge effect with a potential well depth of about 0.17 eV, whereas from equation (3.6.5) we know that the unneutralised well depth for a

20 μA current might be as little as 0.32 eV (depending on the radius of the enclosing grounded structure). The details of this thermal effect are very difficult to calculate since they depend critically on the effective radius of the beam and on the geometry of the surrounding structure. However, it is clear from these calculations that, with the kinds of currents and energies that we are dealing with, the thermal motion of the ions in the plasma will greatly reduce the effectiveness of the neutralisation.

c. So far it has been assumed that there are no other electric fields except those due to the space charge of the ion beam and the plasma created by it. However, the electric field gradients due to these effects are really very small (typically of the order of 100 Vm^{-1}), and so any external electric fields that are likely to be encountered at, for example, gridded lenses and suppression electrodes, will totally disrupt the potential well in which the plasma is contained and if space charge neutralisation is to occur anywhere near these, careful attention must be paid to the screening of the beam line.

d. In the situations in which space charge is normally considered to be important, the confining potentials are substantially larger than those with which we have to deal. Our interest in space charge is due to the subtle changes that it can make in the distribution of the ion beam in the phase space, whereas the subject is normally tackled in situations where the effect is rather more drastic. In such cases, assuming that the beam is not pulsed with a period smaller than the time constant for the build up of the ions in the plasma, it is frequently possible to make neutralisation virtually complete. (See, for example ref. [22], for the treatment of these cases.) It is then

possible to assume a detailed correspondence between the charge distributions in the plasma and the beam thereby making it possible to define the degree of neutralisation, f, which is some fraction close to, but below, unity. However, once the neutralisation falls below unity, and particularly if it is far from unity, as it is in this case, there is no longer a direct correspondence between the two charge distributions. The distribution of the ions in the plasma is governed by their energy distribution and this, in turn, depends on where in the potential well the ions were formed (a consideration that does not arise if the potential well has been almost neutralised). The effect of this is, in general, that the plasma charge distribution will be rather less well localised than the charge distribution of the beam, so that it is no longer possible to give a meaningful value for f; the space charge forces will be reduced somewhat by the partial neutralisation, but their functional dependence will also alter. Mathematically the problem becomes totally intractable.

It is therefore clear, that in the conditions that prevail in a typical injection system for AMS, we do not expect space charge neutralisation to be complete, but we do expect it to play some part in the transport of the beam as was found with the ion source test bench. Unfortunately, a full mathematical treatment of the plasma distribution is not feasible and so one can only assume that the straight-forward space charge calculations outlined in the previous chapter put an upper limit on the scale of the effect, and will almost certainly give results which are in fairly good agreement with the physical reality. In relating the measurements made on the ion source test bench (where the neutralisation factor was found to be about 0.9) to the calculations which are to be carried out on the accelerator system, it should be remembered that the

residual gas pressure is an order of magnitude lower on the latter. This will reduce the neutralisation factor considerably, and a value of 0.5 will be assumed for a stable beam and 0 for a pulsed beam in the calculations which are presented in chapter 8.

Summary

Theories and measurements have been discussed which relate to scattering and charge changing reactions. Using this material, the practical effects of residual gases on the ion beam are investigated.

Beam attenuation is found to be greatest in the region just before the gas stripper (ie in the low energy accelerator tube) where electron detachment from the negative ion is the dominating effect. This demonstrates the necessity for stripper gas recirculation. Attenuation is a possible source of fractionation as the reaction cross sections are velocity dependent.

Scattering is also a source of fractionation as there is a large mass dependence. The emittance growth from this mechanism occurring in the stripper canal is found to be a substantial proportion of the total beam emittance. This is an important effect because anything which introduces differences in the brightness profiles for different isotopes makes variable fractionation possible if any changes to the beam occur.

Scattering is also important in the high energy beam line where it can result in spurious ^{14}C counts. This can be remedied by improving the vacuum quality or by using more discriminatory detection techniques.

The stripping process is also a source of fractionation and, as the gas is appreciably heated when high currents are injected, the fractionation will be dependent on the current if the gas pressure is below optimum.

Space charge neutralisation is discussed in some detail and the reasons for expecting the neutralisation to be incomplete are presented. This process is, however, found to be too complicated for analytical investigation.

References

[1] L.I. Shiff, Quantum Mechanics (3rd ed.) (McGraw-Hill, Tokyo, 1968) p. 289.

[2] B.H. Brandsen and C.J. Joachain, Physics of Atoms and Molecules (Longman, London, 1983) p. 507.

[3] B.H. Brandsen and C.J. Joachain, Physics of Atoms and Molecules (Longman, London, 1983) p. 599.

[4] B.M. Smirnov, Negative Ions (McGraw Hill, New York, 1982) p. 71.

[5] H.S.W. Massey, Negative Ions (3rd ed.) (C.U.P., Cambridge, 1976) p. 607.

[6] K.B. Winterbon, Nucl. Instr. and Meth. 144 (1977) 311.

[7] O.B. Firsov, Soviet Phys. J.E.T.P. 36 (1959) 1076.

[8] H.S.W. Massey, Negative Ions (3rd ed.) (C.U.P., Cambridge, 1976) p. 583.

[9] D. Rapp and W.E. Francis, J. Chem. Phys. 37 (1962) 2631.

[10] R. Browning and H.B. Gilbody, J. Phys. B 1 (1968) 1149.

[11] R. Browning, C.J. Latimer and H.B. Gilbody, J. Phys. B 2 (1969) 534.

[12] R. Browning, C.J. Latimer and H.B. Gilbody, J. Phys. B 3 (1970) 667.

[13] E. Segre, Nuclei and Particles (2nd ed.) (Benjamin/Cummings, Reading, Massachusetts, 1977) p. 28.

[14] B.H. Brandsen and C.J. Joachain, Physics of Atoms and Molecules, (Longman, London, 1983) p. 549.

[15] H.J. Hofmann, G. Bonani, E. Morenzoni, M. Nessi, M. Suter and W. Wölfli, Nucl. Instr. and Meth. B5 (1984) 254.

[16] P. Sigmund and K.B. Winterbon, Nucl. Instr. and Meth. 119 (1974) 541 (also see erratum, Nucl. Instr. and Meth. 125 (1974) 491).

[17] C.B. Fulmer and B.L. Cohen, Phys. Rev. 109 (1958) 94.

[18] H.D. Betz, Rev. Mod. Phys. 44 (1972) 465.

[19] J.B.A. England, Techniques in Nuclear Structure Physics, (Macmillan, London, 1974) p. 419.

[20] J.B.A. England, Techniques in Nuclear Structure Physics, (Macmillan, London, 1974) p. 466.

[21] W. Henning, B. Glagola, J.G. Keller, W. Kutschura, Z. Liu, M. Paul, K.E. Rehm and R.H. Siernssen, Workshop on Techniques in A.M.S., Oxford Radiocarbon Accelerator Unit (1986) 196.

[22] A. Septier (ed.), Adv. Electron. Electron Phys., Suppl 13 part C (1980).

Chapter 7

Computer Programs

Introduction

In this chapter the computer programs that have been developed for ion optics calculations will be described. It has long been evident that the first order treatment of accelerator systems intended for AMS was insufficient, since ion beams that should be well matched to the accelerator acceptance under the first order approximation cannot be made to pass through with 100% transmission. This means that the transmission (and isotope ratios) are likely to be sensitive to variations in the ion beam emittance. Perhaps more seriously, the ion beam transmission seems to be current dependent and this may well be related to the effect of space charge on the ion beam transport (see chapter 5). In order to investigate these effects, and to establish methods of circumventing them, a series of programs has been developed which calculates the phase space transformations that take place during the ion beam transport taking account of aberrations and space charge effects.

The three main programs are: one to carry out the phase space transformation calculations; a second to trace ion trajectories through various types of lens and to fit the phase space transformations to a polynomial expression and finally a program to display the ion beam profiles in phase space.

The tracing of trajectories through individual optical elements is not new and much more generally applicable programs exist (for example [1]). The importance of these programs lies in their ability to investigate the performance of an entire system once the properties of individual elements

have been ascertained.

All of these programs are written in VAX/VMS Fortran 77 running under the VAX/VMS version 4.4 operating system.

1. Phase Space Transformations

The fundamental assumption underlying these programs is that the phase space can be adequately represented in only two dimensions. The way in which this approximation is treated is slightly different in the different parts of the program. In the sections dealing with space charge effects the phase space is assumed to be separable, since calculations on the ion source test bench showed that this approximation gave phase space profiles very close to those measured (see chapter 3). However in the lens systems, which are normally cylindrically symmetric, skew rays are ignored because this is the only way of rendering the calculations tractable and because, at lenses, the ion beam is usually far from a waist this is actually a fairly good approximation. The most important shortcoming in the two dimensional description of the beam is that the energy spread of the ion beam is ignored. This is particularly important where magnetic analysis takes place. There are, however, techniques for including this effect once the geometric calculations have been carried out (see chapter 8).

1.1 The Phase Space

The phase space is represented by a 2 x 41 x 21 array which carries the position and angle of single 'rays' to be traced through the optical system. The initial values of this array are taken to be a grid of points in a rectangular region of phase space (the range of this rectangle being set by the program user). Thus, one might have the set of values shown in table 1.1.1 for the range 4 mm, 40 mrad (where the angle is shown in curly

brackets). The symbols i and j represent the position and angle indices of the phase space. It will be noticed that the rectangle in phase space is to one side of the beam axis; this is because all transformations are assumed to be symmetric for a sign change in both position and angle, and so this ensures that there is no redundancy in the calculations.

j \ i	1	2	3	4	21	41
1	-4.0	-3.8	-3.6	-3.4	0.0	4.0
	{0.}	{0.}	{0.}	{0.}	{0.}	{0.}
2	-4.0	-3.8	-3.6	-3.4	0.0	4.0
	{2.}	{2.}	{2.}	{2.}	{2.}	{2.}
3	-4.0	-3.8	-3.6	-3.4	0.0	4.0
	{4.}	{4.}	{4.}	{4.}	{4.}	{4.}
4	-4.0	-3.8	-3.6	-3.4	0.0	4.0
-	{6.}	{6.}	{6.}	{6.}	{6.}	{6.}
-						
-						
21	-4.0	-3.8	-3.6	-3.4	0.0	4.0
	{40.}	{40.}	{40.}	{40.}	{40.}	{40.}

Table 1.1.1
Example of initial phase space positions

Associated with each of these rays there is an ion beam brightness value. Because of Liouville's theorem (see chapter 1) this remains the same under transformations of the phase space (assuming separability). The values for this brightness array are read in from a file specified by the user.

The purpose of the program is to calculate what happens to an ion travelling on each one of these paths.

1.2. First Order Transformations

As it is not always necessary to consider the aberrations due to every optical element in the system, one must be able to perform first order transformation on the phase space. To do this the code for the computer

program OPTRYK [2] was converted into a subroutine. This allows files created by OPTRYK for sections of beam line to be used for performing linear transformations on the phase space.

1.3. Aberrating Elements

In order to perform the transformations necessary for aberrating systems the parameters for a function of the type described in equation (4:2.4.1) are read in from a data file, and this function is used to perform the calculations. The parameters which best fit the performance of a particular system are found by a separate program described in section 2. The use of this function is essential in order to keep the CPU time requirements of the program within reasonable limits.

1.4. Space Charge Effects

In order to treat the effect of space charge on the ion beam transport through regions in which the ions are drifting, each drift length is split up into a number of short lengths (this is set to be 100 because increasing the number of divisions beyond this was found to make no difference to the results of the calculations on the systems with which the program was tested). First of all, the radial charge distribution is determined in 0.1 mm steps (assuming separability). Then, for a particular point in phase space that is to be transformed, the amount of charge closer to the axis is estimated from the charge distribution using cubic interpolation. The next stage is to determine the radial electric field using the methods outlined in chapter 5. Having done this, the transformation of the point in phase space under consideration can be found. This calculation is done for each point and then the entire process repeated for each of the short lengths.

The program is not designed to make any assumptions about space charge neutralisation and therefore the user must reduce the currents used for the

calculation by the neutralisation factor, always remembering the caveat from chapter 6 that the electric field distribution will not necessarily be the same if partial neutralisation is taking place.

1.5. Accelerating Regions

Although, strictly speaking, this could be performed by the OPTRYK code, it was found to be more convenient to deal with accelerating sections of beam line separately. Uniform fields in the axial direction are assumed. As yet, space charge has not been included although this could be important for very high ion beam currents since no neutralisation takes place in the accelerator tubes. However, if the neutralisation outside the accelerator is only partial, as it is for small ion beams, the space charge effect in the accelerating regions will be small in comparison because of the greater velocity of the ions.

For the exit and entrance lenses formed at either end of an accelerator tube, the code described in section 1.3 must be used, and the program described in section 2 is capable of dealing with this type of lens.

1.6. Data Output

Once the phase space has been transformed there is the problem of what to do with the data. There are three options which have been catered for:

a. A file containing the apertures in front of the ion source and in the region of the final point to which the phase space has been transformed can be read in from a data file. This is then used to calculate the ion beam transmission through both sets of apertures. In addition, to get some feeling for how critical the transmission through the final set of apertures is, a file can be created which

gives the transmission through the final apertures with a series of offsets; thus, for example, the value corresponding to 1 mm would give the transmission if the beam were misaligned by 1 mm. This procedure can be employed regardless of the complexity of the transformation.

b. Some simple transformations can themselves be approximated to an equation of the type described by (4:2.4.1). The program described in section 2 is capable of fitting such a function and so a file suitable for manipulation by that program can be produced as a result of the phase space transformation.

c. Finally, it is also possible to write out all of the final phase space co-ordinates to a file in a standard format. These co-ordinates can then be plotted as a distorted grid, showing the transformation directly (see section 3 below).

2. Lens Analysis and Function Fitting

The second computer program deals with the idealised lenses described in chapter 4 and with the fitting of phase space transformations to a function.

2.1. Phase Space Transformations for Lenses

In order to analyse the aberrations caused by a particular lens, 66 rays are traced through the lens. The initial phase space co-ordinates are chosen to cover a range similar to that with which the lens is expected to work, and are arranged in a fashion similar to the phase space array for the previous program (see table 1.1.1) except that this array is smaller, being only 2 x 11 x 6.

The electrical potentials are calculated using the expressions derived for the three idealised lens types described in chapter 4. The gridded lens and tube lens solutions are based on a series of Bessel functions. These series are evaluated to 500 elements and are sufficiently convergent to give phase space transformation results which are accurate to within 0.1% (estimated by looking at the effects of altering the number of elements in the series); the zeros of the first Bessel function used in the calculations have been calculated by a subsidiary program and are stored in a data file. The Bessel functions themselves are evaluated using the NAG routine S17AEF [3]. The potentials for the aperture lens are calculated to a precision of better than 0.1% using the NAG integrating routine D01AKF which is well suited to oscillating functions.

In order to trace particle trajectories through the lenses, the particle paths are divided into short steps in the axial direction. These steps get closer together as the centre of the lens is reached, where the field intensities are generally greatest. (The step lengths are given by $z^2/(200\ R) + R/50$, where z is the distance from the central plane of the lens and R is the radius of the lens.) The average fields are calculated over each of these steps and the particle trajectories thereby established.

The particle trajectories are scrutinised in this way over a region extending six lens diameters in each direction. The initial phase space positions are linearly traced back from the plane of the lens; thus, an initial phase space position of 4 mm, 40 mrad is taken to correspond to a particle trajectory such that, if the lens had no effect, the particle would arrive at this point in phase space when it reached the plane of the lens. The final phase space positions are treated in the same way. This means that in using these transformations (or functions fitted to them) in general calculations, the lenses can be treated as elements with no length. (This does not mean that a thin lens approximation is employed since the

results of the calculations are unaltered by the use of this method.)

The output from this section of the program consists of a file of 66 lines each with four numbers corresponding to the initial and final phase space positions of the 66 trajectories considered.

The results given in chapter 4 demonstrate the efficacy of this method.

2.2. Function Fitting

The phase space transformations are fitted to two functions of the type given in equation (4:2.4.1). The fitting is done using the NAG routine E04FDF [3] and the 18 coefficients of the polynomials are scaled to be of the order of one (this is necessary for the routine E04FDF to be able to function properly). In practice the coefficients c_1, c_3 and c_7 are fitted first and then all eighteen coefficients at once; this, together with the expected focal length of the system, gives the fitting function a sufficiently good starting point from which to work.

The trajectories to which the function is fitted are read in from a file of the type described at the end of section 2.1. This type of file can also be produced by the program described above (see section 1.6.b).

The sum of the squares of the deviations of the traced positions in phase space and those calculated by the function are also given by the program for each of the functions. From this a standard deviation can be calculated which indicates how good the fit is.

2.3. Future Developments

The next stage in the development of this suite of programs will be to allow trajectories to be calculated using the method of successive over-relaxation (probably by adapting an existing program). This will enable the characteristics of particular optical elements to be calculated, rather

than just those of the idealised generic lens types considered here.

3. Displaying the Results

There are two special types of display used in the presentation of the results from this suite of programs. These are contour plots of the brightness profiles in phase space, and plots of the destination points in phase space of the trajectories given by the first program described above (see section 1.6.c).

3.1. Contour Plots of Brightness Profile Measurements

The first function of this program is to plot the results of measurements made on the ion source test bench (see chapter II/1). These measurements are made on a 41 x 41 grid, and can be displayed using the NAG graphics routine J06GAF [4]. The program user can define the type of contours used; these are either integrated contours, in which case each successive contour contains 10% less of the total beam (ie. the lowest contour contains 90% of the beam, the next lowest 80%, et cetera), or else they represent 10% fractions of the peak brightness. In this thesis all of the contours are of the integrated type. In order to achieve this integration, the 1681 measurements are sorted by size and then added from the largest to the smallest, thereby discovering the level of contours required to enclose particular proportions of the beam.

It should be noted that, as the brightness profiles are approximately separable into the two dimensions x and y (see chapter 1), the overall transmission will only be 25% if a system which is symmetric in these two dimensions has an acceptance which allows it to transmit 50% of the beam when the x brightness profile alone is considered (and likewise for the y profile).

Examples of this type of plot are shown in chapter 3.

3.2. Contour Plots for Phase Space Transformations

As indicated in sections 1.6.b and 2.2., if a phase space transformation is sufficiently simple it is possible to fit it to a function in the manner described in section 2.2.. If this is done, the display program can use this fitted function to calculate the expected brightness profile in phase space at the final point in the phase space, given a function which describes the initial brightness profile of the ion beam. The function describing the initial brightness profile is taken to be a Gaussian, i.e. of the form:

$$g(q_x,a_x) = C \exp(-(q_x/pq)^2 - (a_x/pa)^2) \qquad (3.2.1)$$

where C is a constant and the parameters pq and pa are chosen to match the performance of the ion source under consideration.

The brightness profile is calculated on a 161 x 161 grid and again plotted using the NAG routine J06GAF [4] with the levels being calculated as above. (A 41 x 41 grid is used for the contour level calculation to reduce CPU time usage.)

3.3. Phase Space Plots

The program described in section 1 calculates the trajectories for particles with initial phase space co-ordinates which are arranged in a rectangular grid (see table 1.1.1.). The final points in phase space at which these trajectories arrive can be written out to a file (see section 1.6.c), and this display program can then plot these points on a phase space diagram. The ranges of the phase space diagram are chosen by the program user, and the points that represent trajectories which at the ion

source either had common angles or common positions are joined with a line. In addition to this, those points with an initial axial position are marked with an (x) while those with no initial transverse momentum are marked with a (+). Such a plot of the initial points in phase space would appear as a rectangular grid (see figure 1); any linear transformation will only shear, enlarge or rotate this grid, and so a good visual impression of the aberrations of the system are given by this type of plot. In order to evaluate such a plot it is also necessary to know the initial phase space points and everywhere that such plots are used in this thesis the initial phase space points are taken to have a range of $\pm$ 4 mm and $\pm$ 40 mrad (as shown in figure 1 or table 1.1.1). It will be noticed that, whereas a grid of only 41 x 21 phase space co-ordinates is used for calculations (because of the symmetries discussed in section 1.1.), a symmetric pattern of 41 x 41 points is actually plotted.

Summary

A series of programs has been written which is capable of calculating the phase space transformations which take place in an ion optical system. They take into account the aberrations caused by three generic types of lenses and by space charge effects during the ion beam transport.

These programs should be of particular value to those interested in producing very high transmission accelerator systems (i.e. with geometric transmissions of greater than 90%) for isotopic ratio measurements using AMS.

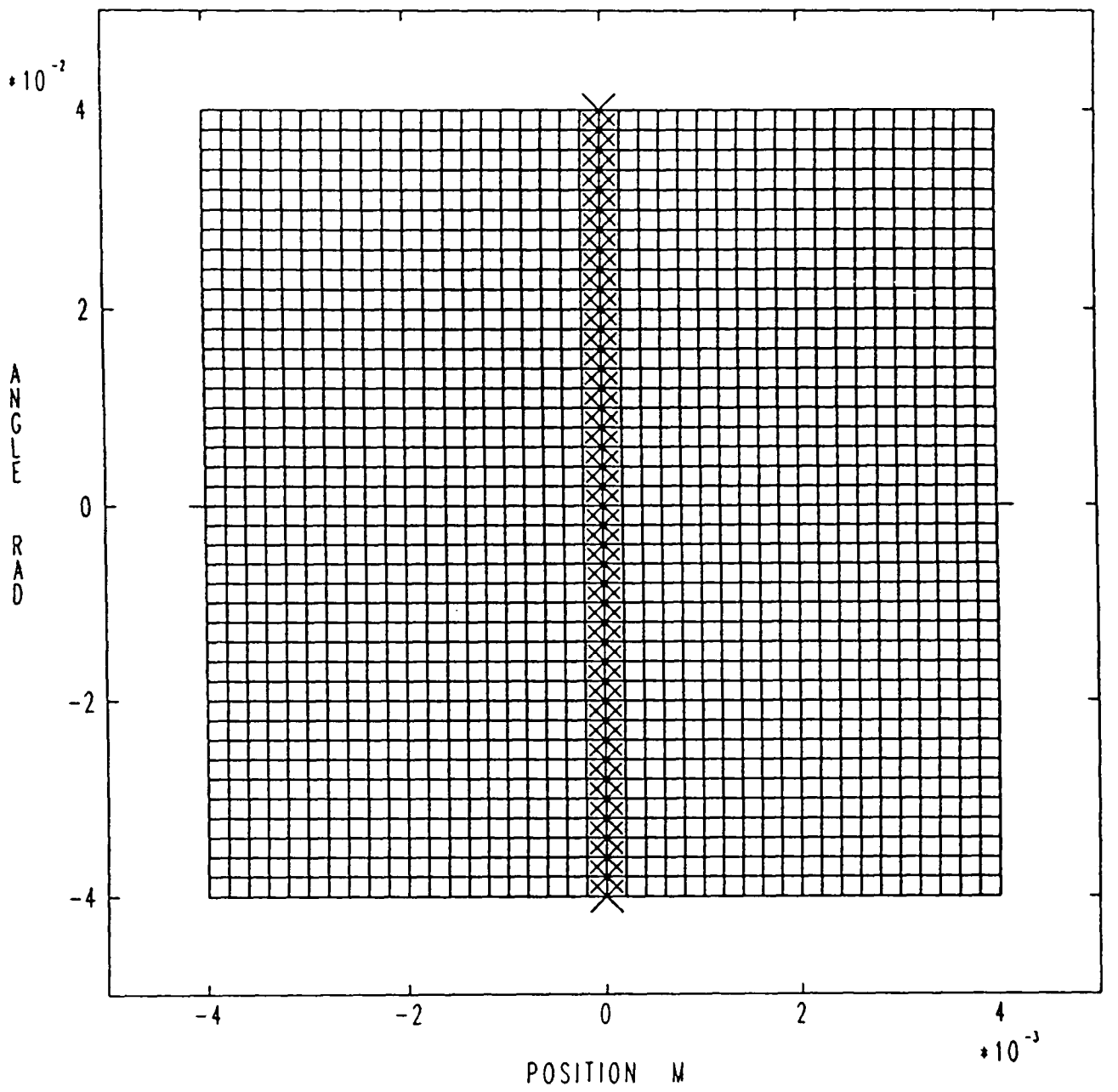

Figure 1

Phase space plot showing the initial points in phase space used for the calculations carried out in this thesis

References

[1] D. Dirmikis, Computer Program for Numerical Analysis of Electron Flow Systems, University of Sheffield, (1975).

[2] T.J.L. Greenway, Computer Program OPTRYK, Nuclear Structure Lab., Oxford University.

[3] NAG Fortran Library (Mark 12) (Numerical Algorithms Group Ltd, Oxford, 1987).

[4] NAG Graphical Supplement (Mark 2) (Numerical Algorithms Group Ltd, Oxford, 1985).

Chapter 8

Calculations

Introduction

In this chapter the results of the calculations that have been made on the transport of ion beams will be presented. These calculations are intended to investigate the physical processes underlying the observed behaviour of accelerator mass spectrometry systems so that criteria for design improvements can be established.

1. Calculations and Measurements on the Ion Source Test Bench

The emittance measuring capability of the ion source test facility described in chapter II/1 gives the opportunity for testing the assumptions made in the programs outlined in the last chapter. The results of these calculations have already been given in chapters 4 and 5, but it is worth drawing together the information that can be gleaned.

1.1. The Ion Beam

In chapter 1 the models that can be used to describe an ion beam in a two dimensional approximation were described. It transpired that the only feasible functional form for the brightness profile which would allow separability of the x and y dimensions of the phase space was the Gaussian form (see section 3.5.). The measurements and calculations on the ion source test bench indicate that the brightness profile of the ion beam emerging from a HISS type ion source (see chapter II/3) is well described by such a function (see chapter I/4), and the measured brightness profile

can be well reproduced using calculations based on the principles of separability. If instead one assumes that there are no skew rays, the calculated ion beam profiles are very different from those observed.

Measurements have been also been made on the modified UNIS ion source [1] currently in use on the Oxford radiocarbon accelerator system, but those made on this type of source indicate that the emittance area is much more variable (see section II/2:7) and that the shapes of the profiles are not as well defined. This is in line with the findings of others [1].

The brightness profiles at the sources are assumed to be of the form given in equation (7:3.2.1), and the parameters pq and pa which were found to give the best descriptions of the two sources are given in table 1.1.1.

Ion Source	pq	pa
HISS	0.58	23.2
modified UNIS	0.5	26.52

Table 1.1.1
Ion source parameters for equation (7:3.2.1)

These parameters are used for all of the calculations which have been carried out on the accelerator system, but on the ion source test bench where brightness profile measurements were available values of pq and pa which best fit the particular observations are used. We can actually learn something about the ion source from the ratio of these two parameters which best describes its performance. (See section II/3:7 for a more detailed discussion of this in relation to the HISS type of source.)

1.2. Aberrations

As indicated in chapter 4, the aberrations affecting the transport of the ion beam in the ion source test bench can be adequately modelled by

assuming that they come from the gridded lens which is present in the system. This gridded lens has a diameter of 70 mm and a focal length of 0.391 m. The coefficients of the function which is fitted to the phase space transformation produced by this lens are given in table 1.2.1. There are two functions (of the type described by equation (4:2.4.1)), one for the final position and one for the final angle; 18 coefficients are given for each of these. In addition to this, standard deviations are quoted; these give some indication of the quality of the fit. (See section 7:2.2. for a description of the program used to obtain this fit.) It should be noted that the coefficients are calculated on the basis of mm and mrad units.

coeff.	position	angle
1	1.00	-2.54
2	5.07E-05	0.99
3	6.68E-07	-7.25E-04
4	3.23E-07	1.62E-06
5	-5.43E-07	-5.62E-07
6	1.40E-07	-1.77E-07
7	-2.53E-09	-1.05E-06
8	2.02E-09	5.28E-09
9	-1.44E-10	-1.25E-10
10	9.87E-13	-1.16E-10
11	-5.73E-14	-4.23E-13
12	-6.80E-15	-2.97E-13
13	-2.58E-13	2.24E-14
14	4.58E-15	-4.49E-13
15	-2.37E-15	2.48E-15
16	2.41E-16	5.97E-16
17	3.74E-18	-2.81E-19
18	-4.03E-19	-3.43E-19
σ	3.56E-04	4.26E-02

Table 1.2.1
Test bench lens coefficients

1.3. Space Charge Effects

In calculating the space charge effects it is necessary to evaluate the total current in the region before mass analysis has taken place. In

the case of sputtering from graphite, one is principally interested in the current present in the clusters C_2^-, C_3^-, et cetera. Information on these is given elsewhere (see ref. [1] for the modified UNIS source and [2] for the HISS source) and is summarised in table 1.3.1. For C^- currents from carbon dioxide the oxygen current provides the main extra contribution and this is typically twice that of the C^- current (see chapter II/4). The effect of these extra currents is essentially just to increase the fields due to the space charge effect by a factor φ (in fact since the phase space profiles are different for the clusters [3], it will be more complicated than this). This factor is given in table 1.3.1.; (the velocity of the ions must be taken into account in establishing this factor, as slower ions give a higher charge density for the same current).

Ion Source	C_2^-/C^-	C_3^-/C^-	C_4^-/C^-	C_5^-/C^-	C_6^-/C^-	O^-/C^-	φ
HISS	0.65	0.05	0.07	0.01	0.03	-	2.24
modified UNIS	0.50	<0.09	<0.07	-	-	-	2.00
OXGIS with CO_2	-	-	-	-	-	2.0	3.31

Table 1.3.1.
Additions to the C^- current before mass analysis for the three ion sources considered in this chapter

Using the information in table 1.3.1 for the HISS ion source, calculations were made on the ion beam transport through the optical system of the ion source test bench including the effects of space charge. The results of these calculations were presented in chapter 5. From these results it is clear that some space charge neutralisation is taking place. (see section 6:3.6 for a discussion of this effect.) In order to model the

observed effects (see chapter 3), it is necessary to reduce the currents in the calculations by a factor of about 10, suggesting that the neutralisation factor f is 0.9.

As mentioned in chapter 5, the functional form of the effect of space charge on the ion beam transport is very well modelled by the calculations.

2. Calculations on the Oxford Radiocarbon Accelerator

This study of ion optics was intended to allow investigation of the fundamental effects underlying the behaviour of accelerator mass spectrometry systems. In particular, the reasons for the incomplete transmission of the ion beam through the accelerator and the current dependent aspects of this were to be investigated since these have particular significance for the accuracy of isotope ratio measurements.

All of the calculations presented in this section are made with the arrangement which has been used for the past three years. (The details of this will be given below.) In the next section improvements that have just been implemented will be discussed, along with other possible future changes to the system.

2.1. The Accelerator Injection System

Before giving the details of calculations carried out on the accelerator system at Oxford, it is necessary to summarise the main optical elements which are present and their characteristics. The first order properties of these elements are shown in table 2.1.1.. Not included are the effective gap lenses which are formed because of the energy pulsing of the ion beam passing through the injection magnet. (See section 4:1.3. for a discussion of their importance.) The calculations described are made assuming that all of the elements are adjusted to provide the first order

properties given here. Using the program OPTRYK, this arrangement is found to give good matching of the ion source emittance to the acceptance of the accelerator. In practice, of course, the system is adjusted for maximum transmission and so the real behaviour will be expected to be slightly different from that calculated; it is not feasible to emulate this modus operandi with the computer programs because of excessive use of computer time.

No.	optical element	characteristic properties	
1	ion source	energy = 20 keV	
2	drift length	length = 0.25 m	
3	gridded lens	focal length = 0.172 m	diameter = 0.075 m
4	drift length	length = 0.52 m	
5	drift length	length = 0.90 m	
6	injection magnet	radius of beam curvature = 0.45 m	angle = 45^{o}
		entrance angle = 26.6^{o}	exit angle = 26.6^{o}
7	drift length	length = 0.90 m	
8	drift length	length = 1.181 m	
9	gridded lens	focal length = 0.361 m	diameter = 0.125 m
10	drift length	length = 0.51 m	
11	drift length	length = 0.112 m	
12	accelerator tube	length = 0.076 m	voltage = 60 kV
		diameter = 0.039 m	final energy = 80 keV
13	drift length	length = 0.305 m	
14	accelerator tube	length = 1.753 m	voltage = 1.74 MV
		diameter = 0.051 m	final energy = 1.82 MeV
15	drift length	length = 0.076 m	
16	stripper canal	length = 0.864 m	
17	drift length	length = 0.076 m	

Table 2.1.1
The Oxford radiocarbon accelerator injection system

Under the first order approximation, waists are formed between elements 4 and 5, 7 and 8, 10 and 11, as well as in the stripper canal (element 16).

2.2. Aberrations in the Accelerator System and Low Energy Accelerator Tube

Because it is desirable for an AMS system to analyse a very large

proportion of the ion beam produced by the ion source in order to obtain sufficient counts, the acceptance of the system must be very high. This means that, in practice, it is not really possible to restrict the ion beam to such an extent that one can ignore everything but the first order effects of the optical elements.

	ion source lens (3)		injection lens (9)	
coeff.	position	angle	position	angle
1	1.00	-5.78	1.00	-2.67
2	3.15E-04	0.99	2.64E-04	0.99
3	-3.06E-06	-1.51E-03	-1.17E-06	-2.89E-04
4	4.58E-06	9.13E-06	1.85E-06	2.49E-06
5	-1.31E-06	-1.06E-06	-1.01E-06	-5.32E-07
6	1.50E-07	-4.29E-07	2.51E-07	-3.32E-07
7	-2.70E-08	-1.28E-06	-7.96E-10	-5.54E-08
8	8.54E-09	1.58E-08	6.75E-10	7.99E-10
9	-3.76E-10	-1.28E-10	-1.26E-10	-2.96E-11
10	1.18E-11	-3.08E-10	4.51E-12	-1.01E-10
11	-4.28E-13	3.30E-13	-7.05E-13	2.99E-14
12	-4.61E-14	-1.06E-12	-3.45E-14	4.79E-14
13	-4.99E-13	1.55E-13	-2.09E-14	1.31E-14
14	5.96E-15	-5.50E-13	7.50E-16	-3.70E-14
15	1.39E-15	8.56E-15	1.83E-15	3.47E-15
16	-1.00E-16	1.09E-15	-4.85E-18	-1.00E-15
17	1.42E-18	-5.01E-18	-1.96E-18	-4.72E-18
18	-1.19E-19	7.47E-19	-4.48E-20	-4.48E-19
σ	1.65E-03	3.89E-02	3.03E-05	5.85E-04

Table 2.2.1.
Characteristic coefficients for the gridded lenses in the accelerator injection system

Initially it was thought that most of the aberrations would be caused by the gridded lenses (elements 3 and 9), and in particular by the gridded lens between the injection magnet and the accelerator (element 9), which is in a position where the ion beam diameter is fairly high. The characteristics of these lenses were determined using the computer programs described in the previous chapter. The coefficients for the function fitted to the phase space transformation caused by these lenses are given

in table 2.2.1.

The diameter of this lens was increased from 0.075 m to 0.125 m without any appreciable change either to the transmission of the beam through the accelerator or to the sensitivity of the transmission to small changes in the focussing and steering of the ion beam. Calculations indicate the reason for this. Figure 1 shows the phase space transformation which takes place from the ion source to the centre of the stripper canal (this type of plot is specified in section 7:3.3.) with only the aberrations due to the gridded lenses considered; figure 2 is of the same transformation, but including the effects of the aberrations in the accelerator aperture lenses. It can, therefore, be seen that the aberrations that limit the system are those of the accelerator itself, and little will be gained by redesigning the optical elements of the injection system. The coefficients characterising the performance of the aperture lenses in the accelerator are given in table 2.2.2.

Another interesting observation relating to these lenses is the marked difference in performance of aperture and tube lenses. The calculations here assume aperture lenses, as this is what is assumed in the first order calculations on which the optimum settings are based. In fact, the real entrance and exit lenses will have stronger transverse fields and, consequently, the aberrations are likely to be worse than those calculated. Ideally these calculations would be carried out for the specific geometry of the tubes, but the problem of finding the optimum transmission conditions would still remain.

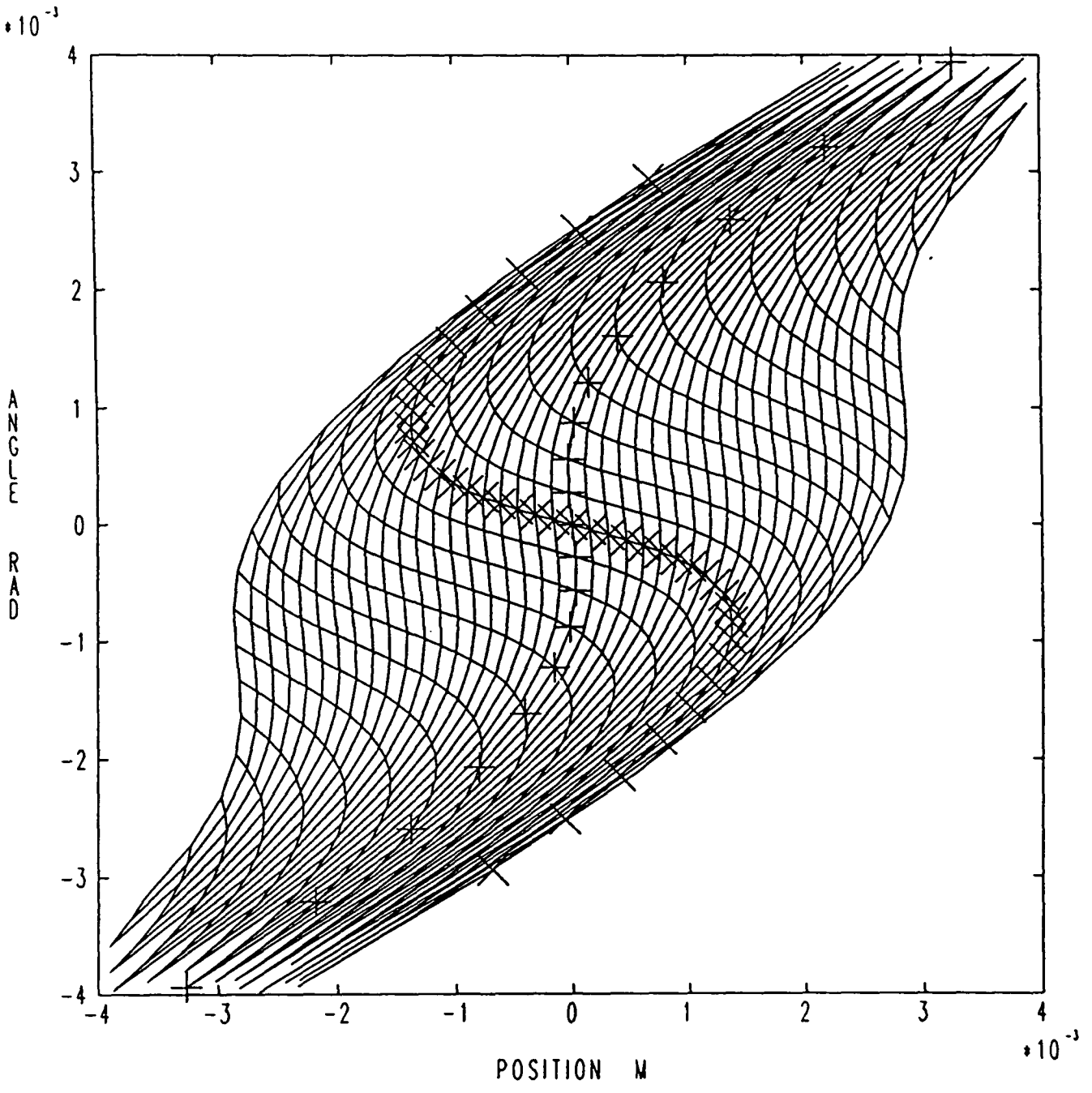

Figure 1

Phase space plot calculated for the accelerator terminal showing the effect of the aberrations in the gridded lenses of the accelerator injection system

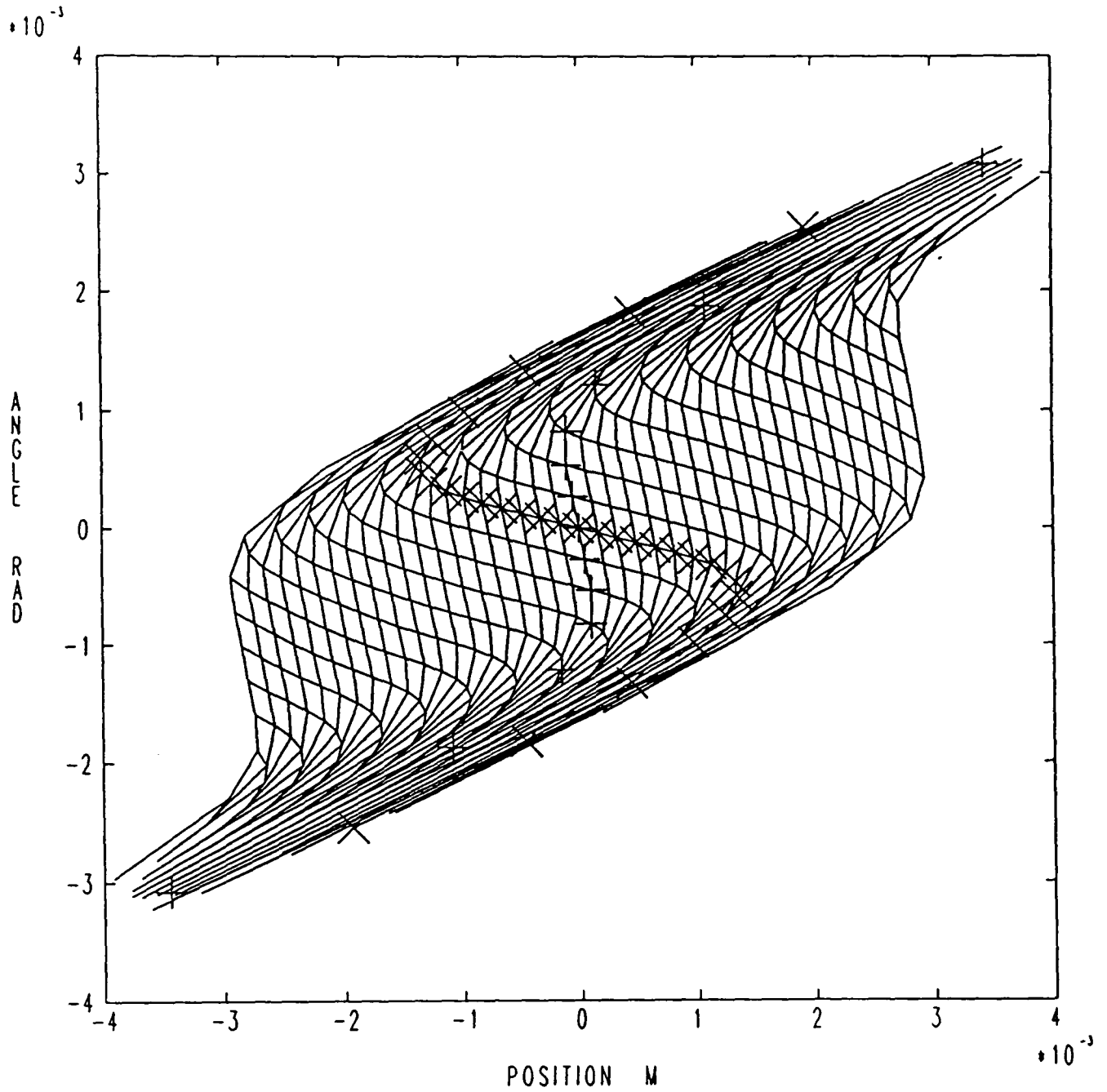

Figure 2

Phase space plot calculated for the accelerator terminal showing the effect of the aberrations both in gridded lenses and in the accelerator itself

position coeff.	accelerator aperture lenses			
	entrance 1	exit 1	entrance 2	exit 2
1	9.84E-01	1.00	1.00	1.00
2	-4.30E-04	4.28E-06	-2.29E-04	5.89E-06
3	1.15E-05	7.11E-07	-1.02E-06	-8.09E-08
4	-1.43E-06	1.74E-06	-5.16E-07	-2.56E-07
5	5.18E-09	3.17E-07	8.03E-09	-1.56E-07
6	3.80E-08	4.31E-08	5.31E-08	-1.29E-07
7	1.93E-07	-1.01E-07	2.32E-07	6.24E-09
8	-1.96E-09	-2.62E-09	-2.26E-10	1.82E-08
9	-2.67E-09	-1.65E-09	-2.57E-09	8.42E-08
10	3.50E-12	-5.25E-10	-2.99E-10	1.59E-07
11	-5.41E-12	8.01E-12	-1.45E-11	1.20E-08
12	1.17E-13	-6.31E-12	-4.20E-12	1.28E-08
13	1.44E-10	9.75E-11	1.03E-10	-4.44E-09
14	1.37E-12	2.54E-11	-5.50E-13	-1.00E-08
15	1.47E-12	7.52E-13	4.10E-12	-4.69E-09
16	-2.71E-15	9.54E-13	6.64E-13	-9.73E-09
17	-7.89E-14	-1.12E-14	-1.50E-13	2.23E-10
18	-7.65E-16	-4.00E-14	-4.45E-15	6.05E-10
σ	7.14E-05	8.68E-06	3.63E-05	2.86E-06
angle coeff.				
1	-8.03	2.68	-2.82	0.13
2	1.01	0.99	1.00	1.00
3	9.63E-03	-9.62E-03	9.50E-03	-4.05E-04
4	-4.87E-05	8.48E-06	-3.16E-06	-3.67E-07
5	-2.62E-06	1.45E-06	-7.98E-07	-8.59E-07
6	-3.48E-07	1.57E-08	-1.62E-07	-9.27E-08
7	-4.00E-04	5.11E-04	-5.83E-04	2.42E-05
8	2.76E-06	4.49E-07	1.87E-08	2.42E-08
9	1.69E-08	-4.14E-07	-8.73E-09	1.52E-07
10	1.80E-08	-2.00E-08	5.42E-09	1.40E-07
11	-6.12E-13	-2.36E-09	-8.29E-11	5.74E-08
12	-6.67E-14	-7.92E-11	2.52E-12	1.23E-08
13	-7.13E-10	3.25E-08	4.12E-10	-5.25E-09
14	-1.10E-09	2.13E-09	-2.51E-10	-9.54E-09
15	-2.53E-12	1.01E-09	2.09E-11	-1.09E-08
16	9.95E-14	8.38E-11	-2.98E-12	-9.90E-09
17	2.65E-13	-8.03E-11	-1.13E-12	4.22E-10
18	-2.09E-14	-8.81E-12	1.88E-13	6.26E-10
σ	1.41E-01	5.55E-02	8.84E-02	3.55E-03

Table 2.2.2
Parameters calculated for the accelerator aperture lenses

2.3. Space Charge Effects

The space charge effects that take place in the accelerator system can also be calculated, but there is some uncertainty in the magnitude of f, the neutralisation factor. As indicated above, this seems to be about 0.9 for the ion source test bench in which the vacuum is slightly greater than 10^{-9} atmos. In the Oxford accelerator injection system the vacuum is usually an order of magnitude below this. This has two effects: firstly, as the ion production rate is so much lower, the neutralisation factor will be less (by how much, it is difficult to estimate; see section 6:3.6); secondly, the time constant τ will be large (see equation 6:3.6.2). In these calculations a neutralisation factor of 0.5 will be assumed for the d.c. beam and τ is calculated to be around 5 ms; since the ^{12}C beam pulse time is only about 1 ms, the neutralisation factor for the pulsed beam is taken to be zero which will give an upper limit to the size of the effect.

Figure 3 shows the calculated phase space transformation assuming a current of 20 μA before the injection magnet and no current after it. This is the situation that prevails when ^{14}C and ^{13}C are injected into the accelerator. Figure 4 shows the effect of having a 20 μA current after the injection magnet too (as is the case if ^{12}C is being injected). Both of these figures should be compared to figure 2 (no space charge effect). There are two things to be noticed: firstly, the phase space diagrams show the defocussing effect of the space charge (an overall shear in the distribution), and secondly, the centre of the distribution is distorted or aberrated. The former will result in different focussing conditions for optimum transmission of the ^{12}C beam from the others, while the latter will result in a larger effective emittance for the ^{12}C beam which will reduce the optimum transmission. The conjunction of these two effects will lead to complicated current effects, but for most focussing conditions, as currents increase, one would expect the ^{12}C transmission to be reduced

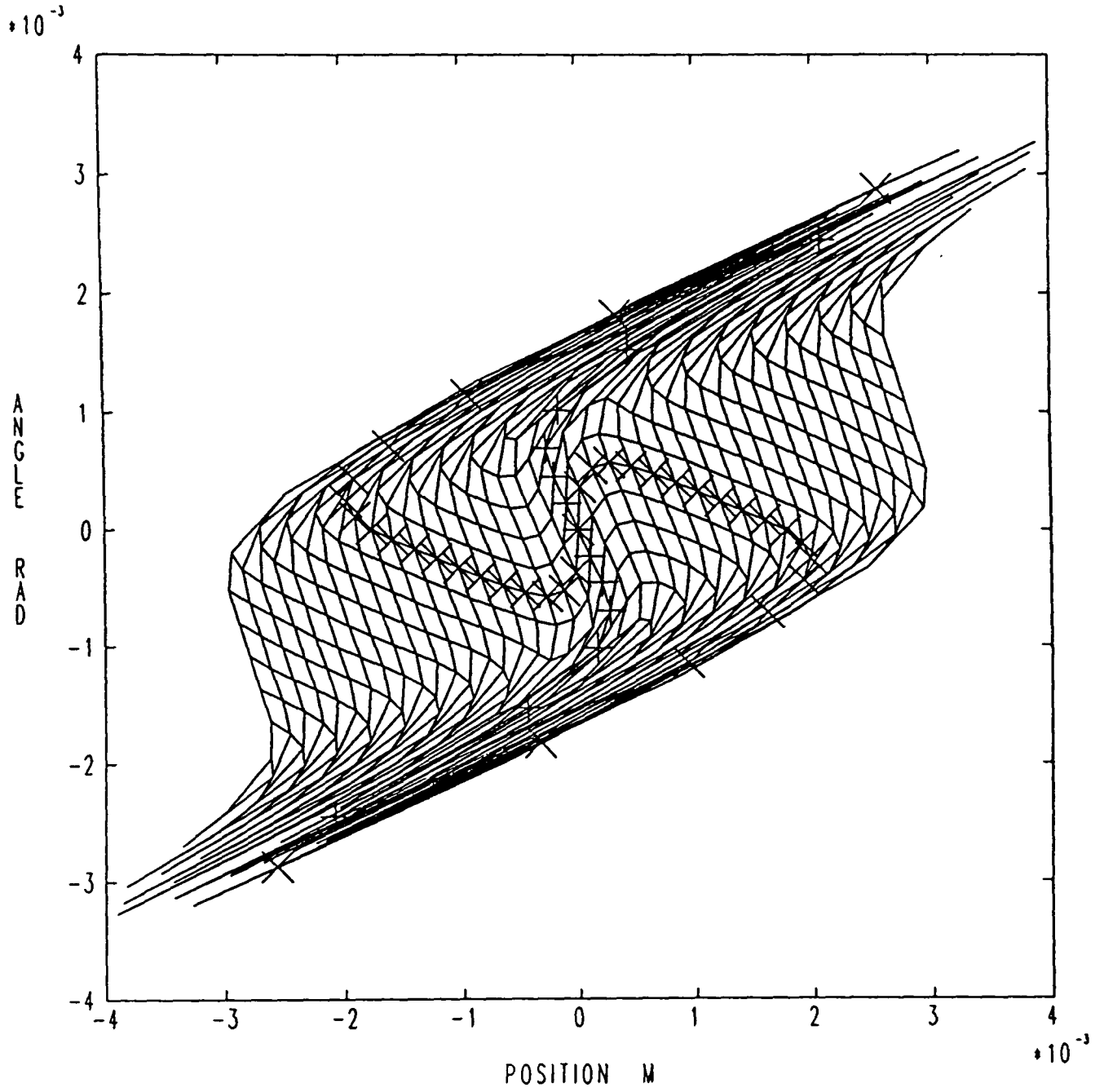

Figure 3

Phase space plot showing the effect of having a 20 μA C^- beam before the injection magnet

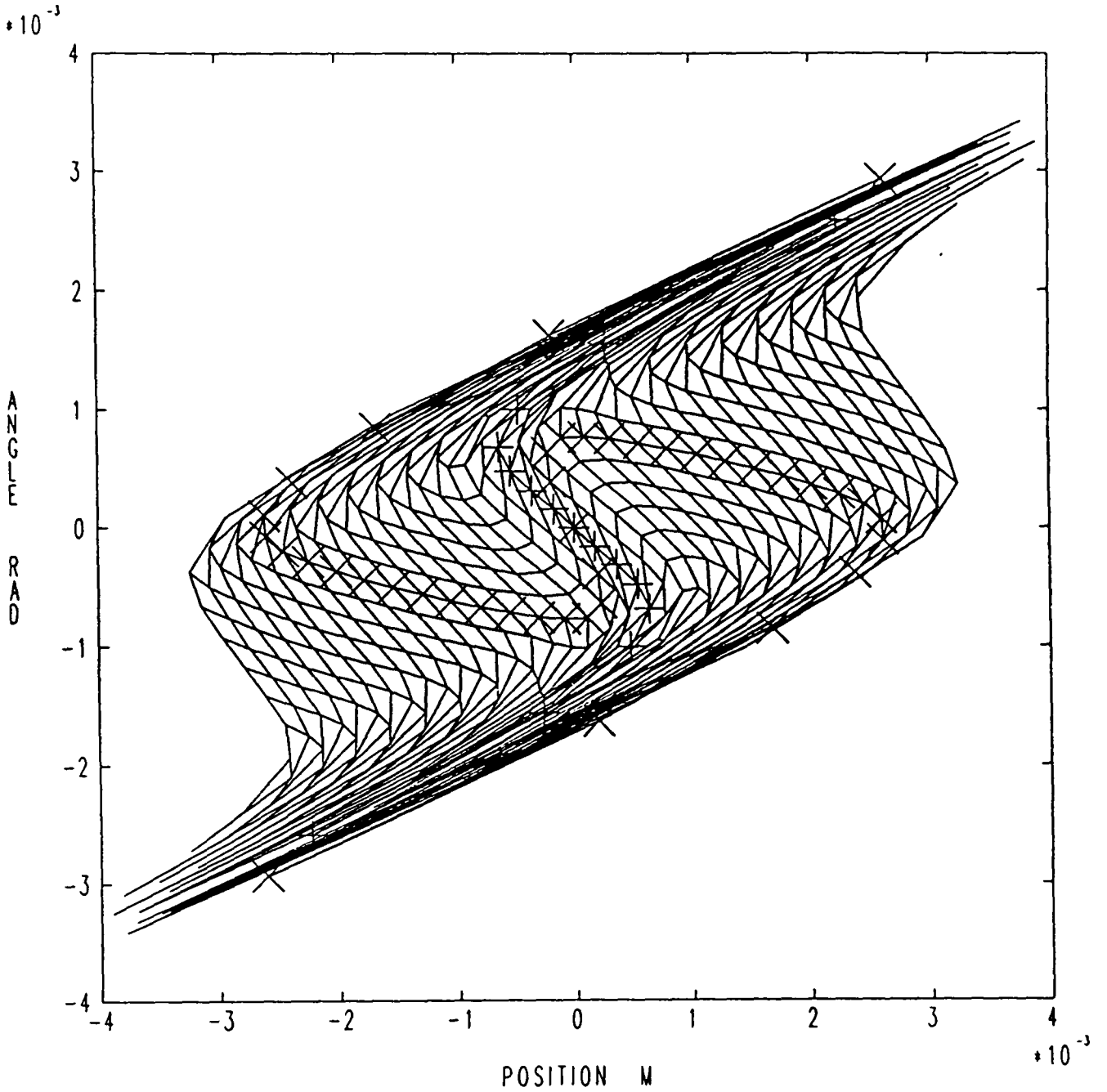

Figure 4

Phase space plot showing the effect of having a 20 μA C^- beam before and after the injection magnet

relative to that of the other isotopes.

2.4. Scattering and Apertures

As discussed in the previous chapter, the computer program for calculating phase space transformations allows one to find the effect of apertures, both at the ion source and at the destination of the transformation. Thus, for these calculations the effects of different stripper canal dimensions can be tested. The program, as it stands, is capable only of geometric 'ray-tracing' but at the stripper the effects of scattering will obviously be very important (see section 6:3.2.). The effect of this scattering is to increase the emittance of the beam leaving the stripper canal, relative to that of the beam entering. There is no way to introduce such an effect into a 'ray-tracing' algorithm and, instead, it is assumed that the result of the scattering is to reduce the effective aperture at the end of the stripper canal. In reality the effective aperture is indistinct, but here it is just assumed that its radius is reduced by 1 mm (see figure 6:1 for the justification for this). A 6 mm stripper canal of length 1 m is treated as five apertures with distances z_a from the centre and diameters d_a, as shown in table 2.4.1.

distance z_a	diameter d_a
-500.	6.0
-250.	5.5
0.	5.0
250.	4.5
500.	4.0

Table 2.4.1
The distances and diameters of apertures used to model the effect of a 6 mm stripper canal (all values given in mm)

As discussed in section 6:3.2, the scattering actually alters the

emittance of the different isotopes by different amounts, and this clearly has important implications for AMS measurements. It means that if the ion beam emittance varies for any reason, either as a result of space charge effects (see chapter 5) or because of variable ion source emittance (see section II/3:7 for relevant measurements of this), the transmission of the different isotopes will vary by different amounts and result in fractionation which might be current dependent.

2.5. The Ion Beam Energy Spread

The ion beam energy spread cannot realistically be included in a geometric 'ray-tracing' calculation. Consequently, a simple method has been employed to simulate the effect of this on the transmission through the accelerator. As indicated in section 7:1.6.a, it is possible to produce a file which contains the transmission values for a series of offsets (beam misalignments). By using first order calculations, it is possible to calculate the beam offset, O, at the stripper canal for a change ΔE in the energy of the beam. For the Oxford system $O/\Delta E$ is 0.03 mm/eV for a 20 keV beam. Assuming an ion beam energy spread which is similar to that of neutral sputtered carbon (see sections 2:1.1. and 2:1.5.), a new relationship between transmission and offset can be calculated. A program for doing this has been written. To simulate the effect of introducing energy filtration, the distribution can be also be truncated.

A small isotopic effect arises from the fact that the various isotopes pass through the injection magnet at different energies. This gives different values for $O/\Delta E$ for each and the transmission profiles are therefore slightly different. This effect is very small, however, accounting for only a fraction of a percentage difference in the transmission of adjacent isotopes; it is also expected to be fairly

constant and therefore of little consequence.

2.6. Calculated Transmission Profiles

Using all of the techniques outlined above, transmission profiles were calculated for the existing radiocarbon accelerator system at Oxford. The ion source was assumed to be a modified UNIS source with an aperture of 9 mm at a distance of 180 mm to limit the phase space (this aperture reduces the current by about 30% according to the calculations, and this is in line with the measurements made). Transmission profiles are calculated assuming the conditions found using first order techniques. It is assumed that optimum transmission is obtained by forming a waist just before the centre of the stripper (see p. 191 of [1]), but the geometric transmission is actually improved by moving the waist into the centre of the stripper (by defocussing the beam slightly) and this should be borne in mind.

Figure 5 shows three profiles: the first is calculated assuming that there is no space charge effect; for the second, there is assumed to be a 20 μA C^- beam before the injection magnet and no space charge after it, which is the situation pertaining when ^{13}C and ^{14}C are injected into the accelerator; the third is relevant to ^{12}C injection as 20 μA C^- beams are assumed both before and after the injection magnet. In all cases the currents are adjusted for the presence of other ion beams and for space charge neutralisation as outlined above.

Despite the increased emittance due to space charge, the second curve in figure 5 shows a peak transmission that is almost as great as that shown by the first. This is because the slight defocussing of the beam is beneficial to transmission, and the plotted curve is close to the optimum for ^{13}C and ^{14}C transmission (as determined by making small changes to the focal length of the first gridded lens). Under these conditions, however, the ^{12}C transmission is substantially worse (by about 6%). More seriously,

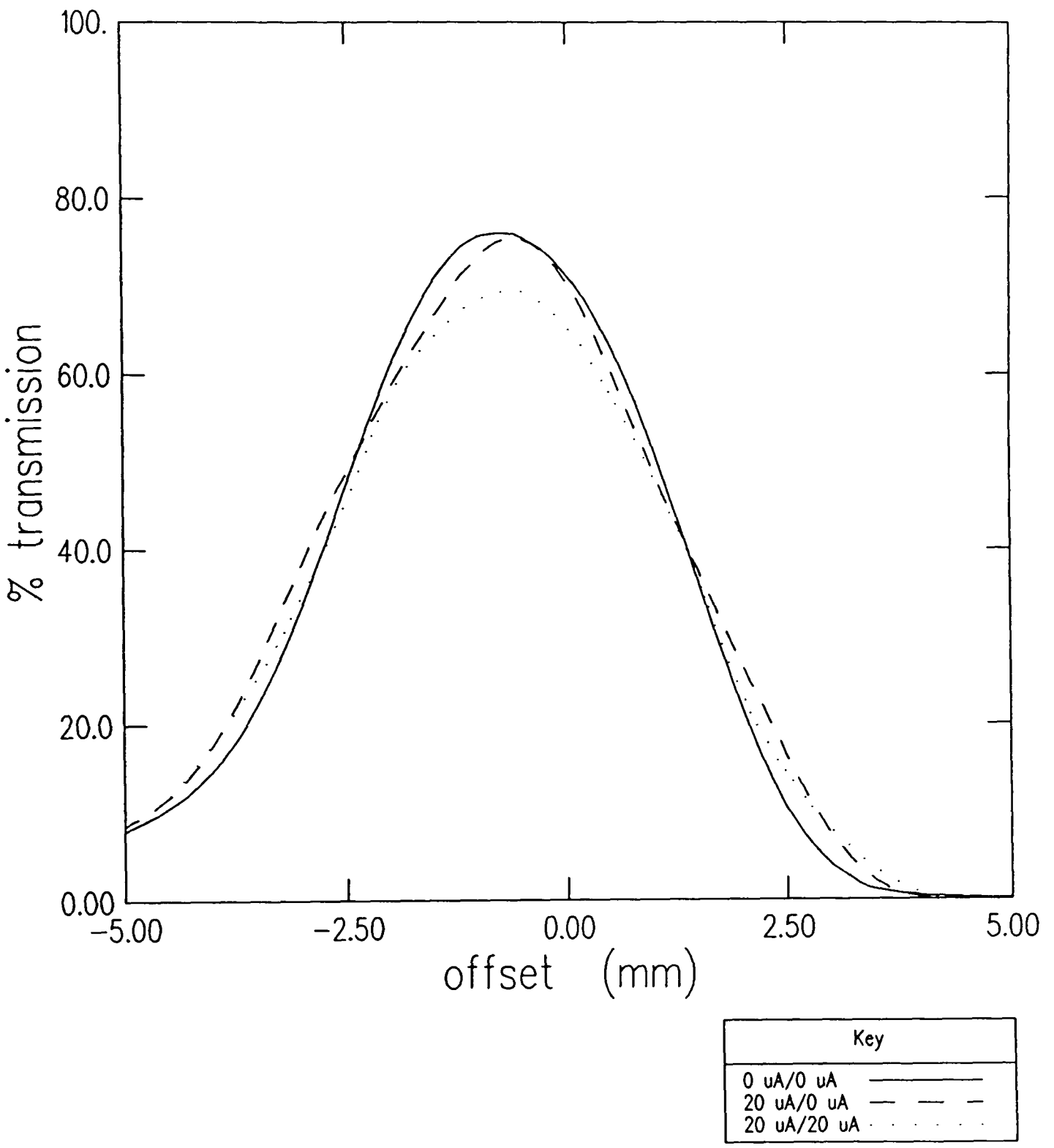

Figure 5

Transmission profile for a 6 mm ϕ stripper canal and modified UNIS source showing the effect of space charge (the two currents given in the key refer to the C^- current before and after the injection magnet)

small changes in the current make a large difference to the ^{12}C transmission, as can be seen in figure 6 where the effect of increasing the current from 20 to 21 μA is shown: this decreases the transmission by about 1.5%. The observed current effect is about 1% per μA which is very much in line with these calculations. The relative loss of transmission of ^{12}C with increasing current can be understood in terms of two related effects:

a. The increase in the current results in a growth of the effective emittance of the ^{12}C beam, which is greater than that of the ^{13}C and ^{14}C beams; this leads to a faster fall off in transmission.

b. The optimum focussing conditions for the accelerator are slightly different for the ^{12}C beam than for the others, and these optimum conditions will change faster with current for the ^{12}C beam, too; thus with increasing current, unless the actual focussing is continuously optimised for ^{12}C transmission, this will drop relative to the transmission of the other isotopes.

It is not really clear whether the other two possible mechanisms for current dependent transmission (current loading of the accelerator tubes and heating of the stripper gas; see sections 4:3 and 6:3.3.) actually play an important role. There seems to be little change in the size of the current effect with ^{12}C pulse length, whereas if the effect were entirely due to space charge one would expect it to be smaller for longer pulses (because of greater neutralisation); the other mechanisms, however, would have more effect for long pulses. It seems plausible, therefore, that the other two mechanisms may be significant.

These calculations have all been made under the assumption that the ion beam is always the same. In practice, the ion beams suffer a great

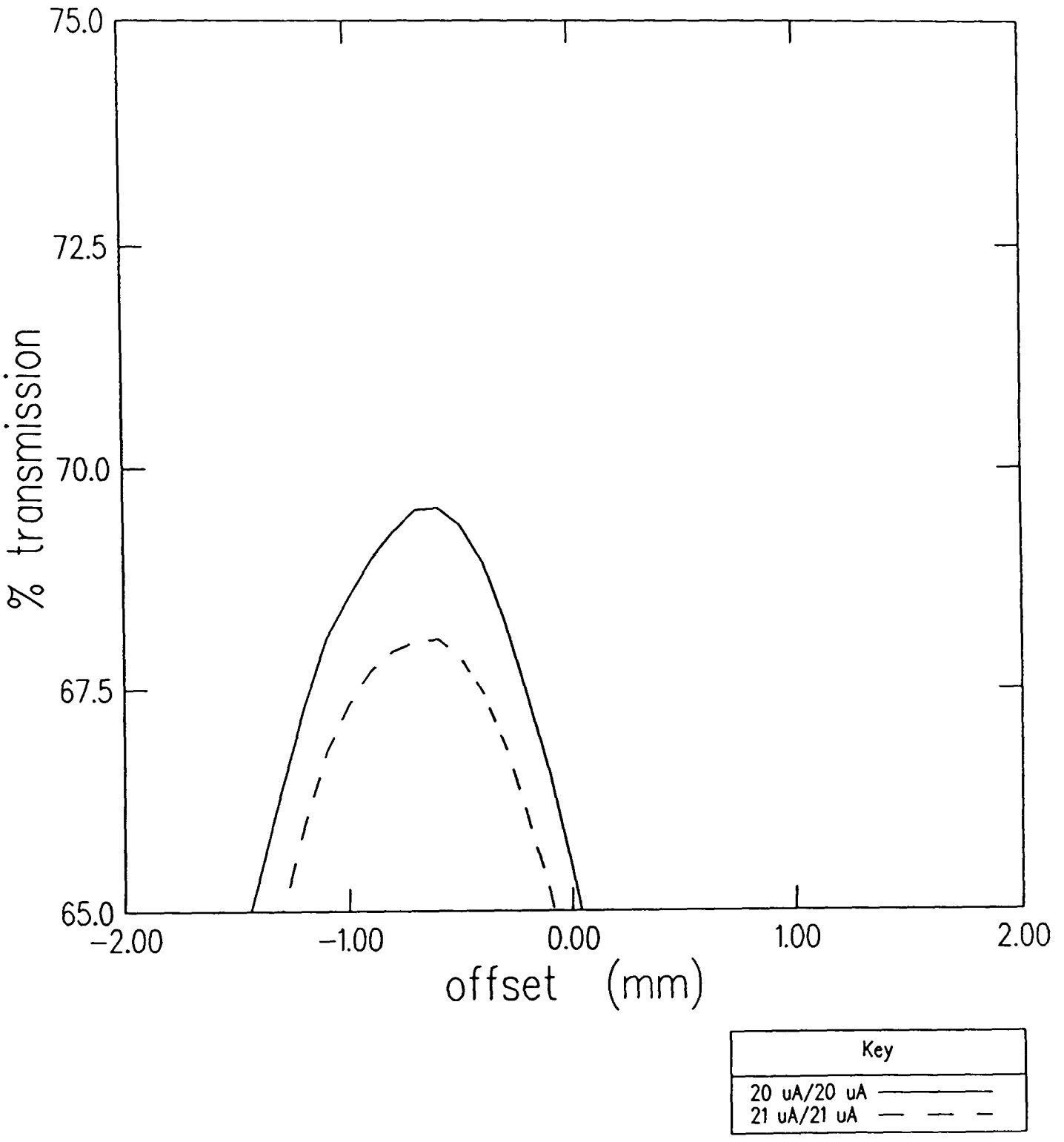

Figure 6

Transmission profile showing the effect of a 1 μA rise in the $^{12}C^-$ current

deal of variation (see section II/3:7). Given the isotopic dependence of the acceptance of the accelerator which arises from the scattering of ions in the gas stripper (see section 6:3.2), these variations will inevitably lead to changes in the isotopic ratios measured.

3. Improvements to the Oxford Radiocarbon Accelerator

3.1. Changes to the Stripper Canal

There are many reasons for wishing to improve the stripper canal in the accelerator. The original design had a 6 mm diameter canal into which the stripper gas was bled fast enough to maintain the gas pressure required for stripping. The principal disadvantage with this was that the gas pressure in the low energy tube was high enough to attenuate the ion beam significantly (see section 6:3.1). It is also possible that the collisions taking place in the tubes were yielding numbers of secondary electrons large enough to distort the field in the tubes which could be a possible cause of current dependent transmission (see section 4:3). The high gas pressure limits the terminal voltage which has further implications for the transmission, equilibrium charge state distribution and stripping fractionation. In addition to this, the beam attenuation makes it necessary to have sub-optimal gas stripper pressures and thereby risk further, and possibly variable, fractionation (see section 6:3.3).

To overcome these problems, a terminal pump has been installed to recirculate the stripper gas. At the same time the stripper canal has been increased in diameter to 9 mm. The implications of this will be considered here.

The potential advantages of these modifications can be seen in relation to the two problems that were encountered in section 2.6 above.

a. The current dependent increase in the effective emittance is greatest in the central regions of the ion beam where the aberrations due to space charge are greatest (see figures 3 and 4) and therefore, if the phase space limitation at the terminal is fairly wide compared to the central part of the beam, this increase will have a much less significant effect.

b. The sensitivity of the accelerator acceptance to the focussing conditions (ie. the position of the waist formed) will be greatly reduced if the diameter is increased. In order to remove the current effect altogether, it would be essential that the transmission was completely insensitive to small changes in the focussing or, in other words, 'flat-topped' with respect to this variable parameter.

Figure 7 shows the result of calculations made with precisely the same assumptions as those shown in figure 5. The conditions are again approximately optimal for transmission of the ^{13}C and ^{14}C beams, but this time the ^{12}C transmission is very similar. The difference due to the space charge which occurs between the injection magnet and the accelerator is no longer large enough to change the transmission by more than 1 or 2%. (The exact value will clearly depend on the settings of the optical elements in the accelerator injection system.)

The preliminary measurements made with the new stripper canal suggest that the $^{13}C/^{12}C$ ratios are now stable, often to within about 0.5% over a wide range of currents. This is very encouraging since, assuming the $^{14}C/^{12}C$ ratio can be measured to the same accuracy this would enable radiocarbon measurements to be made to an accuracy of about 50 years, which is the requirement given in the preface to this thesis.

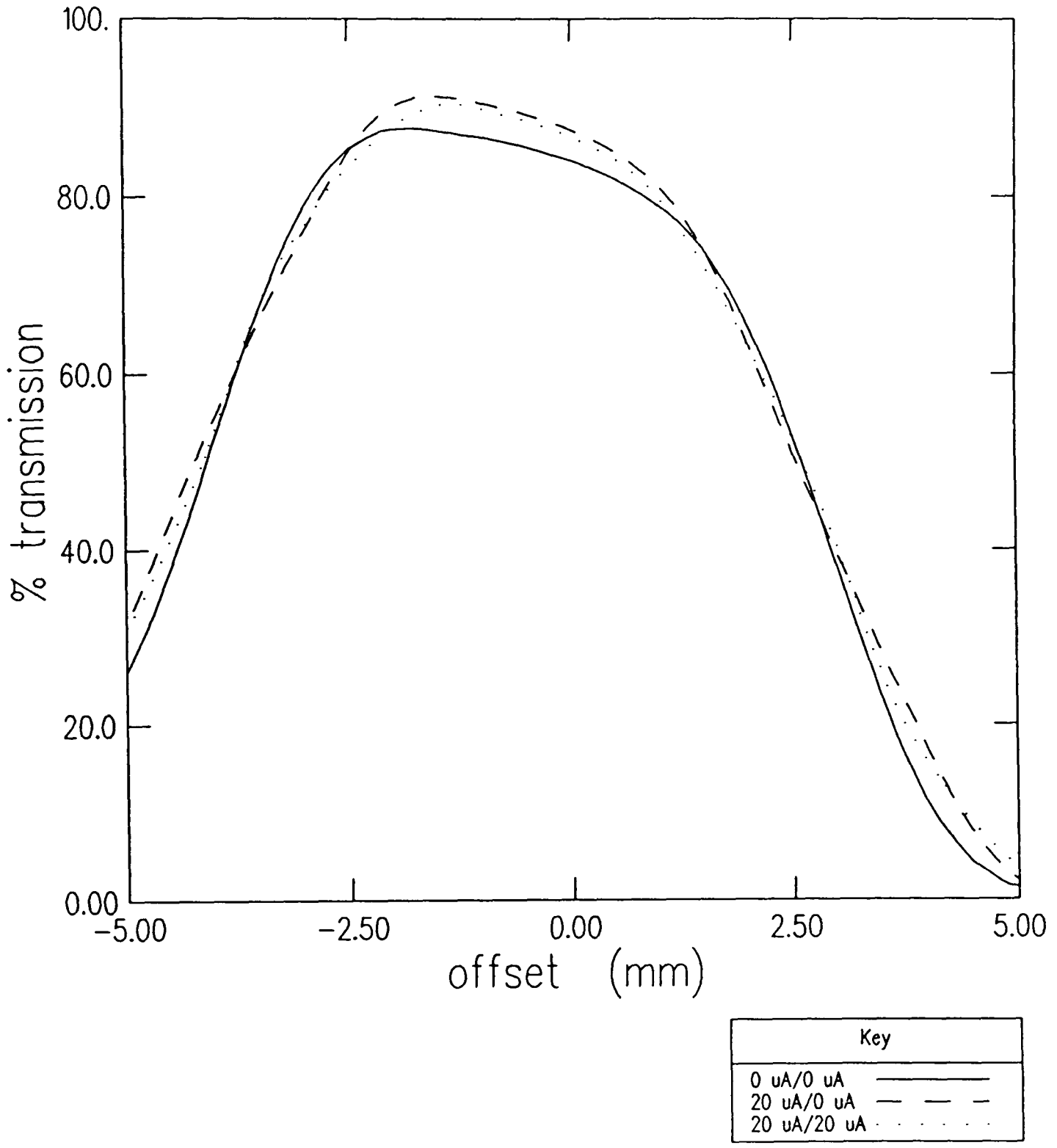

Figure 7

Transmission profile showing the effect of increasing the stripper canal diameter to 9 mm

3.2. Electrostatic Analysis

One possible future development is the introduction of an electrostatic analyser before the injection magnet. One advantage of this should be to improve the transmission characteristics of the accelerator. To investigate this effect calculations were made, under the assumption that only ions with an energy of less than 100 eV are used. The resulting transmission curves are shown in figure 8. They show that the chief advantage is that the curve has a flat top, making the optimisation of the beam control variables much easier. The analyser has no real effect on the space charge and in fact it will reduce the neutralisation factor in its vicinity to zero because of the strong electrostatic fields.

The principal reason for having electrostatic analysis at this stage in an AMS system is that it greatly reduces the injection of unwanted isotopes that takes place because of the 'energy tails' of the beam. These are particularly troublesome if one is trying to detect a rare isotope which is adjacent to an abundant lighter isotope; this is because of the high energy tail from the sputtering process. For radiocarbon measurements the molecular ion ^{13}CH is in fact the dominant interference, and so electrostatic analysis is of limited use, but it would allow the investigation of the energy tails and might shed some light on the sputtering process.

3.3. The Oxford Gas Ion Source

It is clearly essential to look at the effect of using the Oxford Gas Ion Source (or OXGIS) in conjunction with the accelerator system. One potential problem with this source is the high O^- current produced (see section II/4:4). In the region of gas flow normally used, this is at least twice the C^- current. To demonstrate the effect of this, figure 9 shows

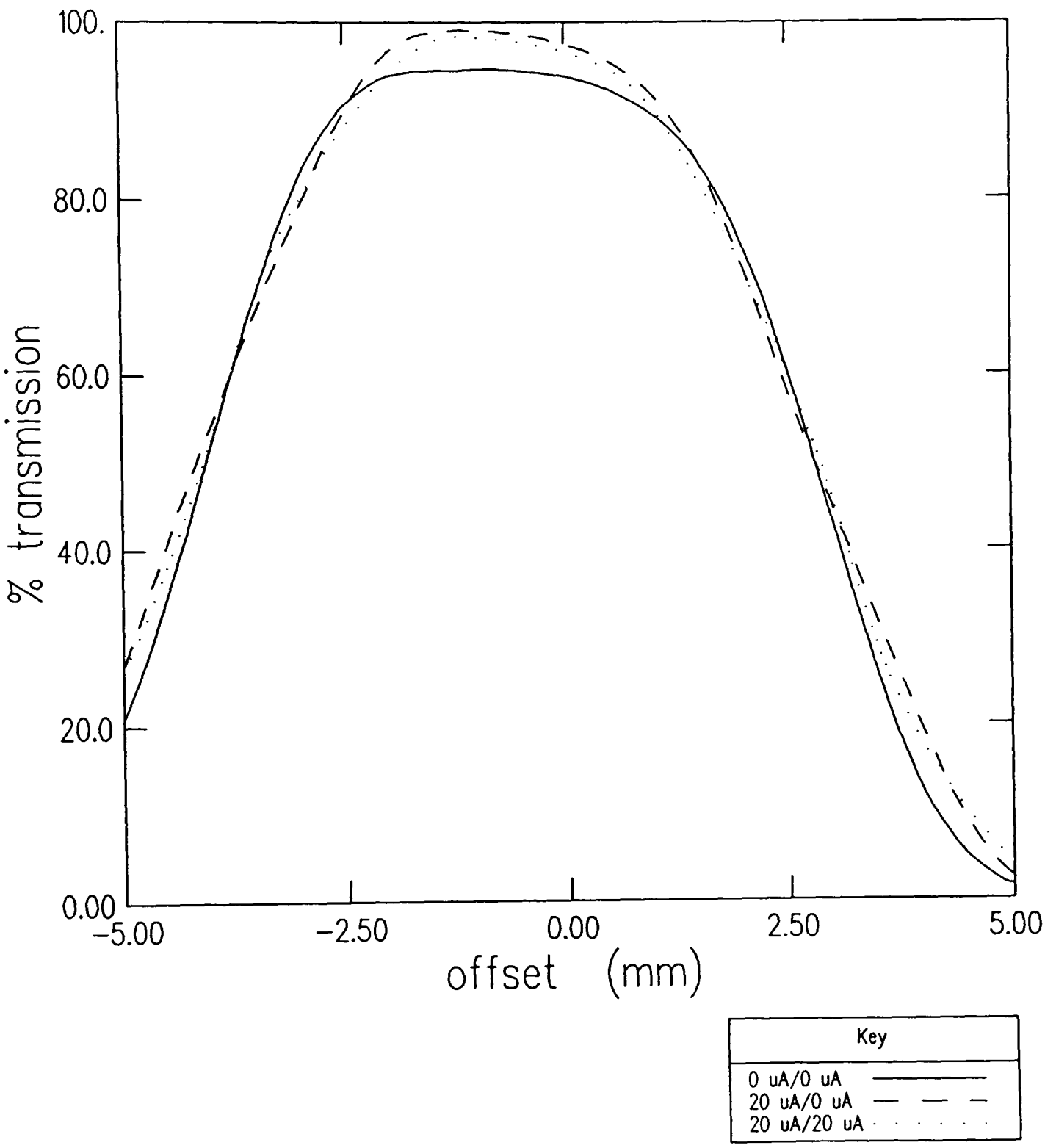

Figure 8

Transmission profile showing the effect of restricting the beam energy spread to 100 eV

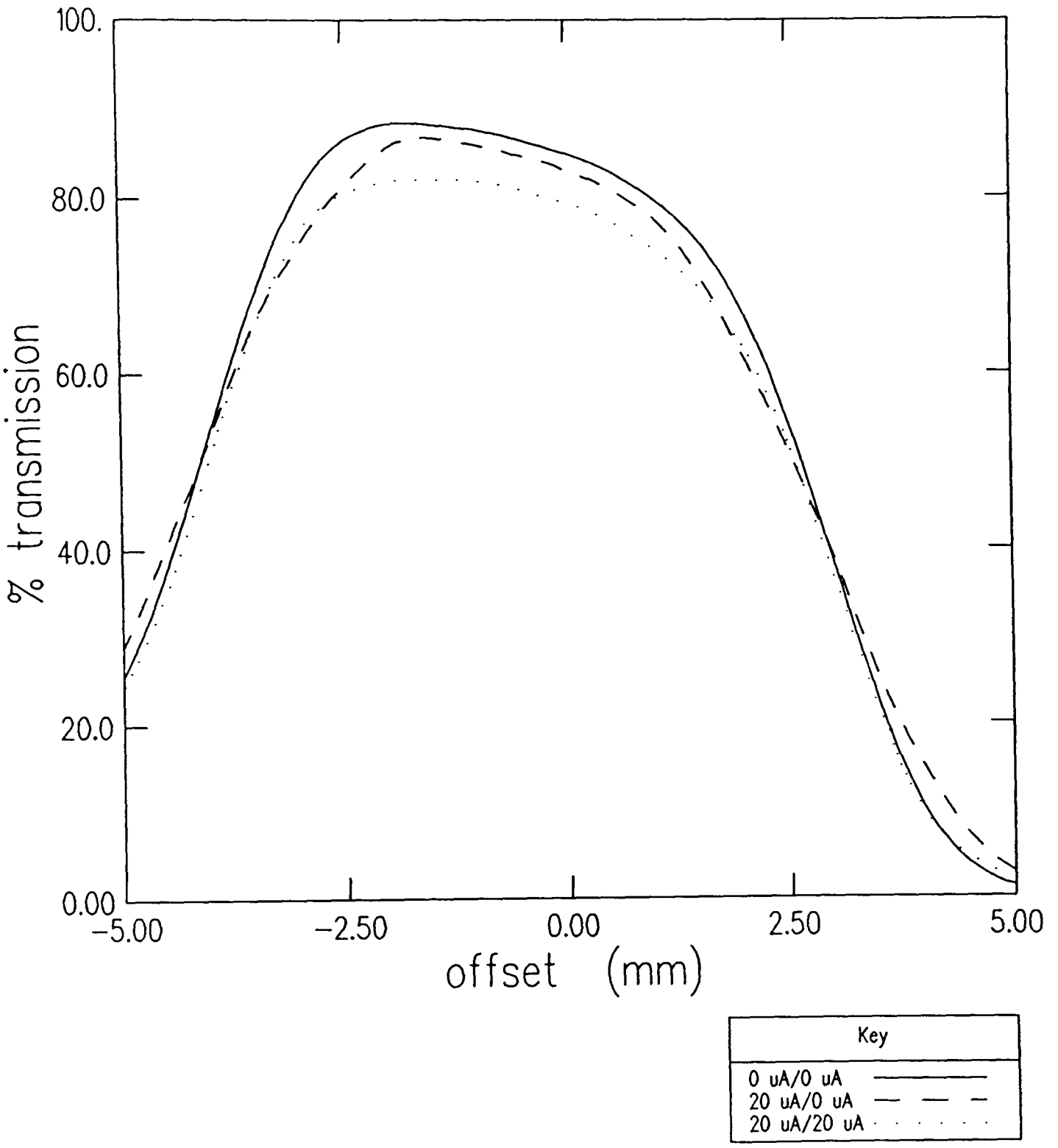

Figure 9

Transmission profile for a 9 mm ϕ stripper canal and OXGIS ion source without optimising for ^{13}C transmission

the transmission figures obtained using the same conditions under which the modified UNIS source usually operates. These conditions are clearly so far from optimum that the current ^{13}C and ^{14}C beams behave differently from the ^{12}C beam. This can easily be remedied by adjusting the focal length of the first gridded lens (that between the ion source and the injection magnet) for optimum transmission of the ^{13}C and ^{14}C beams through the accelerator. When this is done the transmission profiles shown in figure 10 are obtained. This is perfectly satisfactory in that there is little difference (about 1%) in the transmission of different isotopes, but it is clear from the zero current profile that re-optimisation will be essential if the overall current produced by the ion source changes.

The predicted behaviour of this source in conjunction with the rest of the accelerator system can be summarised by two propositions:

a. The high current in the region before the injection magnet (see table 1.3.1.) increases the effective emittance (hence the overall slightly lower transmission than that of the modified UNIS source) and defocusses the beam slightly. This defocussing can be remedied by increasing the voltage on the first gridded lens (element 3 in table 2.1.1), but this must clearly be re-optimised if the current changes.

b. The space charge effects on the $^{12}C^-$ beam after analysis are too small to make serious changes to the transmission of this isotope relative to the others if, and only if, the focussing of the ion beam is optimised (as described in section a).

It was thought that the space charge effect might be improved by removing the first gridded lens altogether and placing the ion source at the position of the first waist, but the transmission was calculated to be

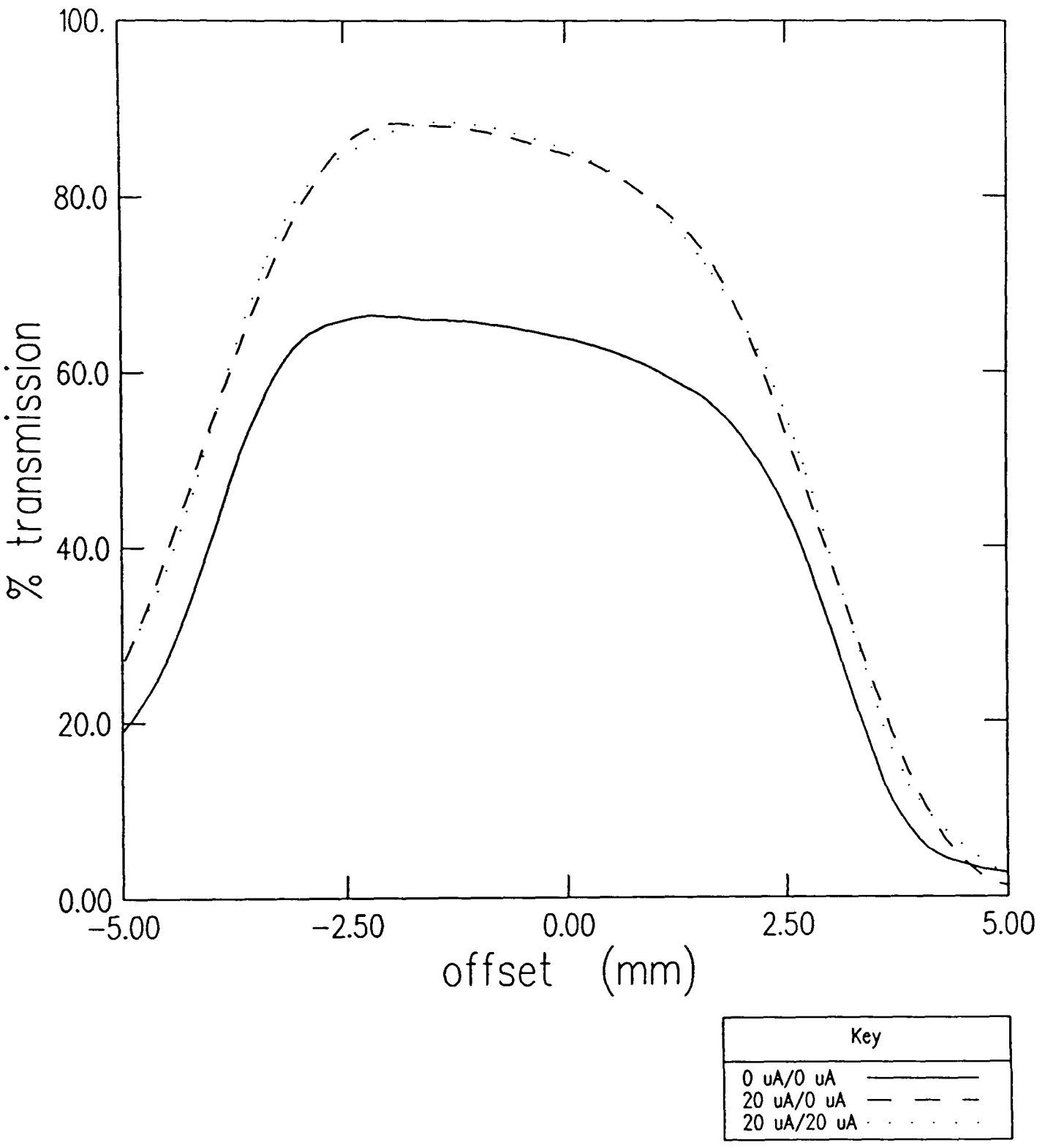

Figure 10

Transmission profile showing the effect of optimising for ^{13}C transmission cf. figure 9

low because of the poor matching of the emittance of the ion beam to the acceptance of the accelerator (this experiment was actually tried briefly with the modified UNIS source and the transmission was indeed much lower). In order to find the optimum magnification, transmission profiles were calculated for a range of beam magnifications and they showed a broad maximum from 2.0 to 3.0 within which the transmission varied by only a few percent. This means that the ratio of the parameters pq/pa (see table 1.1.1.) are ideally matched to the present injection system. A lens is, in fact, essential both for matching purposes and for counteracting the space charge defocussing of the ion beam as it leaves the source.

The calculations described above were done assuming phase space limiting apertures which reduce the current from the source by about 70%. These were one aperture of 1.75 mm diameter at the source, and another with a diameter of 5.8 mm at a distance of 125 mm from the source. These were chosen to maintain the optimum ratio of pq to pa. The effect of further limiting the phase space has also been studied. If the two apertures are reduced to 1.5 mm and 4.9 mm respectively, the ion beam is reduced by a further 70% to about 50% of the total. Figure 11 shows the transmission profiles calculated under these conditions. There is a slight improvement in the maximum transmission through the accelerator, and a small diminution in the difference between the zero current profile and the others, but the improvement is not really significant enough to make the sacrifice in current worthwhile. There is an important lesson to be learned from this: the transmission properties of the ion beam are dominated by the increases in effective emittance due to aberrations and space charge, and there are only slight gains to be made by reducing the emittance of ion sources (especially as the more dense the concentration of ions in phase space, the stronger the space charge forces will be).

It has been predicted, therefore, that it will be possible to operate

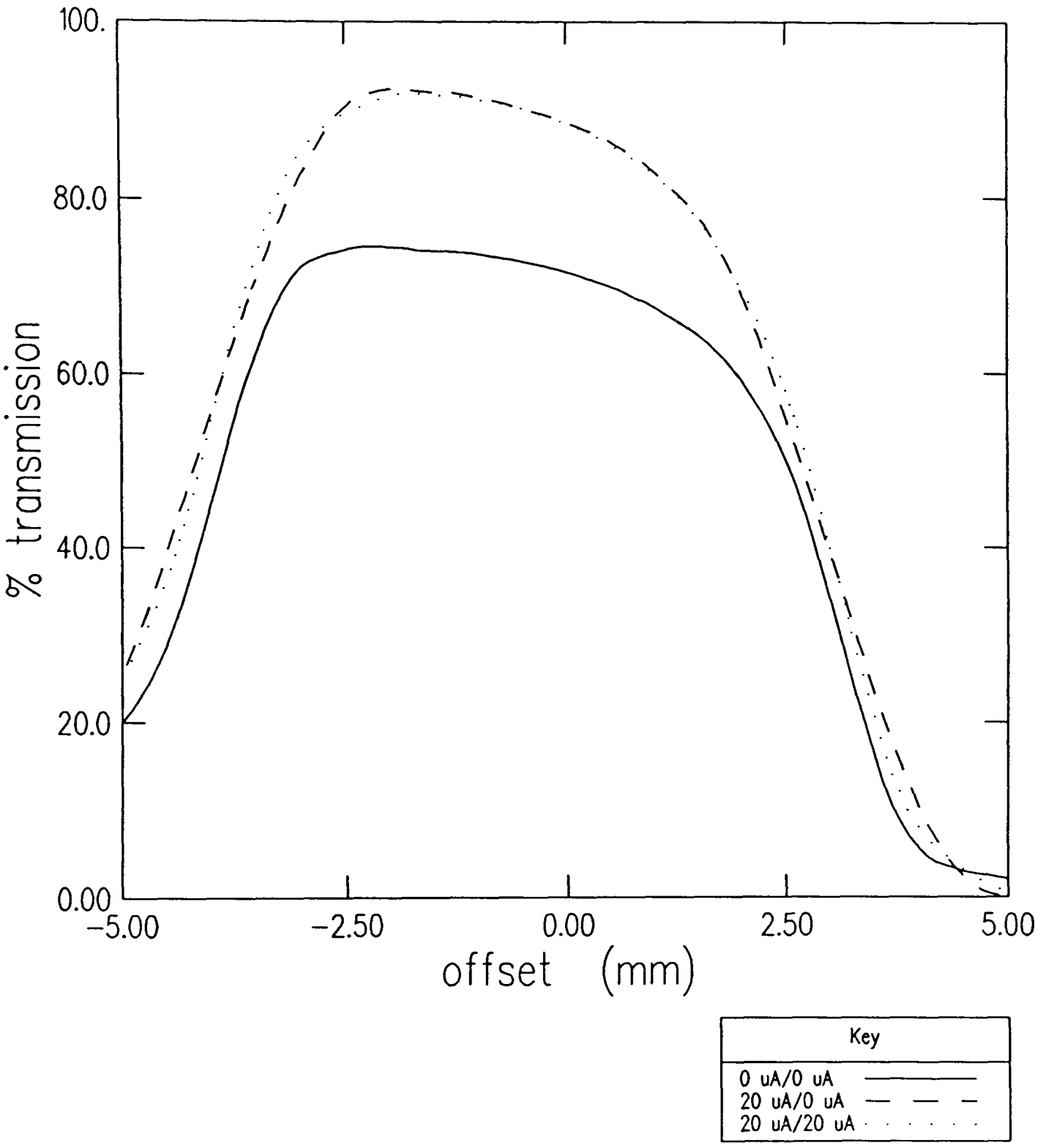

Figure 11

Transmission profile showing the effect of further restricting the ion beam phase space so that only 50% of the beam is used
cf. figure 10

the OXGIS without current dependent fractionation. Furthermore, it should be stressed that it is, in fact, possible to operate this source at a constant current (see chapter II/4), thereby ensuring that there is no fractionation of this kind. The emittance of the HISS type source is also less variable than that of the modified UNIS source (see section II/3:7), and so it is expected that measurements of isotope ratios with an accuracy of better than 0.5% should be easily attainable (assuming other requirements are satisfied).

3.5. The Prospects for High Current Radiocarbon Measurements

Despite the improvements obtained by changing the design of the stripper canal, it is clear that space charge is still going to be a major problem if very high currents are to be used (for example C^- current of greater than 100 μA from a HISS). There are four major problems:

a. The growth in the effective emittance in the region before the injection magnet will be large enough to make the maximum obtainable transmissions small.

b. The defocussing that takes place before beam analysis will make continuous reoptimisation of the focussing necessary.

c. The space charge effect on the $^{12}C^-$ beam after analysis will be sufficiently great to alter significantly the transmission properties of this beam relative to the others.

d. There are also problems associated with the heating of the stripper gas and the secondary electron current loading on the accelerator terminal and tubes.

Problem c might be remedied by altering the voltage of the gridded lens between the injection magnet and the accelerator while c and d might be tackled by using a beam attenuator. To reduce the significance of a and b the space charge neutralisation would have to be improved by increasing the residual gas pressure and carefully screening the beam from electric fields over most of its length.

Clearly, calculations of the type presented in this chapter will be essential if such a development is to be useful for accurate radiocarbon measurements.

Summary

The calculations made on phase space transformations in the ion source test bench are discussed in relation to the measurements made. The deductions that can be made concerning the form of the ion distribution in phase space are presented, along with a discussion on the aberrations and space charge effects that take place.

Calculations on the accelerator system are then presented showing that the aberrations of the accelerator tubes themselves are dominant. Methods employed in introducing the effects of ion beam energy spread and scattering are given. The transmission profiles for typical ion beams passing through the accelerator demonstrate that space charge is likely to be responsible for current dependent fractionation (although other mechanisms may also be important).

Improvements already made to the accelerator at Oxford are analysed with the help of these calculations, showing that the observed improvement in performance is in line with these predictions. The proposed introduction of electrostatic analysis is also discussed and, more

importantly, the effect of changing from a modified UNIS source to the Oxford Gas Ion Source described in chapters II/2 and II/4. It is shown that given optimised focussing, there should be no current dependent transmission and it is predicted that isotope measurements with an accuracy of better than 0.5% should be easily attainable (assuming other requirements are met).

It is found that the growth in effective emittance which results from the aberrations and space charge are sufficiently great that there is little to be gained from reducing the emittance of ion sources used.

Finally the problems associated with trying to use the very high currents obtainable from a HISS operated with graphite are discussed briefly with some suggestions as to how they might be overcome.

References

[1] N.R. White, D. Phil. Thesis, Oxford University (1981).

[2] R. Middleton, Nucl. Instr. and Meth. 214 (1983) 139.

[3] J.L. Yntema and P.J. Billquist, Rev. Sci. Instr. 57 (1986) 748.

Summary

There are many physical mechanisms involved in the production and transport of ion beams. The purpose of this first part of the thesis is to consider the importance of these in relation to AMS measurements. The introduction explains in very general terms the implications of the most important processes. Space charge, interactions with residual gases and aberrations are identified as being of crucial significance.

In chapter 1 the theory of ion optics is explained in some detail; this material is essential for the arguments that follow. A simple proof is given for Liouville's theorem and for the other similar constraints on phase space transformations. The validity of Liouville's theorem is discussed, both in general and in relation to restricted descriptions of the phase space.

Sputtering is the mechanism by which ion beams for AMS are usually produced; there is a detailed discussion of this in chapter 2. The theories behind this are evaluated in relation to the sputtering of carbon by graphite, and it is found that the velocity dependence is expected to be small. Experimental evidence from chapter II/4 is also used to support a model for the sputtering process in which the ion production probability for carbon atoms sputtered from the surface layer is expected to be close to unity. The implications of this are that the isotopic fractionation for ions produced in this way is expected to be negligible. The implications of sputtering on ion optics are also discussed, and it is clear that ion beams for different isotopes will be very similar unless there is significant fractionation in the ion production process.

As a prelude to the following two chapters, a series of brightness profiles measured on the ion source test bench are presented in chapter 3

and the observed effects are qualitatively explained in terms of aberrations from the ion source test bench gridded lens and from the space charge effect.

Chapter 4 includes a discussion of the aberrations present in the injection system of an AMS facility. Simple methods for analytical calculations of the electrostatic potentials in three generic lens types are then presented, and a suitable function for modelling the phase space transformations of cylindrically symmetric lenses is introduced. This function could equally well be used in conjunction with some more comprehensive 'ray-tracing' method (such as successive over-relaxation). It is demonstrated that the generic gridded lens models the behaviour of that found in the test bench very well. A possible source of current dependent aberration is the loading of the accelerator tubes by secondary electrons. This can be minimised by keeping the gas pressures in the tubes low, and by ensuring that ions do not strike the tube walls.

Chapter 5 introduces methods for calculating space charge effects. It is shown that using these methods the observations made on the ion source test bench can be very well modelled, assuming a space charge neutralisation factor of 0.9 and an initial ion distribution in phase space which is gaussian.

Space charge neutralisation is just one of the important mechanisms which is dependent on the residual gases in the vacuum. All of these effects are discussed in some detail in chapter 6. The theories and measurements relevant to the interactions between ions and gas molecules are first introduced, and then the practical effects of these interactions are considered. As well as significantly attenuating the negative ion beam because of electron detachment, the residual gases reduce the quality of the ion beam (i.e. increase its emittance). The latter effect is strongest at the stripper where the gas pressures are highest and Monte Carlo

calculations have been made showing the magnitude of this effect and demonstrating that it is strongly dependent on isotope. Large angle scattering is also important in the high energy beam line where it can be responsible for ions of the wrong mass entering the detector. It is pointed out here that the energy from an intense ion beam passing through a gas stripper is likely to reduce the gas density significantly which is another mechanism for current dependent fractionation; this can be avoided by ensuring that the gas pressure is slightly above optimum. Finally, the subject of space charge neutralisation is discussed and several reasons for expecting the neutralisation factor in the accelerator injection system to be well below unity are considered.

Chapter 7 is a description of the computer programs which have been written for phase space transformation calculations. It is expected that these will be of particular value to those involved in the design of AMS facilities where the ion beam transmission must be very high.

In chapter 8 the calculations that have been carried out on both the ion source test bench (described in chapter II/1) and the injection system of the radiocarbon accelerator at Oxford are presented. The former demonstrate the validity of the techniques used while the latter, together with a simple treatment of the energy spread of the ion beam, allow predictions to be made concerning the size of the current dependent transmission. It is shown that this effect can be explained in terms of the space charge effect, and the implications of this for the Oxford Gas Ion Source and the possible use of High Intensity Sputter Sources with graphite are discussed. The improvements that have been made to the stripper in the Oxford accelerator are predicted to allow accurate isotope measurements (better than 0.5%) to be made. Radiocarbon measurements of this accuracy clearly depend on other factors (such as counting statistics and contamination), but an ion optical system which is capable of

measurements of this accuracy is clearly a very important step towards that goal.

PART II

and

Associated Techniques

The fountain from the which my current flows

[William Shakespeare: Othello]

Introduction

As discussed in the introduction to this thesis the ion source is one of the most critical components of an accelerator mass spectrometry (AMS) system. This is both because the ion source determines the type of sample that can be used and because it determines the characteristics of the ion beam on which the subsequent measurements must be made.

1. Ion Beam Production from Carbon

The first requirement for an ion source which is to be used for radiocarbon AMS is that it should produce negative ions. This is necessary because it enables complete separation of ^{14}C from the abundant isobar ^{14}N which has no stable negative ion, and also because of the convenience of being able to use a tandem accelerator.

There are essentially only two feasible types of ion source for the production of C^- ions. These are the caesium sputter ion source which produces negative ions and a positive ion source coupled with some system of charge exchange. The caesium sputter ion source is particularly suitable for producing ions which have high binding energies (the sputtering provides a very efficient way of ejecting such ions in comparison with other techniques such as surface emission) and large electron affinities (needed to get a high ion to atom ratio for the sputtered material: see chapter I/2).

As discussed elsewhere [1] the charge exchange process is difficult to control and, in addition, is prone to further fractionation over and above that produced by the ion source itself; this is because the cross sections for charge exchange depend on the velocity of the ions which is different

for different isotopes. For these reasons all AMS radiocarbon systems now in operation use caesium sputter ion sources.

2. Ion Source Design

There are several different permutations of the caesium sputter source currently in use (for example the ion sources currently used at Oxford [2], Zurich [3], and Toronto [4]). Most of these are similar in that they use a caesium ion source which is well separated from the target that is to be sputtered. These will be referred to as conventional sputter sources.

2.1. Conventional Caesium Sputter Sources

In these the caesium ions are produced by surface ionisation. The beam thus produced is then focussed onto the target either from behind [2] or from the side [3,4]. The advantage of having a large distance between the ioniser and the target is that there is little danger of the caesium ioniser being contaminated by the sputtered material as there is with, for example, the Inverted Spherical Sputter Ion Source [2]. The first main disadvantage is that these sources do not have cylindrical symmetry; this makes them produce ion beams with complicated brightness distributions in phase space [2] and also makes some steering and focussing of the caesium beam necessary. The second main disadvantage is that the long path length of the caesium beam limits the caesium currents which can be obtained because of space charge effects; this obviously limits the secondary ion currents that can be obtained.

Another slightly less obvious problem is that the caesium ions in these sources are usually produced by diffusing the metal vapour through a heated porous frit. The conductance of these frits is constant neither over the surface nor with time, and so the caesium beam produced varies in

magnitude and in the shape of its brightness profile. The result of this is that the sputtering ion beam is not easily reproduced and requires frequent adjustment of the steering and focussing voltages for optimum performance.

2.2. High Intensity Sputter Sources (HISS)

In order to overcome the problems associated with the conventional sputter ion sources, ion sources have been developed which have the ioniser just in front of the sputter target [2,5,6]. The use of porous ionisers in this position [2] proved to be impractical because of damage caused by the sputtered material. However, solid tantalum ionisers used in conjunction with a target chamber which is filled with caesium vapour have been found to be very successful in producing high negative ion currents from a variety of different target materials [7]. This type of source has not yet found wide applicability for radiocarbon AMS for three reasons: firstly the current dependent effects discussed in part I of this thesis will almost certainly make it difficult to make accurate measurements with currents as large as 100 μA; secondly it is difficult to make suitable targets for this type of ion source as the thermal conductivity must be very high; and thirdly it is hard to change samples quickly in an ion source of this type (see ref. [5] for a detailed description). However, the simple ion optics involved in the high intensity sputter sources make them very simple to control and they behave fairly reproducibly over an extended period.

3. Ion Sources for Carbon Dioxide

As a by-product of the high sputtering rate of the HISS it has been found that this type of source produces relatively high currents from gases and in particular from CO_2 from which C^- currents of about 20 μA can be

produced [1]. For this reason, along with the other advantages, it was decided that the HISS provided the best basis for the development of an ion source specifically for radiocarbon.

There are, however, a number of outstanding problems:

a. The background currents from this type of source (with no gas flowing) are about 0.5 - 0.7 μA [1].

b. There is no easy way to change samples quickly.

c. The cross contamination has not been determined.

d. The mechanisms for the production of C^- ions from CO_2 are not well understood.

It should be mentioned that experiments have also been carried out on the Aarhus Negative Ion Source to determine whether or not this was suitable for operation with CO_2. This ion source does not fit into the categories mentioned above but is based on a Penning type discharge. The details of this experiment are outlined in ref. [8]. The overall efficiency was found to be about 0.15% and the C^- ion currents 2 - 4 μA. However the chief problem was cross contamination which was far too severe to consider using this kind of source for radiocarbon.

Summary

The most promising type of ion source for use in radiocarbon AMS is the High Intensity Sputter Source as it is simple to operate and capable of producing currents of the order of 20 μA when used with CO_2.

The purpose of the work described in this part of the thesis is to characterise the performance of this type of source, to overcome the outstanding difficulties and, thereby, to develop an ion source which uses CO_2 directly and is suitable for radiocarbon dating with AMS.

References

[1] R. Middleton, Nucl. Instr. and Meth. B5 (1984) 193.

[2] N.R. White, D. Phil. Thesis, Oxford University (1981).

[3] R. Balzer, G. Bonani, M. Nessi, Ch. Stoller, M. Suter and W. Wölfli, Nucl. Instr. and Meth. B5 (1984) 204.

[4] C.G. Wilson, J.C. Rucklidge, W.E. Kieser and R.P. Beukens, Nucl. Instr. and Meth. B5 (1984) 200.

[5] R. Middleton, Nucl. Instr. and Meth. 214 (1984) 139.

[6] R. Middleton, Workshop on Techniques in A.M.S., Oxford Radiocarbon Accelerator Unit (1986) 82.

[7] R. Middleton, Nucl. Instr. and Meth. 220 (1984) 105.

[8] J. Heinemeier and H.H. Andersen, Radiocarbon 25 (1983) 761.

Chapter 1

The Testing of Ion Sources

Introduction

The development of new ion sources is a time consuming undertaking and it is clearly not feasible to carry out all of the necessary experiments on the main beam line of an accelerator facility. It was therefore decided at the start of this work that an ion source test bench (ISTB) should be built. In this chapter the test bench will be described and its qualities and limitations discussed.

2. The Requirements for an Ion Source Test Bench

The requirements of an ion source test bench at the most basic level are very simple:

a. an evacuated beam line

b. some method of separating different ion species

c. current measurement capability

d. the ability to investigate brightness profiles in phase space

The pressure of the residual gases in the vacuum are important if they attenuate the beam significantly or alter its emittance. In practice this means that the vacuum should be circa 10^{-8} atmos. or better (see section I/6:3).

Obviously the separation of different ion species is important in evaluating the performance of an ion source. However, to characterise the

ions completely one really needs a complete AMS system and so the ability of an ion source test bench to perform this task will clearly be limited.

The current measurement capability is largely a function of the ability to resolve the different components of the ion beam. Ion beams derived from sputter ion sources are not particularly well localised in phase space, and so intense beams will tend to interfere with the measurement of smaller beams of different species with similar masses.

The scope for investigating the brightness profiles of ion beams in the six dimensional space is clearly enormous and in any practical test bench only a small subset of such measurements is possible.

3. The Design of an Ion Source Test Bench

The overall design of the test bench built for this work is shown in figure 1.

3.1. The Vacuum System

The vacuum is provided by a Balzers 150 l/s turbo-molecular pump which gives pressures of better than 10^{-8} atmos. (measured just above the pump). The beam line is sealed with nitrile O-rings and so is not really suitable for attaining UHV conditions.

As hydrocarbons were found to be a particular problem when operating with the gas ion source a liquid nitrogen trap was added in front of the ion source.

3.2. Ion Mass Resolution

This is provided by a double focussing 45^{o} analyser-magnet with pole angles of 10.4^{o} and 13.7^{o} respectively which bends the beam in the horizontal plane. The beam is focussed both by this and by a gridded lens

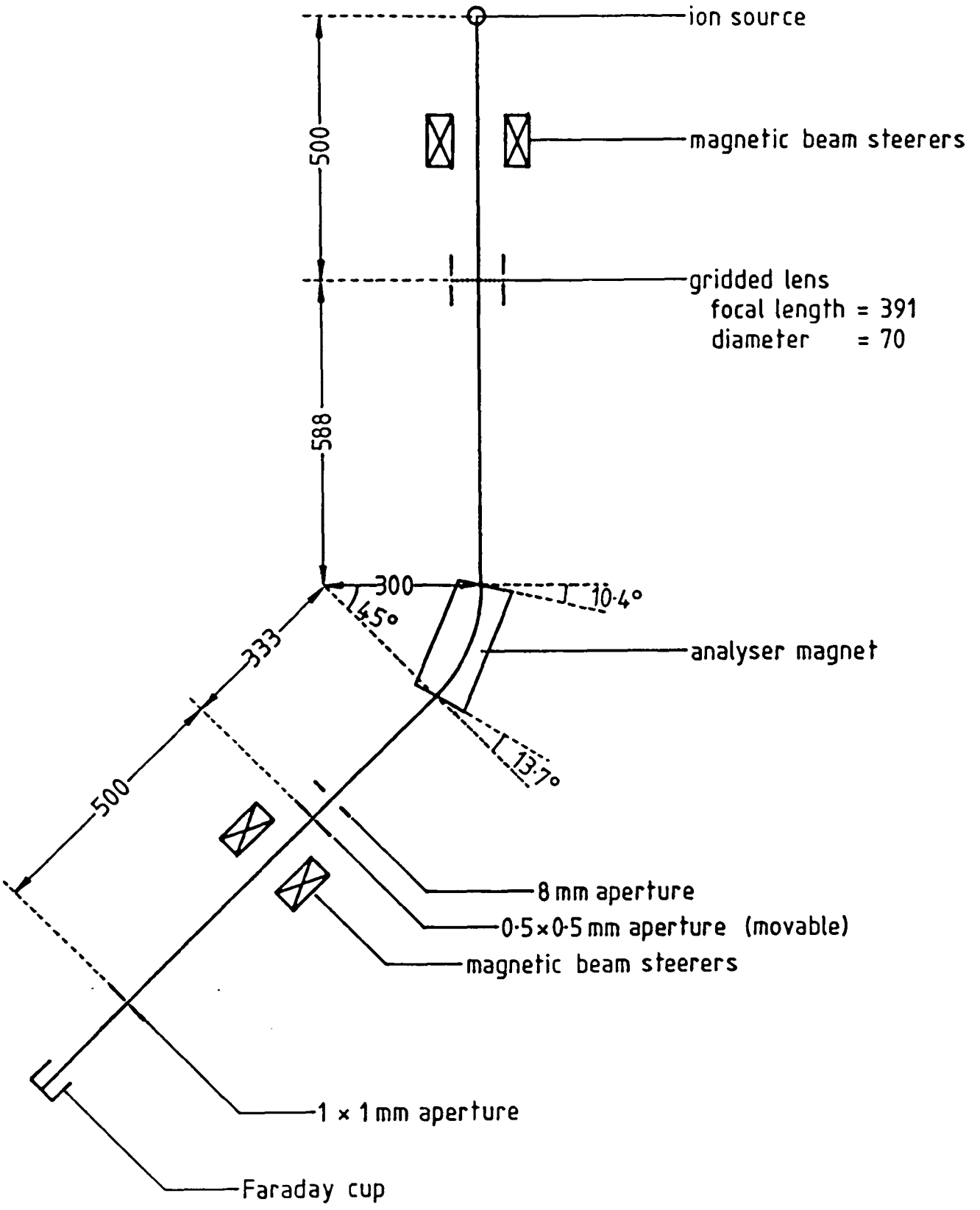

Figure 1

Schematic drawing of the ion source test bench

which is situated between the ion source and the magnet.

As it was intended that the system should be used for optical measurements, considerable care was taken over the fringing fields produced by the magnet. The magnet pole pieces were first machined to approximately the right angle and then measurements of the magnetic field were made along lines parallel to the intended beam axes. The effective edge was determined for each of these lines by numerical integration. This gave the distance of the effective edge from the pole tip and its angle relative to it. Using the results from both ends of the magnet which had different pole tip angles, it was possible to estimate the real pole tip angles required to give effective edges in the right place.

Measurements were also made on the magnet for homogeneity of the magnetic field more than 30 mm inside the magnet (the fringing region having already been taken into consideration). This was found to be constant to within 0.1% in the regions where the ion beam was expected to pass.

From the measurements on the effective edge and field homogeneity it was estimated that ion trajectories in the horizontal plane equidistant from the pole pieces would not suffer from aberrations which would alter their destination at the image waist after the magnet by more than 1 mm. The problem with this estimate is that the ions do not actually follow the lines along which the field measurements were made, and so the effective edge of the magnet for the ions may well be slightly different from that estimated. Focussing also takes place in the vertical direction but the effective edge for this will be different from that for the horizontal focussing and the aberrations will also be different. For the theory of dipole magnets see ref. [1]

The magnet power supply is such that at a ion energy of 24 keV, ions of up to mass 40 can be deflected through 45^{o}.

3.3. Current Measurements

As mentioned above, the abilities to measure currents and resolve different ion masses are closely related. The resolving power of the magnet at the image waist following it is $(0.131/M_I)$ m, where M_I is the mass of the ion. There is a large aperture of 8 mm diameter which is designed to capture the whole ion beam for any given mass and should be capable of resolving equal sized peaks with a mass difference of 1 at mass 12. The aperture has to be this large to allow brightness profile measurements (see below). It is used for determining absolute beam currents and so it should be noted that the beam currents quoted here are almost certainly larger than those that could be injected into the accelerator (by 10% or 20%). There is also a 0.5 mm aperture at the waist which gives very good mass resolution (0.15 amu at M_I = 40) and by integrating the currents passing through this as the magnet field is scanned a mass spectrum can be obtained which gives relative ion currents. The resolution is in practice limited by the image waist size (and therefore ultimately by the ion source) which is approximately 2 mm in diameter for 70% of the beam and this gives a mass resolution of only 0.6 amu at M_I = 40.

3.4. Brightness Profile Measurements

Considering the co-ordinate set in the expression (I/1:1.2.3) we see that the six dimensions of interest are:

(3.4.1) $$q_x \, , q_y \, , \Delta t \, , p_x \, , p_y \, , \Delta E$$

Figure 2 shows how these dimensions apply to the trajectory of an ion and figure 3 shows the co-ordinate system used in this thesis for phase

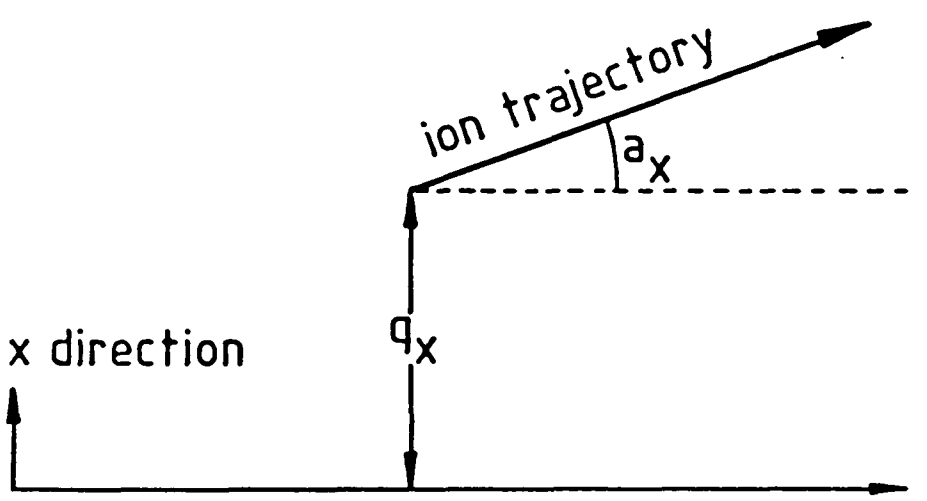

Figure 2

Diagram showing the meaning of the phase space dimensions

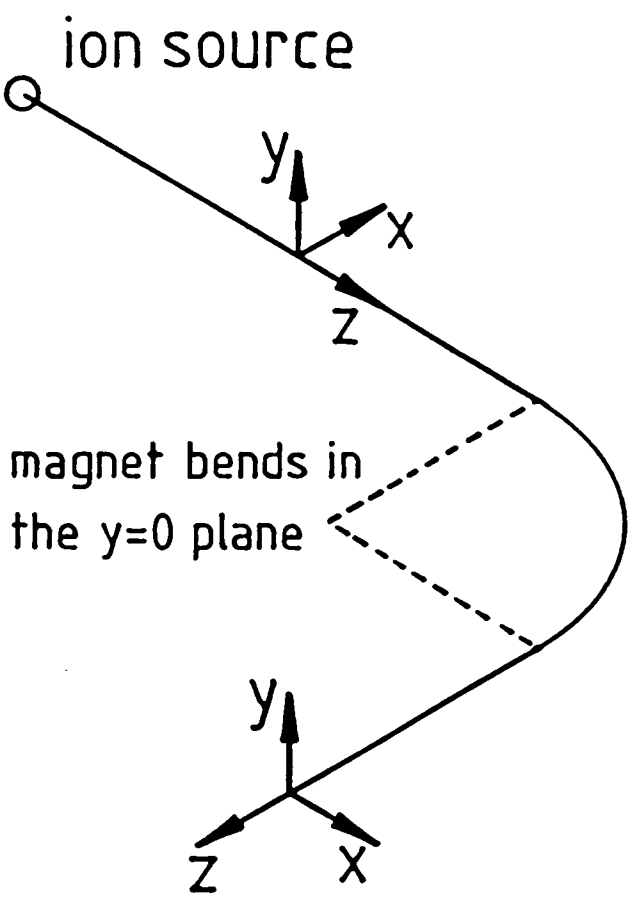

Figure 3

Isometric drawing showing the meaning of the phase space directions as used in this thesis

space measurements.

With ion beam currents of many microamperes at keV energies, it is clearly not possible to make time of flight measurements. The energy spread of the beam could be measured with a retarding field analyser [2] or, with less resolution, by using an electrostatic analyser. Measurements have already been undertaken on the energy spread of sputtered carbon beams [3], and it was decided that for this work the investigations would be restricted to the transverse dimensions. The measurements made on this test bench are integrated over the time of flight and energy dimensions (this is not strictly true as the momentum dispersion of the magnet will introduce mixing between the horizontal x dimension and the energy; however the dispersion is only about 0.5 mm at the image waist for 100 eV and so, given the energy distributions normally found [3], this is not very significant although it does cause some problems in the separation of intense ion beams from those with a slightly higher mass). The co-ordinates used for these measurements are, therefore:

(3.4.2) $$q_x \, , q_y \, , p_x \, , p_y$$

In designing brightness profile measurement equipment it is necessary to decide whether the measurements to be made should be of the type described by equation (I/1:3.5.1) or equation (I/1:3.5.2). The former (in which one integrates over all of the unwanted co-ordinates) has the advantage that the emittance areas measured in this way, for example in the x direction, are a constant of the beam if there is no mixing between the x and y co-ordinates in phase space. In practice, both aberrating fields and space charge violate this condition and so the value of the emittance area is only valid for one particular situation and is not a constant parameter of the ion beam. The second type of measurement (sectional emittance)

would be ideal if there were no skew particle trajectories from the ion source; this is unfortunately not the case. However, since no information is discarded when this type of measurement is made (as it is if one integrates over the redundant dimensions) it is possible to study the details of high order beam transport effectively using this method (see part I). Assuming that the brightness profile in phase space is separable in the x and y dimensions, the two techniques should give the same results and so, although this is not strictly the case, the second type of measurement should enable a reasonable estimate to be made of the ion source's ability to match the acceptance of an optical system. For these reasons, coupled with the fact that they are technically easier to make, it was decided to opt for sectional emittance measurements.

To make these measurements possible there is a 0.5 mm x 0.5 mm aperture at the beam waist following the magnet which can be moved over an 8 mm x 8 mm square in the x, y plane. Following this there is a magnetic beam steerer and a 0.5 m drift length which is terminated by a 1 mm x 1 mm aperture giving an angular resolution of 2 mrad in the x and y planes. The current can be measured before the first aperture (total current measurements), before the second aperture (for measuring the beam intensity over the image waist), and after the second aperture (for measurements of the brightness in the four dimensional phase space given by (3.4.2)). Comprehensive suppression eliminates the risk of spurious currents from secondary electrons.

4. Computer Control

Because of the very large number of measurements that must be made to gain any understanding of the brightness profiles in phase space, some degree of automation is clearly essential. In order to maintain maximum

flexibility it was decided that complete computer control of the test bench was desirable.

4.1. Control Hardware

The computer chosen for this application was the BBC model B microcomputer. This was interfaced to specially designed electronics using two parallel 8-bit ports. The A to D converters of the computer were used directly for all analogue measurements. Those items under this control system are:

a. the first set of beam steerers
b. the analysing magnet
c. the position of the image aperture
d. the range of the meter used for current measurement
e. the second set of beam steerers

and the measurements that can be made are:

a. the hall probe reading in the analysing magnet
b. the current entering the 8 mm diameter aperture
c. the current entering the 0.5 mm x 0.5 mm aperture at the image waist
d. the current entering the final 1 mm x 1 mm aperture

The current measurements b and c are made with a Levell picoammeter with custom built computer controlled range changing, and the current d is measured by a Keithley electrometer.

4.2. Control Software

Software for operating the test bench has been written in BBC basic

and performs the following operations:

a. Initial set up: this sets the magnetic field of the analyser magnet to the correct value for the transmission of $^{12}C^-$.

b. Beam steering: this is done by the operator, using software control. The settings for the first set of steerers are optimised for maximum transmission through the 0.5 mm x 0.5 mm image aperture.

c. Mass selection: this sets the magnetic field of the analyser magnet to the correct value for transmission of the desired ion mass/charge ratio and scales the settings of the first set of magnetic beam steerers appropriately.

d. Mass spectrum measurement: as for c, the mass is scanned through the desired range and the current passing through the 0.5 mm x 0.5 mm image aperture is integrated and normalised to give a relative intensity mass spectrum.

e. Optical measurements: there are essentially four different types of measurement that are catered for at present; these are:

1. the current density across the image waist $I(q_x,q_y)$
2. the brightness profile $g(q_x,a_x)$
3. the brightness profile $g(q_y,a_y)$
4. the brightness profile $g(a_x,a_y)$

All of these are taken on a 41 x 41 grid giving a total of 1681 individual measurements for each. The position co-ordinates q_x and q_y

mechanically scanned
are defined by the 0.5 mm x 0.5 mm aperture, and the angular distribution of the beam in a_x and a_y is sampled by scanning the second set of beam steerers with due allowance for the position of the slits and the magnetic rigidity of the ions.

measurement	expression
$I(q_x,q_y)$	$\int_{a_x=-\infty}^{+\infty}\int_{a_y=-\infty}^{+\infty} f(q_x,q_y,a_x,a_y)\,da_x da_y$
$g(q_x,a_x)$	$\int_{q_y=-\Delta q}^{+\Delta q}\int_{a_y=-\Delta a}^{+\Delta a} f(q_x,q_y,a_x,a_y)\,dq_y da_y$
$g(q_y,a_y)$	$\int_{q_x=-\Delta q}^{+\Delta q}\int_{a_x=-\Delta a}^{+\Delta a} f(q_x,q_y,a_x,a_y)\,dq_x da_x$
$g(a_x,a_y)$	$\int_{q_x=-\Delta q}^{+\Delta q}\int_{q_y=-\Delta q}^{+\Delta q} f(q_x,q_y,a_x,a_y)\,dq_x dq_y$

Notes:

Measurement resolution: $\pm$ 0.25 mm, $\pm$ 1.0 mrad

Δq = 0.25 mm Δa = 1.0 mrad

* in practice the limits are about 40 mrad rather than ∞

Table 4.2.1
Definition of measurements made on the ISTB

The results of these measurements are displayed on a false colour scale as they are taken; they are also stored on floppy disc for subsequent transfer to another computer so that they can be analysed.

For reference, table 4.2.1 gives the mathematical description for the optical measurements described above with the integration over the Δt and ΔE co-ordinates assumed to be implicit. (See chapter I/1 for a

complete discussion of the notation and theory.)

All of the software for these measurements is menu driven, so that the equipment can be operated without a detailed understanding of the workings of the system.

An interface has also been designed and built so that the same measurements can be made on the injection beam line of the Oxford radiocarbon accelerator but problems with suppression have so far made this of only limited use.

Summary

An Ion Source Test Bench has been built which is capable of monitoring the output from an ion source and of making optical measurements on the ion beam produced. These measurements are of a kind which is useful in the study of ion optics and also of use in determining the emittance of an ion source which is required for matching to the acceptance of a different optical system.

References

[1] J.J. Livingood, The Optics of Dipole Magnets (Academic Press, New York, 1969).

[2] G. Doucas, Int. J. Mass Spectr. Ion Phys. 25 (1977) 71.

[3] G. Doucas, J. Phys. D 17 (1984) 429.

Chapter 2

Ion Source Design

Introduction

As discussed in the introduction to this part of the thesis, it was decided that ion sources similar to Middleton's High Intensity Sputter Source (or HISS) [1,2] showed the greatest potential for improvements in radiocarbon dating by AMS. The design criteria for this type of source are discussed here and details of the Oxford Gas Ion Source (or OXGIS) designed specifically for this work are given.

1. The High Intensity Sputter Sources

Figure 1 is a sectional drawing of a typical version of the HISS and shows all of the main features of the design. The design strategy which has been employed in the design of this type of source can be looked at in relation to different aspects of its operation:

1.1. Overall Voltage Configuration

Figure 2 shows the potentials of the different parts of the source. The ioniser is at a higher potential than the sputter target by V_{sp} so that the Cs^+ ions formed are accelerated on to it. This potential also provides the initial acceleration for the negative ions produced. The target is at a potential V_{ex} relative to the extract electrode which is normally grounded so that the negative ion beam produced by the source has an energy of $-V_{ex}$ eV. Typical values for V_{sp} and V_{ex} are 5 kV and -20 kV respectively. It is a feature of this type of source that the sputtering

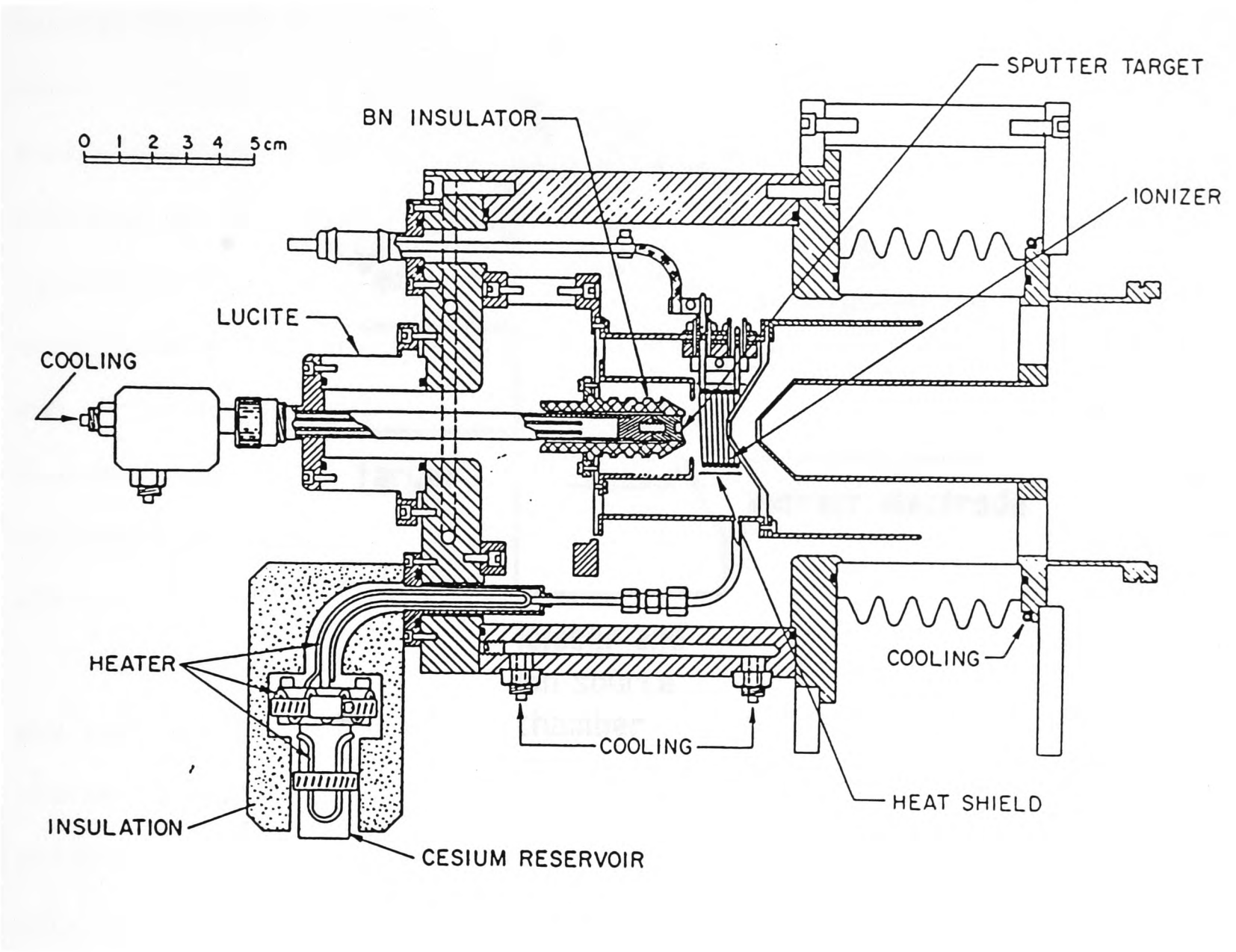

Figure 1

A sectional view of a High Intensity Sputter Source (from ref. [2])

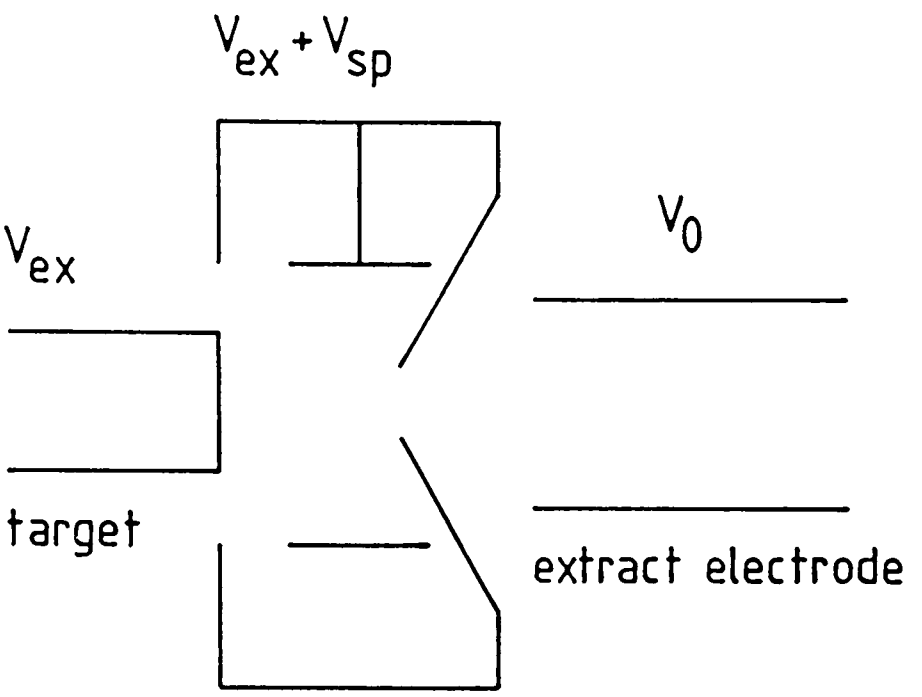

Figure 2

The electrostatic potentials in a HISS

energy can be varied independently of the extract energy.

1.2. Caesium Vapour Production and Control

A reservoir of caesium is maintained in an oven which is situated outside the ion source housing; this can be loaded with ampoules of the metal. From here the metal vapour diffuses along a tube into the ion source chamber. The oven is heated to a temperature T_{ov} at which the caesium vapour pressure gives the required flow down the tube; it is essential that the tube itself is kept at a temperature which is significantly higher than T_{ov} or else the caesium flow will be attenuated and no longer controllable by altering T_{ov} (for this a trace heater is employed; see figure 1). The caesium vapour pressure in the oven can be estimated from ref. [3], but typical oven temperatures lie between 410 and 470 K.

Once inside the ion source chamber the caesium must not condense on any part of the source other than the target and so the entire ion source chamber (including the target insulator) is kept at a high temperature (circa 670 K [2]). The vapour is fairly well contained in the chamber, the only mechanisms for loss being diffusion through the extract aperture and condensation on the sputter target. The temperature is maintained by radiation from the ioniser.

Because of the benefits of caesium on the target surface (see chapter I/1 and ref. [4]) the target itself must be cooled. It should be noted that most of the caesium arriving at the sputter surface will be from the Cs beam rather than in the vapour phase; this is essentially because of the very large ratio of the ioniser area to the sputter surface area [5]. The target head is cooled from behind with paraffin which is fed down the target probe by way of two concentric tubes (a third is used for feeding gas to the target when that is required).

Recent developments [6] suggest that if the caesium leaving the feed tube is directed towards the ioniser the confinement provided by the chamber is not necessary and this also underlines the fact that caesiation of the target from the vapour phase is not important.

1.3. Caesium Ionisation and Focussing

The caesium is ionised on a hot tantalum surface. This can be either a coiled tantalum coaxial cylinder as shown in figure 1, or by a machined spherical ioniser [6]. Preliminary indications are that the performance of the coiled ioniser is less variable and the ioniser less prone to ioniser contamination (as it does not lie directly in front of the sputter target) [6]. The advantages of the spherical ioniser are slightly higher currents with solid targets and possibly lower emittance areas (see ref. [7] for measurements of the emittance); these advantages arise because of the better focussing of the caesium beam. (Ref. [6] gives a beam spot size of <0.7 mm diameter; spot sizes for the cylindrical ioniser in OXGIS are <1.0 mm diameter; the main difference is probably a reduction in the 'halo' around the central intense part of the beam.) In prolonged operation there is also another advantage: the repeated cooling and heating cycles can cause the coiled ioniser to shift with time, and the machined cylindrical ioniser clearly does not have this problem. (It can be overcome by spot welding tantalum strips to the coil [2].)

The ionising surface is kept at a temperature of T_i (typically about 1400 K [2]) by resistance heating. The power dissipation is quite considerable (about 400 W) and so the housing for the ion source must be cooled.

1.4. Sputter Targets and Sample Changing

The sputter targets for a HISS are usually set in aluminium or copper

and are firmly attached to the target probe with which they must have good thermal contact (see section 1.2); this arrangement is shown in figure 1. The target itself is typically 1 to 2 mm in diameter as this is the approximate size of the caesium beam.

The main problem with this arrangement is that there is clearly no very simple method of changing targets: the probe, which carries the target at about 25 kV, must be withdrawn from the source, another target fitted, and then the probe reintroduced. In the source shown in figure 1 this must be done through a vacuum interlock.

A different source geometry, without a comprehensive source chamber, might overcome these problems for some applications [6].

1.5. Extraction of the Secondary Ion Beam

The secondary negative ions are accelerated from the surface by the electric fields used to focus the caesium beam. This causes the secondary ion beam to pass through the extract aperture after which it is further accelerated, reaching the energy $-V_{ex}$ eV. The net effect of this is that the beam forms a waist somewhere in the region of the extract aperture. The arrangement normally used is that shown in figure 1 with two truncated conical electrodes forming the extract gap.

One problem with this arrangement is the condensation of caesium on the electrodes which eventually causes voltage breakdown across the extract gap. This can be overcome by introducing a caesium condenser between the ion source chamber and the extract gap [6].

1.6. Secondary Electrons

Because of the high currents at which the HISS can operate there can be considerable problems with secondary electrons. To deal with these, permanent magnets are sometimes used [1,2,6] to deflect the electrons to

some part of the source where they will not do any damage. The main difficulty in dealing with the secondary electrons is the loading of power supplies (the extract power supply and those associated with subsequent electrostatic optical elements).

2. The HISS used for this Research

A version of the HISS very similar to that shown in figure 1 was used for many of the preliminary measurements made for this research. The modus operandi will be discussed in the next chapter, but as they have direct bearing on the design of OXGIS it is useful to mention two aspects of the performance at this stage; these are related to the design of the extract electrode and the position of the target within the ion source chamber.

2.1. The Extract Electrode

In attempting to make measurements on the distribution of the ion beam from the HISS in phase space, it was discovered that the position of the waist at the measurement plane of the ion source test bench was not very stable and the brightness profiles were too unreproducible to enable any useful measurements to be made. This problem was largely overcome when the extract geometry was altered to reduce the intensity of the transverse fields at the point of extraction. In order to achieve this, the aperture in the extract electrode was widened, thereby forming an immersion lens. Figure 3a shows the new extract configuration.

It is an important point to bear in mind in the design of ion sources for AMS, or for any other application where beam stability is important, that regions of intense electric fields are likely to lead to greater fluctuations in the beams profile in phase space when inevitable small changes take place in the conditions of the source.

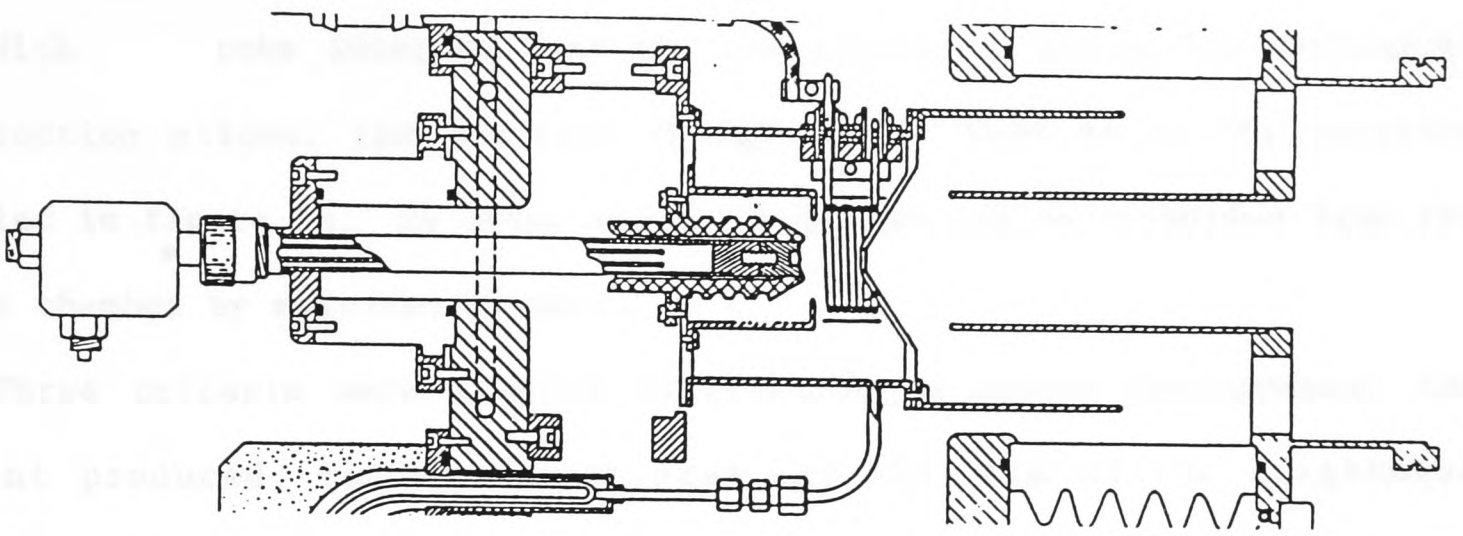

a: NEW EXTRACT ELECTRODE CONFIGURATION

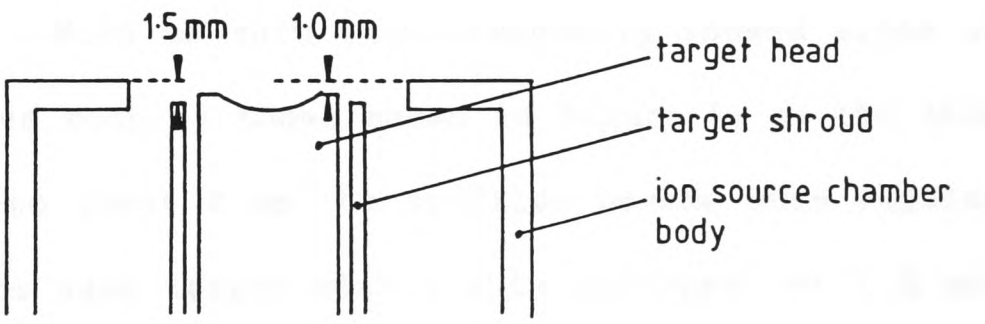

b: DETAILS OF THE TARGET POSITION

Figure 3

Details of the HISS design

2.2. The Position of the Target in the Ion Source Chamber

The position of the target can be varied by moving the probe in or out of the source. Experiments were done to try to determine the optimum position.

With the probe inserted into the ion source as far as the mechanical construction allows, the position of the target head is in the position detailed in figure 3b. By using shims the target can be withdrawn from the source chamber by measured amounts.

Three criteria were studied in relation to source performance: the current produced, the emittance area and the form of the brightness profile. Figure 4 shows the variation in the current produced by the source with different shim thicknesses. Increasing the shim thickness was found to reduce the emittance area slightly (see the next chapter for a discussion of these results) but large differences were found in the form of the brightness profiles. With no shim they frequently showed signs of multiple peaks in phase space such as those shown in figure 5; as the shim was increased in thickness to about 2 mm the profiles became more regular in shape (figure 6 shows the same target with a shim thickness of 1.3 mm) with no noticeable improvement beyond this.

The reasons for multiple peaked distributions are similar to those pertaining to the extract geometry: when the target is further into the source chamber, the transverse fields at the sputtering surface will be more intense and so there is the opportunity for higher order aberrations of the extracted beam. In this position the ion beam profile will be more sensitive to small changes in target geometry.

The increase in the current as the target is moved closer to the extract aperture is presumably because of greater extraction efficiency. It is not clear whether the usable current from the source would be greater

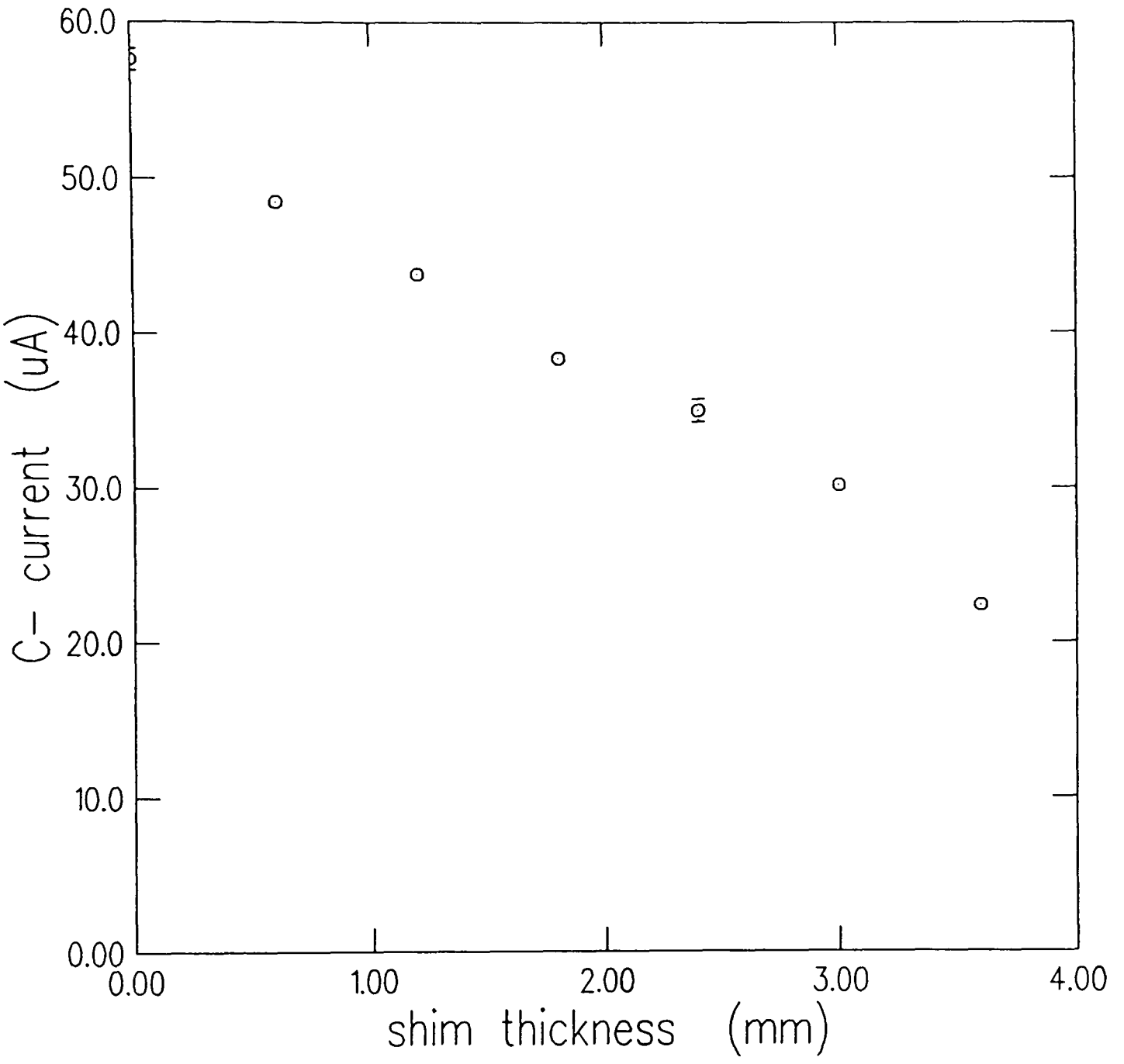

Figure 4

The Variation in C^- current with shim thickness

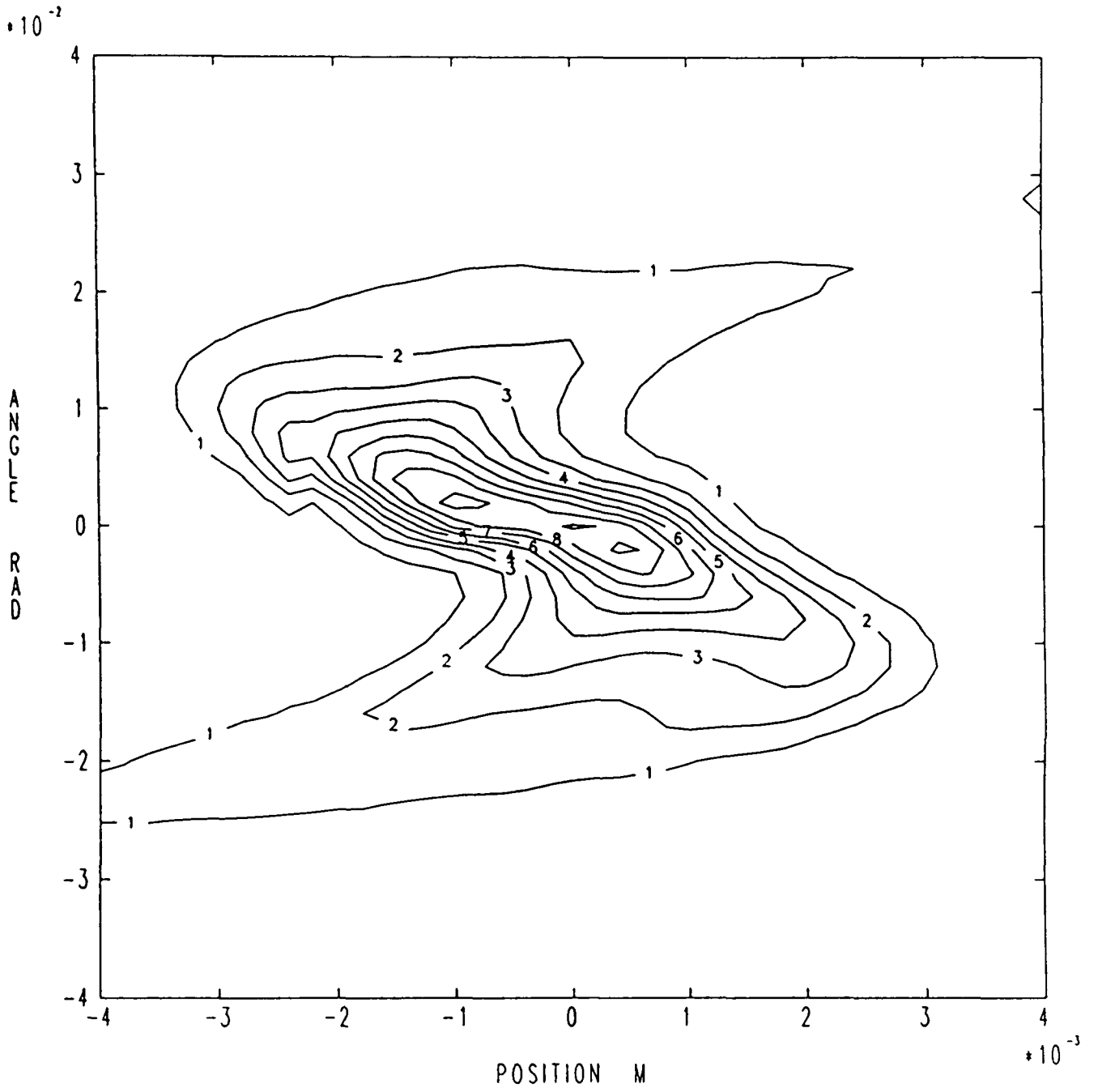

Figure 5

Brightness profile with no shim

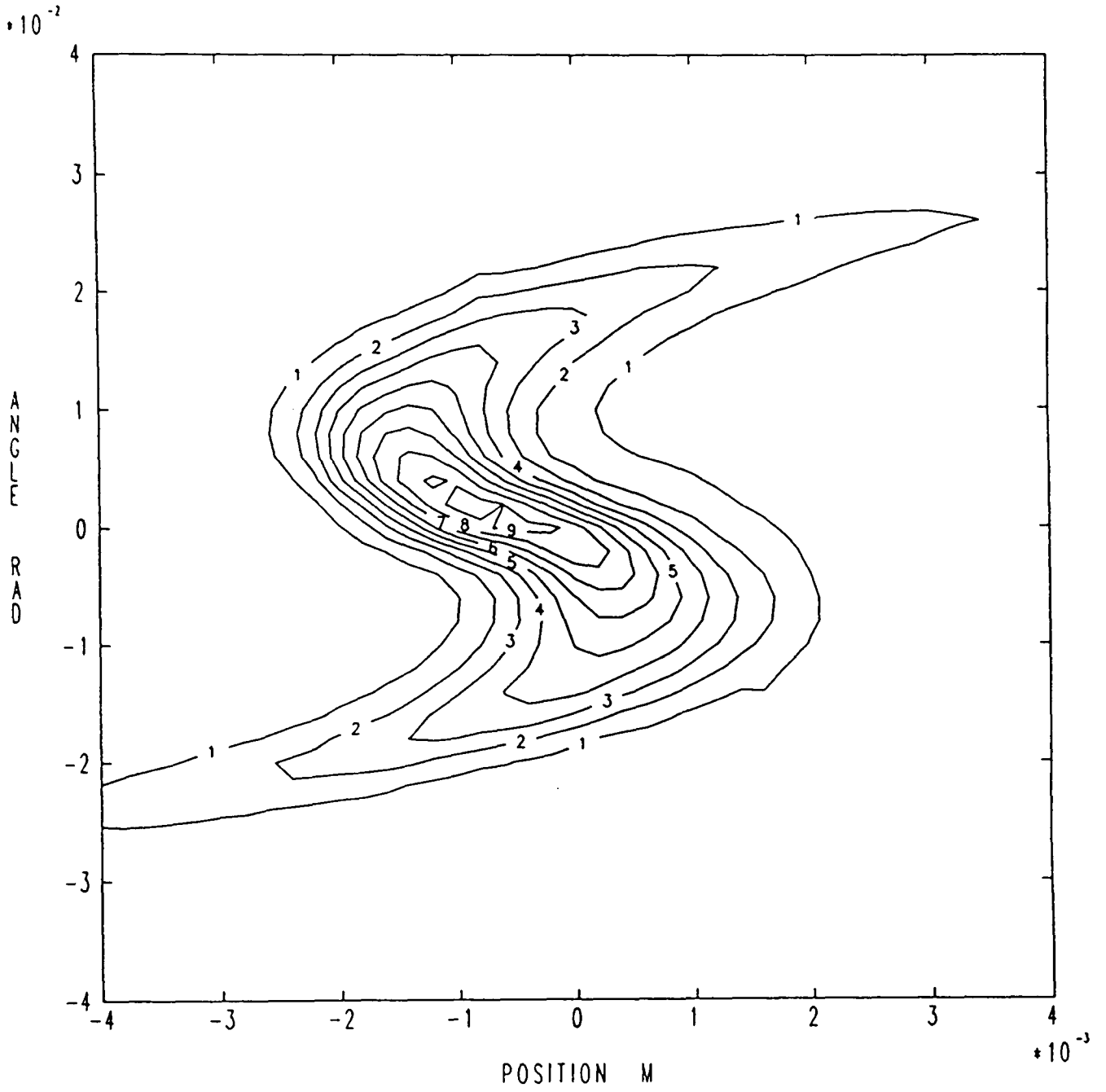

Figure 6

Brightness profile with a 1.8 mm shim
cf. figure 5

in these conditions.

To conclude: the position of the target within the source chamber is to a certain extent a compromise between current and ion beam reproducibility. It would seem that for most applications the target position corresponding to a 2 mm shim in this source would be the most useful.

3. The Oxford Gas Ion Source

The development of a new ion source can be a very lengthy and expensive operation (see for example ref. [1]), and so it was decided that in designing an ion source for the direct use of CO_2 in radiocarbon dating, the tried and tested optical geometry of the HISS described in sections 1 and 2 should be used. This enabled experience that had been gained with the HISS to be directly applied.

3.1. The Ion Source Chamber

Figure 7 is a sectional drawing of the ion source chamber in OXGIS. The most fundamental difference between this and the ion source chamber of the HISS described above is the integral provision for cooling the target. The sputter targets are cooled by pressing them against the chamfer which is itself cooled by compressed air which passes through a tube silver soldered into the chamfer. This is simpler than providing each target with its own cooling circuit. The bulk temperature of targets during operation is believed to be about 400 K (estimated by withdrawing targets and measuring their temperature within one minute), although the temperature of the sputter surface may be higher than this and is difficult to estimate accurately. A liquid such as dodecane can be used for cooling, but there is no improvement in the performance of the source and there is the

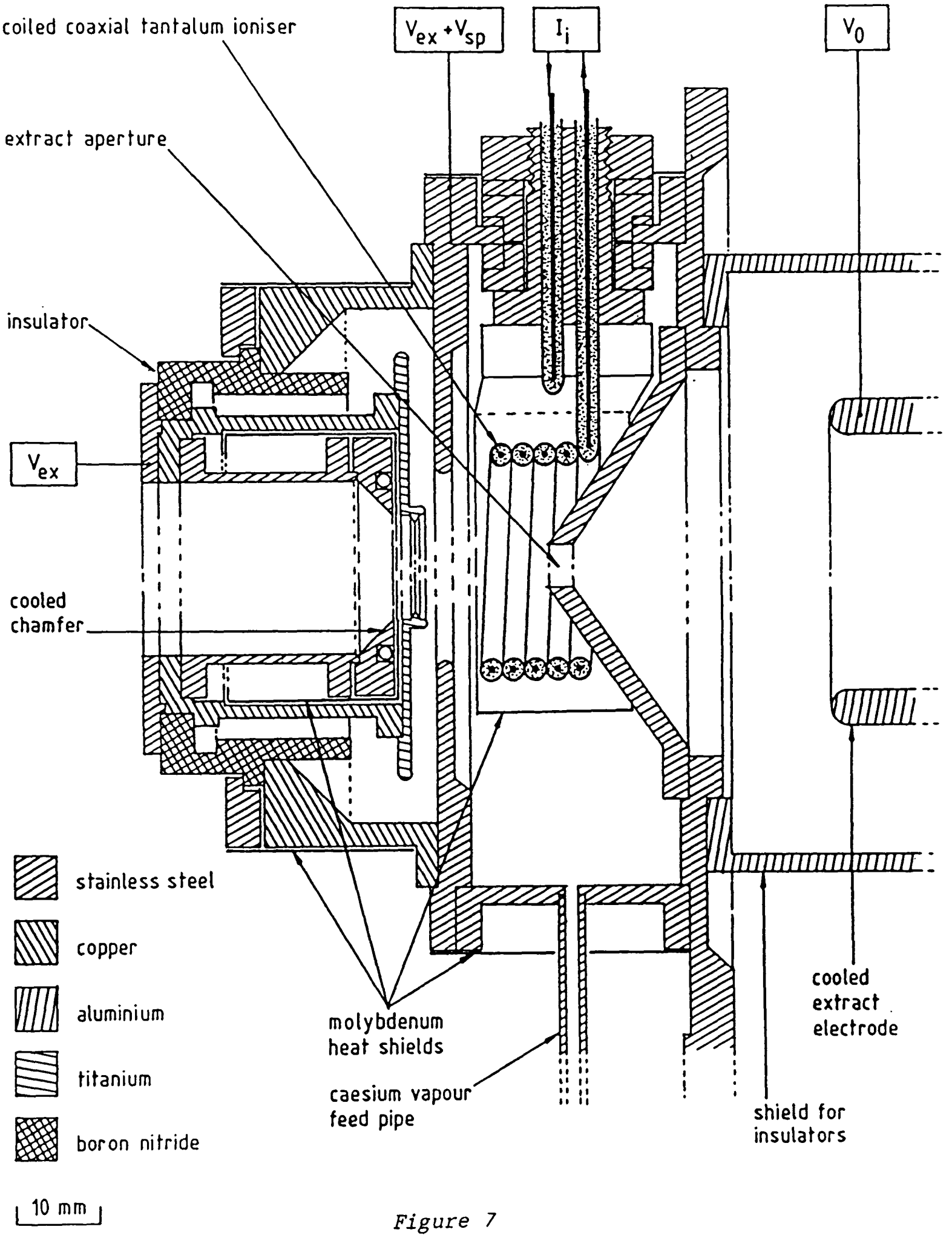

Figure 7

Sectional view of the ion source chamber of OXGIS
Note that the target and its mount are not included

constant danger of the liquid leaking into the ion source and producing large carbon currents (a condition observed on several occasions).

Special care has been taken over the thermal properties of the source. This is necessary because of the proximity of the cooled chamfer and the boron nitride insulator (to see how troublesome this can be, see ref. [1]). The latter must be kept at a high temperature along with the rest of the ion source chamber so that caesium condensation does not take place. To achieve this, heat shields are used to maximise the chamber temperature and high thermal conductivity is maintained between the hottest parts of the source and the insulator, while the cooled chamfer is only connected to the rest of the source by a thin stainless steel cylinder. With the enlarged extract aperture (as described in section 2.1) it is possible to make the extract electrode act as a caesium condenser without risking voltage breakdown across the extract gap.

Secondary electron suppression is not provided as it is not found to be essential, and the introduction of magnetic fields into the region where the ions are not travelling very fast would provide a possible mechanism for isotopic fractionation because of the resulting different beam trajectories for different isotopes: if the field is strong enough to alter the electron trajectories by 1 radian then it would also deflect $^{12}C^-$ ions through more than 6 mrad.

3.2. The Sputter Targets and Sample Changing

Figure 8 shows the design of the sputter targets used with this source for operation with graphite and carbon dioxide. The performance of the different designs for operation with carbon dioxide will be discussed in detail in chapter 4.

In order to avoid the use of a vacuum interlock for changing between different sputter targets, a wheel holding twelve targets is housed in a

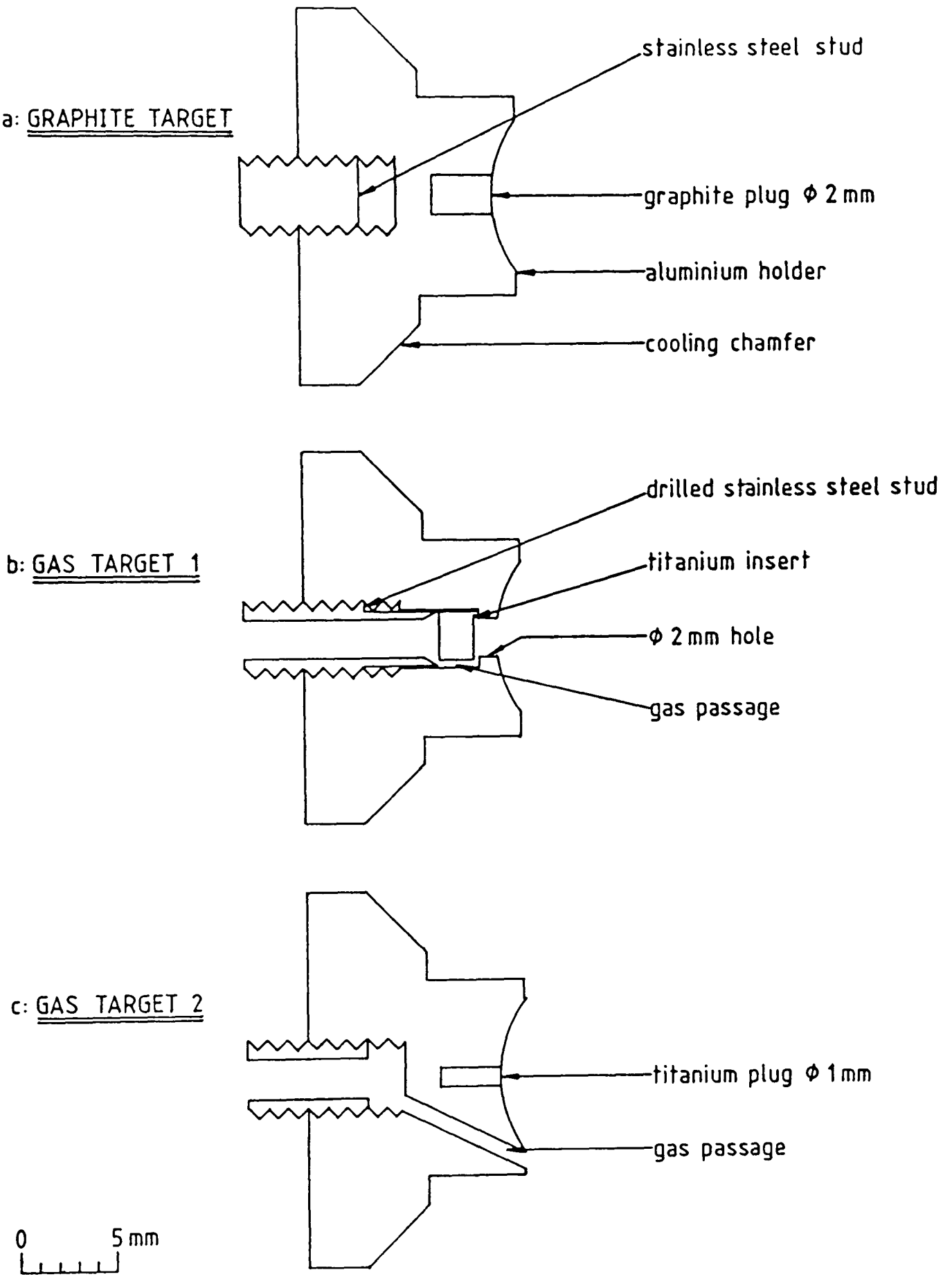

Figure 8

Sectional views of the sputter targets used in OXGIS

chamber behind the ion source. This wheel is turned using a kind of Geneva mechanism which is operated pneumatically. The targets are picked up from this wheel by another pneumatically operated plunger (the target probe) and pushed into the ion source. When the target probe is withdrawn it pulls the target back into the wheel and the whole process can be repeated with the next one. The entire source is shown schematically in figure 9.

Initially, there were many problems with the operation of the sample changing mechanism. The targets must be positively retained in the wheel (so that they do not fall off) and they must also engage with the target probe for insertion into the ion source chamber and, more critically, for withdrawal and replacement in the wheel. Both of these tasks are done by ball detente mechanisms which worked very well in atmosphere but not when warm (about 100^{o}C) and under vacuum. This problem was eventually overcome by using sapphire balls instead of steel ones. Special care was required in ensuring that the contact between these sapphire balls and the other parts of the mechanism had a linear rather than point distribution. It was also found to be essential that the targets had as small a contact area with the sample wheel as possible in order to stop them from binding to it as they are pulled back. All of the mechanical problems have now been overcome.

3.3. The Ion Source Housing and Vacuum System

The fact that ion sources of this type can produce carbon currents at a high efficiency from carbon dioxide [8] is testament to their ability to act as very sensitive residual gas analysers. It is therefore clear that a source for radiocarbon measurements must have a very low concentration of residual hydrocarbons in the vacuum. To achieve this OXGIS has an all stainless steel housing which is sealed with aluminium wire. The only elastomer seal in the system is on the VAT gate valve which separates the

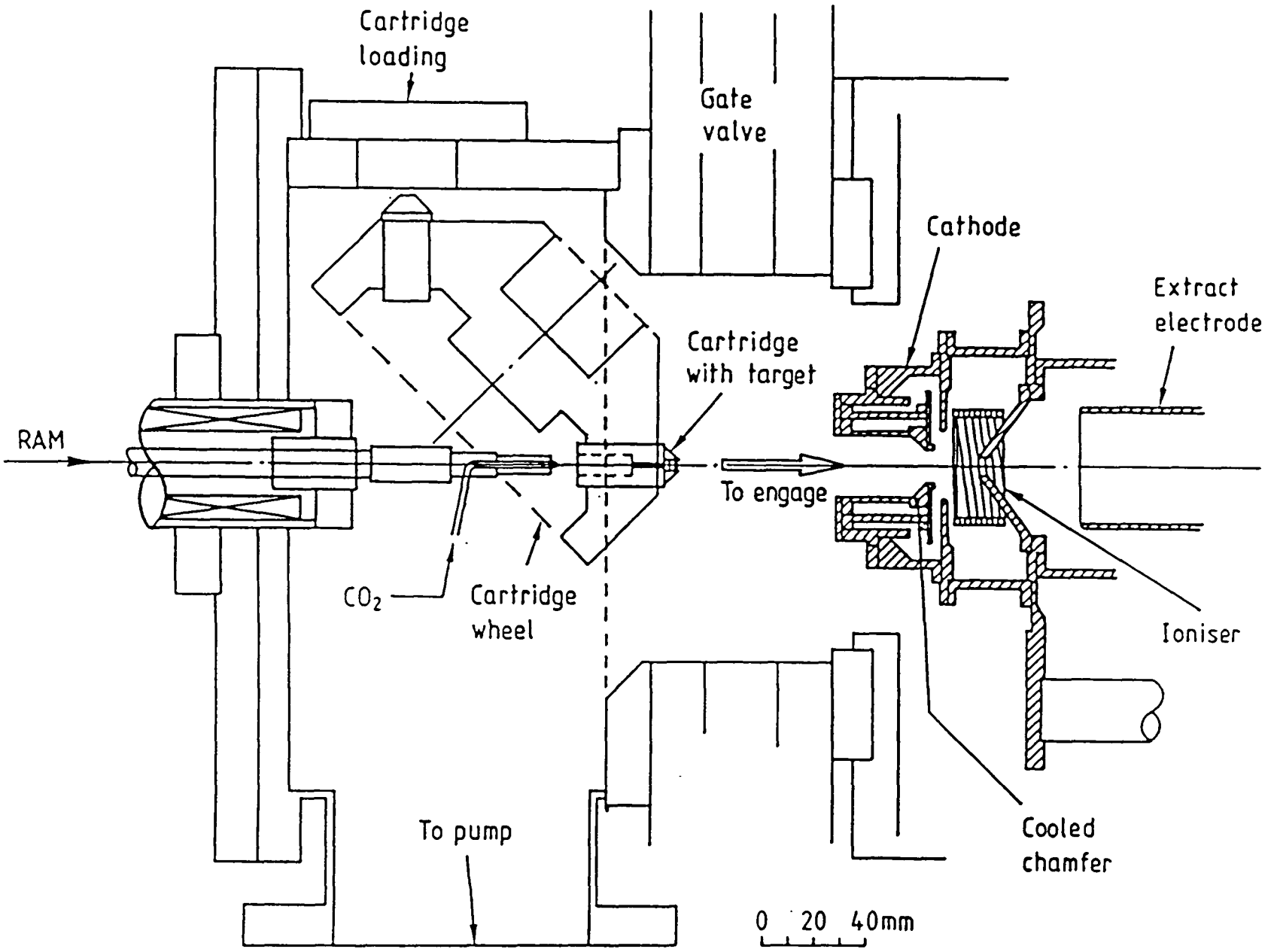

Figure 9

Schematic view of OXGIS

ion source housing from the sample changing mechanism housing; this is necessary to allow the twelve targets to be changed without interfering with the vacuum in the ion source itself. The pneumatically operated rams for rotating the sample wheel and pushing in the target are sealed with welded stainless steel bellows to minimise the risk of contamination.

The ion source is pumped from the beam line side and also from behind via the sample changing mechanism which has its own turbo-molecular pump. The pumping in front of the source is improved by the provision of a liquid nitrogen trap.

3.4. The Gas Handling System

A prerequisite of using a gas ion source for radiocarbon dating is a gas handling system which will allow gases from different samples to be let into the ion source.

A simple gas handling system which is capable of operating with only two different samples has been built and it is this which has been used in the experiments described in chapter 4. It is based around a Balzer sapphire seated UHV gas dosing valve. This allows gas to pass into a 5 ml volume in which the pressure can be monitored so that the flow rate can be measured; a capillary tube (outside diameter: 0.5 mm; inside diameter 0.25 mm) connects this volume with the sputter target holder. All of the volumes in the system can be purged with argon and pumped out. Figure 10 shows a schematic view of this gas handling system.

The gas handling apparatus that will be used for radiocarbon dating is currently under development and figure 11 shows the proposal. Glass ampoules containing the carbon dioxide for measurement are broken in the the evacuated sample reservoirs. Each reservoir is connected to a liquid nitrogen trap which can be heated electrically (such traps have been built; a 5 mg CO_2 sample can be evaporated in 30 s with 100 W heating power and

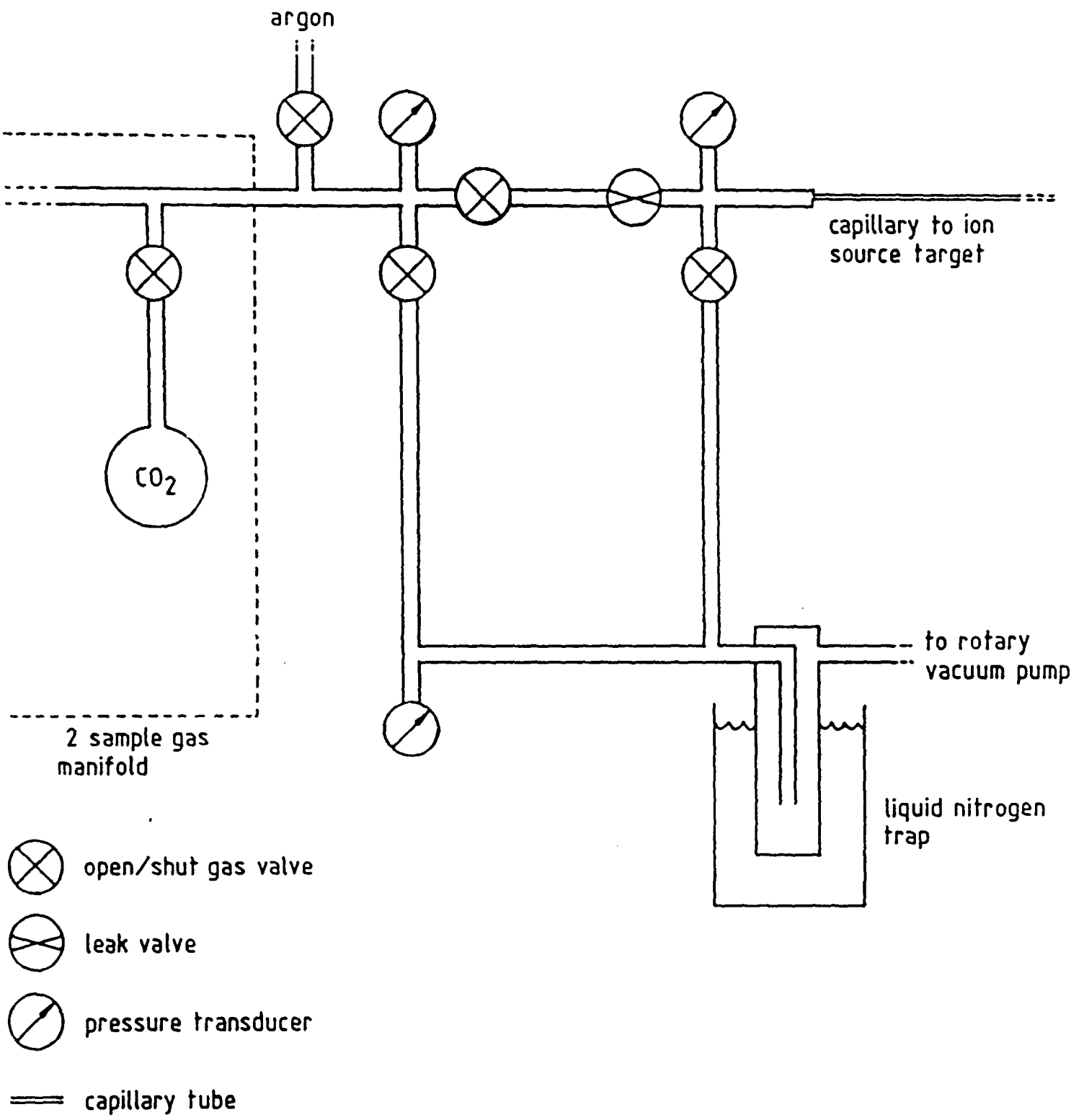

Figure 10

The provisional gas handling system

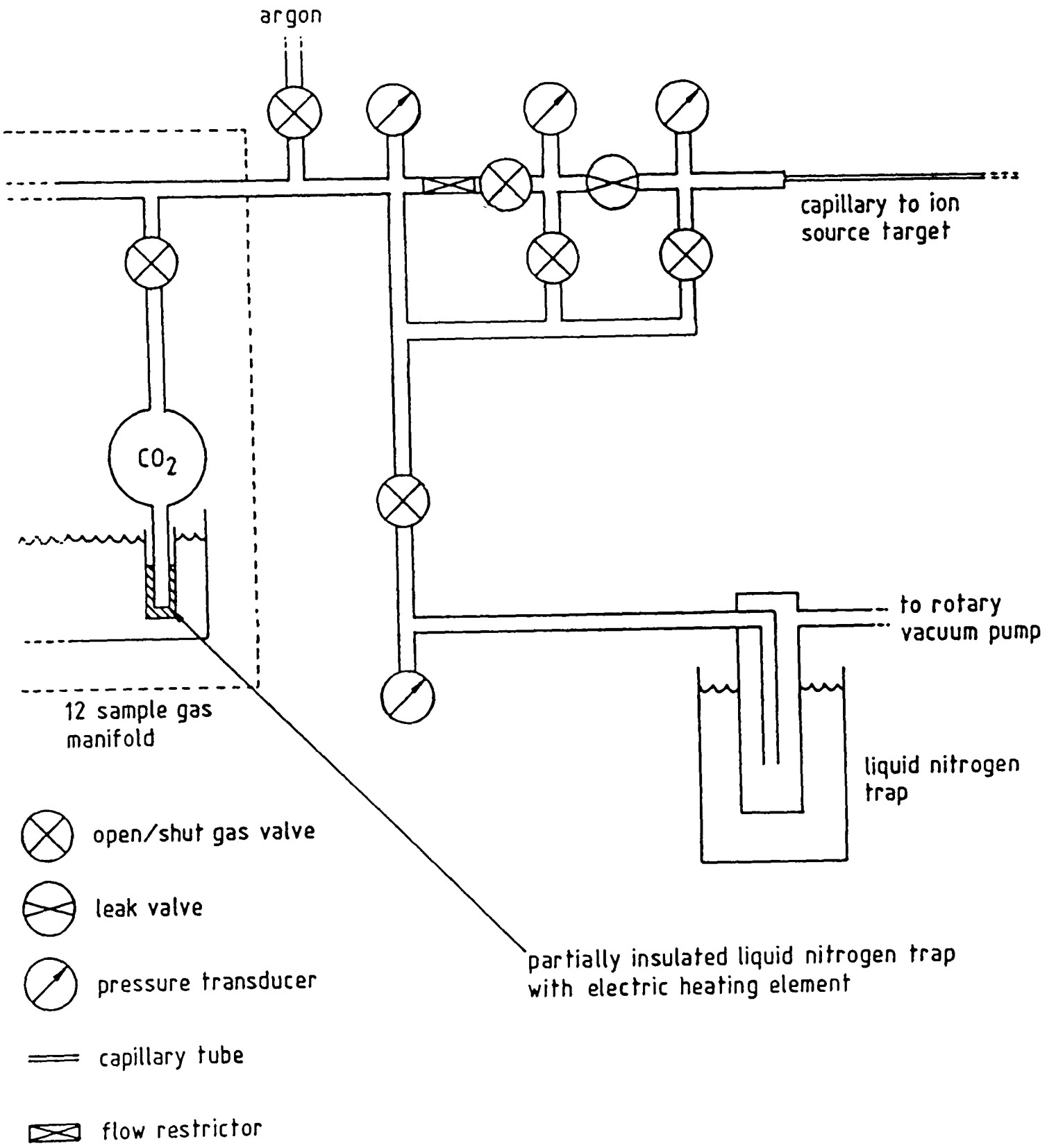

Figure 11

The proposed gas handling system

then retrapped within a similar period). When the gas from a particular sample is required, the valve connecting the reservoir to the rest of the system is opened and the liquid nitrogen trap heated until all of the carbon dioxide has been driven off. Evaporation must be complete so that there is no danger of fractionation. A predetermined quantity of this gas can then be allowed through the flow restrictor and into the space immediately preceding the leak valve (this operation takes place under laminar flow). The gas is bled through the UHV gas dosing valve and through the capillary which leads to the ion source. The pressure between the gas dosing valve and the capillary is used to stabilise the gas flow rate (this will ultimately be controlled so as to maintain a constant C^- current from the ion source). After the gas let into the gas manifold has been virtually exhausted (ie. <5% left), the residual gas is trapped back into the liquid nitrogen trap and the carbon dioxide from a different sample is let into the manifold (meanwhile the sputter target is also being changed). It may prove necessary to flush the manifold with argon between samples but all of the evidence so far suggests that this is superfluous.

One advantage of using liquid nitrogen traps in this way is that the effects of contaminant gases such as H_2O, SO_2, NO_2 et cetera should be kept to a minimum.

With such a system one must be aware of the dangers of isotopic fractionation from the gas transport. The maximum level of fractionation that one can obtain in passing from a high pressure gas to a Knudsen gas during a single continuous process is $(m_L/m_H)^{1/2}$, where m_L is the mass of the light gas molecule and m_H that of the heavy one. For carbon dioxide this gives a maximum $^{12}C/^{13}C$ fractionation of 1.13%. In practice, of course, because the remaining gas is then depleted in the lighter isotope, the overall fractionation decreases as the gas in the gas manifold is used up (see figure 12 for a plot of maximum fractionation versus the proportion

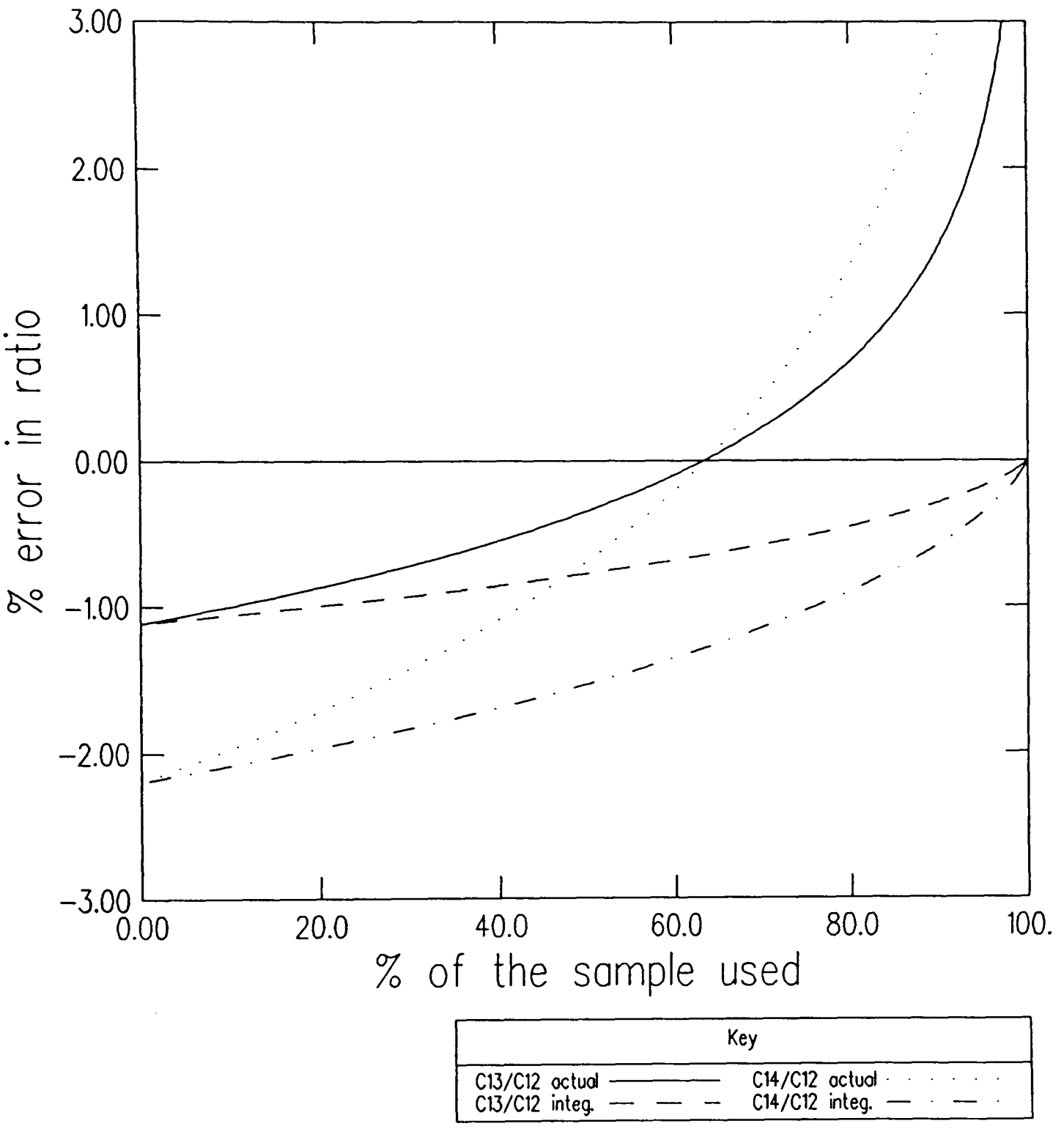

Figure 12

The maximum fractionation due to gas passing from a region of laminar flow to a region of molecular flow versus the proportion of sample used (the instantaneous actual measurement and the integrated measurements are shown)

of the gas used). In this design the problem should be virtually eliminated as the transition from laminar flow to molecular flow takes place part of the way along the capillary which leads to the ion source (the gas entering the capillary under laminar flow will have the original isotopic ratios; under continuous flow conditions, therefore, the gas flowing from the other end must also have the same isotopic ratios). To be sure that very little overall fractionation takes place, a large proportion of the gas that is allowed to enter the gas manifold will be measured. In any case, isotopic effects will cancel if the proportion of samples and standards used is the same.

3.5. Computer Control

A computer control system has been developed for supervision of the ion source, the sample changing mechanism and the gas handling apparatus. The computer used for this task is based on the Z80 microprocessor and runs the CPM 3+ operating system. This allows a high level language to be used (Modula-2) which gives a degree of portability and makes the software very flexible. Because both some of the power supplies for the ion source and the entire gas handling apparatus are at high voltage, the control is effected by passing serial data down optical fibres.

Particular care has been taken with spark protection for the electronics which is directly connected to the ion source. All of the digital and analogue control lines are buffered with resistors and clamping diodes.

The software for this system has been specially written and is operational.

Summary

The features fundamental to the operation of a high intensity sputter source have been evaluated and, by making measurements on such a source, the changes that are needed to make an ion source which is suitable for AMS radiocarbon measurements have been ascertained. Such an ion source has been designed and built complete with a computer control system and gas handling apparatus. A more comprehensive gas handling systems which is now under development is described; this will allow the ion source to be used for routine measurements.

The performance of this type of source will be discussed in the next two chapters.

References

[1] R. Middleton, Nucl. Instr. and Meth. 214 (1983) 139.

[2] R. Middleton, Nucl. Instr. and Meth. 220 (1984) 105.

[3] A.N. Nesmeyanov, Vapour Pressure of the Chemical Elements (Elsevier, Amsterdam, 1963) pp. 146 & 445.

[4] G. Doucas, J. Phys. D 17 (1984) 429.

[5] With a caesium current of 1 mA incident on a 1 mm diameter spot one would need a vapour pressure of 10^{-5} atmos. to get a similar collision rate directly from the vapour phase whereas typical vapour pressures are more than an order of magnitude below this. (All pressures are taken to be at typical source temperatures which are about 670 K)

[6] R. Middleton, Workshop on Techniques in A.M.S., Oxford Radiocarbon Accelerator Unit (1986) 82.

[7] G.D. Alton, J.W. McConnell, S. Tajima and G.J. Nelson, Nucl. Instr. and Meth. B24 (1987) 826.

[8] R. Middleton, Nucl. Instr. and Meth. B5 (1984) 193.

Chapter 3

Ion Beams from Graphite

Introduction

In order to investigate the performance of the high intensity sputter source and OXGIS without the complications introduced in using carbon dioxide, the HISS was used with graphite targets. These experiments yielded useful information about the operation of these sources as well as being of interest in the light of possible future applications of this source with graphite (discussed below). All of the experiments described here were performed on the HISS described in the previous chapter, but all comments concerning the general operational behaviour apply to both the HISS and OXGIS.

The operation of these sources can be divided into several distinct parts each of which will be considered in the course of this chapter:

1. the maintenance of electric fields
2. the control of caesium flow
3. the ionisation of the caesium
4. the focussing of the caesium beam
5. the sputtering of the target
6. the extraction of the secondary beam

1. The Maintenance of High Voltage

1.1. Typical Voltages

The extract voltage V_{ex} is largely constrained by the subsequent ion

optical elements in the accelerator injection system. For the reduction of space charge effects and in order to reduce the spacial components of the phase space before the beam is injected, it is clearly advantageous to have as large an extract voltage as possible. This is usually limited by the strength of the injection analyser magnet or the energy pulser (which allows different isotopes to pass through the same magnetic field). With the modified extract geometry described in the previous chapter, voltages of up to -30 kV can be used. (This is the limit of the power supply and is also close to the breakdown limit of the feedthroughs, isolating transformers, et cetera, and so no attempt was made to apply higher voltages.) The extract voltage applied during the experiments described here was -25.84 kV.

The optimum sputter voltage V_{sp} is determined by the sputtering process and the factors relating to this will be discussed in section 5. Typical values are around 5 kV but voltages of up to 10 kV can be used (again this is the limit of the power supply but there is nothing to be gained by increasing V_{sp} beyond this: see below).

1.2. Voltage Breakdown on Insulators

No problems have been encountered with voltage breakdown across the insulators inside the ion sources (HISS or OXGIS). This characteristic is ascribed to the careful thermal design of the sources which keeps the boron nitride insulators at a high temperature, and to the shielding of the other insulators from caesium vapour.

1.3. Excessive Currents

The power supply used for providing V_{sp} has a limited current load capacity of 10 mA, and if the caesium vapour pressure in the source is too high the power supply becomes overloaded by the secondary electron current.

To remedy this, the caesium vapour pressure, the ioniser temperature or the sputter voltage must be reduced. These currents can also cause problems for subsequent optical elements (see last chapter, section 1.6).

1.4. Debris Induced Voltage Breakdown

If debris from the sputter target falls into the gap between the sputter target and the ion source chamber, voltage breakdown can occur. This effect has been observed on OXGIS and was believed to have been a consequence of mixing copper target holders with the aluminium ones usually used. There is normally a build up of the target holder material inside the source and it is possible that the copper was not able to adhere satisfactorily to the aluminium already deposited.

After prolonged use, the ion source must be cleaned. It is not yet clear how frequently this is necessary and this will clearly depend on how the source is operated. Intervals of 300 to 500 hours of operation between cleaning are certainly possible.

2. The Control of the Caesium Flow

The control of the caesium vapour pressure in the ion source chamber is effected by varying the temperature of the oven, T_{ov}. An oven temperature of about 430 K is typical if C^- currents of about 100 μA are required from graphite (or 20 μA from carbon dioxide). As discussed in the previous chapter it is essential that the caesium vapour feed pipe is kept at a temperature which is greater than T_{ov}. If the ion source has been cleaned and there is no caesium in the feed pipe it can take several hours for the caesium flow to come to equilibrium, and if the oven has been opened to air it is often necessary to heat it to a higher temperature than normal in order to make the source function properly. If, as is normally

the practice, the source is cooled down fairly quickly so that there is a distribution of caesium throughout the length of the caesium vapour feed pipe it takes only about an hour to reach normal operating conditions once the source has been heated up.

3. The Ionisation of the Caesium

The electric fields within this type of ion source are not high enough to affect the ionisation probability. The ionisation energy of caesium is 3.94 eV and the work function of tantalum is 4.1 eV so ion formation is energetically favourable. The probability that an ion forms when a caesium atom strikes the ioniser will depend on the residence time on the surface, the form of the valence electron's potential barrier between the atom and the surface, and the surface temperature.

3.1. The Temperature of the Ioniser

Because the ioniser coil is suspended in vacuo, most of the heat transfer between the coil and the ion source will be by radiation. The power radiated by a body is proportional to the fourth power of its temperature (Stefan's law). As the temperature of the ioniser is approximately twice that of the ion source chamber (see section 1.3 of the previous chapter) the radiative heating by the rest of the source will be $(1/2)^4$ times lower than the radiative loss. Thus one can write the approximate equation:

$$T_i = k\,(V_i I_i)^{1/4} \tag{3.1.1}$$

where V_i is the voltage across the ioniser, I_i is the current through it and T_i is the temperature of the ioniser. A lower limit for the constant k

can be determined from Stefan's law for black body radiation; this gives $k > 260$ K $W^{-1/4}$. In practice k will be higher than that predicted by Stefan's law because the ioniser is a clean metal and because of the heat shields.

The ioniser has been operated with power dissipations of up to about 400 W which will, from the above equation, correspond to a temperature of greater than 1200 K (believed to be about 1400 K [1]). The temperature of the ioniser is unlikely to be constant over its entire surface, and this should be borne in mind when considering the next section.

3.2. The Variation of Caesium Current with Ioniser Temperature

Because of high electron currents, the load on the power supply that maintains the voltage V_{sp} is not a good measure of the caesium current. A better monitor of the caesium current is the C^- current produced from graphite which is thought to be typically a third of the caesium current (as measured on a modified UNIS source [2]). Although, obviously, this will be affected by many other factors such as the temperature of the target, the variation with caesium current is likely to be the dominant effect. The C^- current was measured against ioniser temperature. The results are plotted in figure 1; the temperature scale has an arbitrary magnitude but 1 corresponds to the maximum operating temperature discussed above. The fact that the caesium current reaches a plateau at around the normal operating temperature indicates that a large proportion of the caesium atoms striking the ioniser are ionised. Hence the vapour pressure of caesium needed to produce 1 mA of Cs^+ (assuming an effective ionising surface of about 10 cm^2) is roughly 10^{-8} atmos. which is at least a hundred times larger than the estimated vapour pressure of the caesium in the oven [3]. (This is expected because of the poor conductance between the oven and the ion source chamber relative to the conductance out of the

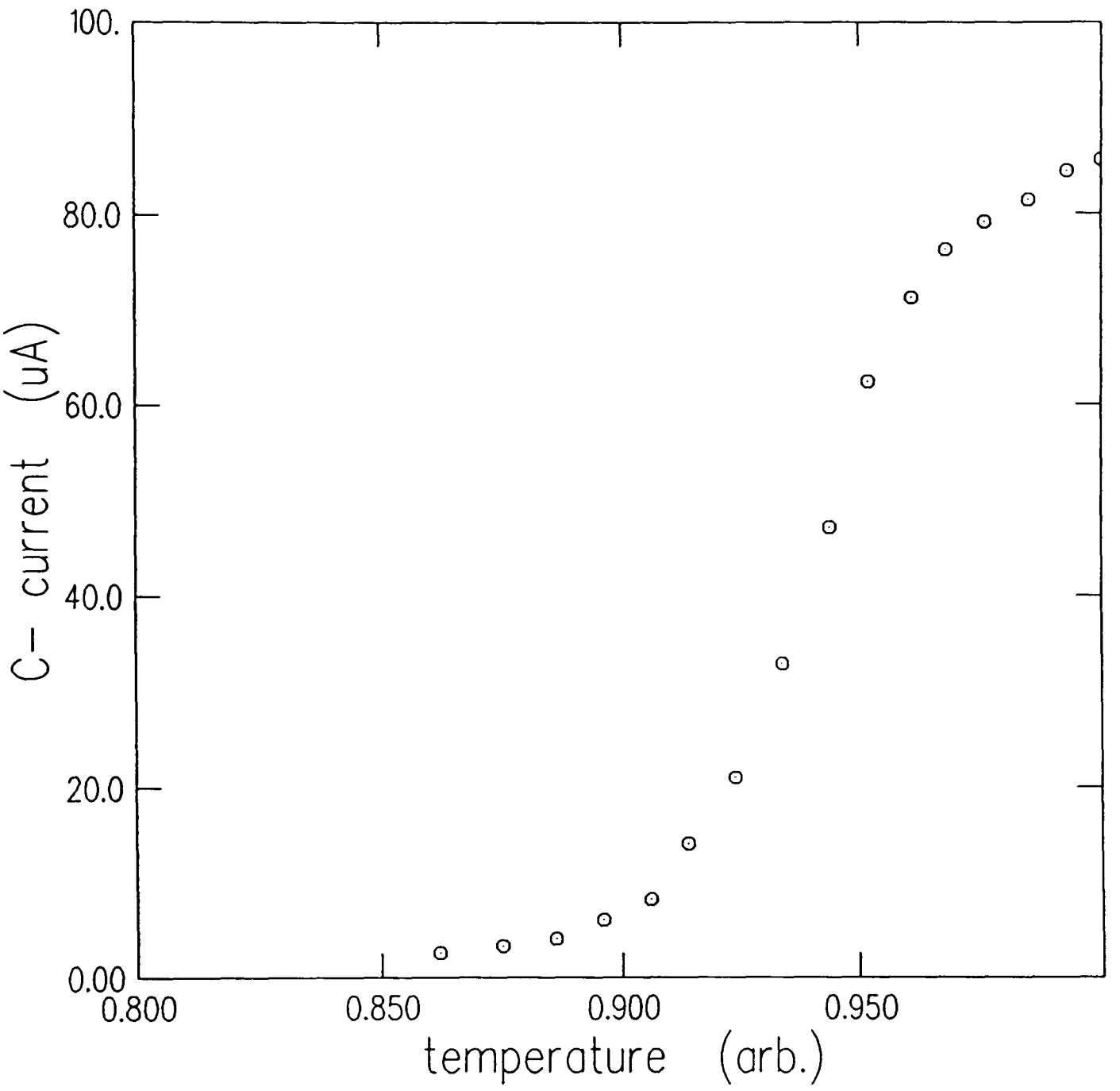

Figure 1

The variation in C^- current with ioniser temperature

chamber.)

4. The Focussing of the Caesium Beam

The focussing of the caesium beam in these ion sources is dependent only on the geometry of the ion source and on space charge effects. Because of the thermal velocity distributions of the ions at formation, there could also be a small effect when V_{sp} is changed, but this change will be difficult to distinguish from changes in the sputtering process and in the space charge forces. Because the emittance of the ion source is ultimately determined by the primary caesium beam it is worth investigating changes in the emittance when the source geometry is altered. Similar investigations in relation to changes in the caesium current might also shed some light on space charge effects within the source.

4.1. Ion Source Geometry

As indicated in the last chapter, it was decided that changes in the design of the optics of the ion source was beyond the scope of this project, and so the only alteration that has been made to the geometry of the source itself is the change in the target position (for the effect of altering the extract electrode, see section 6). The effect of this on the emittance was not significant within the scatter of the data, although from the current it is clear that a greater proportion of the secondary ion current is extracted if the target is nearer the extract aperture. There are probably four effects which are important here: firstly, the position of the target will affect the focussing of the caesium beam; secondly, if the target is withdrawn from the source, an effective immersion lens is formed at the target which will smooth out the beam's distribution in phase space thereby decreasing the effective emittance (but not the actual or

measured emittance); thirdly, the further the target is from the exit aperture the less of the beam is extracted and this should reduce the beam emittance; finally there are the effects of secondary ion beam transport (see below). It is difficult to unravel these different factors.

Some indication of the caesium focus can be determined from the sputter damage to targets and this is how one checks for misalignment of the ioniser during operation. With the range of target positions investigated, the sputter damage was always concentrated in a region with a diameter of circa 1 mm surrounded by a large region (up to about 5 mm in diameter) with less substantial sputter damage. In order to get any detailed information from this one would have to measure sputter rate distributions; this was not done as it was already clear that using a spherical ioniser one could reduce the halo of the caesium beam [4], although recent experiments suggest that this may not have an appreciable effect on the emittance [5].

4.2. Caesium Beam Current

Attempts were made to measure the effect of the caesium current on the emittance. The results of these experiments are shown in figure 2. The square data points represent emittance measurements made on a single target while keeping all other source conditions the same; the data points marked with crosses represent measurements made under a variety of conditions but as no systematic variations in emittance with these other conditions were observed, it seems reasonable to include these points.

The rise in the emittance with current, particularly in the region where the carbon current is between 40 and 70 μA, could be explained in terms of space charge defocussing the caesium beam, however the subsequent fall shows that there is another effect. This is believed to be a result of the aberrations caused by the space charge of the secondary ion beam

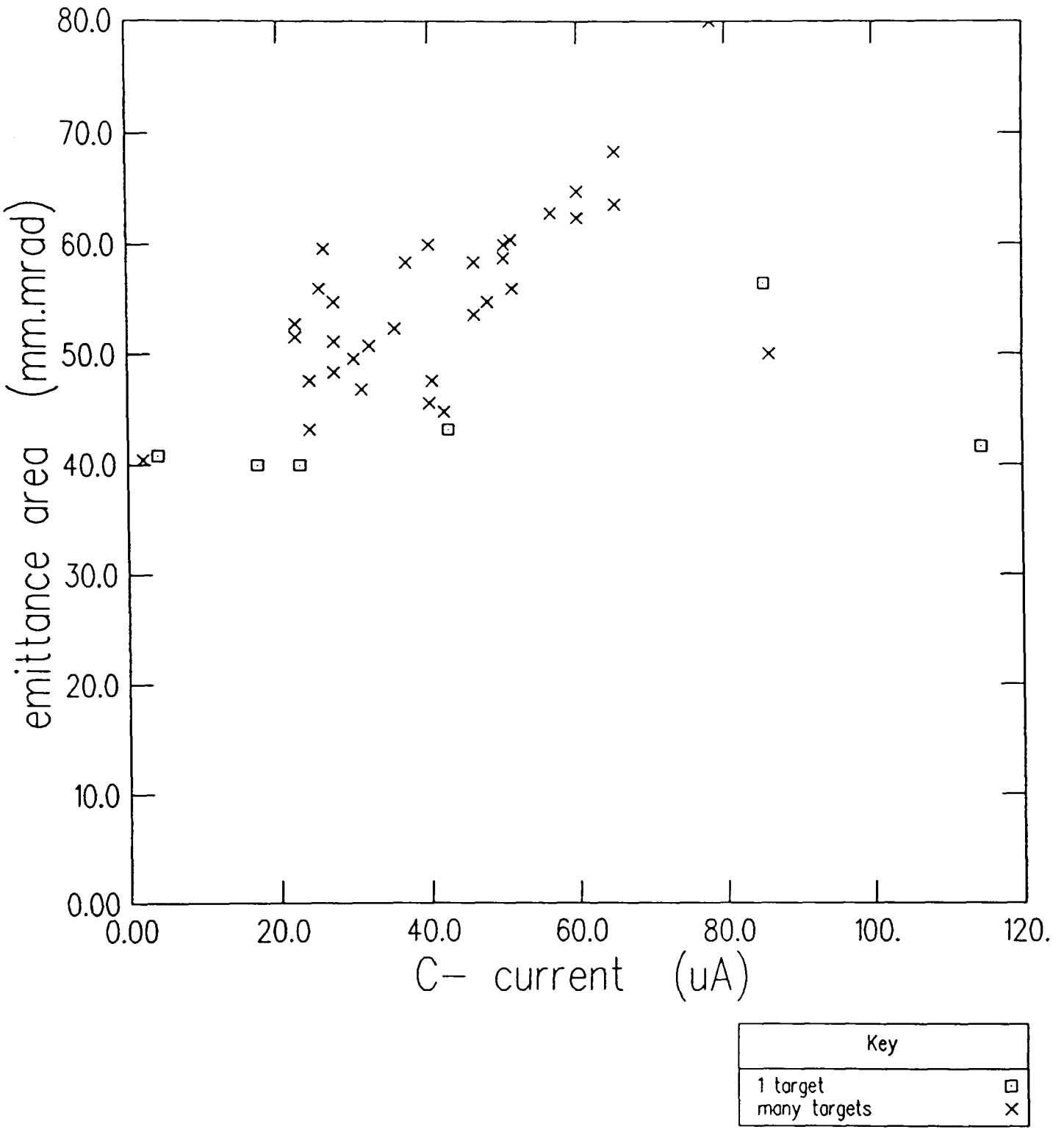

Figure 2

The variation in beam emittance with C^- current (70% of the beam)

(see part I of this thesis) which make the assumptions about separability inherent in the emittance measurements unrealistic (see chapter 1). This will have unpredictable effects on the results, and should perhaps make us wary of deducing too much from the emittance variations with current.

5. The Sputtering of the Graphite

In order to investigate the sputtering process, variations in emittance and current with sputter energy were measured. It should be noted that these variations will also affect the extraction of the secondary ion beam and possibly the focus of the primary caesium ion beam.

5.1. The C^- Ion Beam Emittance

Emittance measurements were made with sputter energies in the region of 3.0 to 7.5 keV. No systematic variations were observed. This is not surprising as the only effect that one would expect from this is a change in the high velocity cut off limit for the sputtered ions (see chapter I/2) and an increase in the extraction efficiency of the sputtered ions which have large transverse velocities; these will form only a small proportion of the ion beam and therefore no large change in emittance is expected.

5.2. The C^- Ion Beam Current

A typical plot of ion beam current against sputter energy is shown in figure 3. The basic shape of this curve can be explained by the neutral sputter yield which is expected to rise towards a plateau of about 2 carbon ions per caesium ion at a sputtering energy of around 5 keV [6]. However considerable variation was found from target to target, particularly with different caesium currents. More specifically it is found that with low

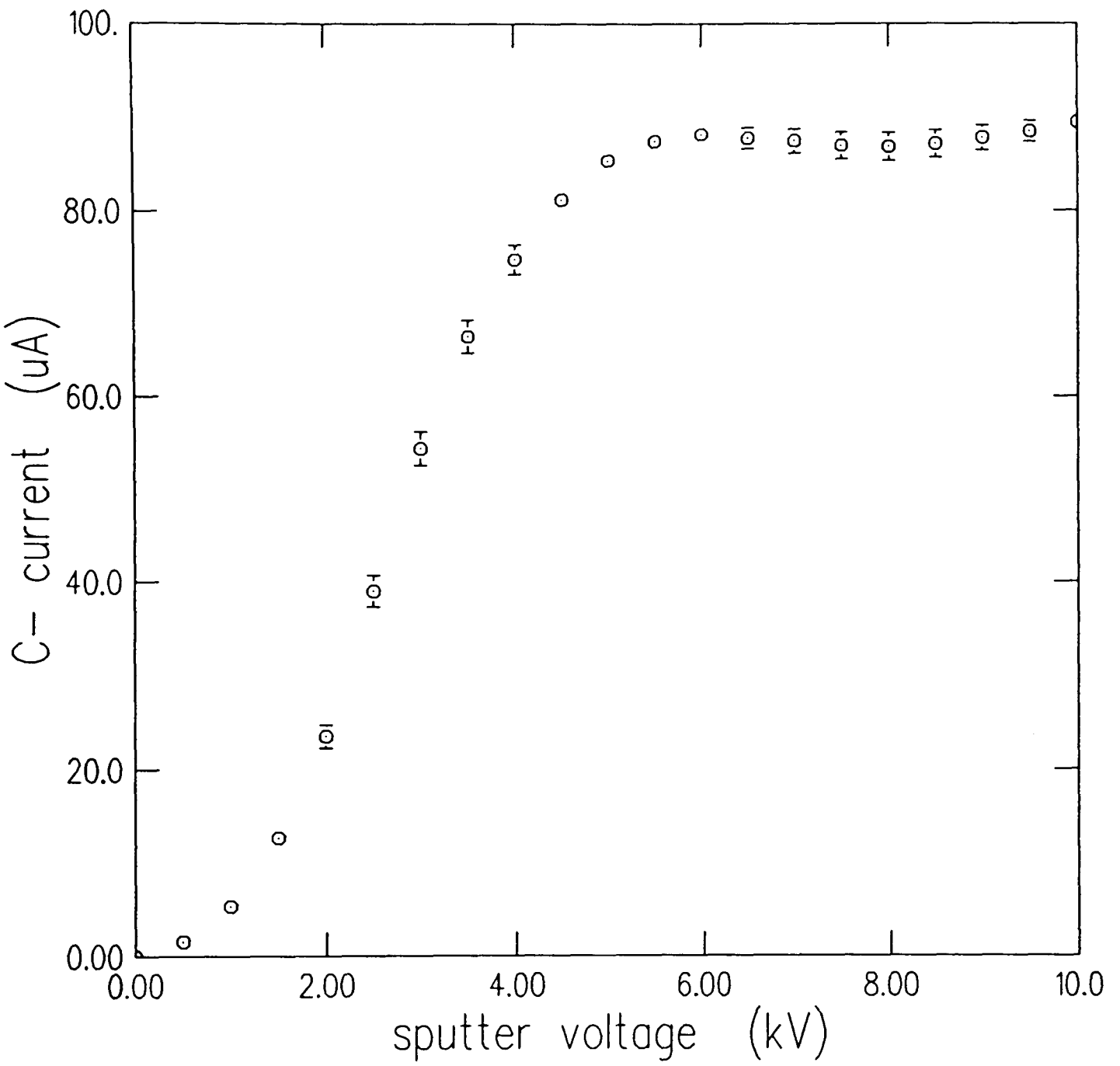

Figure 3

The variation in the ion beam with sputter voltage for a typical target (means and standard errors are shown)

caesium currents there is a rise in the C^- current as the sputter energy increases over the region 5 to 10 keV which is not the case with high caesium currents (sufficient to give 100 μA of C^-).

When variations in the sputter voltage are made, it takes about a minute for the ion beam to come to equilibrium (this depends somewhat on the size of the change in sputtering voltage). The length of this time constant suggests that there is a thermal effect involved.

For graphite which is being caesiated by the sputtering beam there is an optimum target temperature of about 480 K [7]. This is because as the target temperature rises the caesium concentration falls (see ref. [2] for a detailed explanation of this process) and there is a surface caesium concentration which gives a minimum work function [8]. (See chapter I/2 for a discussion of the significance of this.) The temperature of 480 K presumably gives the minimum work function. The behaviour described above can then be explained in terms of variations in surface temperature due to the thermal load from the caesium beam. At low caesium currents the temperature is below optimum and so increasing the sputter voltage will increase the ionisation probability, whereas at high caesium currents, when the surface temperature is probably close to optimum, this will not happen, and the ionisation probability may even decrease (seen on some occasions). The target to target variations arise as a result of the slightly different thermal properties of the targets.

Because the secondary electron current rises with V_{sp} while the caesium current does not do so, the maximum caesium currents can only be obtained with low V_{sp} since the power supply which maintains the voltage V_{sp} has a limited current load. Given the behaviour described above, the maximum C^- currents are obtained with a sputter energy of about 5 keV. The variation in beam currents between different targets is also less at this energy and so 5 keV is probably the optimum sputter voltage for most

purposes.

If V_{sp} is maintained at 5 keV the C^- current is determined largely by the caesium current which can be increased by raising the vapour pressure as described above. By this means, currents of over 200 μA of C^- have been obtained, this being limited by the power supply of the gridded lens in the ion source test facility rather than by the ion source itself.

6. The Extraction of the Secondary Ion Beam

The changes made to the extract geometry of the HISS are detailed in the previous chapter. They amount to the introduction of an immersion lens after the extract aperture. This, if anything, increases the measured emittance of the beam (as the fine structure of the ion beam is lost) but the effective emittance remains the same, and the ion beam brightness profile is rendered less sensitive to small changes in the ion beam which leaves the sputter target. Another effect of this change is to alter the aspect ratio of the brightness profile in phase space: the angular divergence is reduced somewhat while the apparent source size is increased. This is beneficial for matching the ion beam emittance to the accelerator (see part I of this thesis).

7. The Emittance of the C^- Ion Beam

Although the treatment of ion beam transport in the first part of this thesis demonstrates the difficulties in using a straight-forward emittance area to assess the suitability of an ion source, it is worth giving the emittance areas for this type of source operating with graphite: figure 4 shows the areas in two dimensional phase space which enclose particular proportions of the beam; the 21 measurements represented in this figure are

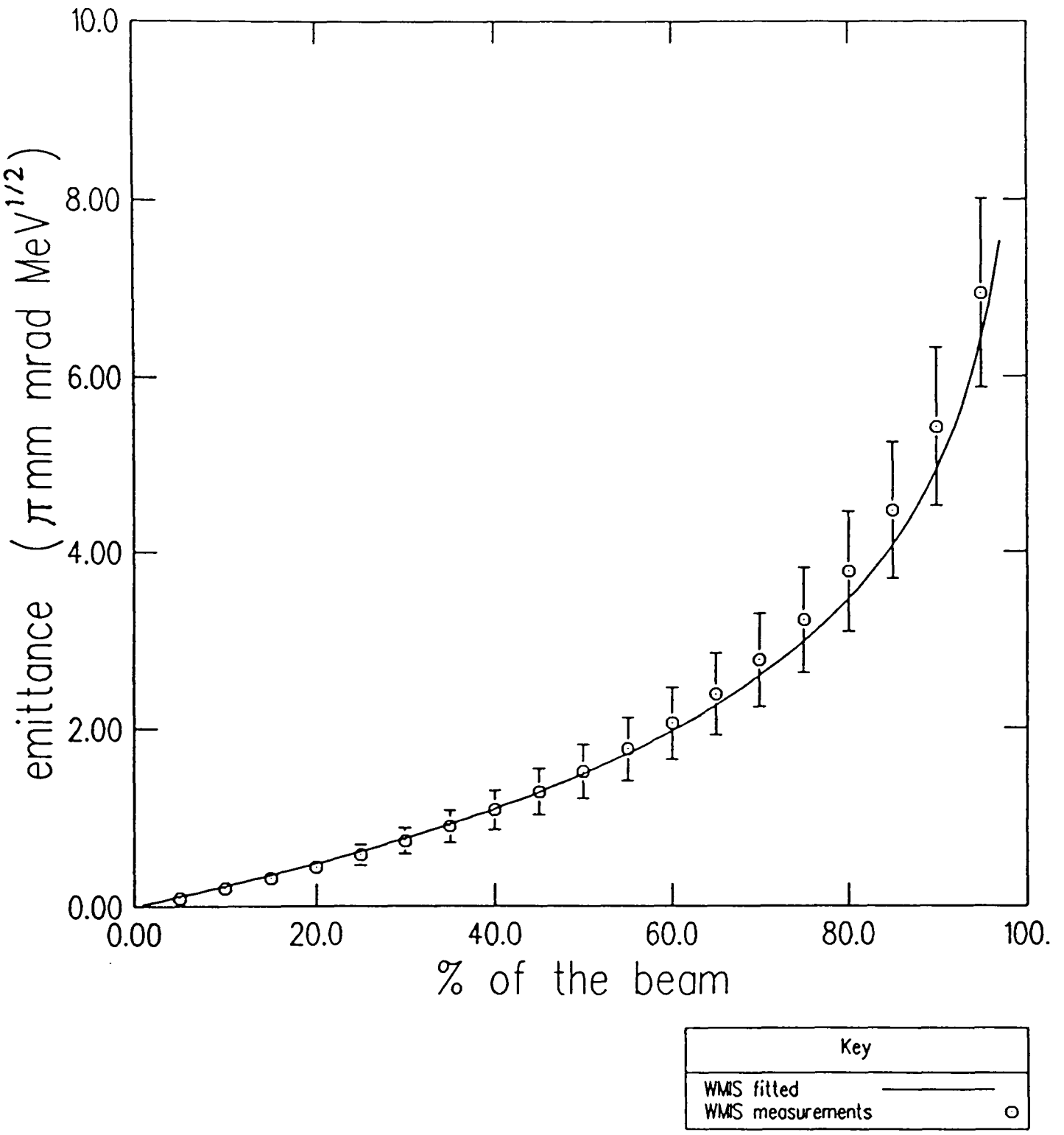

Figure 4

Emittance areas for a HISS source
compared to a fitted Gaussian distribution
(means and standard deviations are shown for 21 measurements)

all made with V_{ex} = -25.84 kV and V_{sp} = 5 kV (three with V_{sp} = 5.3 kV) but with a variety of ion currents. The 'theory' line corresponds to the Gaussian distribution used to model the behaviour of this source in chapter I/8. For comparison, figure 5 shows the comparable measurements for a version of the modified UNIS source similar to that now used for radiocarbon determinations at Oxford. This plot represents 76 measurements all under fairly similar conditions and so it is very interesting to see that the variation in the emittance of this source is so much higher, particularly in the most relevant high transmission region. The line on this graph also represents the Gaussian model used for this source in chapter I/8 and one can see that the fit is not so good. In both figures 4 and 5 the errors are simply the standard deviations of the measured points and the Gaussian functions are fitted by weighting the points in inverse proportion to their errors.

In trying to model the transport of ion beams from the HISS in the ion source test bench (see section I/8:1) for ion beams of different currents it was found that the variables pq and pa (see table I/8:1.1.1 and equation I/7:3.2.1) which gave the best fits to the measurements altered slightly with current. pq/pa is the ratio of the spatial to angular dimensions of the emittance of the ion source and it is found to grow with increasing current (about 20% for 100 μA) while the measured emittance area remains almost unchanged. This is thought to be the result of space charge effects on the C^- ions as they leave the target.

8. Using Graphite for Radiocarbon Measurements

The high C^- currents produced by the HISS when used with graphite might seem to be well suited to the task of making radiocarbon measurements. However, as well as the problems associated with the

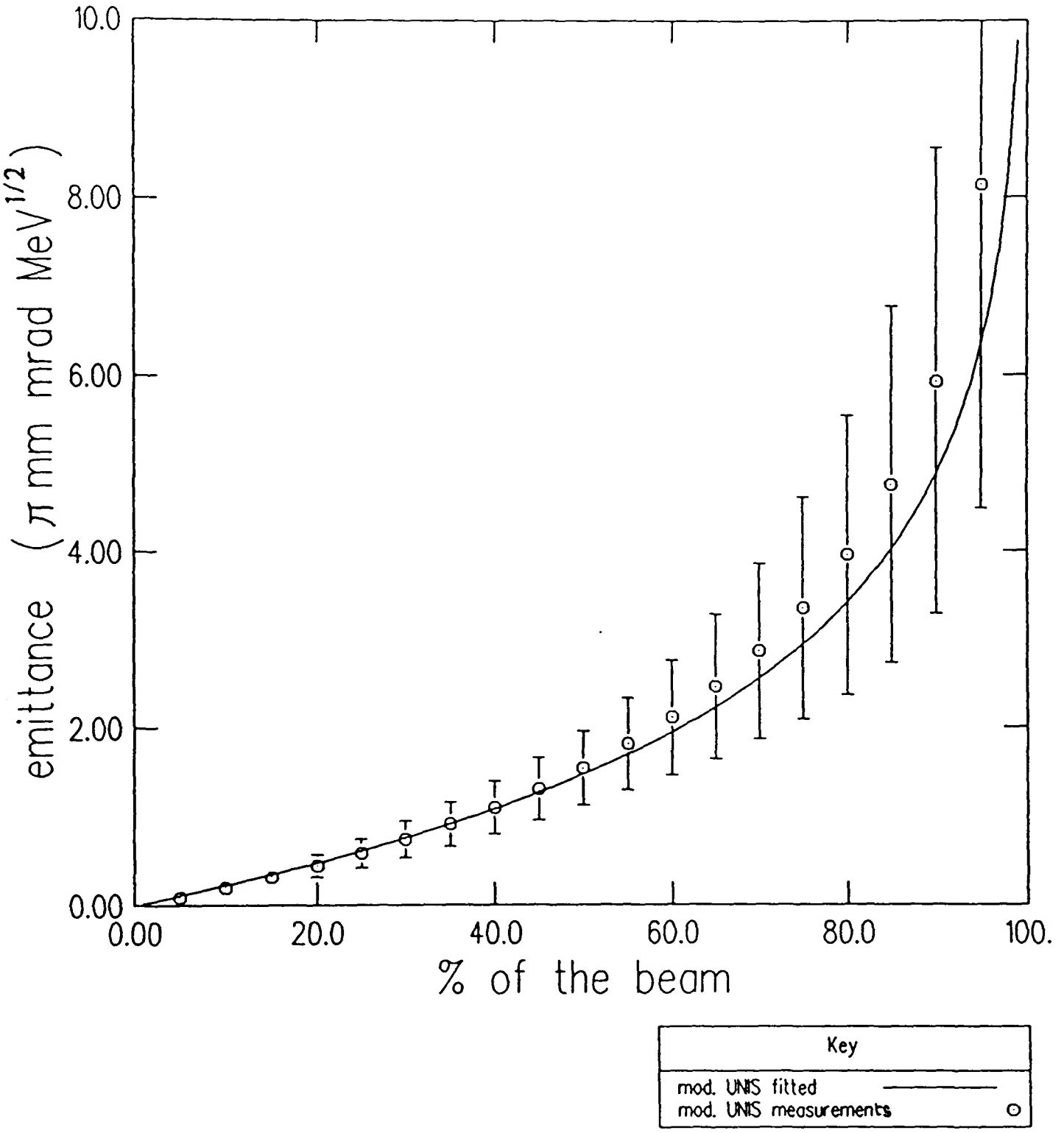

Figure 5

Emittance areas for a modified UNIS source compared to a fitted Gaussian distribution (means and standard deviations are shown for 76 measurements)

accurate measurement of isotopic ratios in a high current ion beam (see part I of this thesis), there is also a considerable problem in producing suitable graphite targets. In the first place there are problems of contamination introduced in the graphitisation process which is a particular problem for the very old samples for which high currents would be most desirable (and for which the problems of accuracy are less severe). In addition to this the HISS requires samples with very good thermal conductivity. Pilot experiments with graphite coated iron samples (similar to those described in ref. [9]) gave C^- currents of only about 30 μA under conditions which would give about 100 μA from the commercial graphite normally used.

Summary

The performance of a high intensity sputter source used with graphite has been investigated and experiments are described which shed light on the physical phenomena which underlie the source's operation. Explanations for the ion source's behaviour have been put forward and the optimum operating conditions established.

Measurements of the emittance of the HISS show that it is much less variable than that of the modified UNIS source.

References

[1] R. Middleton, Nucl. Instr. and Meth. 220 (1984) 105.

[2] N.R. White, D. Phil. Thesis, Oxford University (1981).

[3] A.N. Nesmeyanov, Vapour Pressure of the Chemical Elements (Elsevier, Amsterdam, 1963) pp. 146 & 445.

[4] R. Middleton, Workshop on Techniques in A.M.S., Oxford Radiocarbon Accelerator Unit (1986) 82.

[5] G.D. Alton, J.W. McConnell, S. Tajima and G.J. Nelson, Nucl. Instr. and Meth. B24 (1987) 826.

[6] Ch. Lukner, Nucl. Instr. and Meth. 167 (1979) 249.

[7] G. Doucas, J. Phys. D 17 (1984) 429.

[8] M.L. Yu, Phys. Rev. Lett. 40 (1978) 574.

[9] J.S. Vogel, J.R. Southon, D.E. Nelson and T.A. Brown, Nucl. Instr. and Meth. B5 (1984) 289.

Chapter 4

Ion Beams from Carbon Dioxide

Introduction

The reasons for wishing to produce C^- ion beams directly from carbon dioxide were discussed in the introduction to this thesis. Although experiments had been undertaken by others before this work was started [1,2], there still remained considerable difficulties. An ion source designed specifically for use with carbon dioxide has been described in section 2:3 and in this chapter the remaining problems will be discussed. The intention is to come to a clearer understanding of the physical processes taking place in such a source and in particular to understand all possible mechanisms for cross contamination. In addition, the ion current produced without any gas flow must be reduced to acceptable levels because, as reference [2] shows, this is clearly the greatest problem (values of greater than 3% have been quoted [2]).

All of the experiments described in this chapter were, unless otherwise specified, carried out on OXGIS using a target of the type shown in figure 2:8b (gas target 1). The sputter energy used was 5 keV and the extraction energy of the ion beam produced was 24 keV. The conditions of the ion source are such that, were a graphite target introduced into the source (of the type shown in figure 2:8), the C^- current produced would be in the region of 100 μA.

1. The Production of C^- Ions

1.1. The Sputtering Mechanism

Unlike the traditional gas plasma ion sources used for producing positive ions, the HISS type of ion source when used with CO_2 is not really a gas ion source at all. The sputtering of the carbon atoms takes place from the surface of the sputtering target where the carbon dioxide molecules are adsorbed. (This is also different from the ANIS source [1] which ionises the gas, focusses the positive ions onto the sputter target and then sputters them off again.) This can be demonstrated in two ways. Firstly the ion currents which can be obtained from these sources is directly correlated with the getter ability of the material used as a target: table 1.1.1 shows the C^- currents that can be produced in a HISS with different target materials (from ref. [2]). It should be noted that the currents are high because the target area is large; the arrangement used for these measurements was found to give high emittance and low efficiency (see ref. [2] for a complete discussion of this).

material	current (μA)
titanium	55
zirconium	40
scandium	35
tantalum	30
nickel	13
magnesium	8
copper	3
gold	1

Table 1.1.1.
C^- currents obtained from different target materials with CO_2 in a HISS (from ref. [2])

The second indication that the sputtering takes place on the surface is that the efficiency of the whole process is so high (see below) or, in

other words, that currents of about 20 μA can be obtained with gas flows of only 0.25 atmos.cc/hr. These gas flows put an estimated upper limit on the pressure within the ion source of 2×10^{-8} atmos. and, assuming that the cross section for any interaction between the caesium ion and the gas molecules is likely to be less than 10^{-19} m^2 (see chapter I/6), the total interaction rate would be in the region of 2×10^{12} s^{-1}, which would only be enough to yield an ion current of 0.3 μA. Clearly most of these interactions would not produce negative ions and those that are produced might not get out of the ion source. In order to explain the operation of these sources we must therefore have a mechanism which retains the gas molecules in the path of the caesium ions for longer. This mechanism is shown by the measurements quoted in table 1.1.1. to be adsorption on the sputter target.

The probability of a CO_2 molecule which enters the ion source adhering to the sputtering surface is difficult to calculate. The sticking probability for a carbon dioxide molecule striking a titanium surface is 0.5 [3]. The probability for a gas molecule striking the target is hard to estimate for targets of the type shown in figure 2:8b (gas target, type 1) both because the effective target area is difficult to estimate (as the caesium beam size is smaller than the target area) and because the way in which the gas flows is unknown. For those of the type shown in figure 2:8c (gas target, type 2) where the gas is essentially just let into the ion source chamber and where all of the titanium surface is being used as a sputter target the proportion of CO_2 sticking to the surface will be 0.5 A_T/A_E where A_T is the target area and A_E is the area of the extract aperture through which most of the gas will flow. This fraction is 0.02.

Another effect which will reduce the efficiency with which the molecules arrive at the surface is the gettering effect of the neutral titanium sputtered off the target. This will act as a sublimation pump of

very limited pumping speed and will reduce the efficiency of the source at very low gas flows [4].

Once on the target, the carbon atoms must be sputtered off as part of a collision cascade. For a discussion of the theory of the collision dynamics involved see section I/2:1.

If the ion source is operated with a gas flow of about 0.25 cc/hr and with a C^- current of about 20 μA for 30 minutes and the gas flow is suddenly stopped, the current falls virtually instantaneously (in less than one second) to about 4 μA; thereafter the fall off is much slower, the time constant being about 10 minutes. This is important because it indicates that recoil implantation is taking place (see section I/2:1.4). During normal operation material will be adsorbed onto the surface and then some of it will be sputtered off directly from the adsorbed gas phase, while the rest will either be implanted into the target to be sputtered off later or remain there throughout the use of the target. It is useful at this stage to introduce the parameter f_i which is the proportion of the sputtered carbon atoms which come from the implanted phase ($1 - f_i$ is the proportion coming from the adsorbed gas phase).

It is possible that there will be fractionation of the carbon dioxide in the adsorption process but, assuming that the conditions in the ion source remain constant enough to prevent variations in this, it will not alter the accuracy of isotopic ratio measurements.

1.2. The Ionisation Process

The ionisation process is discussed in some detail in chapter I/2. As indicated there, it is moderated by the tunnelling of electrons between the species that is being sputtered and the surface. However, as for graphite, it seems likely that for a caesiated surface ion formation is energetically favourable over the region in which tunnelling is important making the ion

formation fairly independent of velocity. The high ion production probability for sputtered carbon atoms also indicates that the velocity dependence cannot be very strong and therefore the isotopic fractionation will be small.

The ion formation probability will depend largely on the function $\epsilon_a(z)$ which is the variation of the electron affinity of the sputtered atom and φ, the work function of the surface. For both implanted and adsorbed species φ will be very similar, but $\epsilon_a(z)$ will be different for the carbon atoms from the two different species close to the surface. In addition to this, the implanted species will pass through the surface at close to their final velocity, whereas the adsorbed atoms will accelerate from a position of the order of 10^{-10} m outside the surface; because for a caesiated surface this will be close to the position of minimum $\epsilon_a(z)$, one would expect the ion yield from the adsorbed species to be significantly greater than that from the implanted species or indeed from graphite (see below).

The work function will depend on the caesiation of the surface and at its minimum will be slightly lower than the work function of caesium itself (see section I/2:2.3), which is also what is expected for graphite. Thus, broadly speaking, one would expect the ion formation probability for the implanted carbon atoms, p_i, to be similar to that of carbon and the probability for the adsorbed atoms, p_a, to be somewhat larger.

The surface work function will also be increased by the adsorbed gas and this must affect the ion formation probability (see below).

1.3. The Overall Ion Production Efficiency

In practice, the sputtering of the carbon atoms and the ion formation process cannot easily be studied in isolation, and so one must study the overall ion production behaviour. The overall ion production efficiency (defined as the number of C^- ions produced by the source for a given flow

of gas) will be given by the following equation:

$$E = p_{ex}\, p_{st}\, (f_i\, p_i + (1 - f_i)\, p_a) \qquad (1.3.1)$$

where p_{ex} is the probability that negative ions are extracted from the source; p_{st} is the probability that CO_2 molecules entering the source stick to the effective target surface; f_i, p_i and p_a are defined above. p_{ex} is probably close to unity for the arrangement used in OXGIS. The value of E for a target of the type shown in figure 2:8c (gas target 2) is about 0.008 to 0.01 and, as discussed in section 1.1., p_{st} is about 0.02 indicating that $(f_i\, p_i + (1 - f_i)\, p_a)$ is about 0.4 to 0.5. In addition to this we know that the total ion yield from the implanted phase is about 0.2 to 0.25 of that from the adsorbed phase (ie. $f_i\, p_i/((1 - f_i)\, p_a) = 0.2$ to 0.25); this ratio includes the C^- ions produced after the gas flow has stopped. All of this information allows us to put limits on the values of f_i, p_i and p_a. Figure 1 shows the range of possible values calculated from the data given here for a range of values of p_a (note that the errors given on the two quantities are somewhat correlated). It is clear that p_a is likely to be greater than p_i (as expected from the arguments given above) and it must be greater than 0.5. If p_i is similar to the normal values for graphite (10 to 20%), p_a is likely to be greater than 0.6. This is very important because about 80% of the C^- beam is produced from the adsorbed phase, and ion formation probabilities of this magnitude suggest that the isotopic fractionation will be very low (although obviously this should be backed up with direct experiments which are not possible on the ion source test bench).

It should also be noted that if an appreciable proportion of the carbon is sputtered off in the form of clusters (in particular the CO flux is not known) then the ion formation probability for single sputtered atoms

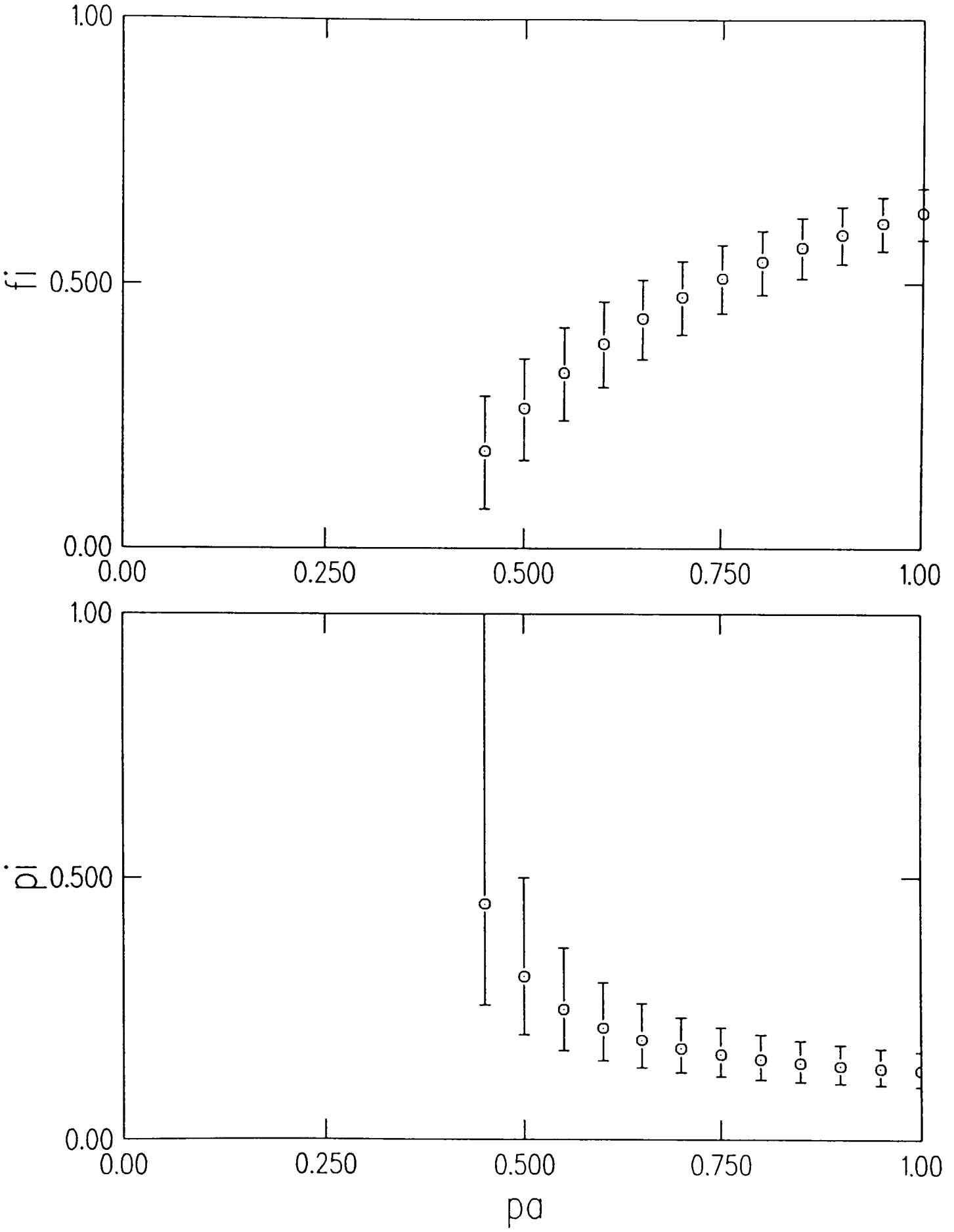

Figure 1

The ranges of possible values of f_i (the fraction of carbon atoms implanted) and p_i (the probability that implanted atoms become negative ions) as a function of p_a (the probability that atoms sputtered from the surface become negative ions); bars represent ranges and points mean values

will be even higher than that estimated above.

Figure 2 shows the ion currents from a typical gas target of type 1. The measurements represented here were made by varying the gas flow over the whole range several times. From this graph a number of observations can be made:

a. Firstly it should be pointed out that the intersection of the points with the y axis is somewhat arbitrary because of the current from the implanted carbon which depends on the history of the target; this is probably also responsible for much of the scatter over the rest of the graph as the quantity of implanted carbon introduces a kind of hysteresis into the variations of C^- current with gas flow.

b. The second point of interest is the approximately linear region of the graph which covers the range of gas flows from about 0.05 to 0.17 atmos.cc/hr. This indicates that the change in the work function which is taking place because of the adsorbed CO_2 molecules is not making an appreciable difference to the ion formation probability in this region.

c. The linear part of the graph does not, if extrapolated, pass through zero. This is believed to be as a result of the reduced value of p_{st} at low gas flows which is a consequence of the gettering effect of the sputtered neutral titanium.

d. At a gas flow of about 0.2 atmos.cc/hr the ion production efficiency starts to drop off fairly sharply. This cannot be due to attenuation of the ion beam in the gas because the pressures are far too low (and moreover the O^- current continues to rise almost linearly), and it

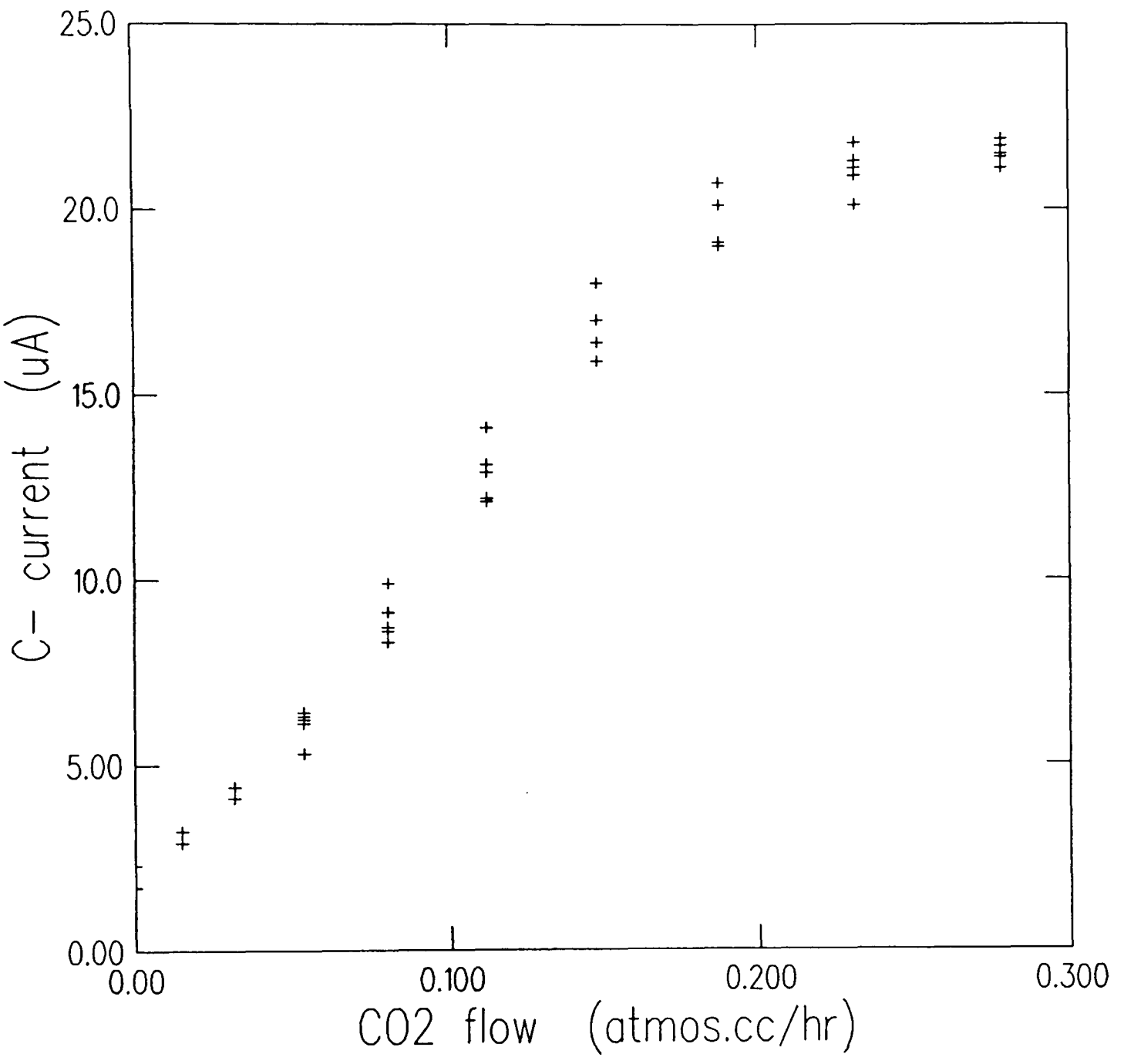

Figure 2

C^- current versus carbon dioxide flow for a typical target

cannot be because of a reduction in p_{st} because the population of adsorbed molecules on the target surface (which is estimated to be only about 5×10^{-17} m^{-2} molecules) is too low (and anyway this could not account for a fall in the C^- yield which is observed at slightly higher gas flows). This phenomenon would therefore seem to be a result of the fall in the work function of the surface which arises because of the population of adsorbed CO_2 molecules.

The fact that the ion formation probability remains fairly constant for low gas flows and then falls off rapidly is rather surprising as one would expect the change in the work function to be approximately linear with gas molecule population. It suggests that this might be a case of Fermi level crossing [5]. If this is so, then it indicates that the ion formation probability (from the adsorbed gas phase) with low gas flows is very close to unity (ie >> 90%).

e. The overall efficiency of ion production, E, is about 0.08 to 0.1 which indicates that extremely small samples of CO_2 could be used in the OXGIS for radiocarbon measurements. Typical measurement requirements for recent samples are circa 8 μA hr and so in theory only 0.1 atmos.cc of carbon dioxide would be required, which corresponds to 50 μg of carbon. The amount actually needed will depend on the gas handling system used.

In order to further investigate the reasons for the fall in C^- current at CO_2 flows of greater than about 0.2 atmos.cc/hr an Ar/CO_2 mixture was used (in the ratio 10:1). The results of the measurements made with this mixture are shown in figure 3; there is clearly some attenuation as the gas flow increases, but the C^- current essentially has the same functional

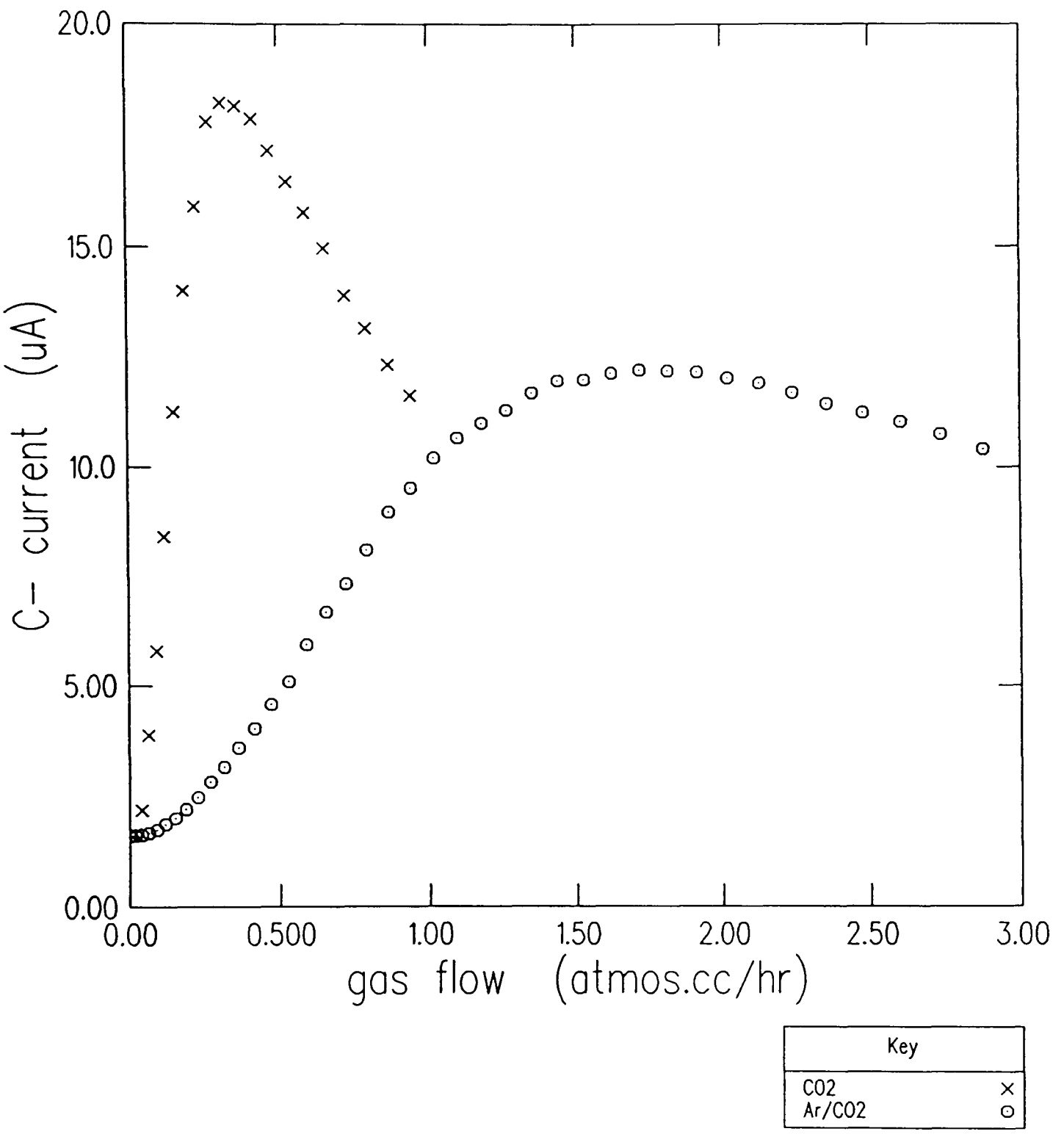

Figure 3

The effect of an argon carrier on the current versus gas flow curve

dependence on the CO_2 flow regardless of the argon present. This supports the hypothesis put forward in section d above.

Another set of measurements which also sheds light on the processes involved is that taken of the C^- current versus gas flow and sputter voltage. Figure 4 shows these measurements and figure 5 is a surface plot of a bivariate Chebychev polynomial fit to the measurements showing the overall pattern. The maximum current that can be obtained at any given sputter voltage is a similar function of that voltage as the C^- current obtained from graphite (see figure 3:3), but the efficiency seems to drop when the sputter energy rises above about 4 keV. The principal reason for this can be discovered if one also notices that the intersection of the approximately linear sections of the gas flow curves with the x axis (of figure 4) increases with sputter energy; this is because the neutral titanium sputtered from the target increases and therefore more of the CO_2 is gettered onto other parts of the source. Indirectly this also explains why there is a rise in the gas flow which gives maximum current as the sputter energy is increased (even at those voltages where there is not much change in the efficiency): increasing the rate of removal of material from the surface allows a greater flux of gas onto the surface for the same surface population and a consequent drop in the work function.

The results shown in figures 4 and 5 also give some indication of the optimum working conditions. When choosing the sputter voltage there is clearly a balance to be struck between efficiency and maximum current. It is also important to realise that gettering of the CO_2 onto other parts of the ion source is best kept to a minimum as it does provide a possible mechanism for cross contamination, although there is no evidence that this mechanism is acting in these circumstances (see below). About 90% of the maximum current can be obtained with a sputter voltage of 5 kV and at this voltage the efficiency is still close to its maximum; this voltage would

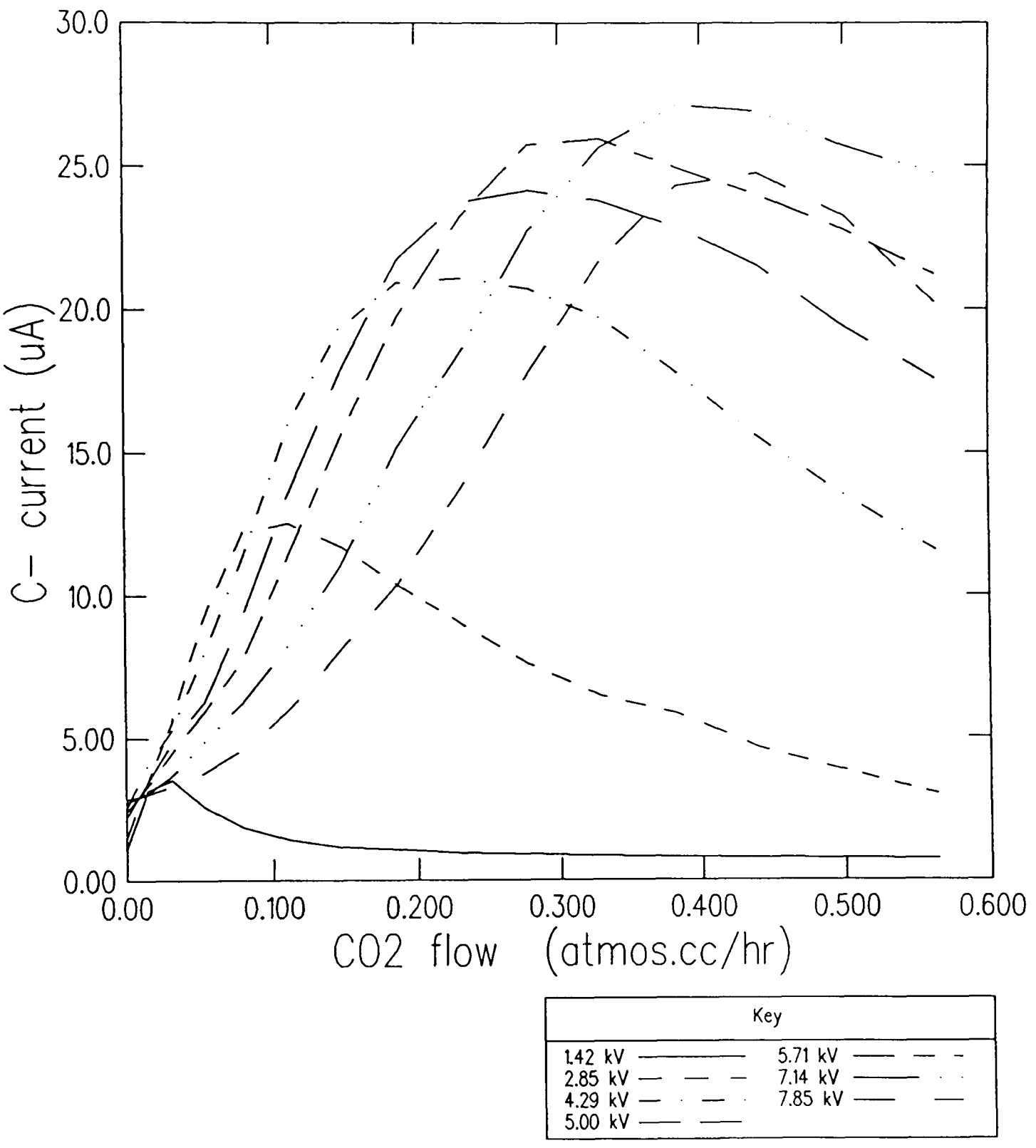

Figure 4

C^- current versus gas flow for different sputter voltages

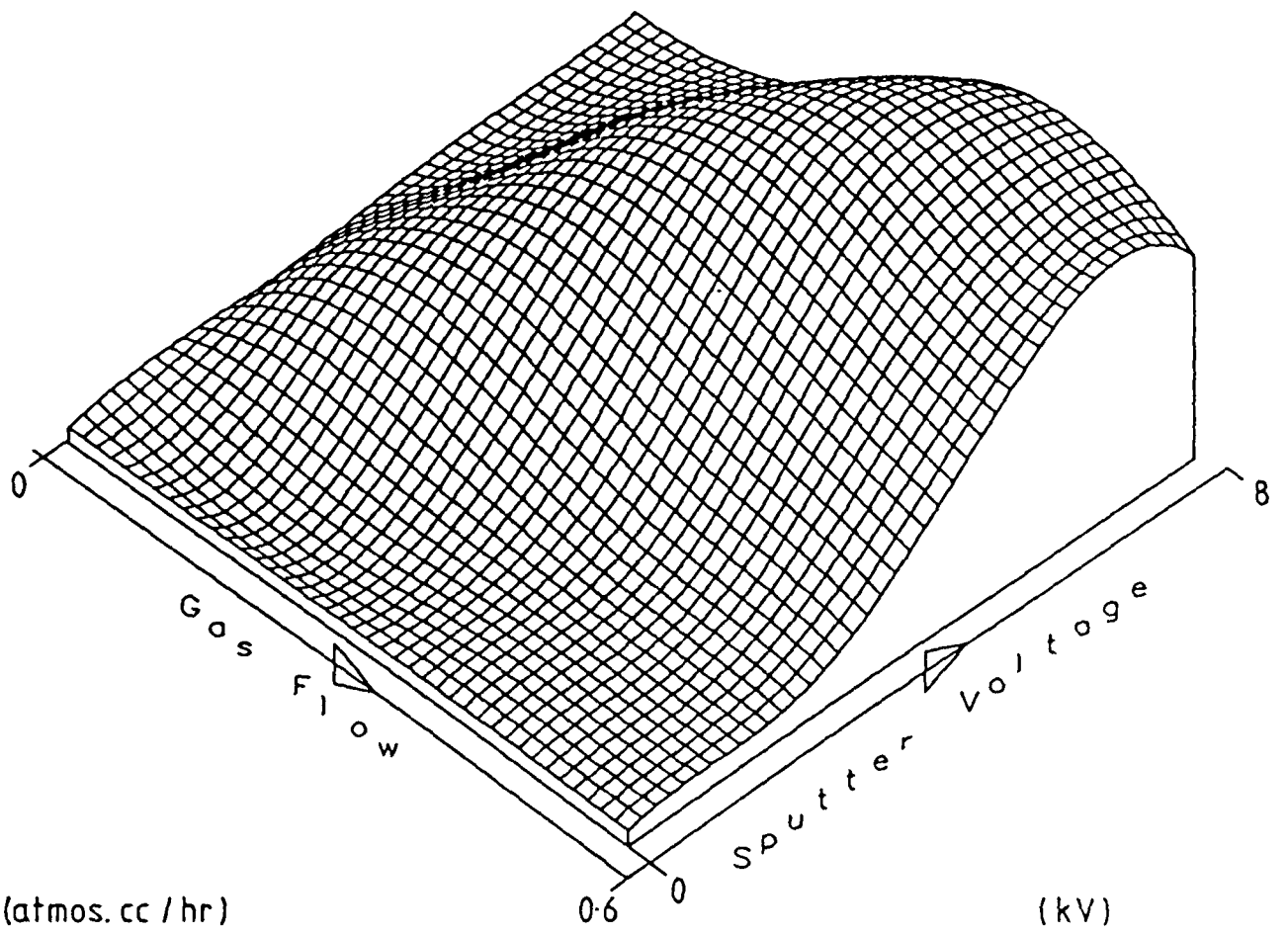

Figure 5

The C^- current surface in gas flow/sputter voltage space

therefore seem to be a good compromise and has been used for all of the work described here.

1.4. The Implications for Radiocarbon Measurements

The implications for radiocarbon measurements of the observations described here are essentially three. Firstly, the fact that most of the ion current is produced from the adsorbed gas phase for which the ion formation probability would seem to be very close to unity indicates that the isotopic fractionation of the ion source due to the sputtering process should be very much smaller than for graphite. Secondly, the high efficiency of the source indicates that very small samples should be measurable (<100 μg) as explained in section 1.3.e. Thirdly, the predictable way in which the C^- ion current varies with gas flow makes it easy to maintain a constant ion current from the source which will minimise the measurement inaccuracies of the rest of the AMS system (see part I). Together these indicate that this ion source should enable more accurate radiocarbon determinations to be made whilst also allowing the use of smaller samples.

2. Background Currents

When this investigation into gas ion sources of the HISS type was started, the currents that were obtained with no gas flowing were certainly the worst problem that had to be addressed [2]. The fundamental reason for this difficulty is the very high efficiency of the source which makes it susceptible to contamination and also makes it into a sensitive residual gas analyser. To underline this problem it is worth pointing out that each monolayer of carbon on the surface of a 2 mm diameter target in principle contains enough atoms to produce about 50 μA s of C^- current.

2.1. Target Contamination

The largest single source of background currents can be the targets themselves. They can pick up carbonaceous contamination in a number of ways:

a. The manufacture of target heads involves the use of machine tools that tend to leave residues of oil. To remove these a solvent such as chloroform ($CHCl_3$) or arclone (CCl_3CH_3) is used. Unfortunately degreasing agents themselves tend to leave residues behind and so the components of the targets heads are ultrasonically cleaned in methanol for three minutes, shockblasted, then ultrasonically cleaned in distilled and deionised water and finally baked in an oven overnight. This undoubtedly still leaves some contamination on the targets and they must be run in the ion source for about ten minutes to remove this before they are ready for use. If sufficient care is not taken with this cleaning procedure, very high currents (up to 40 μA on one occasion) can be obtained when a target is first put in the source; once this has happened a target cannot be used as the recoil implantation that takes place then makes it very difficult to obtain a reasonable background current.

It is also worth pointing out at this stage that the use of compressed titanium powder for the target material makes the problem of target contamination far worse as there is a much higher surface area and it is impossible to clean the target effectively by sputtering. This was the original material used in this kind of source [2] but it was abandoned at an early stage in this research because of the problem of contamination and because the currents yielded were not very stable.

b. Another important source of target contamination in the HISS is the vacuum interlock through which the targets are introduced. Experiments using this arrangement were found to give initial background currents of about 18 μA falling to 5 μA in a few minutes and then to about 2 μA over an hour. Clearly a very large proportion of the current is coming from the implanted phase; this is also indicated by the CH^- current which is high (10 to 20 %) initially but falls off to only a few percent after about 5 minutes. The introduction of a liquid nitrogen trap between the roughing pump and the interlock chamber reduces the background currents by a factor greater than 2. Part of this effect may be due to hydrocarbons entering the vacuum system via the interlock in the gas phase (see below).

In OXGIS this problem has been largely eliminated as the targets are all kept under UHV throughout the operation of the source. The chamber in which they are kept is pumped with a Balzers turbo-molecular pump which operates from atmospheric pressure, thereby minimising the oil backstreaming from the rotary backing pump. The introduction of this turbo pump was responsible for a four-fold decrease in the background currents from the source (from about 300-400 nA down to 70-100 nA). This is probably partly due to the reduced contamination of the target heads and partly to the reduction in the partial pressure of residual hydrocarbons (see below).

c. A much smaller effect which is only observable on OXGIS is the increase in the background current which is obtained when a target is stored in the vacuum chamber behind the source. If a target is

removed from the source and introduced within a few minutes there is no appreciable change in the background current; however if an hour or so elapses the background level of the target will increase by about 100 nA (even greater times do not seem to increase this above about 200 nA) falling off with a time constant of about 2 minutes. This rate of contamination can be increased by running the source with no target which allows caesium to flow into the target chamber.

This type of contamination makes it clear that the vacuum quality in the target chamber is very important, and also that the separation of the source and the targets that are not being used is an essential feature of the design of OXGIS.

d. The use of a target with CO_2 effectively contaminates it because of the recoil implantation that takes place. For this reason a new target must be used for each distinct gas sample. Some indication of the constancy of the background current can be obtained by using $^{13}CO_2$. A target which has been run with this gas continues to produce a substantial $^{13}C^-$ beam after the gas flow has been stopped. If $^{12}CO_2$ is then admitted the $^{13}C^-$ current remains constant (to within about 10%) over the normal operational range of gas flows.

For all types of surface contamination the initial time constant for the removal of the contamination is about 2 minutes but then, as recoil implantation is involved, the subsequent fall off in background C^- currents becomes much slower. With the present design of OXGIS the contamination from these sources in normal running conditions is restricted to that described in section c (and to that described in section a if the targets are not properly cleaned).

2.2. Residual Gas

The importance of vacuum quality is paramount. As mentioned above, the introduction of a turbo-molecular pump behind the ion source was responsible for a four-fold decrease in the background currents from OXGIS. It is also found to be necessary to have a liquid nitrogen trap in front of the ion source when it is operating on the ion source test bench as the vacuum system for this piece of equipment has quite high hydrocarbon partial pressures (probably about 10^{-10} atmos.). This requirement for low residual gas pressures is another reason for not using a vacuum interlock for individual samples because such an interlock inevitably introduces hydrocarbons into the vacuum system.

It is not really clear whether any appreciable proportion of the background currents now obtained from OXGIS (70 - 100 nA) is due to the residual gas. Running the turbo pumps at lower speed seems not to have a noticeable effect and this suggests that the vacuum quality is no longer the limiting parameter.

2.3. Other Sources of Carbon

There are two other sources of carbon that have been considered: the titanium used for the targets and the ion source itself.

Using ultra-pure titanium (99.98% instead of the 99.8% usually used) certainly does not remove the remaining background. This has only been tried for targets of type 2 and these seem to give a background current which is about 3 times smaller than that obtained with targets of type 1, because of their smaller area. The efficiency for this type of target is about 10 times lower but the maximum currents that can be obtained are > 80% of those obtainable from targets of type 1.

There are strong indications that the remaining background current

comes from the ion source itself. The mechanism for this is not clear but it is probably due to the ejection of carbonaceous material from the hot ioniser (this also seems to be the mechanism for cross contamination; see below). The evidence for this is that if the sputtering voltage is switched off for short time (such as a minute) and then switched back on again the residual current is larger and gradually falls back to its previous value; furthermore the total number of extra ions being produced is very close to the 'missing current' when the sputter voltage was switched off. There is no comparable effect if the target head is removed from the ion source chamber while the sputter voltage is switched off.

The residual background current is unaffected if small quantities of Ar or air (up to about 0.2 atmos.cc/hr) are admitted to the source. This suggests that the background current should be constant when CO_2 is used as well (also see the experiment described in section 2.1.d).

2.4. The Implications of the Background Current

The background currents have been reduced to 70 - 100 nA which is about 0.3 - 0.5% of the normal operating current from the source. Once a target has been cleaned by sputtering this background current remains fairly constant (to within 10%) even when gas is admitted to the source. This suggests that the background can be subtracted from a measurement to an accuracy of 0.03 - 0.05%. By using a gas target of type 2 this can be improved by a factor of 2 although with a large loss in efficiency. Work is now under way to improve the efficiency of these targets which have a smaller effective area by better spatial control of the gas flow.

The small size of the effective background (after subtraction) should pose no problems at all for the accuracy of radiocarbon measurements of recent material (an accuracy of 0.05% corresponds to only 4 years) but for very old material it would limit accuracy somewhat. It seems reasonable to

assume that the background current will have approximately 25% of the modern concentration of ^{14}C as this is the value found for many contaminants (such as residual gas hydrocarbons, engineering oils et cetera). This being the case, at 60,000 years the background uncertainty would introduce an additional error of +1,600/-1,400 and it would enable one to establish a terminus ante quem of 74,000 years. If improvements in target design can improve this by a factor of two, as already seems feasible, this would improve these figures considerably (error at 60,000 years +800/-750; terminus ante quem 80,000). It can clearly be seen that other constraints will be much more important than this.

3. Cross Contamination

One of the possible dangers of using a gas ion source is the problem of cross contamination. Experiments aimed at seeing if ANIS was a suitable ion source for this kind of work [1] demonstrate this very clearly. In order to investigate cross contamination effects, experiments have been done to see how the background current from OXGIS depend on the previous usage of the source, and similar experiments with $^{13}CO_2$ have been carried out to check on the findings.

3.1. Cross Contamination from Graphite

One test for cross contamination is to use the source with graphite, producing currents in excess of 100 μA of C^- for 30 minutes and then to introduce a clean gas target (type 1) into the ion source. If this is done the background current from the target is about 1 μA and falls off with a time constant of about 10 minutes. The value of this experiment is that it demonstrates that there is a mechanism for cross contamination in this type of source which is quite independent of the use of carbonaceous gas in the

source. The mechanism for this is believed to be evaporation of carbon from the ioniser. The carbon is deposited here by the high neutral carbon currents from the sputtering of graphite; the ioniser becomes lightly golden in colour after prolonged use indicating the presence of tantalum carbide. It seems likely that this mechanism will act as a cross contamination mechanism at the 0.5 - 1% level if the source is used with graphite (depending on the relative efficiencies of sputtering carbon from graphite and titanium). It should also be noted that the use of a spherical ioniser which would lie almost directly in front of the target might well exacerbate this problem.

3.2. Cross Contamination from Carbon Dioxide

The cross contamination from carbon dioxide can, most easily, be investigated by alternately putting two targets into the ion source for periods of 30 minutes and determining the background currents obtained. The time for changing targets is between 30 and 60 seconds. One of the targets is then put into the source and CO_2 is introduced so that the ion source produces a current of about 20 μA. The other target when it is put into the source then shows an additional background current of less than 20 nA (this is difficult to measure accurately as it is little more than 10% of the total background current). This additional element to the background current falls off slowly and only reappears if CO_2 is let into the source again.

To check these findings $^{13}CO_2$ can be used in the place of $^{12}CO_2$ and this allows a more accurate assessment of the cross contamination current. This is again found to be about 10 nA ($\pm$ 2 nA) and falls off with a time constant of about 10 minutes in the same way as the cross contamination from graphite. The ^{13}C current can be monitored as $^{12}CO_2$ is let into the source and for low flow rates (up to about 0.1 atmos.cc/hr) there seems to

be no change in the extra contribution due to cross contamination. It is difficult to monitor this beyond this flow rate as the natural ^{13}C current from the ordinary CO_2 dominates.

Thus the cross contamination from carbon dioxide is only about 10 nA or 0.05% of the total C^- current obtained under normal operating conditions. Because it falls off, the effective value in measurements will be about half of this. As a consequence, in following a modern sample, one would expect to be able to determine a radiocarbon terminus ante quem of about 68,000 years and so only for extremely old samples would careful sample scheduling be necessary.

There is no evidence for any cross contamination from the gas phase. The time constant indicates that the mechanism which operates for graphite is the same as that which operates for carbon dioxide. That the effect is so small can be explained by the small neutral carbon flux obtained when operating with carbon dioxide which must be 100 times smaller than that from graphite. The C^- current is up to five times smaller but this still indicates that the C^0/C^- ratio is 20 times lower. This must in part be due to the greater ionisation probability and in part to the very low abundance of clusters (C_2, C_3 .. et cetera; see below) which, when operating on graphite, accounts for more than 60% of the negative ion flux and presumably a similar or greater proportion of the neutral flux (see table I/8:1.3.1).

4. Ion Beam Composition

4.1. Ions Produced by the Source

The principal ions produced by a HISS operating with CO_2 are given elsewhere [2]. The ion currents obtained under normal operating conditions with a C^- beam of 20 μA are shown in table 4.1.1. All measurements taken

from reference [2] are marked accordingly; these were difficult to measure on the ion source test bench because of lack of mass resolution or insufficient magnetic field. Separate columns are given for those ions which are specific to particular target holder materials.

The presence of CN^- in the ion beam from OXGIS is believed to be the result of a small air leak in the vacuum system.

mass	current (μA)			identification
	Ti target	Cu holder	Al holder	
1	< 1 [2]			H^-
12	20			$^{12}C^-$
13	circa 0.3			$^{13}C^-$, $^{12}CH^-$
16	60			$^{16}O^-$
17	< 1 [2]			$^{16}OH^-$
18	< 1 [2]			$^{18}O^-$
24	0.2			$^{12}C_2^-$
26	0.3			$^{12}CN^-$
27			0.4	Al^-
28			0.7	AlH^-
32	0.1			$^{16}O_2^-$
48	< 1 [2]			Ti^-
60	< 1 [2]			TiC^-
63		circa 16 [2]		$^{63}Cu^-$
64	circa 6 [2]			TiO^-
65		circa 7 [2]		$^{65}Cu^-$

Table 4.1.1.
Ions produced from a HISS type source operating with carbon dioxide

4.2. Variations in Ion Beam Composition with Gas Flow

It is interesting to investigate the variations in some of the other ion species with gas flow and the two that have been investigated in detail are the O^- and C_2^- beams.

Figure 6 shows the variations in C^- and O^- currents at low flow rates. The slope of the O^- yield with gas flow is about 2.2 times that of the C^- yield in the region in which the C^- yield is linear, but it is difficult to deduce very much from this because of the complications of recoil

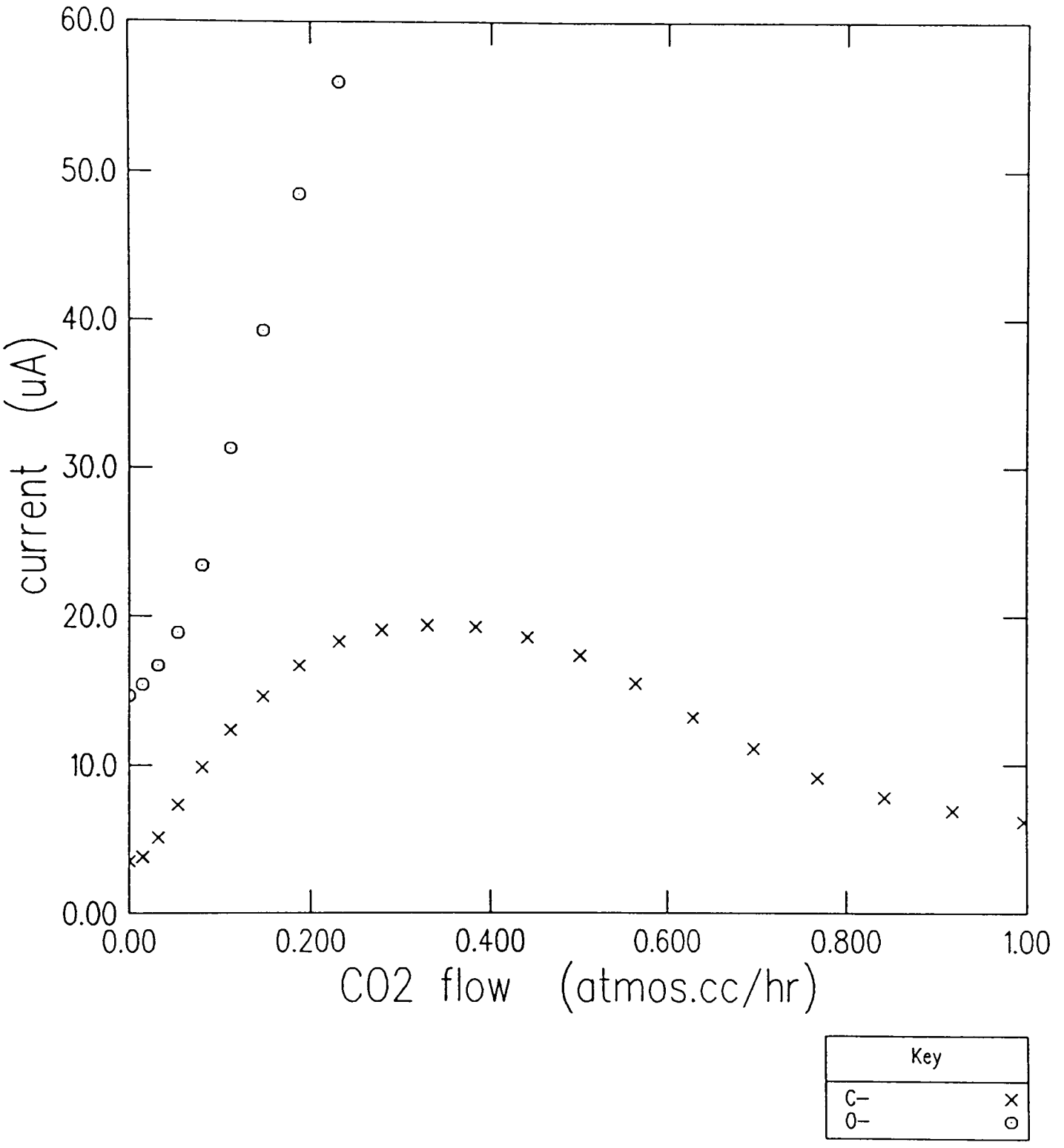

Figure 6

Variations in C^- and O^- currents with gas flow (low flow rates)

implantation. The high O^- current with no gas flowing is partly due to this implantation and is partly caused by water vapour in the vacuum system and a small amount of O_2 from a minor air leak.

Figure 7 represents measurements made with a slightly lower caesium current and shows that the O^- ion beam continues to rise even when the gas flow is greater than 2 atmos.cc/hr. It is not clear how much of the shape of this curve is due to attenuation of the ion beam and how much is due to reductions in the sticking probability of CO_2 molecules on the target and the ionisation probabilities for oxygen atoms. These measurements do, however demonstrate that the fall in C^- currents at high flow rates must be due to a drop in ionisation probabilities.

Figure 8 shows measurements taken of the C_2^- ion beam as a function of gas flow. This beam has very little contribution from the implanted phase and at low gas flows follows an approximate square law. This is exactly what one would expect if the sputtered fragments of the CO_2 molecules on the surface of the target were reacting to form clusters.

Summary

A model for the physical processes taking place in the ion source, OXGIS, has been developed which is consistent with a wide range of measurements. The essential postulate is that there are two sources for the C^- current: the adsorbed gas phase and the implanted phase. Most of the current is derived from the former and the measurements presented here indicate that the ionisation probability for sputtering from this phase is very close to unity. This in turn means that the fractionation taking place in the sputtering process must be very small and so measurements of high accuracy are possible. This is helped by the ease with which the C^- current can be controlled, thereby making it possible to operate the entire

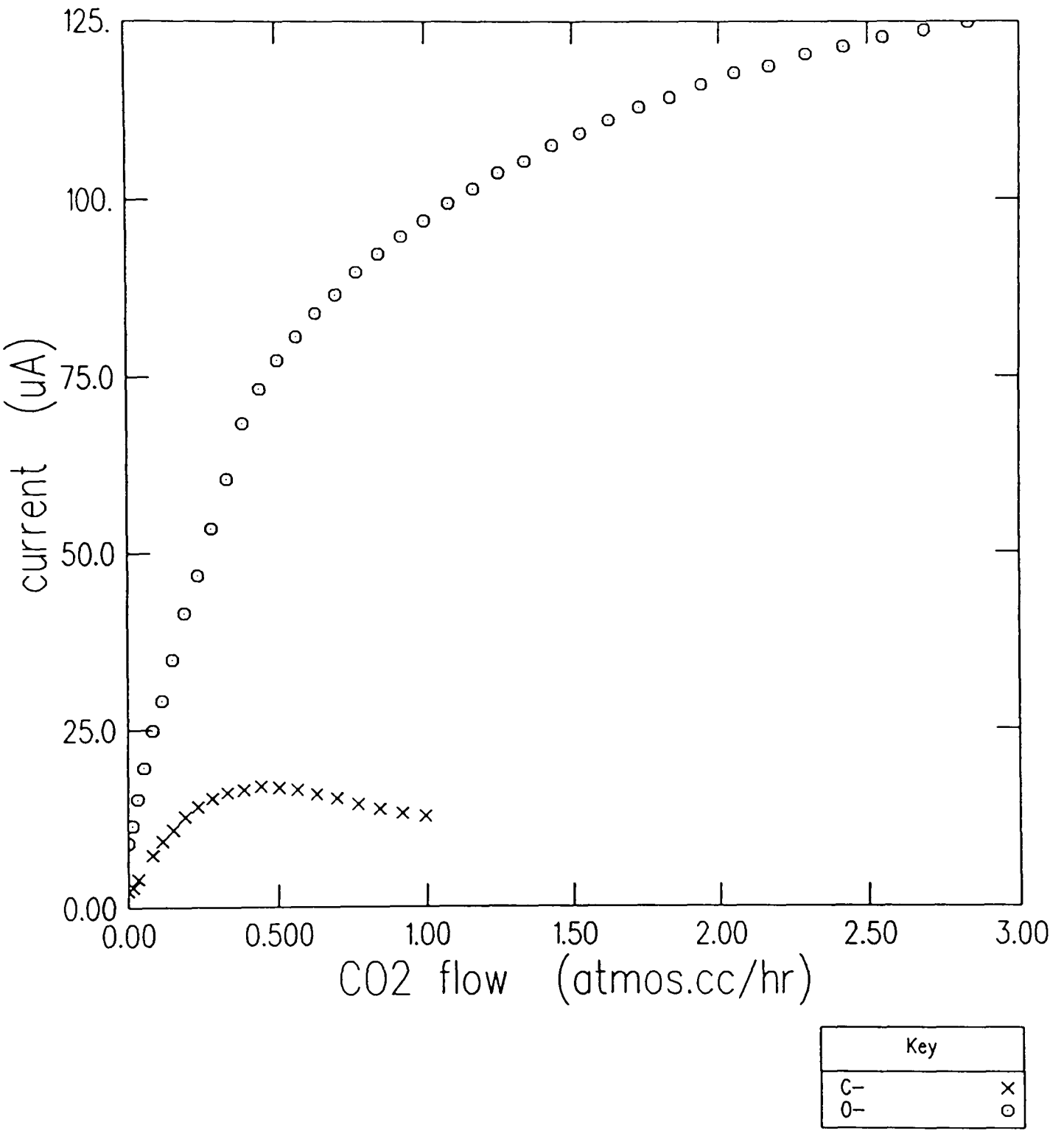

Figure 7

Variations in C^- and O^- currents with gas flow (high flow rates)

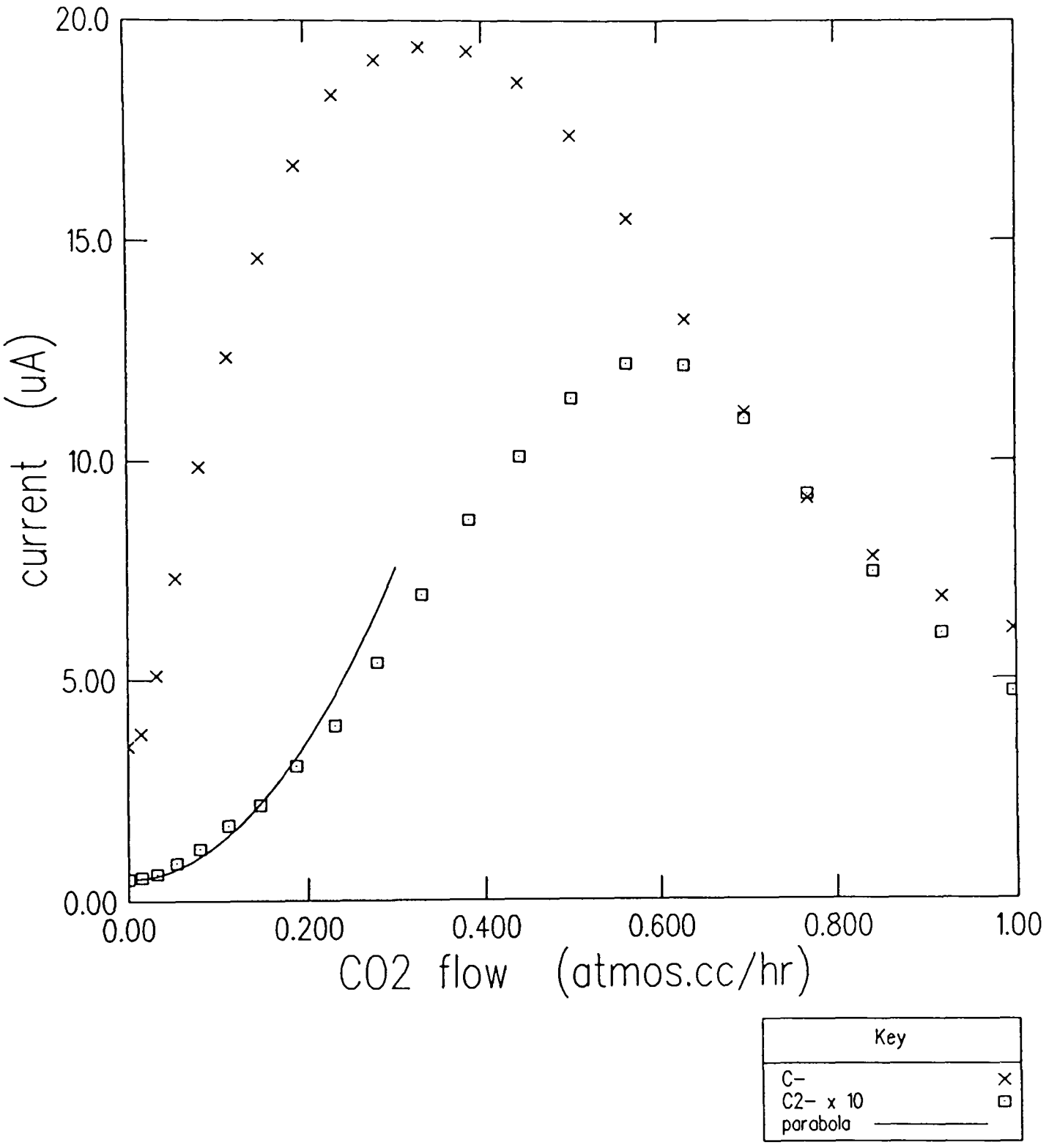

Figure 8

Variations in the C^- and C_2^- currents with gas flow

AMS system under nearly identical conditions for different samples.

The overall efficiency of the ion source is such that very small samples (<100 μg of carbon) can in principle be measured.

The background currents have been reduced to a level where they should allow radiocarbon determinations of high accuracy to be made for samples older than 60,000 years, although this will obviously be limited by other forms of contamination and by counting statistics.

The cross contamination of the source has been evaluated and is found to be less than 0.05% of the typical operating current and it therefore poses no problems for this application.

References

[1] J. Heinemeier and H.H. Andersen, Radiocarbon 25 (1983) 761.

[2] R. Middleton, Nucl. Instr. and Meth. B5 (1984) 193.

[3] P.A. Redhead, J.P. Hobson and E.V. Kornelson, The Physical basis of Ultra-high Vacuum (Chapman and Hall Ltd., London, 1968) pp. 399-403.

[4] A.E. Litherland, private communication.

[5] M.L. Yu and N.D. Lang, Phys. Rev. Lett. 50 (1983) 127.

Summary

This part of the thesis is a description of the quest for an ion source which is well suited to the task of producing ion beams for radiocarbon dating by AMS. The introduction gives the reasons for believing that high intensity sputter sources (HISS's) with carbon dioxide form the best basis for such a development.

In chapter 1 the methods and equipment used for the development and testing of ion sources are discussed. The ion source test bench which has been used for the experiments and measurements presented here is described in some detail and its limitations explained. This information is also important in understanding the brightness profiles given in part I of this thesis.

In chapter 2 the design of high intensity sources is investigated. Experience in the operation of such a source has enabled some changes to be made and design criteria established. A point of particular general interest is that the presence of intense transverse electric fields either within the ion source or in the extract region seems to lead to less regular and more variable current distributions in phase space. The particular problems associated with the need to change samples easily while using an ion source of this kind with carbon dioxide are then discussed in relation to the design of the Oxford gas ion source (OXGIS). The design of this source is described along with its associated sample changing mechanism and computer control system.

The behaviour of a HISS when used with graphite has been studied and the measurements related to this are described in chapter 3 with a discussion of their implications. This information is important because an ion source which is to be used for routine measurements must be well

understood in every aspect of its operation; graphite is a convenient target material for investigating many aspects of the source's operation without introducing the complications of gas flow. Each stage in the production of the final C^- beam is discussed and details of related experiments given. In addition, the emittance of the source has been measured under a large range of conditions demonstrating that this characteristic of the source is less variable than for the modified UNIS source used at the Oxford radiocarbon facility. Experiments with graphite coated iron targets indicate that the use of this kind of ion source with graphite for radiocarbon determinations might well prove difficult because of the problems associated with producing graphite with a sufficiently high thermal conductivity.

Chapter 4 charts the progress that has been made in the use of carbon dioxide in OXGIS. The vacuum quality and target cleanliness are found to be very important in reducing the background currents from the source, as is the use of solid titanium targets instead of porous ones. These currents are now sufficiently low and stable that radiocarbon measurements should be possible for samples older than 60,000 years (subject to other constraints). The processes involved in the production of C^- ions from carbon dioxide are described in detail. Experimental evidence supports the fairly simple model for the process which is expounded. This indicates that the isotopic fractionation from the sputtering process should be small. The efficiency of the source is high (8 - 10%) which allows the use of very small samples (less than 100 μg of carbon), another very important characteristic for an ion source to be used for this kind of work. The cross contamination has also been measured and found to be very small (less than 0.05%); the mechanism for this is investigated and found to involve the neutral sputtered carbon atoms. This ion source is clearly very suitable for radiocarbon dating by accelerator mass spectrometry.

CONCLUSIONS

and

EPILOGUE

CONCLUSIONS

In the introduction of this thesis the improvements which were most needed in the application of accelerator mass spectrometry to radiocarbon dating were cited. It is important, therefore, to look back at the progress that has been made in the course of this research in order to see the degree to which these needs have been met.

The first of these requirements is an increase in the total number of radiocarbon measurements that can be made and this clearly depends on many factors, some of which have their basis in economics rather than science. However, the development of the gas ion source will have a considerable impact on this, both because the small sample size required (less than 100 μg instead of the 1 mg required for the normal graphite targets) will greatly increase the number of objects suitable for measurement and, because it is no longer necessary to turn the samples into graphite, the cost of measurements should be reduced.

Contamination of the samples is clearly important in determining the age range over which radiocarbon dating is useful and the gas ion source will be very important in relation to this too. Contamination already present in samples which are to be measured must be removed by physical and chemical selection. This frequently reduces the size of the sample by very large factors. Because of the reduced sample size it will now be feasible to do this for a much larger proportion of the available material. Furthermore the process of making graphite is itself known to be responsible for additional contamination and this stage can now be eliminated. To set against these advantages are the background currents which come from the gas ion source: the radiocarbon background from these is, however, believed to be smaller than that from graphite production and

is also constant enough to be subtractible. The substitution of a known, measurable background for one that is neither of these is clearly an improvement. It is estimated that it will now be possible to measure accurately radiocarbon ages of greater than 60,000 years (maybe greater than 70,000 years) using the new ion source.

A restriction is also placed on the age limit of radiocarbon measurements by counting statistics. Apart from the fundamental limit to the number of ^{14}C nuclei present in the sample, this is essentially determined by the proportion of these that can actually be counted. For very small samples this is dictated by the overall efficiency of the measurement. With the gas ion source this is very high (about 3% if the transmission through the accelerator is 30% which is typical; this compares to less than 1% for measurements using graphite) and for a given sample size should enable measurements of approximately double the accuracy to be made. For larger samples the limiting factor is the time spent on making the measurement and so accuracy can only be improved by increasing the rate at which carbon is sifted for ^{14}C or, in other words, the current produced by the ion source. This is slightly higher for the gas ion source than for most graphite based ion sources used for radiocarbon measurements. Although using a high intensity sputter source with graphite would be very useful from this point of view problems of accuracy and target production preclude the use of such an arrangement at the moment. With samples of any size, the improvements that have been made to the transmission of the accelerator are also clearly beneficial to this aspect of the measurements.

As with any form of mass spectrometry, the accuracy of radiocarbon measurements is, in part, determined by the degree to which isotopic fractionation can be kept constant. In eliminating the production of graphite from the whole process one source of fractionation has been removed. This essentially leaves the fractionation which takes place

during ionisation and in the ion beam transport. The insensitivity of the efficiency of ion production from CO_2 to small changes in the work function suggests that there will be little fractionation due to sputtering in the gas ion source. This is important both in itself and because it indicates that the ion beams of different isotopes should have the same distribution in phase space, thereby reducing the chances of fractionation at a later stage in the measurement. Detailed consideration of the theory of sputtering also suggests that fractionation should be minimal but its complete elimination has yet to be demonstrated experimentally. The causes for fractionation in ion beam transport have been investigated and improvements to the stripper canal of the Oxford radiocarbon accelerator seem to have reduced these to such an extent that isotopic measurements of an accuracy of better than 1% are now possible. In particular the current dependent transmission of the ^{12}C ion beam through the accelerator which was due to the space charge effect has now been eliminated and this will make the correction of the $^{14}C/^{12}C$ ratio with the $^{13}C/^{12}C$ ratio possible. This enables all other sources of fractionation to be taken into account, including the incorporation of radiocarbon into the original living organism, and is essential if high accuracy is to be attained.

The research presented here on ion optics and related physical phenomena is also important for the general advancement of the now rapidly growing field of accelerator mass spectrometry. Many of the isotopes of interest (such as ^{41}Ca, ^{26}Al and ^{10}Be) have much lower negative ion formation probabilities than carbon and so a clear understanding of the fractionation due to sputtering is essential. With the expected increase in the use of high intensity sputter sources, the subject of space charge and how this relates to ion beam transport will also be important. As the accuracy demanded of these techniques increases it will clearly be necessary to look at all of these factors together.

CONCLUSIONS

The primary intention in undertaking this research was to make possible improvements in the accuracy and age range of radiocarbon measurements. Through the understanding of the physical mechanisms that underlie this technique and with the development of an ion source specifically for this purpose these objectives have now been attained.

CONCLUSIONS

EPILOGUE

It is one of the great advantages of this kind of applied research that one can, at the end of a project, still say that the best is yet to come. The fruits of this work, in terms of archaeological scholarship, will undoubtedly take time to ripen. There are many fascinating areas of research in which radiocarbon dating can play an important role: some of these, such as the study of the emergence of *homo sapiens sapiens*, may be possible for the first time because of the extension of the age range of the technique; others, like the investigation of the spread of agriculture or the end of the palace period in the Aegean will benefit from the improvements that have been made in accuracy.

In addition to these direct applications, accurate age measurements will also have an impact on the development of other archaeological techniques and on such fundamental subjects as the reliability of association and stratigraphy.

It was with these things in mind that I embarked on this project and, with optimism, I look forward to seeing the progress that is made.

..what's past is prologue, what to come
In yours and my discharge.

[William Shakespeare, The Tempest]